

SVALBARD METEOROLOGY

GUEST EDITORS: IGOR ESAU, STEFANIA ARGENTINI, RAJMUND PRZYBYŁAK, IRINA REPINA,
AND ANNA SJÖBLÖM





Svalbard Meteorology

Advances in Meteorology

Svalbard Meteorology

Guest Editors: Igor Esau, Stefania Argentini,
Rajmund Przybylak, Irina Repina, and Anna Sjöblom



Copyright © 2012 Hindawi Publishing Corporation. All rights reserved.

This is a special issue published in "Advances in Meteorology." All articles are open access articles distributed under the Creative Commons Attribution License, which permits unrestricted use, distribution, and reproduction in any medium, provided the original work is properly cited.

Editorial Board

Paulo Artaxo, Brazil
R. Barthelmie, USA
Guy Brasseur, USA
M. Ćurić, Serbia
R. Desjardins, Canada
K. Dethloff, Germany
P. Devara, India
E. Dutton, USA
Shouting Gao, China
Luis Gimeno, Spain

Sven-Erik Gryning, Denmark
Ismail Gultepe, Canada
H. Hashiguchi, Japan
D. Hauglustaine, France
Qi Hu, USA
I. S A Isaksen, Norway
Yasunobu Iwasaka, Japan
Hann-Ming Juang, USA
George Kallos, Greece
Harry Kambezidis, Greece

Markku Kulmala, Finland
Richard Leaitch, Canada
Monique Leclerc, USA
Barry Lefer, USA
Zhanqing Li, USA
Edward Llewellyn, Canada
Kyaw Tha Paw, USA
Sara Pryor, USA

Contents

Svalbard Meteorology, Igor Esau, Stefania Argentini, Rajmund Przybylak, Irina Repina, and Anna Sjöblom
Volume 2012, Article ID 818473, 3 pages

Tracing Atlantic Water Signature in the Arctic Sea Ice Cover East of Svalbard, Vladimir V. Ivanov, Vladimir A. Alexeev, Irina Repina, Nikolay V. Koldunov, and Alexander Smirnov
Volume 2012, Article ID 201818, 11 pages

Applying a Mesoscale Atmospheric Model to Svalbard Glaciers, Björn Claremar, Friedrich Obleitner, Carleen Reijmer, Veijo Pohjola, Anna Waxegård, Florian Karner, and Anna Rutgersson
Volume 2012, Article ID 321649, 22 pages

Wind Climate in Kongsfjorden, Svalbard, and Attribution of Leading Wind Driving Mechanisms through Turbulence-Resolving Simulations, Igor Esau and Irina Repina
Volume 2012, Article ID 568454, 16 pages

Estimate of the Arctic Convective Boundary Layer Height from Lidar Observations: A Case Study, L. Di Liberto, F. Angelini, I. Pietroni, F. Cairo, G. Di Donfrancesco, A. Viola, S. Argentini, F. Fierli, G. Gobbi, M. Maturilli, R. Neuber, and M. Snels
Volume 2012, Article ID 851927, 9 pages

Distribution, Composition, and Vertical Fluxes of Particulate Matter in Bays of Novaya Zemlya Archipelago, Vaigach Island at the End of Summer, N. V. Politova, V. P. Shevchenko, and V. V. Zernova
Volume 2012, Article ID 259316, 15 pages

Climatology of Total Cloudiness in the Arctic: An Intercomparison of Observations and Reanalyses, Alexander Chernokulsky and Igor I. Mokhov
Volume 2012, Article ID 542093, 15 pages

Solar Activity and Svalbard Temperatures, Jan-Erik Solheim, Kjell Stordahl, and Ole Humlum
Volume 2011, Article ID 543146, 8 pages

Temperature and Precipitation Development at Svalbard 19002100, Eirik J. Førland, Rasmus Benestad, Inger Hanssen-Bauer, Jan Erik Haugen, and Torill Engen Skaugen
Volume 2011, Article ID 893790, 14 pages

Short-Period Internal Waves under an Ice Cover in Van Mijen Fjord, Svalbard, E. G. Morozov, S. V. Muzylev, A. S. Shestov, and A. V. Marchenko
Volume 2011, Article ID 573269, 6 pages

Characteristics of Temperature and Humidity Inversions and Low-Level Jets over Svalbard Fjords in Spring, Timo Vihma, Tiina Kilpeläinen, Miina Manninen, Anna Sjöblom, Erko Jakobson, Timo Palo, Jaak Jaagus, and Marion Maturilli
Volume 2011, Article ID 486807, 14 pages

Spectral Analysis of the Svalbard Temperature Record 19122010, Ole Humlum, Jan-Erik Solheim, and Kjell Stordahl
Volume 2011, Article ID 175296, 14 pages



20-Year Climatology of NO_3^- and NH_4^+ Wet Deposition at Ny-Ålesund, Svalbard, Rafael Kühnel, Tjarda J. Roberts, Mats P. Björkman, Elisabeth Isaksson, Wenche Aas, Kim Holmn, and Johan Ström
Volume 2011, Article ID 406508, 10 pages

Editorial

Svalbard Meteorology

Igor Esau,¹ Stefania Argentini,² Rajmund Przybylak,³ Irina Repina,⁴ and Anna Sjöblom⁵

¹Nansen Environmental and Remote Sensing Centre (NERSC), Thormohlensgt. 47, 5006 Bergen, Norway

²Istituto di Scienze dell' Atmosfera e del Clima (ISAC), Consiglio Nazionale delle Ricerche (CNR), Via Fosso del Cavaliere 100, 00133 Roma, Italy

³Department of Climatology, Nicolaus Copernicus University, ul. Gagarina 11, 87-100 Torun, Poland

⁴A. M. Obukhov Institute for Atmospheric Physics, Russian Academy of Science, Pyzhevsky 3, 119017 Moscow, Russia

⁵University Centre in Svalbard, 9171 Longyearbyen, Norway

Correspondence should be addressed to Igor Esau, igore@nersc.no

Received 9 September 2012; Accepted 9 September 2012

Copyright © 2012 Igor Esau et al. This is an open access article distributed under the Creative Commons Attribution License, which permits unrestricted use, distribution, and reproduction in any medium, provided the original work is properly cited.

The Svalbard archipelago (Spitsbergen is the name of the main island, whereas Svalbard is the official name of the whole archipelago between 76°26'N (Bjørnøya) and 80°50'N (Sjuøyane) and 10°30'E and 28°10'E) is one of the most remote places on the Earth with the North Pole located just a thousand kilometers away. The total land area of the archipelago is 62,450 km², about 60% of which is covered by ice. The islands' coastline is very complex with many fjords—long, narrow inlets with steep sides or cliffs, created in a valley carved by glacial activity. Svalbard's location and topography create its unique polar-maritime climate, which is shaped by continuous fight between open water of the North Atlantic Ocean, Arctic sea ice, and mountain glaciers. Winters here are less cold than they are at any other location on these latitudes. The required heating is delivered by both the meridional atmospheric circulation and the ocean currents. It makes the climate strongly sensitive to the global scale variability. Locally, the West Spitsbergen current is the primary source of heat and moisture along Spitsbergen's west coast. This makes the climate of western and northern coasts relatively mild, with little sea ice. Eastern parts of Svalbard are influenced by a cold current coming from the northeast. This current brings cold polar water masses and a lot of drifting sea ice from the polar ocean even in the summer.

At present, inhospitable land and waters of the archipelago witness tremendous climate change and therefore attract considerable attention of the international research community. Distinct to other places in the Arctic, a significant share of the Svalbard research is driven not as episodic expeditions or field experiments but using permanent research stations.

Moreover, the Svalbard research is truly international, for example, the international research station situated at Ny Ålesund (78°55'N, 11°56'E) is operated by about 150 Norwegian, German, Japanese, Italian, French, and UK researchers and open for researchers of other nations. This station is included into the International Arctic System for Observing the Atmosphere (<http://iasoa.org>). The University Centre in Svalbard (UNIS) is the world's northernmost institution for higher education and research, located in Longyearbyen, Spitsbergen at 78°N.

The combination of the challenging research problems and opportunities to drive the high quality research on the archipelago has already resulted in extensive scientific production. Figure 1 shows historical development of the number of publications (according to ISI Web of Science) discussing one or another aspect of the Svalbard meteorology. In total, more than 1500 publications appeared since 1980. The recent International Polar Year has brought more research results to be reported. This development and importance of the polar research to humanity motivated us to organize this special issue.

Regular meteorological observations on Svalbard are known since the period of the first International Polar Year (1882-1883). Since 1911, observations were regularly conducted in the area of Isfjorden on the west coast. This long observational record in the high latitude region with large natural variability makes Svalbard particularly interesting and important for climate studies. Therefore it is not surprising that a large part of contributions to this issue is dealing with the analysis of the temperature record from Isfjorden

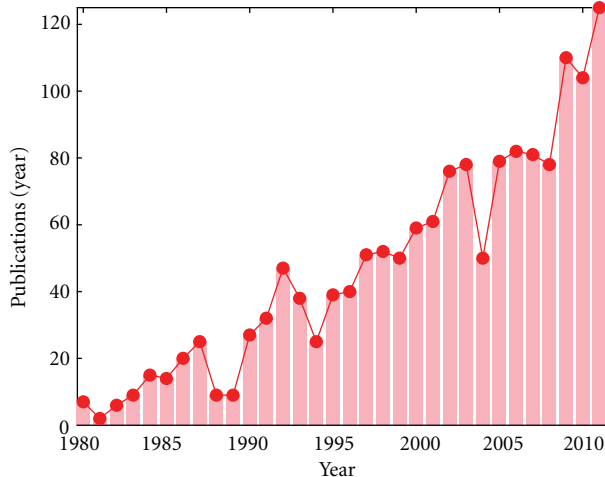


FIGURE 1: Number of publications by years dealing with one or another aspect of Svalbard meteorology according to ISI Web of Science data base.

(see Figure 2). Many authors have analyzed temperature and precipitation development, variability and trends. For all temperature series, positive linear trends were found for annual values as well as spring, summer, and autumn series. A very strong winter warming was identified for the latest decades. Significant changes were also observed in other essential climate variables, for example, in the total cloudiness, aerosols, and precipitation. Mean annual total nitrogen deposition was $74 \text{ mg N}/(\text{m}^2 \text{ yr})$ but exhibited large interannual variability and was dominated by highly episodic “strong” events. Trends of reactive nitrogen emissions from Europe are uncertain, and increasing cyclonic activity over the North Atlantic caused by a changing climate might lead to more strong deposition events in Svalbard.

Although the temperature trends are clearly identified in observations, attribution of specific climate change causes remains less certain in the region due to the mentioned large impact of nonlocal advective processes, teleconnections, and long-term variability. This makes the attribution of the regional climate records distinct to the attribution on the larger continental and global scales published elsewhere. Temperature trends downscaled from global climate models forced with observed greenhouse gas emissions span the observation-based trends at Svalbard Airport 1912–2010. Novel projections focusing on the Svalbard region indicate a future warming rate for winter months up to year 2100 three times stronger than that observed during the latest 100 years. The average winter temperature in the Longyearbyen area at the end of this century is projected to be around 10°C higher than in present climate. Also for precipitation, the long-term observational series indicate an increase and the projections indicate a further increase up to year 2100. At the same time, natural variability is also strongly decreasing the signal-to-noise ratio in attribution studies. It was found that temperature at Svalbard is negatively correlated with the length of the solar cycle. The strongest negative correlation is found with lags of 10–12 years. The relations between

the length of a solar cycle and the mean temperature in the following cycle are used to model Svalbard annual mean temperature and seasonal temperature variations. These models show that 60 per cent of the annual and winter temperature variations are explained by solar activity. XXIst century temperature prediction by a statistical model is rather opposite to the prediction of the green-house gas forcing driven models. The statistical model predicts an annual mean temperature decrease for Svalbard from solar cycle 23 to solar cycle 24 (2009–20) and a decrease in the winter temperature could be as large as -6°C . As Figure 2 shows, there is no clear signal yet.

It is worth to emphasize that the Svalbard surface layer climate is significantly modified by the specific climate conditions of fjords and mountain valleys. Hence, interpretation of numerical simulation results where those specific conditions are not properly reproduced, such as in the state-of-the-art climate models, must be done with care. Similarly, the statistical relationships could depend on dominant circulation patterns in the region and therefore must be also extrapolated with care. Chapman and Walsh [2] and Alexeev et al. [3] disclosed particularly large discrepancies between different reanalyses and models in the Svalbard–Barents Sea region. Fine-resolution regional simulations by Kilpeläinen et al. [1, 4] demonstrated that climate conditions in the fjords could be significantly different from those over open areas. Moreover, the modeled temperature can differ by several degrees depending on model resolution and weather conditions.

Observational studies in Svalbard fjords (e.g., Isfjorden and Kongsfjorden) are now done using the most advanced instrumentation, for example, applying three tethered systems and a new lidar system (MULID). The inversion strength and depth were strongly affected by weather conditions at the 850 hPa level. Strong inversions were deep with a highly elevated base, and the strongest ones occurred in warm air mass. Unexpectedly, downward longwave radiation measured at the sounding site did not correlate with the inversion properties. Most low-level jets were related to katabatic winds. Over the ice-covered Kongsfjorden, jets were lifted above a cold-air pool on the fjord; the jet core was located highest when the snow surface was coldest. At the ice-free Isfjorden, jets were located lower. The conclusions that most jets are of katabatic origin are challenged with turbulence-resolving simulations. This work suggested the leading roles of the thermal land-sea breeze circulation and the mechanical wind channeling in the modulation of the valley winds. The characteristic signatures of the developed down-slope gravity accelerated flow, that is, the katabatic wind, were found to be of lesser significance under typical meteorological conditions. Modellers simulated the atmospheric conditions over three Svalbard glaciers using the ERA-Interim reanalysis for boundary forcing and three nested model grids with 24 km, 8 km, and 2.7 km resolutions. They concluded that the choice of different physics schemes only slightly changed the model results. The polar-optimized microphysics scheme outperformed a slightly simpler microphysics scheme, but the two alternative and more sophisticated planetary boundary layer (PBL) schemes

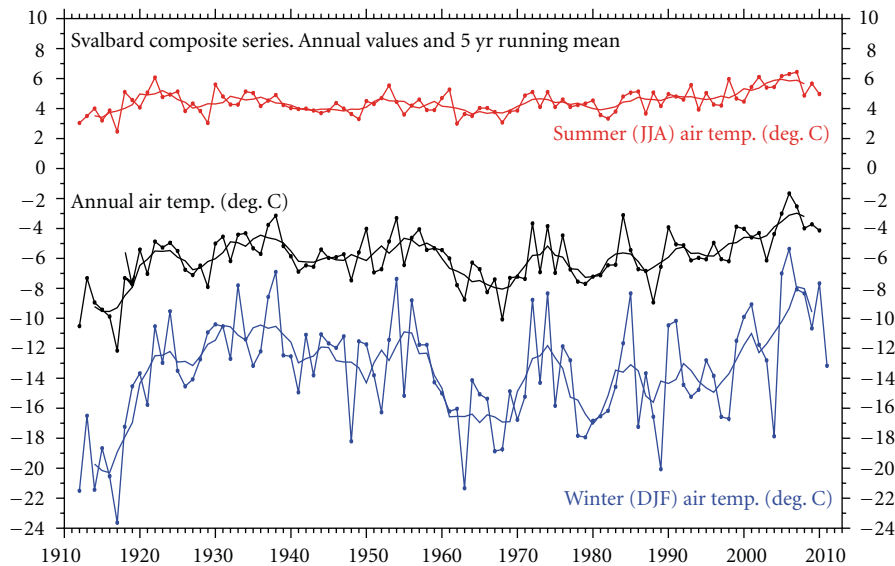


FIGURE 2: The Svalbard temperature record 1912–2010, showing the mean annual air temperature (MAAT), the average summer temperature (JJA), and the average winter temperature (DJF). Thin lines show annual values, and thick lines show the simple 5 yr average (extracted from [1]).

improved the model score. It should be noted that the polar PBL is rather different from its low- and midlatitude counterparts as the horizontal heat advection and negative surface radiation balance maintain temperature inversions over long periods of time.

The Svalbard meteorology is considerably affected by processes in the ocean surrounding the archipelago. Studies of the Arctic Ocean between Svalbard and Franz Joseph Land elucidate the possible role of Atlantic water (AW) inflow in shaping ice conditions. Ice conditions substantially affect the temperature regime of the Spitsbergen archipelago, particularly in winter. The hypothesis is that intensive vertical mixing at the upper AW boundary releases substantial heat upwards that eventually reaches the underice water layer, thinning the ice cover. Analysis of 1979–2011 ice properties revealed a general tendency of decreasing ice concentration that commenced after the mid-1990s. AW temperature time series in Fram Strait feature a monotonic increase after the mid-1990s, consistent with shrinking ice cover.

The contributions to this special issue present not only diversity of the research activity at Svalbard but also complexity of the specific high-latitude environmental phenomena to be studied. They also indicate the need for better integration of research in different scientific fields and disciplines. Unfortunately, the large amount of meteorological observations and other research data remains unavailable for broader research community. Many datasets need careful quality control and homogenization. The discrepancies between model results and observations are to be better attributed and need to be significantly reduced. Recently, these needs were finally met and addressed in European and national research programs, for example, the Norwegian Polar Program (http://www.forskningradet.no/prognett-polarforskning/Home_page/1231229969357).

Acknowledgments

We, the guest editors of this special issue of *Advances in Meteorology* (AMET), are grateful to all of the authors, reviewers, and AMET staff and especially to Ghada Ali whose help and polite guidance we appreciate a lot.

Igor Esau
Stefania Argentini
Rajmund Przybylak
Irina Repina
Anna Sjöblom

References

- [1] T. Kilpeläinen, T. Vihma, and H. Ólafsson, “Modelling of spatial variability and topographic effects over Arctic fjords in Svalbard,” *Tellus A*, vol. 63, no. 2, pp. 223–237, 2011.
- [2] W. L. Chapman and J. E. Walsh, “Simulations of Arctic temperature and pressure by global coupled models,” *Journal of Climate*, vol. 20, no. 4, pp. 609–632, 2007.
- [3] V. A. Alexeev, I. Esau, I. V. Polyakov, S. J. Byam, and S. Sorokina, “Vertical structure of recent Arctic warming from observed data and reanalysis products,” *Climatic Change*, vol. 111, no. 2, pp. 215–239, 2012.
- [4] T. Kilpeläinen, T. Vihma, M. Manninen et al., “Modelling the vertical structure of the atmospheric boundary layer over Arctic fjords in Svalbard,” *Quarterly Journal of the Royal Meteorological Society*. In press.

Research Article

Tracing Atlantic Water Signature in the Arctic Sea Ice Cover East of Svalbard

Vladimir V. Ivanov,^{1,2,3} Vladimir A. Alexeev,² Irina Repina,⁴
Nikolay V. Koldunov,⁵ and Alexander Smirnov¹

¹Arctic and Antarctic Research Institute, St. Petersburg 199397, Russia

²International Arctic Research Centre, University of Alaska, Fairbanks, AK 99775, USA

³Scottish Marine Institute, Oban PA37 1 QA, UK

⁴A.M. Obukhov Institute of Atmospheric Physics of RAS, Moscow 119017, Russia

⁵Institute of Oceanography, University of Hamburg, 20146, Hamburg, Germany

Correspondence should be addressed to Vladimir V. Ivanov, vladimir.ivanov@sams.ac.uk

Received 7 February 2012; Revised 20 March 2012; Accepted 22 March 2012

Academic Editor: Igor N. Esau

Copyright © 2012 Vladimir V. Ivanov et al. This is an open access article distributed under the Creative Commons Attribution License, which permits unrestricted use, distribution, and reproduction in any medium, provided the original work is properly cited.

We focus on the Arctic Ocean between Svalbard and Franz Joseph Land in order to elucidate the possible role of Atlantic water (AW) inflow in shaping ice conditions. Ice conditions substantially affect the temperature regime of the Spitsbergen archipelago, particularly in winter. We test the hypothesis that intensive vertical mixing at the upper AW boundary releases substantial heat upwards that eventually reaches the under-ice water layer, thinning the ice cover. We examine spatial and temporal variation of ice concentration against time series of wind, air temperature, and AW temperature. Analysis of 1979–2011 ice properties revealed a general tendency of decreasing ice concentration that commenced after the mid-1990s. AW temperature time series in Fram Strait feature a monotonic increase after the mid-1990s, consistent with shrinking ice cover. Ice thins due to increased sensible heat flux from AW; ice erosion from below allows wind and local currents to more effectively break ice. The winter spatial pattern of sea ice concentration is collocated with patterns of surface heat flux anomalies. Winter minimum sea ice thickness occurs in the ice pack interior above the AW path, clearly indicating AW influence on ice thickness. Our study indicates that in the AW inflow region heat flux from the ocean reduces the ice thickness.

1. Introduction

Steady reduction of the Arctic sea ice cover throughout 1990s has accelerated in the 2000s [1, 2]. As demonstrated in the recent studies, causative mechanisms for the extreme ice area/volume decay include an anomalous atmospheric circulation which forced ice out of the Canadian Basin towards Fram Strait [3, 4], the influence of warm inflow through Bering/Fram straits [5, 6], and the melting effect of warmed surface water [7]. However, long-term preconditioning occurred during three decades of steady ice thinning [8, 9]. This was largely a result of the fact that the Arctic has warmed up about twice as fast as lower latitudes due to the so-called polar amplification [10–12]. Years of reduced ice growth in winter and enhanced ice melt in summer led to the dominance of first-year ice over multiyear ice after 2004 [13].

Under conditions of enhanced seasonality, the influence of ocean heat on Arctic ice cover is expected to grow. The retreating summer ice edge increases the size of the marginal ice zones (MIZs)—the transient areas between open water and totally ice-covered ocean. For the Spitsbergen region, this process is particularly important due to the existence of an extended open water area (a quasi-steady-state polynya) bordered by an MIZ, the so-called Whalers Bay, close to the northern coast of the archipelago. In winter the presence of the large-scale open water zone substantially shapes local weather conditions, keeping air temperature well above average values for similar latitudes around the Arctic.

Large changes in the state of the ocean surface over the limited distance of MIZs build up high horizontal gradients of properties in the oceanic and atmospheric boundary layers below and above the MIZ. High gradients trigger horizontal

motions in both media, providing favourable prerequisite conditions for intensive heat, moisture, and momentum exchange across the ocean-ice-air interface. This is true for the Pacific sector (circa 120°E–120°W), where the most dramatic ice edge retreat was reported in 2007 and 2011 (<http://nsidc.org/arcticseaicenews/>). On the opposite side of the Arctic Ocean the ice edge deviation from the climatic mean location was substantially smaller, for example, Figure 1 in [7]. Such anisotropy indicates that despite the fact that the strongest heat input to the high Arctic is associated with the eastward moving Atlantic cyclones and warm inflow of Atlantic-origin water through the Nordic Seas, the ice cover in the Atlantic sector seems to be rather insensitive to the increased heat impact from the lower latitudes [14]. In the present study, we use observational/reanalysis data and recent findings on the properties of the Atlantic water (AW) inflow to figure out whether this is actually the case.

We focus on the region of the Arctic Ocean between Svalbard and Severnaya Zemlya archipelagos, which is further referred to as the Western Nansen Basin (WNB: 15–60°E, 81–83°N). This is an area of complex ocean-ice-atmosphere interactions resulting in isolation of the inflowing AW from direct contact with ice and atmosphere. We base our study on the hypothesis that this isolation is primarily the consequence of intensive vertical mixing at the upper AW boundary. As a result, a substantial fraction of heat is released upwards contributing to the heat budget of the under-ice water layer and impacting the ice cover. Recent findings show conservation of a strong seasonal signal in the AW temperature at the location where the warm current encounters pack ice [15]. This conservation allows extensive penetration of warm “summer” AW into the subsurface layer (above 100 m) below the pack ice. We examine spatial and temporal variation of WNB ice concentration against relevant time series of wind, air temperature, and AW temperature. The main objective of this analysis is to separate the direct dynamic influence of wind from thermodynamic effects provided by heat fluxes at the ice-air and ice-water interfaces in order to assess the relative importance of the latter.

Following the paper objective, we introduce the physical concept of AW transformation into the intermediate water mass (Section 2), describe temporal and spatial variations of WNB ice concentration from 1979–2011 (Section 3), and discuss possible links between these variations and the most probable influential factors, including wind, air temperature, and AW temperature (Section 4). Discussion of the results and major conclusions are given in Section 5.

2. Atlantic Water Transformation East of Svalbard

A schematic of the two inflow branches is shown in Figure 1. The Barents sea branch of Atlantic water (BSBW) stays at the surface while in the Barents Sea. As a result, after this water finally reaches the Arctic Ocean interior it has substantially cooled and freshened. Contrary to BSBW, the Fram Strait branch of Atlantic water (FSBW) rapidly leaves the surface,

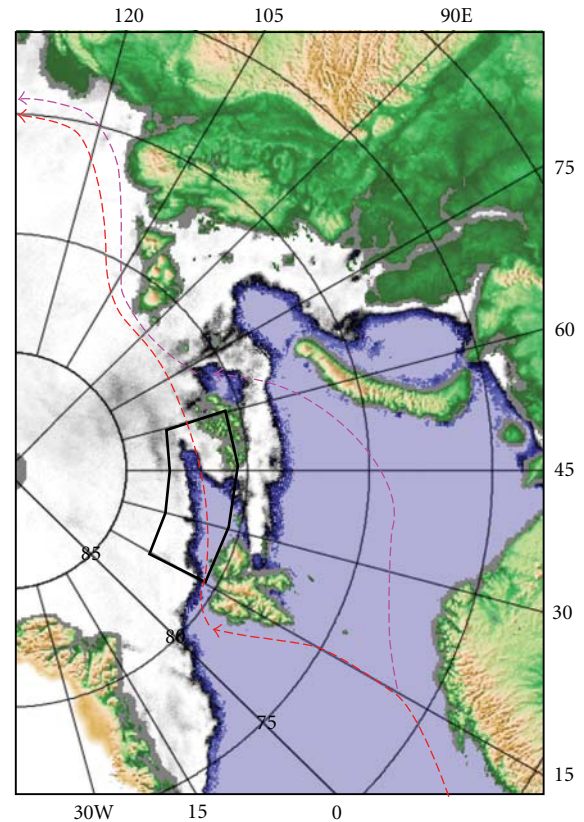


FIGURE 1: Schematic of two inflow branches (FSBW is shown in red and BSBW is shown in pink) of the AW against the special sensor microwave imager/Sounder (SSMIS) visual chart of ice concentration on February 4, 20112 (<http://www.iup.uni-bremen.de:8084/ssmis/index.html>). The Western Nansen Basin (WNB) area is marked by a black trapezium.

transforming into Arctic intermediate water (AIW). Due to this separation from the surface, AIW retains a large amount of its initial heat and salt, which are further transported around the deep ocean interior.

According to the Arctic Ocean climatology, north of Svalbard FSBW is capped by a cold and relatively fresh mixed water layer all year round [16]. The origin of this mixed layer is still under discussion. The traditional hypothesis states that this layer contains Arctic surface water which moves generally towards Fram Strait, opposing the FSBW inflow. Since this water is lighter than FSBW, it overlays the latter causing FSBW to sink beneath the surface mixed layer [17]. Westward flow in the surface mixed layer is consistent with the large-scale ice motion observed in the Arctic Ocean, for example Figure 1(e) in [18]. An alternative hypothesis suggests that the surface mixed layer originates directly in the upper part of inflowing AW, which cools down via heat loss to the atmosphere and freshens due to mixing with melted ice water [19]. This newly formed surface layer follows the warm bulk of AIW moving eastward along the continental slope, except for a very thin under-ice layer, which is deflected westwards by the drifting ice. Basically, both hypotheses agree that there must be some depth inside

the water column at which the current turns around. The difference between these hypotheses is the depth at which this change of direction occurs. Observational data collected using traditional oceanographic methods, like occasional conductivity/temperature/depth (CTD) profiling at a limited number of transects, does not provide reliable justification for either of these hypotheses. For example, the typical inclination of isotherms between Svalbard and Franz Joseph Land (Figure 2) may be caused either by submerging of the AW water as it travels from west to east, or by cooling of the upper part of AW en route.

Recent measurements made at the autonomous moored station within the framework of the Nansen and Amundsen Basins Observational System (NABOS) project (<http://www.iarc.uaf.edu/nabos.php>) revealed strong seasonal variability in the inflowing FSBW (Table 1), which is conserved in the AIW far to the east of Fram Strait [20]. We suggest that this new knowledge provides some clue to understanding the FSBW transformation process. Applying the data from Table 1, we estimate that to increase the temperature of the $H = 217$ m thick layer over a unit square by $\Delta\bar{T} = 4.76$ K (the difference between the May and November vertically averaged temperature, under the assumption that the ocean surface is permanently at the freezing point), 4.2×10^9 J of heat is required (using the specific heat of sea water at constant pressure, $c_p = 4 \times 10^3$ J/kg/K and water density $\rho = 1.028 \times 10^3$ kg/m³). Where does this heat come from? A crucial difference between the Arctic Ocean interior and the waters to the south is that summer warming due to the flux at the sea surface is tiny in the Arctic and is limited to a thin surface layer. A substantial part of the absorbed heat is spent on ice melting, thus it contributes little to the net water temperature increase. Therefore, the observed seasonal increase of heat content could only be caused by advection of warmer water, and not by the local ocean-air energy exchange. In contrast, seasonal cooling might be attributed to high negative local heat loss, which overcomes the positive advective influx.

The heat balance equation in the finite differences form may be written as follows:

$$c_p \rho H \frac{\Delta\bar{T}}{\Delta t} = Q - A, \quad (1)$$

where Δt is the time interval, Q is the heat flux due to all nonadvective processes, and A is the heat flux caused by advection. Presuming that A is always negative, that is, the water coming from the west is warmer than the water at the position of the mooring, the change of sign on the left side of (1) is determined by Q . Positive $\Delta\bar{T}/\Delta t$ means that $Q - A > 0$. This is what happens in the warming season. During the cooling season, $Q - A < 0$. As shown in [15], the most probable reason for high negative Q in winter is thermal convection, which in the area of Whalers Bay (north of Svalbard) is able to reach deep into the water column [21].

Using the data from Table 1, and considering the water at the ocean surface to be permanently at the freezing point temperature, we can estimate heat loss from the upper 217 m, under the assumption of small seasonal

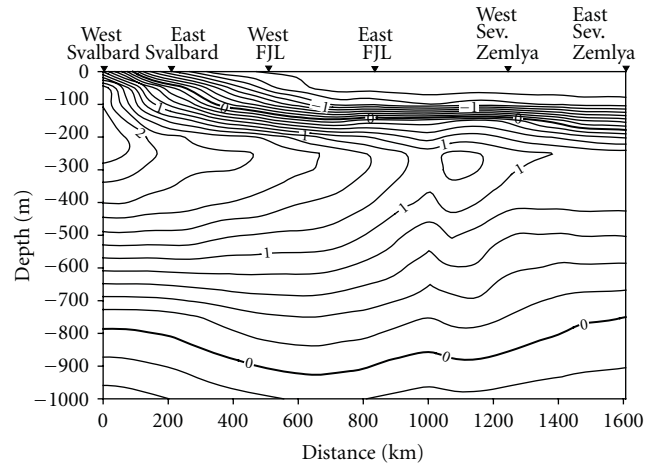


FIGURE 2: Temperature, °C section along the FSBW inflow in summer season (EWG, 1998) (FJL: Franz Joseph Land).

variation of advection [15]. Substituting vertically averaged temperature change between April-May and November in (1) and neglecting Q yields A equal to -235 W/m². Using this number for the cooling phase and taking into account the difference between the duration of warming and cooling seasons, we obtain an average heat loss of 560 W/m². This is a huge heat loss, having the same order of magnitude as is typically estimated for Arctic winter polynyas [22]. This number also matches well with the heat flux calculations done for the MIZ in the Barents Sea in winter [23]. Aagaard et al. [21] estimated winter heat loss in Whalers Bay from the 100–200 m layer to be 230 W/m². Applying the same equation (1) for the 113–217 m layer yields a similar result, 220 W/m². In the light of these numbers, the estimate done in [24], suggesting an increased surface heat loss of about 300 W/m² during pulses of anomalously warm AW inflow through Fram Strait, is also quite reasonable.

Progressive vector diagrams close to the core of the boundary current at 30°E calculated on the basis of 1-year-long continuous current meter measurements with 1-hour resolution show that the entire 70–217 m water layer is moving generally eastward with an average speed of 12–17 cm/s [15]. This indicates that the opposite motion (towards Fram Strait) may occur only in the subsurface layer above 70 m depth. The water at this level is apparently AW all year round despite the fact that its temperature may drop down to the freezing point. The AW “signature” is identified not by characteristic temperature and salinity values, but by the constant shape of the temperature-salinity (T-S) relationship [15]. Taking into account the steadiness of the flow direction and speed, we can argue that the actual cutoff depth of the reverse current is shallower than 70 m. Another argument in favor of this notion follows from the vertical distribution of temperature and salinity at cross-slope sections near the mooring position, see Figure 2 in [15]. In September 2006, the warm water core (over 5°C) resided at 50 m, while positive temperature water spread up to the ocean surface. A sharp salinity gradient at the 25–30 m depth

TABLE 1: Amplitude and phase of seasonal cycle in water temperature at 80°30'N and 31°E [15].

Depth (m)	Maximum, daily data		Minimum, daily data	
	Date	(T) °C	Date	(T) °C
70 ± 5	Nov 16 ± 10	5.12 ± 0.12	Apr 13	-1.77 ± 0.05
113 ± 5	Nov 16 ± 8	4.81 ± 0.17	Apr 23 ± 3	-0.40 ± 0.33
217 ± 5	Nov 24 ± 17	4.27 ± 0.29	May 13 ± 2	2.02 ± 0.06

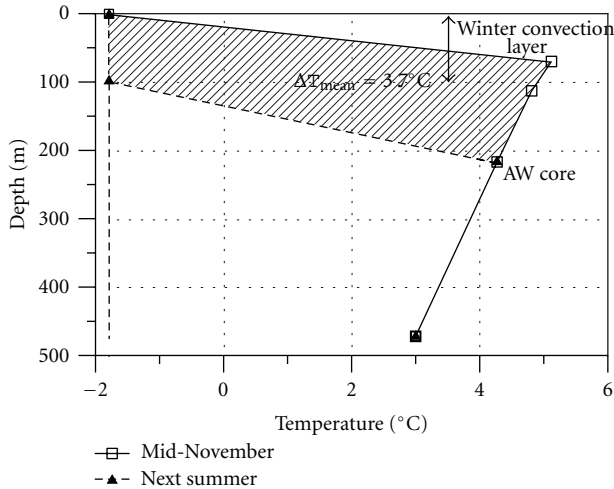


FIGURE 3: Sketch of the upper FSBW transformation during the winter season.

marks the location of the AW upper boundary in the vertical plane. The shape of the T-S relationship inside the 30–70 m layer also matches very well the typical AW T-S relationship, indicating that the water in this layer contains a considerable AW fraction.

The strong seasonal variation of heat content in the upper part of the water column at the mooring position in conjunction with the eastward direction of flow implies that a substantial amount of heat is advected by the boundary current. A persistent current moves warm water further to the east, bringing the upper part of this warm layer into close contact with pack ice drifting in the opposite direction. Taking into account that further to the east (in the Laptev Sea) the upper boundary of AW deepens to 150–200 m, we can anticipate that the heat stored above this depth is released en route, warming the under-ice layer. Applying simple theoretical considerations to the mid-November temperature profile from Table 1 enables us to estimate the order of magnitude of heat loss from the upper part of the water column. The evolution of temperature from mid-November to the following summer is sketched in Figure 3. Presuming that winter convection depth in the WNB is about 100 m [25], we calculate a mean temperature decrease above the AW core of 3.7°C. Applying this decrease of temperature to six winter-spring months yields a total heat loss of about 200 W/m². If only 7% of this heat goes upward [6], we calculate the value of heat flux from the ocean to the ice to be 7 times larger than the conventional mean

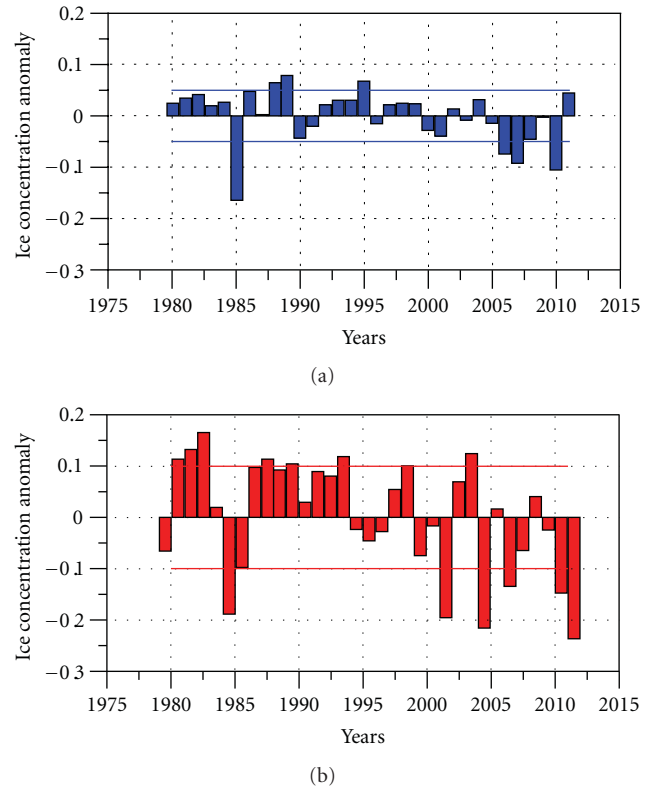


FIGURE 4: Time series of ice concentration (in parts of the unit) in the WNB (winter: blue; summer: red).

value [26]. This estimation points out that a considerable portion of seasonal heat input into the upper part of the WNB water column might be spent on ice melt and released to the atmosphere.

3. Structure and Variability of WNB Ice Conditions from 1979–2011

Data on ice concentration were taken from the Nimbus-7 Scanning Multichannel Microwave Radiometer (SMMR), and the Defense Meteorological Satellite Program (DMSP) Special Sensor Microwave/Imager (SSM/I), and Passive Microwave Data dataset [27, <http://nsidc.org/data/nsidc-0051.html>]. A brief description of these data is given in the Appendix. Time series of mean spatial winter and summer ice concentration (MSIC) in parts of the unit in the WNB are presented in Figure 4. Winter season was defined from November 1 to May 31 and summer season

from June 1 to October 31. In winter, average MSIC is 0.88 ± 0.05 , while in summer, it is 0.72 ± 0.10 . Statistical properties are not uniform across time. Two distinct periods can be seen, with the border between them around 1995–1999. During the 1st time interval (1979–1995), positive MSIC anomalies prevail. There are 13 positive anomalies versus 3 negative in winter season and 12 positive versus 4 negative in summer. Values of anomalies lie within, or slightly exceed simple standard deviation (SSD) bounds. The only exception is the year 1985, which is characterized by large and coherent summer-winter negative anomalies. Anomalies exceed the SSD about twice in summer and more than 3 times in winter. During the 2nd time interval (1999–2011), the general pattern of anomalies is the opposite. In winter there are 8 negative anomalies versus 3 positive, while in summer there are 9 negative anomalies versus 4 positive. The negative anomalies often substantially exceed SSD, especially in summer. Although the time series are too short for performing robust correlation analysis, formal calculation shows that the correlation coefficient between the preceding summer and the next winter anomaly drops from 0.5 (in 1979–1995) to 0.1 (in 1999–2011). This suggests that the processes which control ice concentration during time intervals with high and low ice concentrations are not the same.

The difference between the average ice concentrations during two selected periods are plotted in Figure 5. In both seasons, ice concentration decreased during the 2nd time interval over the entire WNB area. In summer the maximum ice concentration decrease (-0.3) occurs within the WNB. Further to the north, the difference between the two time intervals is close to zero. The latter is explained by the fact that the region to the north of 83°N in the Atlantic sector of the Arctic Ocean is the “pack ice collector” for the new ice forming in Siberian shelf seas and being driven towards Fram Strait in the Transpolar Drift system [17]. In winter season the largest differences extend along two branches of AW (compare with Figure 1). During the 2nd time interval low-concentration “tongues” associated with two branches of AW merge, forming the large area with decreased ice concentration in the northern part of the Barents Sea and over the continental margin of the Nansen Basin (this plot is not shown).

In line with our basic hypothesis, which implies a substantial contribution of oceanic sensible heat in shaping the ice cover in the WNB (see Figure 1), we considered the unique ice thickness measurements made within the framework of the Ice, Cloud, and land Elevation Satellite (ICESat) campaigns [[28] <http://rkwok.jpl.nasa.gov/icesat/download.html>]. Two sequential maps showing ice thickness in October–November, 2007 (ON2007) and February–March, 2008 (FM2008) are presented in Figure 6. Our choice of 2007–2008 is dictated by the record summer minimum ice extent in the Arctic Ocean in 2007. Despite the record retreat of the ice edge in the Pacific sector, summer ice extent in the WNB was close to normal, which is reasonably explained by dynamics [29]. The FSBW pathway along the continental slope between Svalbard and Franz Joseph Land is within the seasonal summer MIZ; this does not provide any arguments

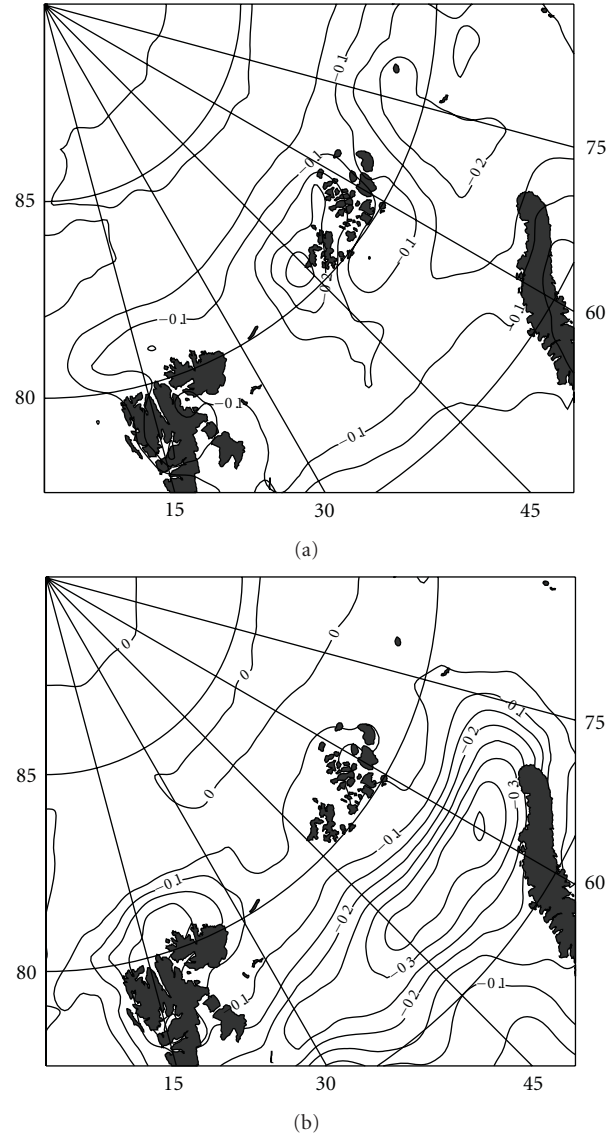


FIGURE 5: Difference between the average ice concentrations in the WNB in 1999–2011 versus in 1979–1995 in summer (a) and in winter (b).

for or against the hypothesis that AW heat impacts ice properties. A very different picture appears during the next winter survey (Figure 6(b)). The ice edge is shifted far to the south of the WNB. However, the local minimum ice thickness, surrounded by thicker ice, stretches from Svalbard to Severnaya Zemlya Archipelagos, visibly marking the FSBW inflow pathway.

Putting together the revealed features of mean seasonal distribution and interannual variability of ice concentration in the WNB and ice thickness data from 2007–2008, we suggest the following. The spatial patterns of ice distribution in winter and in summer are not the same. In winter, zones of decreased ice concentration extend along the branches of AW inflow, while in summer ice concentration decreases uniformly northward. Summer and winter MSIC

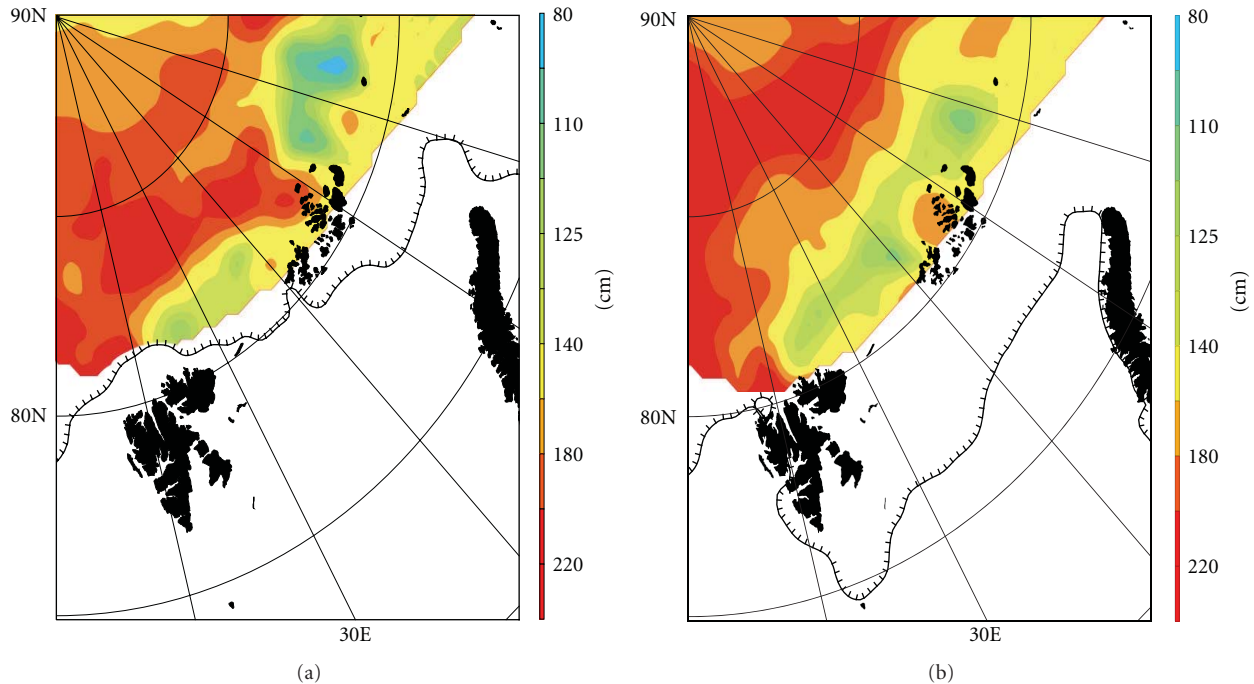


FIGURE 6: October–November, 2007 ice thickness (a); February–March, 2008 ice thickness (b). Black solid lines show the location of the ice edge, defined by 15% ice concentration.

time series are divided into two specific intervals: 1979–1995, with generally higher ice concentration and 1999–2011, with generally lower ice concentration. During the 1st time interval, the winter MSIC inherits features of the preceding season (summer–winter correlation coefficient is equal to 0.5). During the 2nd time interval, there is no link between summer and winter ice concentrations. Available ice thickness measurements support the notion that a substantial amount of heat reaches the under-ice surface and melts ice from below, rendering it thinner and more fragile. This process is especially noticeable in the winter season, when most of the Arctic Ocean is ice covered. In the next section, we test this observation-based hypothesis against available oceanographic and meteorological data and atmospheric reanalysis products in a search for the causative mechanisms that shape the sea ice cover in the WNB.

4. Causative Mechanisms

To elucidate possible mechanisms responsible for the observed features of the WNB ice conditions, we consider the following time series: (i) FSBW temperature at the WNB entry point; (ii) meridional wind component over the WNB; (iii) air temperature and surface–air temperature difference; (iv) sensible heat flux at the ocean surface. For this task, we used reanalysis products (<http://www.ecmwf.int/research/era/do/get/era-interim>). The features of this data set are briefly described in the Appendix.

FSBW interannual variability near the entry point. Annual time series of AW temperature were generated inside the cell bounded by 78–80°N and 5–10°E. This is the mean

climatic position of the West Spitsbergen Current main stream, see Figure 3 in [24]. The data from the Arctic and Antarctic Research Institute (AARI) collection were used [30]. We consider two water layers: 100–200 m and 200–300 m (Figure 7). This choice is explained by the features of AW transformation in the AIW discussed in Section 2. Provided that the concept of AW intensive mixing in the upper part is correct the layer shallower than ~200 m initially contains the heat, which is totally released upwards and laterally during the FSBW transit from Fram Strait to the Laptev Sea. The layer below ~200 m retains a large portion of its initial heat content up to where the AIW terminates its full circuit around the Arctic Ocean interior. Within the considered time interval (1979–2011) the temperature in both AW layers coherently increased. However, this increase was not monotonic, but rather cyclic with an 8–10-year period. The background positive trend is 1.5° per 32 years in the upper layer and 1.25° per 32 years in the lower layer. It is worth mentioning that after the most recent temperature increase, which culminated in 2007, the temperature did not drop back to the initial point as happened earlier, but remained about 1°C higher in both layers, leading to the conclusion that AW in the Arctic Ocean is shifting to a new warmer state [31, 32]. Hence, there is no doubt that the heat input to the Arctic Ocean interior has substantially increased since the end of the 1990s. The question is has this increased heat input provided the major forcing of the documented change in ice properties in the WNB? To answer this question let us examine the other potentially significant mechanisms.

Wind stress is usually considered to be the primary forcing which creates open water zones in the consolidated ice cover in winter [33]. Well-known quasi-steady-state

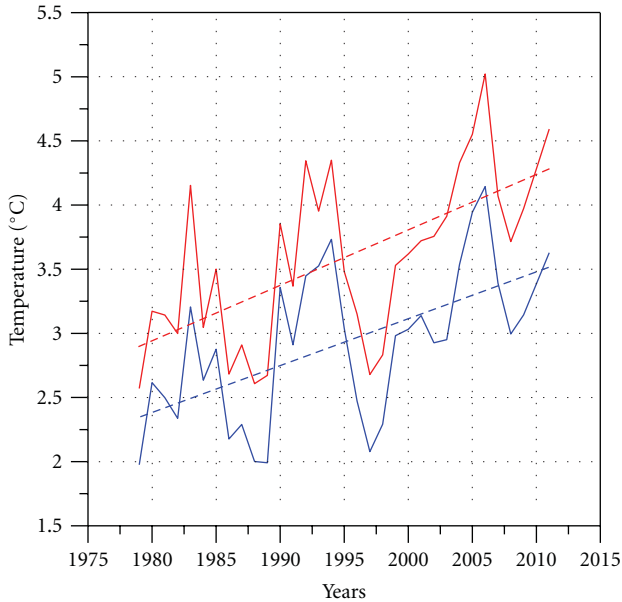


FIGURE 7: Water temperature in the core of the West Spitsbergen current at 79°N; red: 100–200 m layer; blue: 200–300 m layer.

polynyas along the Eurasian and American coastline are formed by katabatic wind and local currents which break up the fast ice and drive ice floes offshore [34]. In the conventional terminology such a polynya is known as a latent heat polynya (LHP) [35]. Another type of polynya, the sensible heat polynya (SHP), is thermodynamically driven and typically occurs when warm water upwelling keeps the surface water temperature above the freezing point. Favorable wind may also assist in maintaining an open SHP, but the major role is played by oceanic heat. To determine whether variation of the WNB open water area in winter is caused by wind stress, we plotted the time series of the meridional surface wind component in two localized regions where an increased area of open water was observed during the 2nd time interval (see Figure 8). No visible trends in the meridional wind component can be inferred from this plot or from the time series of wind speed (not shown), thus removing wind from the list of likely causative mechanisms.

Air temperature variation is another obvious candidate to be linked with the observed changes in the ice cover. In Figure 9, one can see that air temperature changed around the mid-1990s, at which time air temperature started to increase almost monotonically, which is in line with the ice concentration change. At about the same time the air-surface temperature difference decreased and then stayed at almost the same level up until present with a very weak upward tendency (Figure 10).

Wind speed and air-surface temperature difference determine sensible *heat flux* at the ocean ice/air interface [36]. In the absence of short-wave radiation (in winter season), sensible heat flux is the major contributor to the surface-air energy balance. The shape of the sensible heat flux curve in winter season (Figure 11) is very similar to the air-sea temperature difference curve, with a tipping point around

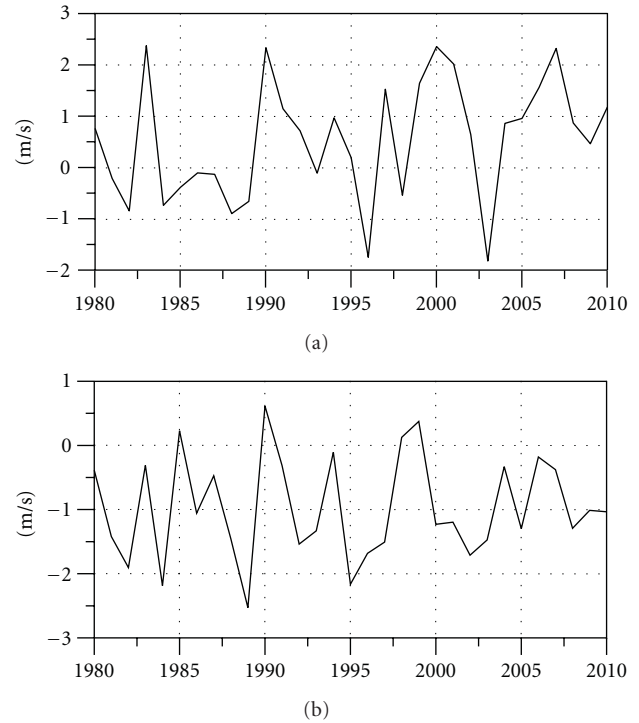


FIGURE 8: Meridional wind component in winter around Franz Joseph Land (a) and north of Svalbard (b).

1995. However, it is important to note that the sensible heat flux shows more of a tendency to increase than does the air-surface temperature difference after 1995.

5. Discussion and Conclusions

Our analysis of WNB ice properties from 1979–2011 allowed us to detect a general tendency towards decreasing ice concentration that commenced after the mid-1990s. Combining the ice concentration data and the available ice thickness data allowed us to demonstrate that the location of local zones with thinner ice and lower ice concentration essentially mirror the pathway of the FSBW in the WNB. Time series of FSBW temperature in Fram Strait feature a monotonic increase after the mid-1990s, consistent with shrinking ice cover. This coincidence provides solid ground for the hypothesis that a substantial amount of the AW heat in the WNB is able to reach the under-ice layer and contribute to the ice melting from below. On the other hand, there is evidence in reanalysis products that WNB air temperature has exhibited trends consistent with those of ice concentration and FSBW temperature. Therefore, the question to pose is as follows. Are one or more of these correlated processes drive the observed changes, or is the driver of something else entirely? To answer this question let us briefly outline the physical background of ocean-ice-air interaction. In the ice-covered seas a key factor controlling the rate of energy exchange is the spatial irregularity of the ice cover. Irregularity primarily depends on the ice concentration and thickness [37]. Under similar

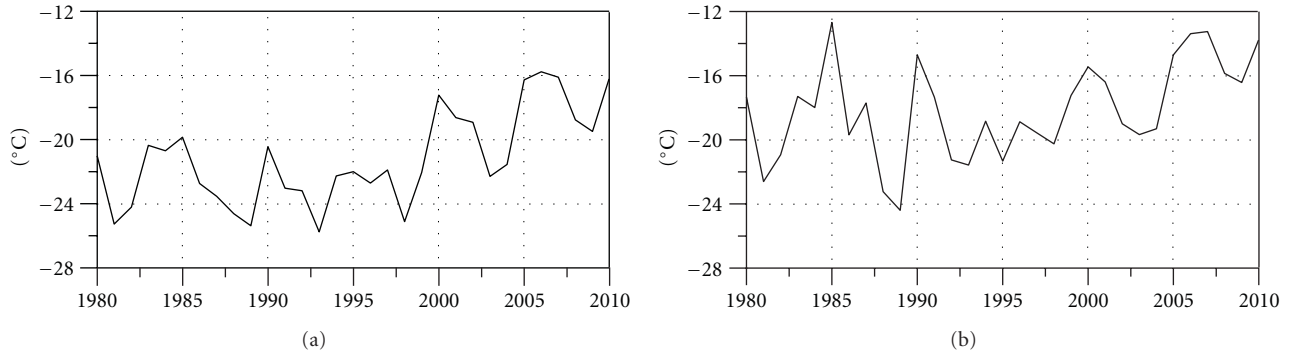


FIGURE 9: Air temperature at the surface in winter around Franz Joseph Land (a) and north of Svalbard (b).

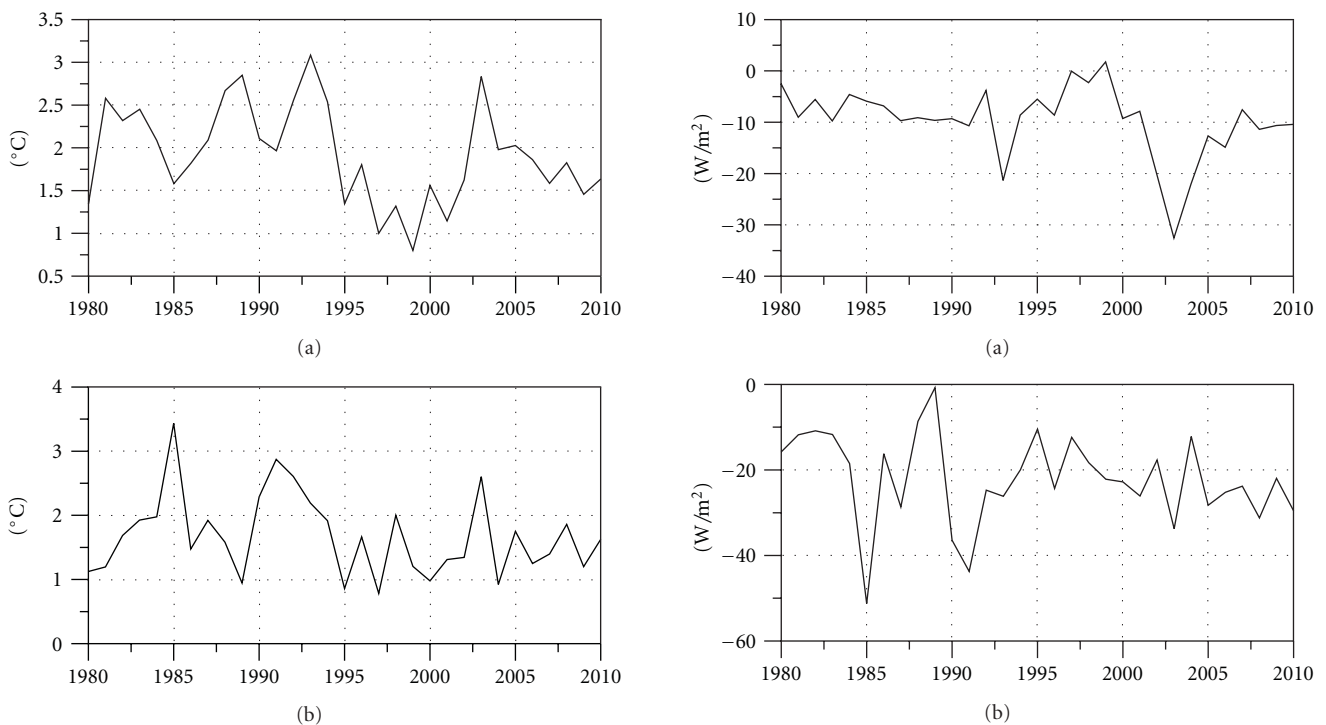


FIGURE 10: Surface-air temperature difference in winter around Franz Joseph Land (a) and north of Svalbard (b).



FIGURE 11: Sensible heat flux at the ocean ice/air interface in winter around Franz Joseph Land (a) and north of Svalbard (b).

meteorological conditions, heat exchange through the ice-free surface is two orders of magnitude greater than that through the surrounding pack ice [35]. Turning back to Figures 6, 7, and 8, we draw attention to the following facts. Air temperature permanently increased after the mid-1990s, as did negative sensible heat flux. Therefore, the amount of heat released from the ocean to the atmosphere increased. At the same time, the air-surface temperature difference did not show any significant trend. European reanalysis (ERA-Interim) surface heat fluxes from partially ice-covered ocean are obtained by averaging fluxes over open water and ice proportionally according to the concentration in a given model cell. Therefore, we argue that an increase of sensible heat flux from the ocean after the mid-1990s is a result of lower sea ice concentration in the area (perhaps due to an

increased number of small-scale leads [38]). Lower sea ice concentration is the consequence of ice thinning under the influence of an increased sensible heat flux from AW because ice erosion from below enables more effective breaking of the thinner ice by wind (which has not visibly changed) and by local currents. Lower sea ice concentrations are collocated with areas of anomalies in the surface heat fluxes (Figure 12). The fact that the minimum sea ice thickness lies in the interior of the ice pack right above the FSBW path (see Figure 6(b)) is a clear indication of the influence of heat flux from the FSBW on ice thickness. The physical processes that deliver warm water from the deep to the under-ice layer are yet to be studied in detail. We assume that in the study area the most likely candidate is winter convective mixing. In the WNB, in the absence of a cold halocline, convective

mixing reaches the depth of ~ 100 m [25], entraining the upper part of AW, which is at its seasonal peak in late fall—early winter [15]. Additional forcing could be provided by upwelling events at the continental slope of Franz Joseph Land [39] and/or by Ekman pumping [14].

The possibility of AW heat impact on the Arctic Ocean ice cover has been debated since Fritjof Nansen's 1890s discovery of a warm water layer under the pack ice. The hypothesis that AW affects ice properties always had its supporters and opponents. However, the absence of robust observational data in specific locations and specific seasons prevented this dispute from growing beyond theoretical speculations and indirect estimations to justified statements, based on observations. In the present study we demonstrate that in the WNB region AW directly affects the ice thickness, providing an efficient thermodynamic mechanism by which ice volume is decreased. The significance of this influence in the pan-Arctic sea ice and fresh water budgets should be the subject of future studies.

Appendix

Data Sources and Uncertainties

For this study we used publicly available data sets. Originators of these data sets provide detailed description of metadata, including methods of measurements, accuracy, and so forth. Here, we briefly describe the sources of data and discuss possible uncertainties in the presented results.

CTD and mooring-based data on WNB temperature and salinity were taken from the NABOS data archive (<http://nabos.iarc.uaf.edu/>). These data had passed thorough quality control and have been used in multiple published studies, see [40]. The AW temperature in Fram Strait has been monitored for an extended period of time by the international scientific community, mainly by Russian, Norwegian, and German researchers [14, 24, 41]. The AW time series used in this study were generated from the oceanographic data base, collected, and routinely complemented by new data at the Arctic and Antarctic Research Institute (AARI). *Ice concentration* data were taken from the Nimbus-7 Scanning Multichannel Microwave Radiometer (SMMR) and the Defense Meteorological Satellite Program (DMSP) Special Sensor Microwave/Imager (SSM/I) Passive Microwave Data dataset [27, <http://nsidc.org/data/nsidc-0051.html>]. The spatial resolution of the regular grid is 25 km. For the year 2011, preliminary data from this dataset were used [42]. We calculated 10 day averages from the daily data and used the resulting products for the analysis. *Ice thickness* data were taken from the ICESat data collection [28] 2008; (<http://rkwok.jpl.nasa.gov/icesat/download.html>). *Meteorological* data and derived parameters (heat fluxes) were taken from the ERA-Interim reanalysis (<http://www.ecmwf.int/research/era/do/get/era-interim>).

ERA-Interim is the latest ECMWF global atmospheric reanalysis covering the period from 1979 to present. It uses 4D variational data assimilation of a wide variety

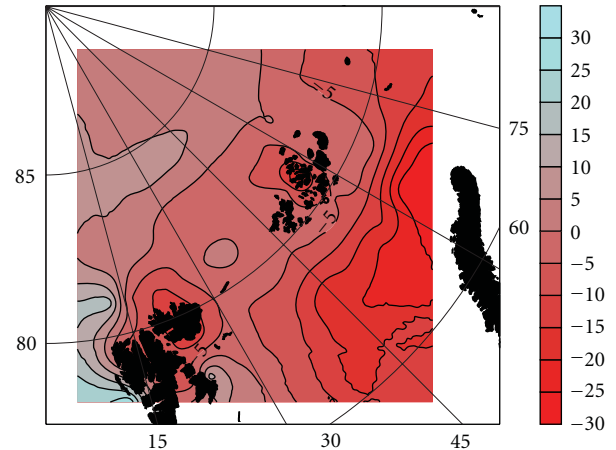


FIGURE 12: Averaged 1980–2010 winter distribution of sensible heat flux at the surface, W/m^2 (a); difference in heat flux between 1999–2010 and 1980–1995 (b).

of observations from surface based to aerological and satellite measurements. Available fields include all major meteorological variables plus important surface diagnostics including surface fluxes. We use the 1.5×1.5 degree resolution version of ERA Interim available from the ECMWF web site: <http://www.ecmwf.int/>.

Uncertainties are an inseparable component of any observation-based investigation, and our study is not free of them. We recognize two types of uncertainties: (i) uncertainties associated with the limitation of the data used and (ii) uncertainties caused by simplifications introduced during the analysis. Uncertainties in hydrographic data are usually caused by changing the location of sequential CTD casts and low horizontal resolution. Since the NABOS CTD data that we used were collected at the recurrent cross-slope section with ~ 5 km distance between stations over the steepest part of the slope, we do not expect a noticeable error in estimation of AW properties. Mooring-based data were collected close to the core of the AW flow, as was shown in [15], which also guarantees small errors of estimation based on these data. Uncertainties in ice concentration data were discussed in [43]. They conclude that according to data documentation in general, the accuracy of total sea ice concentrations is within $\pm 5\%$ of the actual sea ice concentration in winter, and $\pm 15\%$ in the Arctic during summer when melt ponds are present on the sea ice. Although these numbers are close to the MSIC variations presented in Figure 4, we would like to stress our use of ice concentration data averaged over time and space, which reduces the error proportional to the square root of the number of individual measurement points. Ice concentration data (as well as ice thickness data) have rather crude spatial resolution (25 km) and do not resolve small openings in the ice cover (cracks and flaw leads). However, for the purpose of the presented analysis these data fit reasonably well, since we discuss relatively large (\sim hundreds of kilometers) features. Uncertainty in the diagnostic fields provided by ERA-Interim, which are not constrained by any sort of data assimilation procedures, is always a big problem for any

reanalysis products. For example, in [44] it is discussed that the overall performance of ERA-Interim products including fluxes over ocean. They found that the quality of many diagnosed variables (e.g., precipitation and surface fluxes) greatly improved in ERA-Interim in comparison with other products of this kind.

Uncertainties in the presented analysis may be associated with our failure to take ice drift into account. Drift provides key forcing of ice redistribution. We checked the pattern of ice thickness anomalies against the mean ice drift in February-March 2008 [18]. Within this time interval, mean ice drift in the WNB and around it was generally directed southward with speed not exceeding 5 km/day. Therefore, we conclude that the error of failing to take ice drift into account may not noticeably affect our results. Another possible source of error in ice thickness estimation is snow on ice, which is difficult to assess. Since large-scale snow anomalies are collocated with downwelling long wave (DLW) radiation, we estimated total accumulated snowfall from the ERA-Interim dataset by assuming snow density of 0.25, and that snowpack starts developing in September. No correlation between snowfall anomalies and ice thickness anomalies in 2008 was found. ERA-Interim uses satellite observed sea ice concentrations to calculate surface fluxes over the Arctic Ocean. Small-scale features like cracks and polynyas may not be well resolved. However, if sea ice concentration is less than 100% in a grid cell, open water and sea ice are calculated separately. The total heat flux over the grid cell is then calculated according to the proportion of open water and sea ice in that grid cell. Absolute values of air-surface temperature difference decreased according to our analysis. Since the wind change is relatively small, this could only lead to a decrease in the sensible heat flux if the surface properties stayed the same (e.g., ocean remained ice covered). Therefore, sensible heat flux can increase only at the expense of more open water in the area, because heat fluxes from open water are far greater than fluxes over ice-covered ocean. Note that we use the ERA-Interim sign convention: negative surface heat flux means the surface is heating the atmosphere.

We acknowledge that the presented analysis may be not perfect because the available data sets have limitations. However, we believe that the uncertainties of data and analytical method do not call into question the conclusions of this paper.

Acknowledgments

This study was supported by the following research grants/programs: EU FP7 “Arctic Climate Change Economy and Society” (ACCESS) project, NERSC-IAP 196174/S30: “The atmospheric boundary layer structure and surface-atmosphere exchange in the Svalbard area;” RFBR 11-05-12019-ofi-m-2011: “Modern polar climate change estimation on the base satellite microwave database GLOBAL-RT;” RFBR 11-05-01143: “Investigation of tide action on generation and dynamics of internal waves and their manifestation on the sea surface in Russian Arctic seas;” ONR-Global grant 62909-12-1-7013: “Decision Making Support

System for Arctic Exploration, Monitoring and Governance;” European Commission 7th framework program through the MONARCH-A Collaborative Project, FP7-Space-2009-1 Contract no. 242446, NSF Grant ARC 0909525 and Japan Agency for Marine-Earth Science and Technology. ERA-Interim data used for the analysis were downloaded from the website of the European Centre for Medium Range Weather Forecasts (<http://www.ecmwf.int/>). The authors thank Anton Beljaars of ECMWF for providing very useful information on ERA-Interim data assimilation procedures.

References

- [1] J. C. Comiso, C. L. Parkinson, R. Gersten, and L. Stock, “Accelerated decline in the Arctic sea ice cover,” *Geophysical Research Letters*, vol. 35, no. 1, Article ID L01703, 2008.
- [2] M. Wang and J. E. Overland, “A sea ice free summer Arctic within 30 years?” *Geophysical Research Letters*, vol. 36, no. 7, Article ID L07502, 2009.
- [3] B. Y. Wu, J. Wang, and J. E. Walsh, “Dipole anomaly in the winter Arctic atmosphere and its association with sea ice motion,” *Journal of Climate*, vol. 19, no. 1, pp. 210–225, 2006.
- [4] V. A. Alexeev, I. N. Esau, I. V. Polyakov, S. J. Byam, and S. Sorokina, “Vertical structure of recent Arctic warming from observed data and reanalysis products,” *Climatic Change*, vol. 111, no. 2, pp. 215–239, 2011.
- [5] K. Shimada, T. Kamoshida, M. Itoh et al., “Pacific Ocean inflow: influence on catastrophic reduction of sea ice cover in the Arctic Ocean,” *Geophysical Research Letters*, vol. 33, no. 8, Article ID L08605, 2006.
- [6] I. V. Polyakov, L. A. Timokhov, V. A. Alexeev et al., “Arctic ocean warming contributes to reduced polar ice cap,” *Journal of Physical Oceanography*, vol. 40, no. 12, pp. 2743–2756, 2010.
- [7] D. K. Perovich, J. A. Richter-Menge, K. F. Jones, and B. Light, “Sunlight, water, and ice: extreme Arctic sea ice melt during the summer of 2007,” *Geophysical Research Letters*, vol. 35, Article ID L11501, 4 pages, 2008.
- [8] D. A. Rothrock, Y. Yu, and G. A. Maykut, “Thinning of the Arctic Sea-Ice cover,” *Geophysical Research Letters*, vol. 26, no. 23, pp. 3469–3472, 1999.
- [9] J. Rodrigues, “The rapid decline of the sea ice in the Russian Arctic,” *Cold Regions Science and Technology*, vol. 54, no. 2, pp. 124–142, 2008.
- [10] V. A. Alexeev, P. L. Langen, and J. R. Bates, “Polar amplification of surface warming on an aquaplanet in “ghost forcing” experiments without sea ice feedbacks,” *Climate Dynamics*, vol. 24, no. 7-8, pp. 655–666, 2005.
- [11] P. L. Langen and V. A. Alexeev, “Polar amplification as a preferred response in an idealized aquaplanet GCM,” *Climate Dynamics*, vol. 29, no. 2-3, pp. 305–317, 2007.
- [12] R. V. Bekryaev, I. V. Polyakov, and V. A. Alexeev, “Role of polar amplification in long-term surface air temperature variations and modern arctic warming,” *Journal of Climate*, vol. 23, no. 14, pp. 3888–3906, 2010.
- [13] R. Kwok, C. F. Cunningham, M. Wesnahan, I. Rigor, H. J. Zwally, and D. Yi, “Thinning and volume loss of the Arctic Ocean ice cover: 2003–2008,” *Journal of Geophysical Research*, vol. 114, Article ID C07005, 16 pages, 2009.
- [14] S. Lind and R. B. Ingvaldsen, “Variability and impacts of Atlantic water entering the Barents sea from the north,” *Deep Sea Research I*, vol. 62, pp. 70–88, 2011.

- [15] V. V. Ivanov, I. V. Polyakov, I. A. Dmitrenko et al., “Seasonal variability in Atlantic Water off Spitsbergen,” *Deep-Sea Research I*, vol. 56, no. 1, pp. 1–14, 2009.
- [16] Environmental Working Group (EWG), 1998, *Joint U.S.-Russian Atlas of the Arctic Ocean (CD-ROM)*, National Snow and Ice Data Center, Boulder, Colo, USA, 1997.
- [17] Y. G. Nikiforov and A. O. Shpaikher, *Features of the Formation of Hydrological Regime Large-Scale Variations in the Arctic Ocean*, Gydrometeoizdat, Leningrad, Russia, 1980.
- [18] R. Kwok and J. Morrison, “Dynamic topography of the ice-covered Arctic ocean from ICESat,” *Geophysical Research Letters*, vol. 38, Article ID L02501, 6 pages, 2011.
- [19] B. Rudels, E. P. Jones, L. G. Anderson, and G. Kattner, “On the intermediate depth waters in the Arctic ocean,” in *The Polar Oceans and Their Role in Shaping the Global Environment*, O. M. Johannessen, R. D. Muench, and J. E. Overland, Eds., pp. 33–46, AGU Geophysical Monograph 85, Washington, DC, USA, 1994.
- [20] I. A. Dmitrenko, S. A. Kirillov, V. V. Ivanov et al., “Seasonal modification of the Arctic Ocean intermediate water layer off the eastern Laptev Sea continental shelf break,” *Journal of Geophysical Research C*, vol. 114, no. 6, Article ID C06010, 2009.
- [21] K. Aagaard, A. Foldvik, and S. R. Hillman, “The west spitsbergen current: disposition and water mass transformation,” *Journal of Geophysical Research*, vol. 92, no. C4, pp. 3778–3784, 1987.
- [22] M. A. Maqueda, A. J. Willmott, and N. R. T. Biggs, “Polynya dynamics: a review of observations and modeling,” *Reviews of Geophysics*, vol. 42, no. 1, Article ID RG1004, 37 pages, 2004.
- [23] S. Hakkinen and D. J. Cavalieri, “A study of oceanic surface heat fluxes in the Greenland, Norwegian, and Barents Seas,” *Journal of Geophysical Research*, vol. 94, no. 5, pp. 6145–6157, 1989.
- [24] U. Schauer, E. Fahrbach, S. Osterhus, and G. Rohardt, “Arctic warming through the fram strait: oceanic heat transport from 3 years of measurements,” *Journal of Geophysical Research C*, vol. 109, no. 6, Article ID C06026, 14 pages, 2004.
- [25] B. Rudels, E. P. Jones, U. Schauer, and P. Eriksson, “Atlantic sources of the Arctic Ocean surface and halocline waters,” *Polar Research*, vol. 23, no. 2, pp. 181–208, 2004.
- [26] N. Untersteiner, “On the mass and heat balance of Arctic sea ice,” *Archives for Meteorology, Geophysics and Bioclimatology*, vol. 12, pp. 151–182, 1961.
- [27] D. Cavalieri, C. Parkinson, P. Gloersen, and H. J. Zwally, *Updated Yearly. Sea Ice Concentrations from Nimbus-7 SMMR and DMSP SSM/I-SSMIS Passive Microwave Data, 1979–2010*, National Snow and Ice Data Center. Digital Media, Boulder, Colo, USA, 1996.
- [28] R. Kwok and G. F. Cunningham, “ICESat over Arctic sea ice: estimation of snow depth and ice thickness,” *Journal of Geophysical Research C*, vol. 113, no. 8, Article ID C08010, 2008.
- [29] R. Kwok, “Outflow of Arctic ocean sea ice into the Greenland and Barent seas: 1979–2007,” *Journal of Climate*, vol. 22, no. 9, pp. 2438–2457, 2009.
- [30] S. Smirnov and A. Korabely, “A regional oceanographic database for the Nordic Seas: from observations to climatic dataset,” in *Proceedings of the International Conference on Marine Data and Information Systems (IMDIS '10)*, p. 81, Paris, France, March 2010.
- [31] I. V. Polyakov, A. Beszczynska, E. C. Carmack et al., “One more step toward a warmer Arctic,” *Geophysical Research Letters*, vol. 32, no. 17, Article ID L17605, pp. 1–4, 2005.
- [32] I. A. Dmitrenko, I. V. Polyakov, S. A. Kirillov et al., “Toward a warmer Arctic Ocean: spreading of the early 21st century Atlantic water warm anomaly along the Eurasian basin margins,” *Journal of Geophysical Research C*, vol. 113, no. 5, Article ID C05023, 2008.
- [33] S. Martin and D. J. Cavalieri, “Contribution of the Siberian shelf to the Arctic ocean intermediate and deep water,” *Journal of Geophysical Research*, vol. 94, no. 12, pp. 12725–12738, 1989.
- [34] V. F. Zakharov, *Sea Ice in the Climate System*, Hydrometeoizdat, St. Petersburg, Russia, 1996.
- [35] S. D. Smith, R. D. Muench, and C. H. Pease, “Polynyas and leads: an overview of physical processes and environment,” *Journal of Geophysical Research*, vol. 95, no. C6, pp. 9461–9479, 1990.
- [36] T. Uttal, J. A. Curry, M. G. McPhee et al., “Surface heat budget of the arctic ocean,” *Bulletin of the American Meteorological Society*, vol. 83, no. 2, pp. 255–275, 2002.
- [37] I. A. Repina and A. S. Smirnov, “Heat and momentum exchange between the atmosphere and ice from the observational data obtained in the region of Franz Josef Land,” *Atmospheric and Ocean Physics*, vol. 36, no. 5, pp. 618–626, 2000.
- [38] S. Marcq and J. Weiss, “Influence of sea ice lead-width distribution on turbulent heat transfer between the ocean and the atmosphere,” *The Cryosphere*, vol. 6, pp. 143–156, 2012.
- [39] K. Aagaard, L. K. Coachman, and E. Carmack, “On the halocline of the Arctic Ocean,” *Deep Sea Research A*, vol. 28, no. 6, pp. 529–545, 1981.
- [40] I. V. Polyakov, V. A. Alexeev, I. M. Ashik et al., “Fate of early 2000’s arctic warm water pulse,” *Bulletin of the American Meteorological Society*, vol. 92, no. 5, pp. 561–566, 2011.
- [41] I. V. Polyakov, G. V. Alekseev, L. A. Timokhov et al., “Variability of the intermediate Atlantic water of the Arctic ocean over the last 100 years,” *Journal of Climate*, vol. 17, no. 23, pp. 4485–4497, 2004.
- [42] W. Meier, F. Fetterer, K. Knowles, M. Savoie, and M. J. Brodzik, *Updated Quarterly. Sea Ice Concentrations from Nimbus-7 SMMR and DMSP SSM/I-SSMIS Passive Microwave Data, 2010*, National Snow and Ice Data Center. Digital Media, Boulder, Colo, USA, 2006.
- [43] N. V. Koldunov, D. Stammer, and J. Marotzke, “Present-day arctic sea ice variability in the coupled ECHAM5/MPI-OM model,” *Journal of Climate*, vol. 23, no. 10, pp. 2520–2543, 2010.
- [44] D. P. Dee, S. M. Uppala, A. J. Simmons et al., “The ERA-Interim reanalysis: configuration and performance of the data assimilation system,” *Quarterly Journal of the Royal Meteorological Society*, vol. 137, no. 656, pp. 553–597, 2011.

Research Article

Applying a Mesoscale Atmospheric Model to Svalbard Glaciers

Björn Claremar,¹ Friedrich Obleitner,² Carleen Reijmer,³ Veijo Pohjola,¹ Anna Waxegård,¹ Florian Karner,² and Anna Rutgersson¹

¹ Department of Earth Sciences, Uppsala University, Villavägen 16, 75236 Uppsala, Sweden

² Institute of Meteorology and Geophysics, Innsbruck University, 6020 Innsbruck, Austria

³ Institute for Marine and Atmospheric Research, Utrecht University, 3508 TC Utrecht, The Netherlands

Correspondence should be addressed to Björn Claremar, bjorn.claremar@met.uu.se

Received 2 December 2011; Revised 16 February 2012; Accepted 15 March 2012

Academic Editor: Igor N. Esau

Copyright © 2012 Björn Claremar et al. This is an open access article distributed under the Creative Commons Attribution License, which permits unrestricted use, distribution, and reproduction in any medium, provided the original work is properly cited.

The mesoscale atmospheric model WRF is used over three Svalbard glaciers. The simulations are done with a setup of the model corresponding to the state-of-the-art model for polar conditions, Polar WRF, and it was validated using surface observations. The ERA-Interim reanalysis was used for boundary forcing and the model was used with three nested smaller domains, 24 and 8 km, and 2.7 km resolution. The model was used for a two-year period as well as for a more detailed study using 3 summer and winter months. In addition sensitivity tests using finer horizontal and vertical resolution in the boundary layer and using different physics schemes were performed. Temperature and incoming short- and long-wave radiation were skillfully simulated, with lower agreement between measured and modelled wind speed. Increased vertical resolution improved the frequency distributions of the wind speed and the temperature. The choice of different physics schemes only slightly changed the model results. The polar-optimized microphysics scheme outperformed a slightly simpler microphysics scheme, but the two alternative and more sophisticated PBL schemes improved the model score. A PBL scheme developed for very stable stratifications (QNSE) proved to be better in the winter.

1. Introduction

The Svalbard archipelago experienced a significant thinning of its glacial mass over the last century, which contributed about 0.026 mm yr^{-1} sea-level rise over the last 50 years [1–4]. In consequence, the stratification and circulation of fjord systems respond to enhanced fresh water supply by melt water and icebergs from calving glaciers [5]. Significant changes are also observed regarding Svalbard sea ice, permafrost, or land and marine ecosystems [6–10]. The thinning and retreat of glaciers on Svalbard is probably both an effect of the warming that set off after the little ice age and the warming of the Arctic over the last decade that likely is an effect of anthropogenic greenhouse gas forcing [11]. The Svalbard archipelago has also experienced a significantly increased precipitation since the 1960s [12]. Several projects have recently been initiated to better understand these detected environmental changes and the response of the Arctic cryosphere (e.g., SVALI; <http://www.ncoe-svali.org> or

SvalGlac; <http://svalglac.eu>). SVALI (Stability and Variations of Arctic Land Ice) is a Nordic centre of excellence, initiated by the Nordic council of ministers, with the focus to study the interaction between climate change and the cryosphere, with focus on glaciers in the Arctic/North Atlantic area. SVALI's task is to improve the knowledge of the boundary effects and the processes and their parameterisation between the atmosphere and the cryosphere to deliver better prognostics of the future of the glacial systems in the Arctic.

Precipitation, temperature, humidity, wind, radiation, and turbulent heat fluxes are key meteorological factors determining the mass and energy balance of snow and ice in general. The Arctic regions, however, are prone to a notorious lack of corresponding measurement data. Therefore, GCM and global reanalyses data were early considered as important sources for analysis of weather phenomena and climate in these regions. Meanwhile such is increasingly based on statistically or dynamically downscaled output from

regional-scale atmospheric models (RCMs). No doubt, however, observational data still play an important role for process studies, data assimilation, or validation of model results.

The skill of prominent global or regional climate models to simulate the Arctic atmosphere was investigated by numerous validation and model intercomparison studies [13–20]. Major efforts were associated to carefully designed and coordinated observational and model intercomparison projects (SHEBA, Surface Heat Budget of the Arctic Ocean, Perovich et al. [21]; ARCMIP, Curry and Lynch [15]). These studies proved the progressive skill of RCMs to simulate the spatiotemporal structure and evolution of the near-surface air properties while revealing some still remaining conflicts on the other hand. Roughly summarizing the intermodel comparisons by, for example, Tjernström et al. 2004 or Rinke et al. 2005 [16, 18], the seasonal weather patterns are skillfully reproduced by the considered models. The simulated near-surface variables (pressure, air temperature, humidity, and wind speed) agree well with observations with decreasing accuracy in that sequence. This is basically true for the surface radiation fluxes as well, while the turbulent heat fluxes are rather unreliable. On the other hand, some errors such as the turbulent heat fluxes compensate their errors on long-term basis. It was further found that on the long-term some errors tend to compensate (turbulent heat fluxes) and that single models perform significantly better than an ensemble mean depending on the investigated parameter, season, and region.

The availability of RCM model output also fostered the investigation of atmospheric phenomena and processes specific to the Arctic [22–27] thereby mostly addressing katabatic winds and related topographical effects (barrier winds, coastal jets) as well as boundary layer features (gravity waves, aerosol distribution). Moreover output from high-resolution climate models can also be directly coupled to glacier mass and energy balance models, as demonstrated for the large ice caps on earth [28–31] and is currently underway for Svalbard (Van Pelt et al. [32]).

The aim of this study is to perform climate simulations applying the WRF (Weather Research and Forecasting) model over the Svalbard domain and to validate the skill of the simulations with AWS (Automatic Weather Station) observations at three glaciers on Svalbard. WRF is an advanced mesoscale atmospheric model and is capable to simulate atmospheric processes with high spatial and temporal resolution [33, 34]. Part of the development focussed on optimization of the physical schemes in WRF to improve simulation of the conditions over the Greenland and Antarctic ice sheets. This version is called Polar WRF [35] and is largely based on experience from a precursor model (Polar MM5, [23]). Meanwhile it also accounts for optimum representation of effects over Arctic oceans [36] and Arctic land surfaces [37]. Therefore Polar WRF proved most valuable for investigation of Arctic environments in general [38–40] including Svalbard regions [41–44].

The latter studies demonstrated the importance of topography on the formation of low level jets at the southern tip of Svalbard (Reeve and Kolsted 2011 [44]), the spatial variability of near-surface meteorological parameters and

processes in Svalbard fjords (Kilpeläinen et al. 2011 [41] and Mäkiranta et al. [43]). The latter demonstrated that despite of a high horizontal resolution (1 km) the model was challenged to reproduce, for example, the observed wind direction distribution. This was mainly attributed to insufficient description of local topography and sea ice. The WRF model output performed better for air temperature than for wind as was characterized by RMSE of 1°C and 3 m s⁻¹, respectively.

WRF simulations focussing on Svalbard glaciers are in progress, but validation with relevant AWS measurements has not yet been published. However, a preliminary case study demonstrated the dominance of katabatic winds on glaciers in the Kongsvegen area and their response on local topography and upper air flow [45]. The study showed deficiencies in simulating the boundary layer temperature profile and the jet structure in the fjord which was addressed to insufficient parameterization of surface layer processes.

This paper presents a more comprehensive investigation of the skill of the model. The work aims on identifying improvements towards simulating the atmospheric conditions over glaciers on Svalbard in order to apply the model output for investigation of the mass and energy balance of Svalbard glaciers in a climate perspective. Also we want to find out what horizontal resolution is needed to resolve the local topography. Sensitivity analysis is performed by changing (a) the vertical resolution of the model in the lowest 1500 m, (b) the horizontal resolution to 900 m locally around one of the AWS sites and (c) including varying snow albedo and by changing the physics schemes (turbulence and microphysics). WRF is run with the resolutions 24 km, 8 km for 2 years, in 2.7 km for 3 winter and summer months, and in 900 m resolution and a higher vertical resolution in the lowest 1500 m for July and January. It is forced by ERA-Interim data [46] at the lateral boundary, as well as by sea surface temperature (SST) and ice cover. The model output is validated with data from AWSs placed on three Svalbard glaciers (Kongsvegen, Nordenskiöldbreen, and Vestfonna) measuring air temperature, wind speed, specific humidity, incoming and outgoing short-wave radiation, and long-wave radiation during the period 2008–2010. Precipitation analysis is postponed to later investigations.

2. Model and Measurements

2.1. WRF

2.1.1. Model Setup. In this investigation we use the atmospheric model WRF version 3.2.1 over the Svalbard region [33, 34]. The WRF model is an open-source model (<http://www.mmm.ucar.edu/wrf/users/>) widely used in research and is useful in ranges 100 of kilometres down to individual cloud scales of 1–5 km. We use the Advanced Research WRF (ARW) dynamical solver, which is a nonhydrostatic model with fully compressible Euler equations and integrates with a third-order Runge-Kutta scheme. Gravity waves and acoustic waves are resolved with a smaller time step. The top of the model is here set at a constant pressure (50 hPa) and with

28 vertical terrain—following Eta—coordinate surfaces in the main simulations. Temperature, horizontal wind, and humidity are calculated between those levels (Arakawa-C grid), adding up to 27 levels. In the main simulations there are 8 levels below ca 1500 m and the lowest two levels at 26 and 90 m. In the sensitivity study with high resolution below 1500 m there are 12 levels below 1500 m, 3 below 100 m, and the lowest two at 11 and 38 m, in all 31 levels.

We use the WRF model in three domains. When simulating the parent domain with 24 km resolution, the initial and boundary forcing from the ERA-Interim archive fields are used every 6 h. The archive represents a reanalysis of the atmospheric conditions every 6 hours, built from ECMWF's Integrated Forecast Systems (IFS) and available for researchers of member states at <http://ecmwf.int/services/archive/>. Data of temperature, wind, and relative humidity were used from different pressure levels from 50 to 1000 hPa. Lower initial boundary conditions include soil temperature and moisture at two levels, SST, sea-ice, surface and sea-level pressure, and near-surface wind, temperature, and humidity. The fact that sea ice may cover a fraction of a grid cell was accounted for, which means that the meteorological parameters calculated over water and ice were weighted for each grid according to sea-ice fraction.

Because of numerical instability problems, probably caused by land/sea masking incompatibilities between ERA-Interim and the geographical data from the US Geological Survey (USGS), time evolution of SST and sea ice was handled by doing 10-day consecutive runs. In each run the sea ice and SST were constant. The lower boundary of the soil temperature from ERA-Interim (below 1 m depth) was found too high (of order 20°C), but this is only used at the initialization of each run. In the following time integrations the soil model is fully coupled to the atmosphere part and thus soil temperature dynamically adjusts to the surface temperature forcing. However, the soil temperature is not expected to have a significant influence on 2 m temperature due to the isolating effect of the snow. Results from initial time steps were not used in the analysis. This can be interpreted as allowing the model to spin up for 3 h. The use of ERA-Interim data instead of the NCEP Climate Forecast System Reanalysis (CFSR) data was motivated by the 4D assimilation used in ERA-Interim versus 3D assimilation used in CFSR and the fact that CFSR ends in January 2010.

The largest domain with 24 km horizontal resolution covers the whole Svalbard archipelago. We use a one-way nesting technique meaning that only information from the parent domain is passed on to the inner nests. This approach is common and usually avoids stability problems that might appear when using a two-way nesting procedure [47]. The second nested domain has a grid resolution of 8 km. The innermost domain in the main run has the resolution of 8/3 km (hereafter referred to as 2.7 km). In a sensitivity analysis from one winter and one summer month an inner 8/9 km resolution domain centred at Nordenskiöldbreen was used (hereafter referred to as 900 m). The site was chosen because of its more complex terrain, compared to the other AWS sites. The time step in the model is adaptive and has about 432 seconds for the 24 km nest, about 30 s for the

8 km nest. The 2.7 km nest simulations are performed by downscaling the 8 km simulation afterwards. This keeps the time step as long as 48 s. The 900 m resolution kept the time step at 15 s. Output fields are stored every 3 h. Model domain set-ups are shown in Figure 1 which also shows the improved terrain representation with higher resolution.

The main runs were performed with polar-optimized physics according to the Polar WRF physics [35]. The turbulence and microphysics schemes were interchanged in a sensitivity study to find possible improvements. Note that the polar-optimized WRF should not be confused by Polar WRF itself, which also accounts for varying variable sea-ice thickness and snow thickness over sea ice as well as for seasonally varying ice and snow albedo during the melt period. Comparison between the Polar WRF and the WRF version used in this investigation is envisaged in future studies.

2.1.2. Physical Schemes. The physics schemes are in the main run chosen to reflect those used in the development of Polar WRF [31]. Short-wave radiation is calculated with the Goddard short-wave scheme [48] with 11 spectral bands that account for diffuse and direct solar radiation. Both scattered and reflected components are accounted for. Long-wave radiation uses the Rapid Radiative Transfer Model (RRTM) [49] that is developed to better represent clear-sky conditions. The Grell-Devenyi ensemble [50] convective parameterization scheme is utilized as cumulus scheme. The scheme is of mass flux type and it is run over each grid using different static and dynamic controls. This process gives a total of 144 different convective schemes that are averaged to give feedback to the model. For microphysics the Morrison double-moment scheme [51] is used. The scheme includes six hydrometers: vapour, cloud droplets, cloud ice, rain, snow, and graupel/hail. When predicting the number concentration and mixing ratio (double moment), the particle size distribution is well resolved. This facilitates the calculation of the microphysical processes and cloud distribution. The particle size distribution is treated using gamma functions.

Boundary layer turbulence is parameterized using the Mellor-Yamada-Janjic (MYJ2.5) planetary boundary scheme [52, 53] which must be run together with the Eta surface layer scheme [52, 53]. The MYJ scheme contains a nonsingular implementation of the Mellor-Yamada Level 2.5 turbulence closure model [54] that is active in both the PBL and in the free atmosphere. The Eta surface layer scheme is built on similarity theory [55].

In all WRF set-ups the Noah land-surface soil temperature and humidity model (LSM) [56] is used. The scheme provides sensible and latent heat fluxes to the boundary layer and is able to predict snow cover. The model has 4 soil layers at the constant depths 10, 30, 60, 100 cm. These are converted into snow, with associated snow properties, in deep-snow-covered areas like the glaciers at Svalbard. In the scheme the snow density is set to 0.2 kg m⁻³, snow albedo to 0.8, and glacier ice albedo to 0.7. On Svalbard the density of snow is higher, between 0.3 and 0.4 kg m⁻³, because of drifting snow

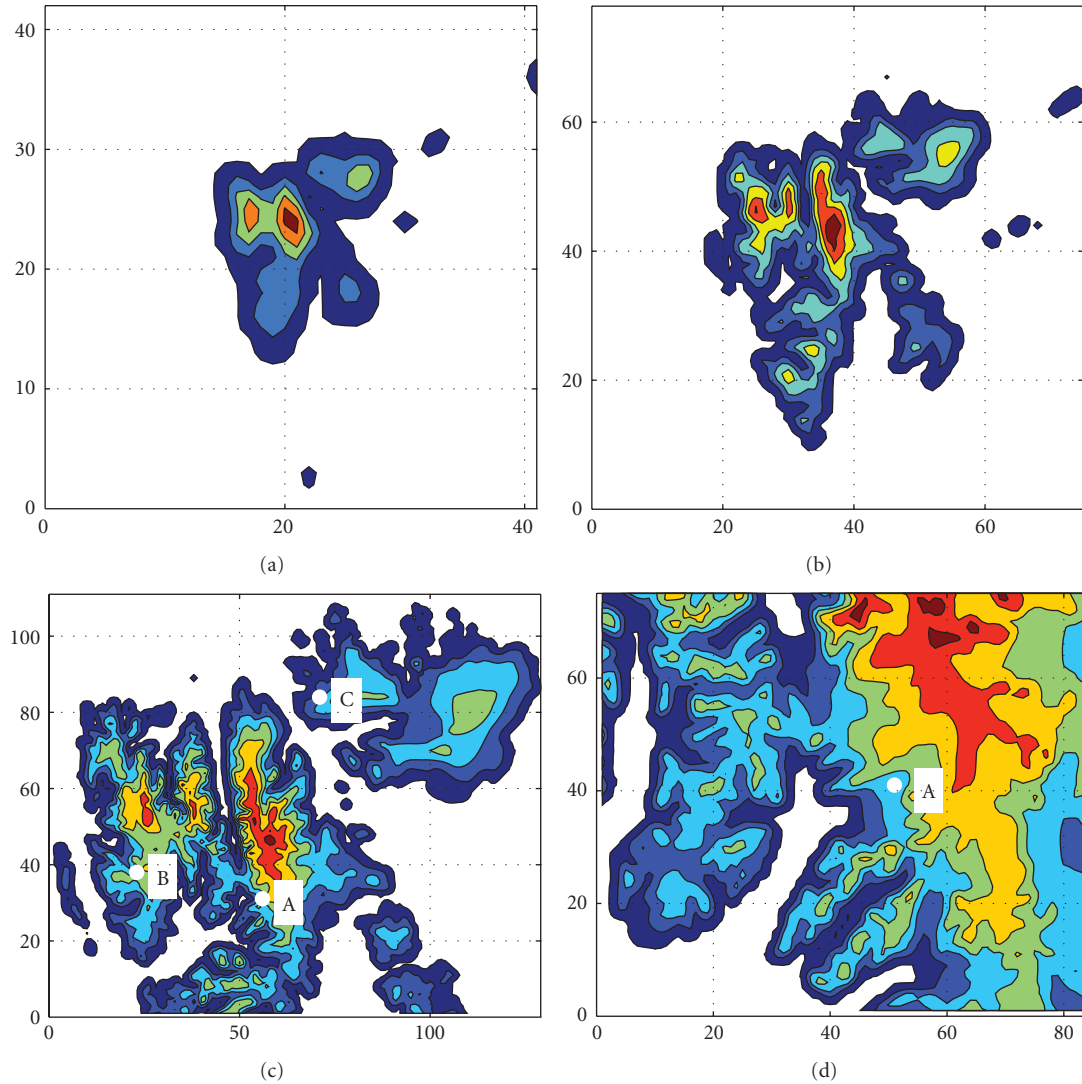


FIGURE 1: Model domains of the nests with 24 km (a), 8 km (b), 2.7 km (c), and 900 m (d) resolution, respectively. Contour lines show terrain with 200 m equidistance (terrain exceeding 1200 m in (c) and (d)) and numbers represent grid points. The AWS sites are marked out in (c) as (A) Nordenskiöldbreen, (B) Kongsvegen, and (C) Vestfonna.

and settling processes [32, 57]. In a sensitivity analysis in the present study monthly climatologic values of the albedo were applied.

In the sensitivity study the WRF single-moment 6-class [58] is utilized. This scheme has the same hydrometeors as the Morrison scheme, but only includes mixing ratios and not particle number concentration. This scheme has been used by Wilson et al. [40] for the Arctic System Reanalysis. For PBL turbulence and surface layer scheme the QNSE or MYNN2.5 scheme is used, respectively. The QNSE scheme (Quasi-Normal Scale Elimination PBL/surface layer) [59] is a k - ϵ model but uses a new theory for stably stratified regions. It accounts for anisotropic turbulence and internal gravity waves and is not based on the shortcomings of Reynolds stress models in very stable stratifications. This scheme was successfully tested in Kilpeläinen et al. [60] over two fjords in Svalbard. The MYNN level 2.5 scheme

(Nakanishi and Niino [61]) includes better interaction of the turbulence with microphysics and radiation in the PBL, compared to the MYJ2.5 scheme.

2.2. Measurements. The model is verified with surface observations from three Automatic Weather Stations (AWSs) located on three different glaciers, namely, Nordenskiöldbreen (NB, $78^{\circ}41'39''\text{N}$, $17^{\circ}09'22''\text{E}$, 530 m a.s.l.), Vestfonna (VF, $79^{\circ}56'03''\text{N}$, $19^{\circ}11'08''\text{E}$, 305 m a.s.l.), and Kongsvegen (KV, $78^{\circ}46'49''\text{N}$, $13^{\circ}9'22''\text{E}$, 537 m a.s.l.). See Figure 1(c) for location of these glaciers, which are representative for the central, northern, and western parts of Svalbard. Close-up maps are shown in Figure 2.

Nordenskiöldbreen (Figure 2(a)) is one of the major outlet glaciers of the ca 600 km^2 large Lomonosovfonna ice field draining towards the Billefjorden in the inner part of Isfjorden. The glacier is about 5 km in width and

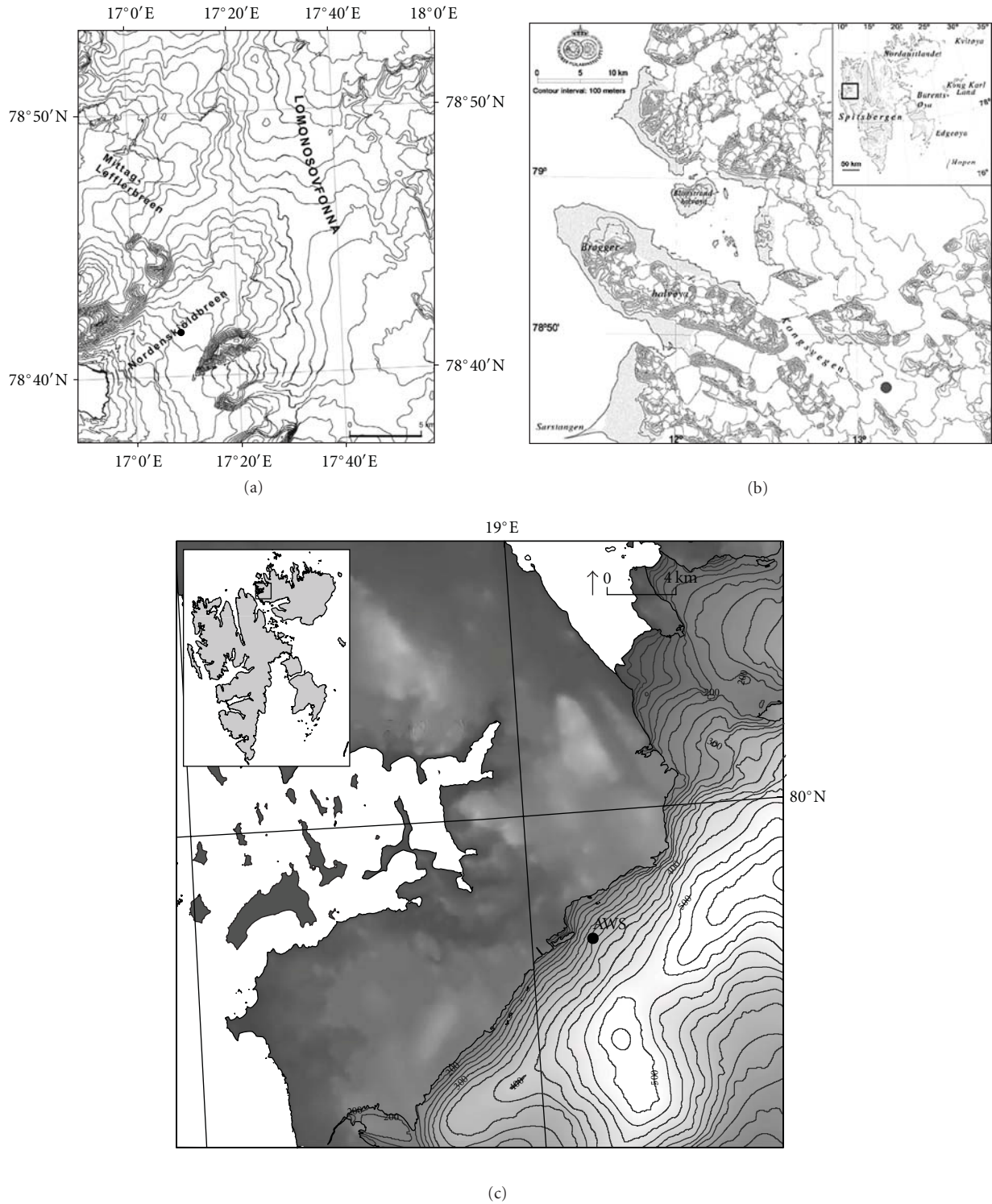


FIGURE 2: The AWS site of (a) Nordenskiöldbreen with 50 m contour lines (drawn by Richard Pettersson), (b) Kongsvegen with 100 m contour lines [62] (modified by Florian Karner), and (c) Vestfonna with 25 m contour lines (drawn by Rickard Pettersson). The DEM data are from Norwegian Polar Institute (NPI).

17 km long and span 193 km². The AWS is situated in the central flow line of the glacier, which is confined by steep slopes to the north (De Geerfjellet, 1023 m a.s.l. and Flemingfjellet, 1124 m a.s.l.) and to the south (Terrierfjellet,

1211 m a.s.l.), respectively. The direction of the downward slope of the glacier at the AWS site is to southwest. Local topography in the direct vicinity of the AWS is fairly smooth and homogeneous, while on a larger scale the surface is

relatively rough due to seracs and open crevasses. Den Ouden et al. [63] and Van Pelt et al. [32] give further details about the topography and the position of the AWS, which is representative for the higher ablation area of the glacier. Descriptions of the site and real-time data are presented on <http://www.projects.science.uu.nl/iceclimate/aws/>.

Vestfonna (Figure 2(c)) is the second largest ice cap on Svalbard (2400 km²) covering the western part of Nordaustlandet. The AWS is located at the western slope of the ice cap. Local topography in the direct vicinity of the AWS is smooth and homogeneous. The site is characterized by north westerly aspect and located in the ablation area of the ice cap. More detailed topographic features and about the instrumentation may be retrieved from [64, 65].

Kongsvegen (Figure 2(b)) is one of the Svalbard benchmark glaciers where long-term mass balance measurements are performed. The glacier originates at a saddle connecting to the south flowing Sveabreen (800 m a.s.l.) and drains into Kongsfjorden. It covers an area of 102 km², has a length of 26 km, and slopes have a north westerly aspect. The AWS on Kongsvegen is representative for the average equilibrium line altitude of the glacier, where the surface is virtually smooth and homogeneous. The closest obstructions of the horizon are Dronningfjella (1263 m a.s.l.) about 6 km to the north and Gjerstadfjellet (1006 m a.s.l.) about 5 km to the south. Further details about the topographic features of the glacier and the measurement site are documented (e.g., in [66]).

The surface conditions at all the three sites are characterized by snow during winter and bare ice during summer except on Vestfonna and Kongsvegen where the snow did not melt in 2008. On Vestfonna the ice surface was snow-free in August–September in 2007. At Kongsvegen and Nordenskiöldbreen, snow-ice transitions usually occur in May and September. Surface roughness is generally higher during summer due to differential ice melt and the formation of melt water channels.

The study focuses on validation of the following model output parameters with AWS measurements of air temperature, wind speed, specific humidity, incoming short-wave, and long-wave radiation. Most meteorological variables were measured by similar instruments at the three sites. Kipp and Zonen CNR1 instruments were used to measure incoming and outgoing short-wave and long-wave radiation at all sites. Wind speed and direction were measured by Young Wind Monitor RM 05103. Humidity and air temperature were measured using Vaisala HMP45A probes mounted within naturally ventilated shields (Vestfonna and Nordenskiöldbreen) while an artificially ventilated device (Rotronic Hygroclip) was used at the Kongsvegen site. The used humidity sensors are calibrated to measure relative humidity with respect to water and the data were converted for reference to ice based on the ratio of saturated vapour pressures. Mean hourly data were stored onto Campbell Sci. CR10X and CR23X loggers and the sites were usually visited in spring for maintenance.

Meteorological data collected by the AWS at Nordenskiöldbreen used in this study are from March 2009 to March 2010. Unfortunately, the temperature readings were erroneous during the summer of 2009 (July to November).

This also affected the humidity, long-wave radiation, and snow height readings. For this period the logger temperature was used. To that end the logger temperature was correlated to the air temperature using a linear regression ($R^2 = 0.89$). Using this method, the estimated air temperatures during periods with high solar input may be overestimated by up to 5°C. All the measurements at Nordenskiöldbreen are observed approximately 4.5 m above the surface. Observations at Kongsvegen and Vestfonna are from January 2007 to December 2010 and May 2007 to April 2009, respectively. On Vestfonna all of the parameters are measured at the height 1.8 m except for the wind speed that is measured at the height 2 m. At Kongsvegen air temperature and humidity are measured about 1 m below the wind measurements corresponding to a height of 3.5 m above the glacier ice. Note, however, that in glacier environments the height of instruments above the surface inevitably varies throughout the year due to accumulation and melt of snow. To exemplify this for the Kongsvegen site, air temperature was measured about 0.9 m above the snow (May 2008) and 3.0 m above the ice surface in September. The initial snow depth at Nordenskiöldbreen in March 2009 was 0.85 m. The varying measurement heights were not corrected for within this study because of the lack of knowledge of the near-surface temperature profile. However, one can qualitatively argue that the 2 m temperature is higher than the recorded temperature when the measuring height is less than 2 m, as a surface inversion is common over the snow and ice surfaces.

Measurements in the harsh Arctic environments impose some further constraints and enhanced treatment of the data. At Kongsvegen, for instance, values of temperature outside the range -40°C to $+20^{\circ}\text{C}$ and humidity data (visual outliers) were removed. High temperature peaks during the summer at Nordenskiöldbreen, thought to be associated with errors caused by short-wave radiation warming, were visually identified and the upper limit of $+5^{\circ}\text{C}$ was used to sort out these occasions. Wind speeds less than 0.5 m s^{-1} were removed due to the inability of the instruments to correctly measure these low winds and also because of the possibility that the equipment might have been covered in ice. Short-wave radiation data in excess of 1000 W m^{-2} were removed and potential snow on the up-facing radiometers was sorted out by values albedo higher than 0.95. Long-wave radiation data at Kongsvegen were controlled by comparison with values calculated according to König-Langlo and Augstein [67] and the 0°C threshold for calculated surface temperature (melting ice), respectively. Remaining gaps in the record were closed by cross correlation using undisturbed data measured concurrently at Ny-Ålesund and at the glacier.

All mentioned data were provided by different research groups as detailed in the acknowledgments.

3. Methodology

The comparison was made using model data from one out of the four grid points that surrounded the AWS station. The closest grid point may deviate in height from the AWS and therefore not be a suitable for comparison. When

TABLE 1: AWS site details with instrumentation.

AWS	Period used	Height/terrain	Instrumentation		
			Temp/hum	Wind	Radiation
Nordenskiöldbreen	March 2009–March 2010	530 m a.s.l. NE gradient	Vaisala HMP45A	Young Wind Monitor RM 05103	Kipp and Zonen CNR1
Kongsvegen	April 2008–March 2010	537 m a.s.l. ESE gradient	Rotronic Hygroclip	Young Wind Monitor RM 05103	Kipp and Zonen CNR1
Vestfonna	May 2008 to April 2009	305 m a.s.l. SE gradient	Vaisala HMP45A	Young Wind Monitor RM 05103	Kipp and Zonen CNR1

choosing grid point corresponding to an AWS the correlation to the observations and the topography was regarded and to some extent also the bias. If there was no significant difference between the correlations among the grid points, the point with the best coincident height was used. It appeared that the wind speed was the most sensitive variable to location. The resulting topographical heights are for (1) Kongsvegen: 278 m a.s.l. (ERA-Interim), 424 m (24 km), 639 m (8 km), and 607 m (2.7 km), (2) Nordenskiöldbreen: 380 m (ERA-Interim), 707 m (24 km), 321 m (8 km) and 648 m (2.7 km), and 607 m (900 m), and (3) Vestfonna: 260 m (ERA-Interim), 188 m (24 km) and 244 m (8 km). The grid points in the 2.7 km resolution consist of 100% of glacier, whereas the 24 km grid points at least are of 53% covered by ice (Nordenskiöldbreen).

In many areas the temperature decreases with height and one can for climate studies use constant lapse rates. The latter is not a good approach when considering the effect of the diurnal cycle and the complex nature of stable boundary layers, which is very common in Arctic areas. Particularly during the winter time when inversions are common, a temperature correction accounting for the altitude differences could even increase the error. In a test of Polar WRF carried out over Greenland by Hines and Bromwich [35] a correction of a decrease in temperature of 0.0071 K m^{-1} [68] was used. In Pohjola et al. [69], a mean lapse rate of -0.0044 K m^{-1} was found for the area of study. Here the temperature was both analysed without a temperature correction and with the -0.0044 K m^{-1} lapse rate. The maximum altitude error between the AWSs and the WRF model or ERA-Interim grid in this investigation is 250 m, which corresponds to approximately 1.8°C . The varying heights of the AWS instruments measuring temperature are not accounted for.

To investigate if the WRF downscaling improved the modelled data compared to ERA-Interim output, the WRF standard output for 2 m temperature, 2 m specific humidity, 10 m wind, and incoming short-wave and long-wave radiation were compared with mean hourly observations from the AWSs every 3 hours. The skills of WRF with polar physics output were evaluated for the four different resolutions: 24 km, 8 km, 2.7 km, and 900 m). The 24 km and 8 km resolution runs were performed for the period April 2008–March 2010, covering 2 years. Because of limited computer resources 2.7 km was only simulated over 3 months in summer (June, July, and August = JJA) 2009 and winter 2009–2010 (December, January, and February = DJF) driven by

3 hourly boundary conditions of the parent 8 km domain. Sensitivity simulations were performed for these summer and winter months. Additional runs with an improved horizontal resolution of 900 m were simulated for July 2009 and January 2011.

In the sensitivity runs with different physics schemes the same physics schemes were used in all nests from 24 km to 2.7 km (and 900 m). Cumulus scheme was turned off for horizontal resolutions below 8 km. In the simulation with higher vertical resolution we expect that the stratification and wind profile of the boundary and surface layer will be simulated more accurately. In a modelling study by Söderberg and Parmhed [70] of katabatic wind jets over an Icelandic sloping glacier with complex surrounding terrain the vertical resolution was set to 2 m in the lowest 21 m while the Mellor Yamada original PBL scheme [54] was used. This was motivated by the large wind gradients in the surface layer. Also stable surface layers are very shallow.

Simulated data were evaluated using correlations coefficient (R^2), mean difference (Bias), mean absolute error (MAE), and skill score coefficient (SSC). Following [71], we defined the latter as the mean of the absolute difference between the modelled data and observations which is normalised with standard deviation of the observations σ_{obs} :

$$\text{SSC} = \frac{|\overline{\text{mod} - \text{obs}}|}{\sigma_{\text{obs}}} \quad (1)$$

4. Results

In the following section the input from ERA-Interim and the output from our runs with WRF 24 and 8 km data during the period April 2008–March 2010 are presented. Because of limited computer resources the fine 2.7 km resolution simulations were only performed during a summer and winter period where data from two out of three AWSs were available. Therefore the periods JJA in 2009 and DJF in 2009–2010 were chosen. This had the consequence that Vestfonna is excluded in that analysis. It was also expected that the finer resolution was more important for the other sites with more complex topography. In the statistical comparisons with 2.7 km the same period is used for 8 km.

4.1. Impact of Improved Horizontal Resolution. ERA-Interim gives overall very good correlations for temperature, probably due to the assimilation of data from synoptic weather stations like Longyearbyen and Barentsburg. The 2-year

TABLE 2: Statistical evaluation of temperature and wind for the 2-year period (April 2008–March 2010). Kongsvegen record is from the whole period, Nordenskiöldbreen record is from March in 2009 until March in 2010 (1 year), and Vestfonna record is from April in 2008 until April in 2009 (1 year). T -corr is height corrected temperatures. Bold numbers indicate the best result for each AWS.

		R^2		Bias			MAE			SSC		
		T	U	T ($^{\circ}\text{C}$)	T -corr ($^{\circ}\text{C}$)	U (m s^{-1})	T ($^{\circ}\text{C}$)	T -corr ($^{\circ}\text{C}$)	U (m s^{-1})	T ($^{\circ}\text{C}$)	T -corr ($^{\circ}\text{C}$)	U (m s^{-1})
Kongsvegen	ERA-Interim	0.93	0.37	3.8	2.6	-1.7	3.9	2.9	2.4	0.45	0.34	0.77
	24 km	0.89	0.44	-1.0	-1.5	1.5	2.3	2.6	2.5	0.27	0.29	0.81
	8 km	0.89	0.42	-1.6	-1.2	0.9	2.5	2.3	2.2	0.30	0.27	0.73
Nordenskiöldbreen	ERA-Interim	0.90	0.21	1.8	1.1	-2.1	2.6	2.3	3.0	0.34	0.30	0.73
	24 km	0.89	0.49	-1.3	-0.6	1.7	2.6	2.4	2.8	0.33	0.31	0.68
	8 km	0.89	0.49	0.5	-0.5	1.4	2.3	2.3	3.1	0.29	0.29	0.73
Vestfonna	ERA-Interim	0.94	0.27	2.5	2.2	-3.8	2.8	2.6	4.5	0.30	0.27	0.83
	24 km	0.89	0.58	-1.5	-2.2	-1.4	2.8	3.1	2.9	0.30	0.32	0.55
	8 km	0.90	0.68	-0.6	-1.0	-1.4	2.4	2.5	2.6	0.25	0.26	0.49

TABLE 3: Statistical evaluation of temperature in summer and winter 2009-2010. Bold numbers indicate the best result for each AWS. Vestfonna data are not used here because of the lack of data during the chosen period. Abbreviation corr denotes height corrected temperatures.

		R^2		Bias ($^{\circ}\text{C}$)				MAE ($^{\circ}\text{C}$)				SSC			
		DJF	JJA	DJF	DJF corr	JJA	JJA corr	DJF	DJF corr	JJA	JJA corr	DJF	DJF corr	JJA	JJA corr
Kongsvegen	24 km	0.80	0.50	-1.6	-2.1	-1.1	-1.6	3.0	3.2	1.6	1.9	0.39	0.41	0.62	0.73
	8 km	0.81	0.54	-2.2	-1.8	-1.7	-1.3	3.3	3.1	2.0	1.8	0.42	0.39	0.76	0.67
	2.7 km	0.80	0.51	-1.2	-0.9	-1.2	-0.9	3.0	2.9	1.8	1.8	0.38	0.37	0.70	0.66
Nordenskiöldbreen	24 km	0.89	0.29	-3.7	-2.9	0.4	1.2	3.8	3.2	1.8	2.1	0.55	0.45	0.76	0.86
	8 km	0.88	0.30	-1.5	-2.4	1.9	1.0	2.2	2.7	2.4	2.0	0.32	0.39	1.00	0.84
	2.7 km	0.88	0.30	-3.1	-2.6	0.7	1.2	3.3	2.9	2.2	2.3	0.47	0.41	0.90	0.94

simulations with the WRF model, compared to ERA-Interim, show only partly improved biases and correlations with the AWS observations. Scores improved hardly with increasing resolution (Table 2). For wind speed it is clearer that the downscaling with WRF increases the ability to simulate the wind speed. ERA-Interim is not able to capture the variability of the wind and the correlation is very low.

The observed temperature at Vestfonna, Kongsvegen, and Nordenskiöldbreen varies in the ranges -35 to 6°C , -34 to 10°C , and -33 to 9°C , respectively. These ranges are underestimated by ERA-Interim but improve with finer resolution, at least to 8 km. The diurnal temperature cycle (not shown) is underestimated in the WRF model and becomes smaller with better resolution. Comparing all three WRF resolutions (winter and summer) there is no significance in that the correlation in temperature increases or that the bias decreases with resolution (Table 3). However, the bias can depend on the actual height of the AWS in relation to the model points. Correcting for this (T -corr) by applying the temperature lapse rate $-0.0044^{\circ}\text{C}/\text{m}$ (discussed in Section 3) the bias, MAE, and SSC are partly improved. This is more important for the ERA-Interim and coarse resolution simulation data (Table 2 and for summer and winter in Table 3). It appears that the WRF model fails especially when simulated long-wave radiation has large errors (Figure 3(a)). Underestimation of incoming radiation gives large underestimation of the temperature in the model

because of the energy balance. Also there is a tendency that the lowest observed temperatures are not captured and that the variation of the summer temperature is underestimated (Figure 3(b)). The humidity is closely coupled to the temperature and follows largely the same reasoning as for temperature (for statistical details confer Table 4). Humidity was not measured during the summer at Nordenskiöldbreen (see Section 2.2).

The wind speed is more problematic to analyse than 2 m temperature. The anemometers at height are all below 10 m at the AWSs and will presumably underestimate the 10 m wind. Therefore one can estimate a 10 m wind speed from the original AWS wind speed based on, for example, Monin-Obukhov theory. Considering all uncertainties of the processes in the stable surface layer we base our analysis on a very simple correction. An increase of the wind speed by 20% at Kongsvegen, 15% at Nordenskiöldbreen, and 25% at Vestfonna was applied. This relatively rough correction is based on a roughness length, $z_0 = 1$ mm, applicable on a snow surface [72] and stable stratification with an Obukhov length of 50 m at Kongsvegen and Nordenskiöldbreen and 100 m at Vestfonna (higher wind speeds). As we do not have any information of the actual atmospheric stratification (apart from the simulated) we start with this approximation. The correction will not change the correlations but the biases, MAEs, and SSCs. The variability of the corrected wind is relatively well captured but the fine resolution

TABLE 4: Statistical evaluation of specific humidity in summer and winter 2009-2010. Bold numbers indicate the best result for each AWS. Vestfonna data are not used here because of the lack of data during the chosen period.

		R^2		Bias (g kg^{-1})		MAE (g kg^{-1})		SSC	
		DJF	JJA	DJF	JJA	DJF	JJA	DJF	JJA
Kongsvegen	24 km	0.81	0.68	-0.1	0.2	0.3	0.4	0.32	0.57
	8 km	0.83	0.72	-0.1	0.0	0.3	0.4	0.32	0.51
	2.7 km	0.84	0.68	-0.1	0.1	0.3	0.4	0.30	0.58
Nordenskiöldbreen	24 km	0.84		-0.1		0.3		0.28	
	8 km	0.88		-0.1		0.2		0.26	
	2.7 km	0.87		-0.1		0.2		0.27	

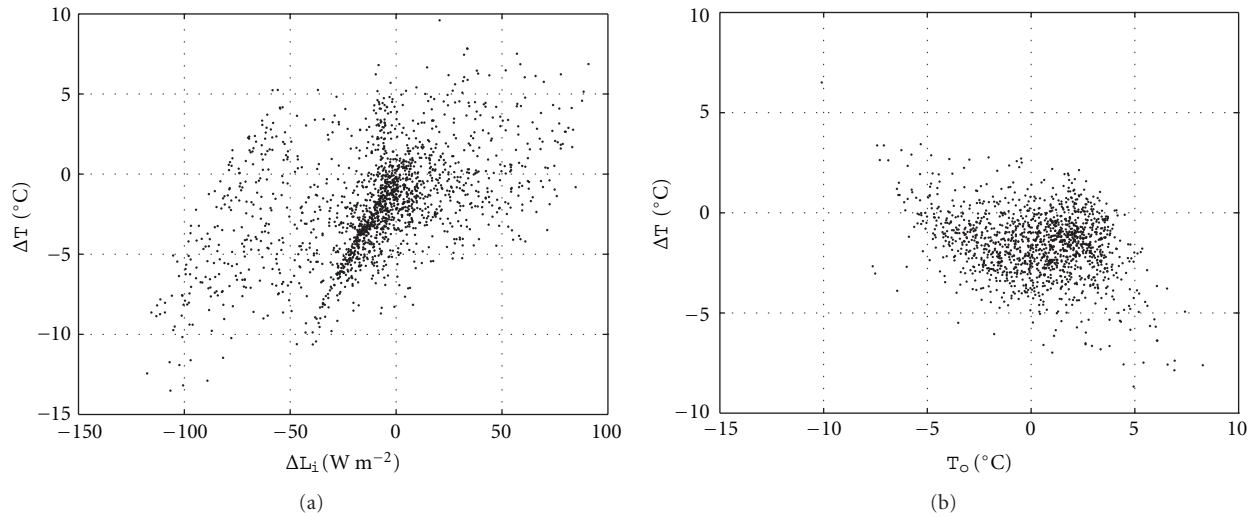


FIGURE 3: Temperature error (model observation) at Kongsvegen for 8 km resolution and as function of, in (a) error in incoming long-wave radiation (model observation) and (b) the observed temperature.

has a tendency to overestimate the highest wind speeds. This is considered as an artefact of the applied constant correction as expected for more neutral stability at high wind speeds. The statistical evaluation is presented in Table 2 and for summer and winter in Table 5. It appears that increasing resolution does not significantly improve the scores at Nordenskiöldbreen and Kongsvegen. At Vestfonna with much less complex topography increased resolution has a higher positive impact (Table 1). This suggests that 2.7 km resolution is not sufficient to resolve the important wind speed determining features of the local topography in more complex terrain. The finding here of better results with coarser resolutions might hence be an artefact, being caused by randomness in the location of the grid point and the neighbouring topographic structure in that resolution. There is no significant dependency on certain conditions found when the simulated wind speed is deviating from the observed.

The wind direction is however rather well described. In Figure 4 wind roses are shown for Nordenskiöldbreen and Vestfonna (Kongsvegen data were not available). It is clear that the WRF model is able to simulate katabatic or other slope winds, even though we cannot not say anything about its vertical profile and the quantitative values. Note that at

the considered Nordenskiöldbreen grid point is located south of the AWS where downward slope is more to the west. Due to the complex topography also the wind direction is more spread out in the simulation.

Due to the high-latitude locations of the AWSs short-wave radiation is limited to the summer period, when there is also midnight sun. The incoming short-wave radiation, both simulated and observed, seldom exceeds 600 W m^{-2} . The statistics are given in Table 6 for summer and winter and it can be concluded that 8 km resolution improves the correlation. However, the bias and errors are not necessarily improved. The overestimation is largest for the finest resolution which indicates a nonlinear problem. The effect of increasing the complexity of the topography affects the cloudiness and if not sufficiently well described by the resolution it may induce more errors in the cloud cover, compared to a coarser resolution. Here it is evident that the model underestimates the cloud cover. The radiation from the sun also penetrates the clouds. The simulated incoming short-wave radiation amount during cloud covered conditions is also very important for radiation balance [73]. The performance of the WRF model and the polar-optimized short-wave radiation scheme during overcast was however not analysed in this investigation.

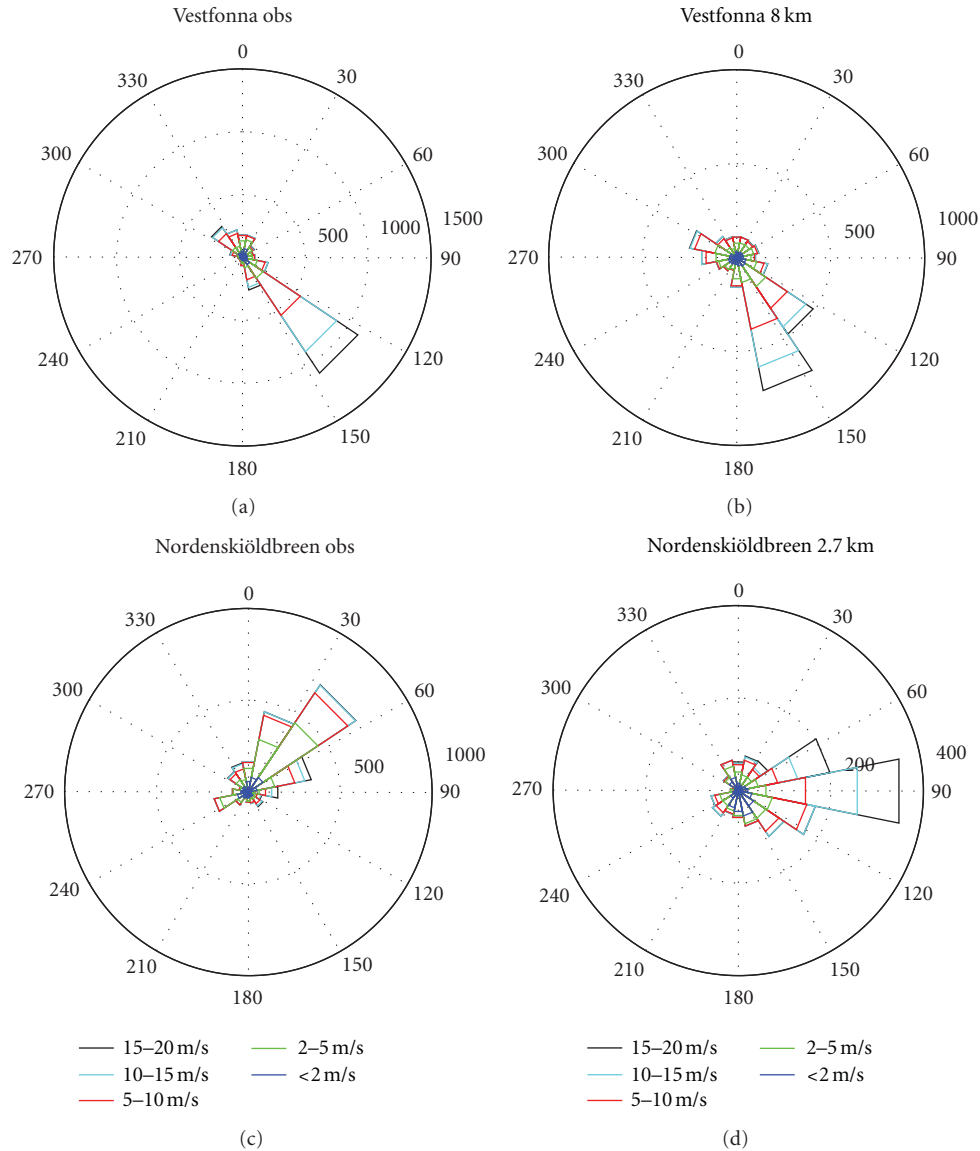


FIGURE 4: Wind roses of observed and simulated wind at Vestfonna and Nordenskiöldbreen. Note that given frequency is absolute (hours).

TABLE 5: Statistical evaluation of wind in summer and winter 2009-2010.

		R^2		Bias (m s^{-1})		MAE (m s^{-1})		SSC	
		DJF	JJA	DJF	JJA	DJF	JJA	DJF	JJA
Kongsvegen	24 km	0.32	0.51	1.7	1.3	3.0	2.0	1.01	0.83
	8 km	0.27	0.43	0.5	1.0	2.6	2.0	0.88	0.82
	2.7 km	0.32	0.47	1.1	0.7	3.0	2.2	1.03	0.88
Nordenskiöldbreen	24 km	0.48	0.54	1.9	0.9	3.0	2.2	0.70	0.58
	8 km	0.43	0.55	2.0	0.4	3.6	2.5	0.85	0.65
	2.7 km	0.48	0.52	1.9	0.4	3.7	2.9	0.89	0.74

For the energy balance at the surface the outgoing short-wave radiation is equally important as the incoming short-wave radiation. The outgoing part is determined by the surface albedo, which in the present setup of the model is set constant to 0.8 for snow surfaces. Figure 5 shows

the measured albedo at Kongsvegen, defined as the ratio of outgoing and incoming short-wave radiation, together with the albedo in the 2.7 km resolution WRF. Typically the albedo decreases rapidly during the melt season, due to snow metamorphism, enhanced liquid water content, enrichment

TABLE 6: Statistical evaluation of incoming short-wave radiation in summer 2009. Bold numbers indicate the best result for each AWS. Vestfonna data are not used here because of the lack of data during the chosen period.

		R^2	Bias (W m^{-2})	MAE (W m^{-2})	SSC
		JJA	JJA	JJA	JJA
Kongsvegen	24 km	0.68	-5	76	0.49
	8 km	0.75	15	67	0.44
	2.7 km	0.74	24	70	0.45
Nordenskiöldbreen	24 km	0.60	28	88	0.52
	8 km	0.65	39	84	0.50
	2.7 km	0.62	57	96	0.56

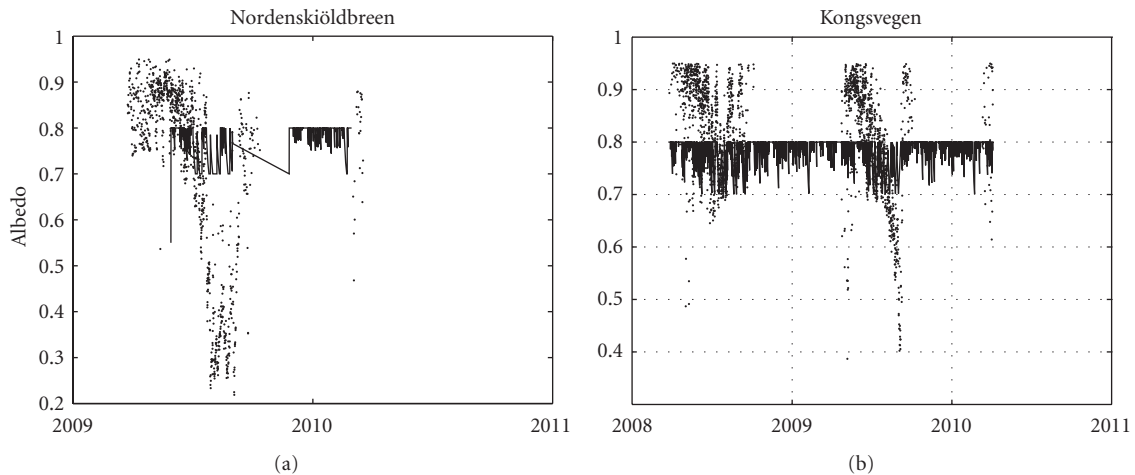


FIGURE 5: Time series of the albedo at (a) Nordenskiöldbreen and (b) Kongsvegen. Dots are measurements and line is WRF with 2.7 km resolution.

of impurities, and dust deposition of for instance black elemental carbon [74, 75]. These effects are implemented in Polar WRF, but not in the WRF version used in the present investigation. In this model version albedo over Kongsvegen is fluctuating due to snow melt thereby episodically exposing the glacier ice surface. Note that according to the measurements new snow has albedo above 0.9, which is not captured by the model. Thus it is clear that varying albedo is not yet realistically represented which is a key issue when simulating ice/snow-air exchange on the other hand. The built-in function in WRF to use monthly climatology values of the albedo was applied and tested in the summer period June–August 2009. However, this study did not yield a significant improvement compared to using the table values used as standard in WRF. At Nordenskiöldbreen it varied between 0.08 and 0.55 and at Kongsvegen between 0.07 and 0.7. The resulting 2-meter temperature was however not significantly affected, only by lowering it by 0.1°C in mean. The diurnal temperature variation was reduced by less than 0.2°C as well. It should here also be stated that the observations might not be completely representative to the model grid.

Incoming long-wave radiation is very dependent on whether the sky is clear or cloud covered. Particularly low clouds increase the incoming long-wave radiation, up to 100 W m^{-2} . Table 7 shows the statistical evaluation during

summer and winter. As in the example of short-wave radiation the 8 km resolution gives somewhat better scores than 2.7 km. The former discussion regarding topography not resolved by the model also applies here. The influence from clouds is well shown in Figure 6, where the four nodes define the ability of the model to capture or miss the presence or nonpresence of clouds. There are occasions where the model both over- and underestimates the cloud cover. It appears that the WRF model simulates the average cloud cover quite well but with a negative bias of order 10 W m^{-2} in the winter and smaller negative or positive bias in the winter.

4.2. Sensitivity Studies. A number of sensitivity simulations were performed for 1- or 3-month summer and/or winter periods. The simulations are summarized in Table 8 together with CPU times. It is evident that the WRF6 microphysics requires less CPU time compared to the more complex Morrison double-moment scheme. The QNSE and MYNN2.5 schemes require more computational resources than the MYJ2.5 scheme. Further it is seen that the finer horizontal resolution simulations are more computer expensive than increasing the number of vertical layers in the lowest 1500 m by 4.

The sensitivity analysis of the different simulations, except the albedo analysis, are presented in the next two subsections.

TABLE 7: Statistical evaluation of incoming long-wave radiation in winter and summer 2009-2010. Bold numbers indicate the best result for each AWS. Vestfonna data are not used here because of the lack of data during the chosen period.

		R^2		Bias (W m^{-2})		MAE (W m^{-2})		SSC	
		DJF	JJA	DJF	JJA	DJF	JJA	DJF	JJA
Kongsvegen	24 km	0.63	0.36	-15.7	9.4	28.4	24.6	0.56	0.62
	8 km	0.65	0.38	-14.0	1.7	27.7	23.4	0.55	0.58
	2.7 km	0.61	0.36	-19.6	-1.5	30.3	24.0	0.60	0.60
Nordenskiöldbreen	24 km	0.70	0.36	-5.5	6.7	23.8	23.8	0.43	0.67
	8 km	0.66	0.41	-5.0	4.1	24.0	24.0	0.43	0.67
	2.7 km	0.68	0.33	-14.6	-6.4	25.8	25.2	0.47	0.71

TABLE 8: Sensitivity runs with different physics, albedo, and resolution.

Comparison run/scheme	CPU time (h)	Test scheme/run	CPU time (h)	Period
Microphysics: Morrison double-moment	44	Microphysics: WRF6 single-moment	40	JJA, DJF
Turbulence: MYJ2.5	44	Turbulence: QNSE	50	JJA, DJF
Turbulence: MYJ2.5	44	Turbulence: MYNN2.5	50	JJA, DJF
Standard albedo	22	Monthly climatologic albedo	22	JJA
2.7 km	15	900 m horizontal resolution	24	July, January
27 levels	15	High vertical resolution in lowest 1500 m, 31 levels	20	July, January

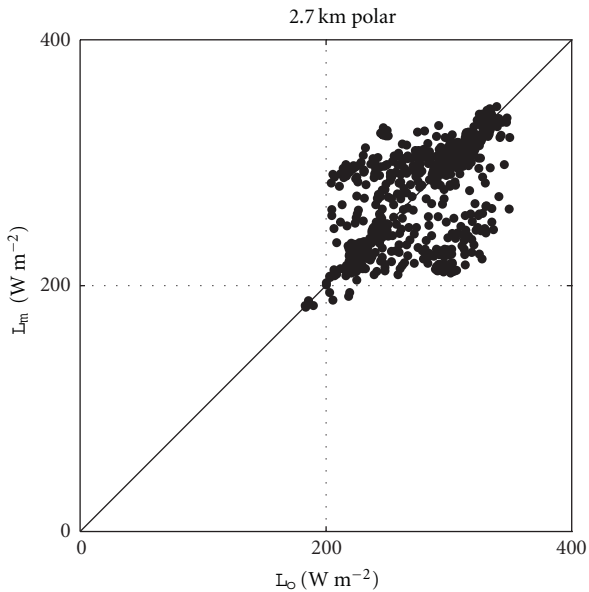


FIGURE 6: Scatter plot of incoming long-wave radiation at Kongsvegen in summer 2009 for 2.7 km resolution.

4.2.1. *Impact of Parameterisation Scheme.* The statistical evaluation of the different physics schemes is given in Tables 9, 10, 11, and 12. For temperature (Table 9) it is evident that the correlation coefficient is not remarkably changed, but the QNSE scheme is slightly better in winter, compared to the polar physics. MYNN2.5 is better correlated to the observations in summer and simulation of air temperature is rather insensitive to the choice of microphysics scheme. The bias and errors show some improvements and follow about the same patterns with the preference to QNSE in winter and

MYNN2.5 in the summer. In Figure 7 it is shown that the different schemes do not change the distribution to a large extent. Both low and high temperatures are often underestimated, but QNSE scheme provides the best distribution. The mean diurnal temperature variation is underestimated in all simulations (not shown), except for the MYNN2.5 scheme in summer at Nordenskiöldbreen. Overall, the MYNN2.5 scheme provides the largest and best diurnal variation.

Also for the wind speed, the choice of microphysics is of minor importance. The QNSE scheme improves the correlation in winter at Kongsvegen but worsens it during the summer. The correlations are very low, R^2 between 0.27 and 0.55. The MYNN2.5 scheme is either worsening or only slightly improving the correlation to observations. The errors and biases should not be analysed in too much detail because of the height corrections made. But although the observed wind is corrected upwards the model still overestimates the mean wind. It is often an improvement to use the QNSE or MYNN2.5 schemes instead of the MYJ2.5 scheme, MYNN2.5 giving the lowest biases. For the wind distribution in Figure 8 (omitting all values below 0.5 m s^{-1}) it appears that the simulated distributions are too flat, that is, the model produces too many cases with low and high winds. There is no clear scheme that outperforms the others but the MYNN2.5 scheme yields less frequent cases with strong winds and is in average closer to the observations.

Long-wave radiation correlation is worsened with the microphysics scheme except in summer at Kongsvegen and biases and errors follow about same pattern. The turbulence schemes, however, improve in mean correlation, biases, and errors with the QNSE scheme being slightly superior to the MYNN2.5 scheme, especially in winter.

The short-wave radiation is, as expected, most affected by the microphysics due to the processes that determine the cloud extent and thickness and how much of the

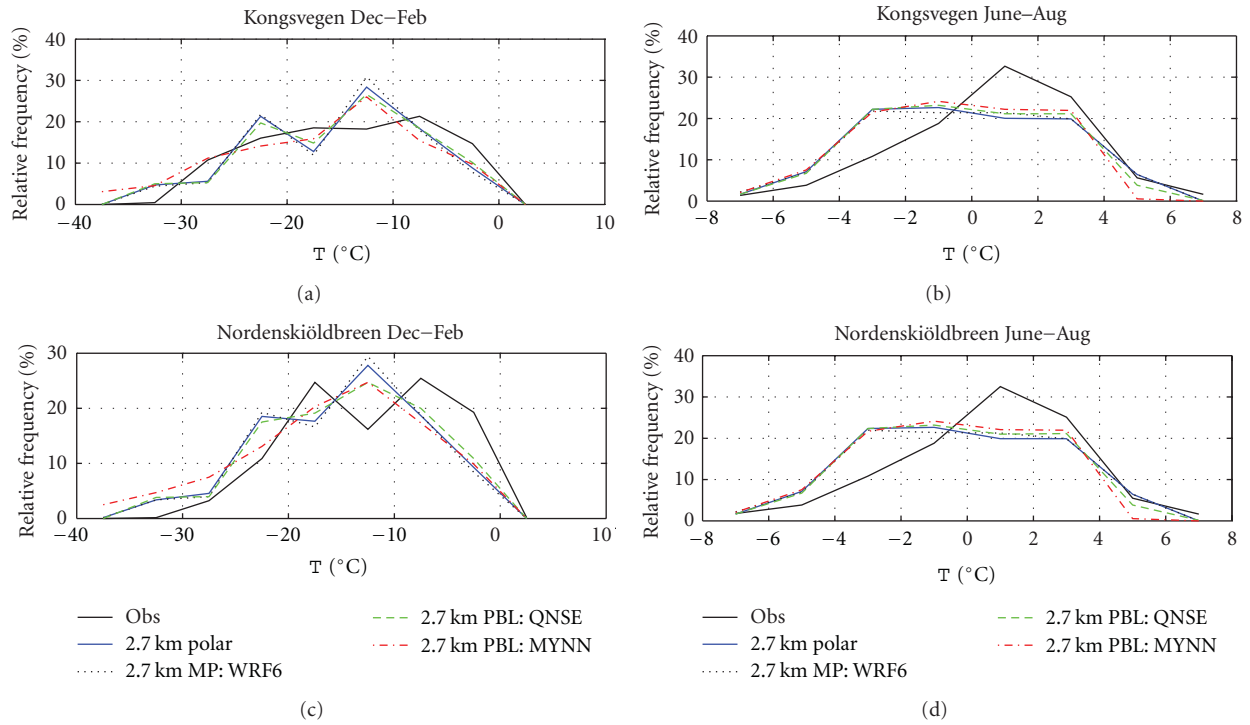


FIGURE 7: Frequency distribution of temperature in Kongsvegen and Nordenskiöldbreen.

TABLE 9: Temperature in 2.7 km resolution. Vestfonna data are not used here because of the lack of data during the chosen period. Bold numbers indicate the best result for each AWS. Abbreviation corr denotes height corrected temperatures.

		R^2		Bias ($^{\circ}\text{C}$)			MAE ($^{\circ}\text{C}$)				SSC				
		DJF	JJA	DJF	DJF corr	JJA	JJA corr	DJF	DJF corr	JJA	JJA corr	DJF	DJF corr	JJA	JJA corr
Kongsvegen	Polar phys	0.81	0.51	-1.4	-1.1	-1.2	-0.9	3.0	2.9	1.8	1.8	0.38	0.37	0.70	0.66
	MP: WRF6	0.80	0.52	-1.4	-1.2	-1.2	-0.9	3.1	3.0	1.8	1.7	0.38	0.37	0.70	0.66
	PBL: QNSE	0.82	0.50	-1.2	-1.0	-1.3	-1.0	2.9	2.8	1.9	1.7	0.36	0.35	0.70	0.66
	PBL: MYNN2.5	0.82	0.55	-2.5	-2.2	-1.5	-1.2	3.3	3.2	1.9	1.7	0.41	0.40	0.70	0.64
Nordenskiöldbreen	Polar phys	0.88	0.28	-3.2	-2.7	1.2	1.8	3.4	2.9	2.3	2.5	0.48	0.41	1.09	1.18
	MP: WRF6	0.88	0.27	-3.2	-2.7	1.2	1.7	3.4	3.0	2.4	2.6	0.48	0.42	1.12	1.21
	PBL: QNSE	0.89	0.28	-3.0	-2.5	1.1	1.6	3.2	2.8	2.2	2.4	0.46	0.40	1.04	1.13
	PBL: MYNN2.5	0.86	0.30	-4.1	-3.5	0.8	1.3	4.2	3.8	2.0	2.2	0.60	0.54	0.95	1.03

TABLE 10: Wind speed in 2.7 km resolution. Bold numbers indicate the best result for each AWS. Vestfonna data are not used here because of the lack of data during the chosen period.

		R^2		Bias		MAE		SSC	
		DJF	JJA	DJF	JJA	DJF	JJA	DJF	JJA
Kongsvegen	Polar phys	0.30	0.48	1.2	0.7	3.1	2.2	1.04	0.88
	MP: WRF6	0.30	0.48	1.2	0.6	3.1	2.1	1.04	0.85
	PBL: QNSE	0.32	0.47	1.2	0.7	3.0	2.1	1.02	0.85
	PBL: MYNN2.5	0.27	0.47	0.4	0.2	3.1	2.1	1.06	0.86
Nordenskiöldbreen	Polar phys	0.49	0.52	2.0	0.5	3.8	2.9	0.90	0.74
	MP: WRF6	0.49	0.52	2.0	0.3	3.8	2.9	0.91	0.74
	PBL: QNSE	0.47	0.54	2.1	0.4	3.9	2.8	0.92	0.72
	PBL: MYNN2.5	0.48	0.53	1.0	-0.2	3.6	3.0	0.85	0.76

TABLE 11: Short-wave radiation in summer and in 2.7 km resolution. Bold numbers indicate the best result for each AWS. Vestfonna data are not used here because of the lack of data during the chosen period.

		R^2	Bias	MAE	SSC
Kongsvegen	Polar phys	0.74	25	70	0.46
	MP: WRF6	0.78	40	68	0.45
	PBL: QNSE	0.76	24	66	0.44
	PBL: MYNN2.5	0.74	24	69	0.45
Nordenskiöldbreen	Polar phys	0.62	57	96	0.57
	MP: WRF6	0.67	69	98	0.58
	PBL: QNSE	0.64	55	91	0.54
	PBL: MYNN2.5	0.62	53	92	0.54

TABLE 12: Long-wave radiation in 2.7 km resolution. Bold numbers indicate the best result for each AWS. Vestfonna data are not used here because of the lack of data during the chosen period.

		R^2		Bias		MAE		SSC	
		DJF	JJA	DJF	JJA	DJF	JJA	DJF	JJA
Kongsvegen	Polar phys	0.65	0.36	-22	-2	30	24	0.58	0.60
	MP: WRF6	0.59	0.43	-27	-6	34	23	0.65	0.58
	PBL: QNSE	0.65	0.37	-21	-1	29	24	0.57	0.59
	PBL: MYNN2.5	0.64	0.39	-23	-2	30	23	0.59	0.59
Nordenskiöldbreen	Polar phys	0.69	0.33	-16	-6	25	25	0.45	0.71
	MP: WRF6	0.68	0.32	-19	-11	27	28	0.48	0.77
	PBL: QNSE	0.70	0.32	-15	-5	25	25	0.45	0.71
	PBL: MYNN2.5	0.70	0.34	-16	-5	25	25	0.45	0.69

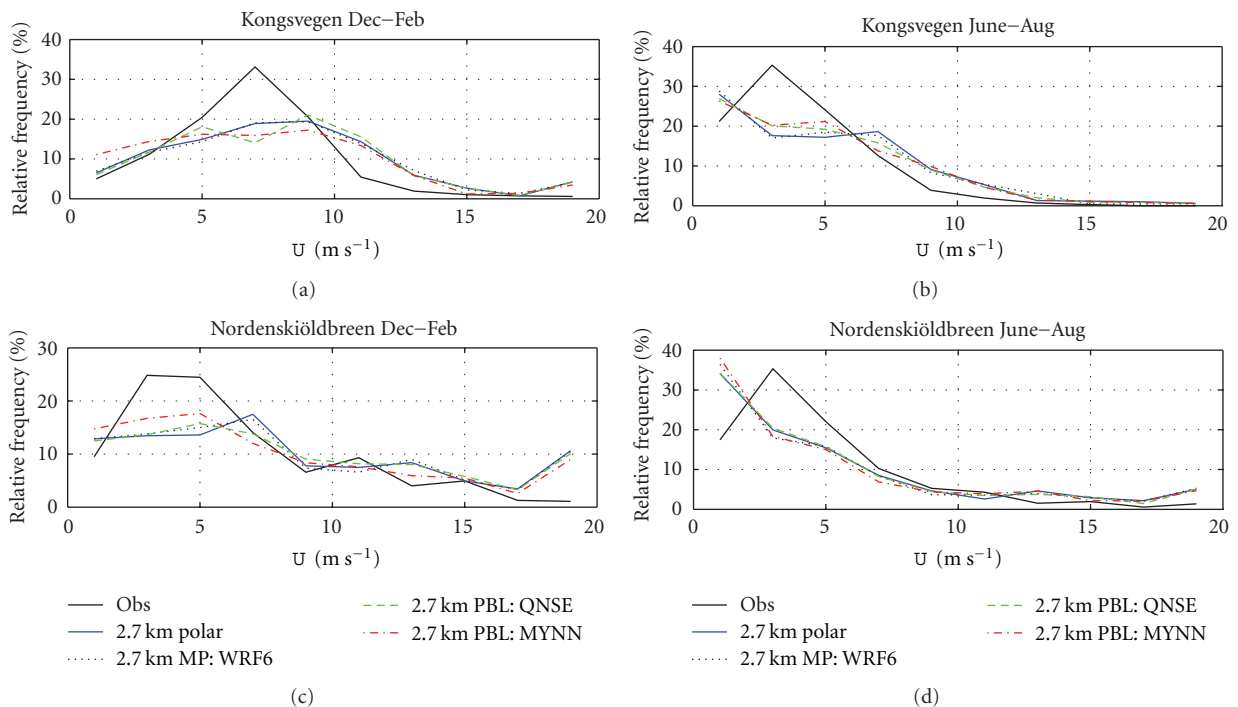


FIGURE 8: Frequency distribution of wind speed in Kongsvegen and Nordenskiöldbreen.

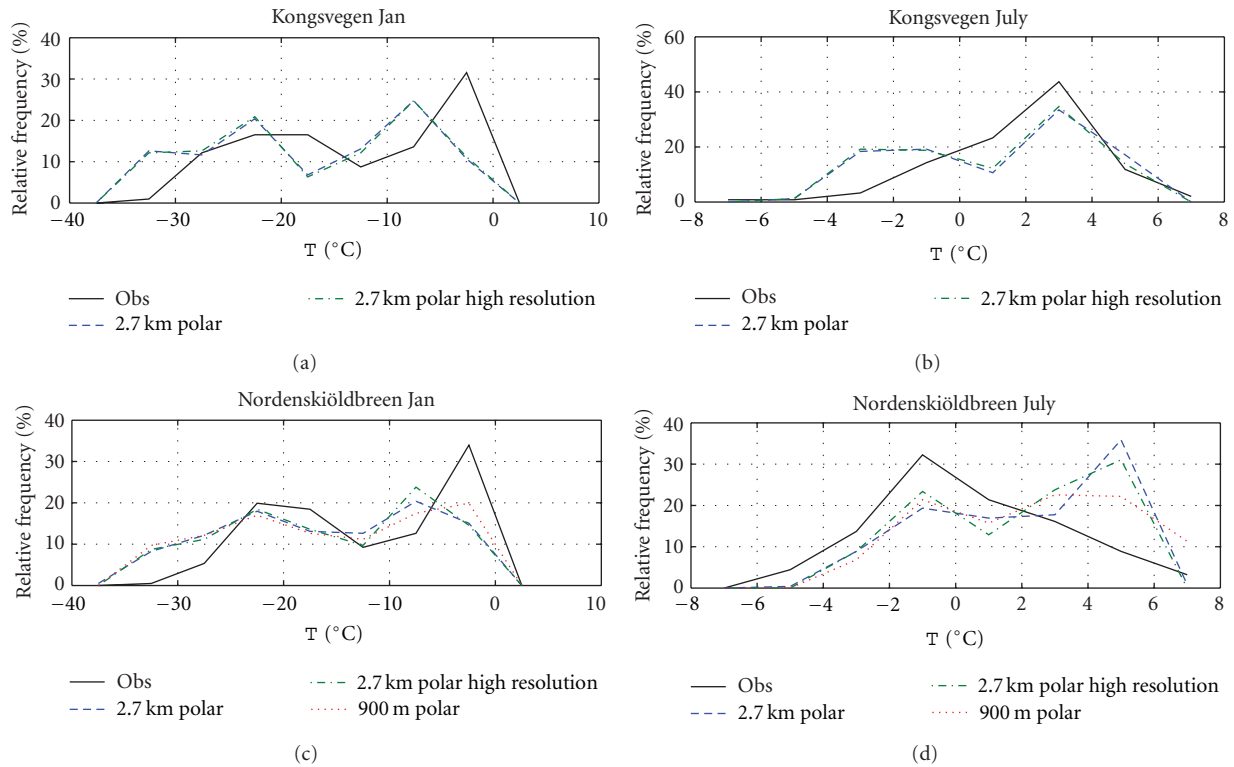


FIGURE 9: Frequency distribution of temperature at Kongsvegen and Nordenskiöldbreen.

moisture leaves the clouds via precipitation. The correlation is increased by the WRF6 scheme (Table 11). However, the bias increases and errors are not improved. The PBL schemes somewhat improve the biases, probably because of changed humidity fluxes over the open sea.

It appears that the use of the simpler microphysics scheme WRF6 in average reduces the skill of the WRF model on average, compared to the Morrison scheme. The improved correlation for short-wave radiation was cancelled by the worsened biases and errors and the worsened skills for long-wave radiation. The shorter CPU times with the scheme might not be worth in relation to model performance. Regarding the turbulence schemes both QNSE and MYNN2.5 improve the model skills, compared to the MYJ scheme. However, finding the best of them may require further investigations. The tendency here is that QNSE works better in winter and MYNN2.5 in the summer.

4.2.2. Impact of Improved Horizontal and Vertical Resolution.

Because of limited computer resources the high-resolution simulations were only performed for July 2009 and January 2010 and the 900 m resolution only over Nordenskiöldbreen. Also the higher vertical resolution caused more numerical instability (when trying to simulate the other winter and summer months) than the other simulations, although an adaptive time step was used (the QNSE turbulence scheme instead of the MYJ2.5 scheme improved the stability but was not analysed). The higher vertical resolution

in the boundary layer improves the correlation of the simulations to observations of some of the meteorological parameters, temperature (Table 13), wind (Table 14), and incoming long-wave radiation (Table 15). The 900 m resolution increases the correlation only for long-wave radiation. For temperature and wind the bias and MAEs are not significantly improved (or worsened). Time series of the high-resolution simulations only occasionally changes the temperature (not shown). In Figure 9 the distribution of temperature at Kongsvegen and Nordenskiöldbreen is shown. The simulated temperatures are bias-corrected based on the January and July bias, respectively. The observations have a double-peak in the winter and a single one in the summer, while the simulated distribution has double peaks in both seasons. The distribution is only slightly improved by the increased vertical resolution. The 900 m resolution shows more significant improvement. The mean diurnal variation is underestimated by the simulations except for Nordenskiöldbreen in winter. The higher vertical resolution decreases the variation, whereas the 900 m resolution increases the variation. Our estimate of the observed 10 m wind speed is rough and we cannot expect that the bias and errors would be improved by the higher vertical resolution. The 900 m resolution however lowers the simulated wind and lowers the errors. The wind distribution (Figure 10) is not much improved by the vertical resolution but the horizontal resolution better simulates all wind speeds above 7 m s^{-1} . The wind direction is very dependent on horizontal

TABLE 13: Temperature statistics in summer and winter 2009-2010 in 2.7 km resolution, with and without increased vertical resolution in the boundary layer (high vert. res.) and in 900 m resolution. Vestfonna data are not used here because of the lack of data during the chosen period. Bold numbers indicate the best result for each AWS. Abbreviation corr denotes height corrected temperatures.

		R^2		Bias ($^{\circ}\text{C}$)			MAE ($^{\circ}\text{C}$)				SSC				
		Jan	Jul	Jan	Jan corr	Jul	Jul corr	Jan	Jan corr	Jul	Jul corr	Jan	Jan corr	Jul	Jul corr
Kongsvegen	2.7 km	0.88	0.46	-4.0	-3.7	-1.0	-0.7	4.5	4.2	1.8	1.7	0.47	0.45	0.76	0.73
	2.7 km—high vert. res.	0.89	0.47	-3.9	-3.6	-1.2	-0.9	4.4	4.1	1.8	1.7	0.47	0.44	0.77	0.73
Nordenskiöldbreen	2.7 km	0.91	0.40	-4.3	-3.8	1.8	2.3	4.4	3.9	2.3	2.7	0.50	0.45	1.11	1.26
	2.7 km—high vert. res.	0.92	0.40	-4.2	-3.7	1.6	2.2	4.2	3.8	2.1	2.5	0.49	0.43	1.02	1.17
	900 m	0.91	0.38	-3.9	-3.5	2.4	2.7	4.0	3.7	2.7	3.0	0.46	0.43	1.28	1.40

TABLE 14: Wind speed statistics in summer and winter 2009-2010 in 2.7 km resolution, with and without increased vertical resolution in the boundary layer (high vert. res.) and in 900 m resolution. Bold numbers indicate the best result for each AWS. Vestfonna data are not used here because of the lack of data during the chosen period.

		R^2		Bias		MAE		SSC	
		Jan	Jul	Jan	Jul	Jan	Jul	Jan	Jul
Kongsvegen	2.7 km	0.25	0.39	1.0	0.7	3.3	2.2	0.97	0.97
	2.7 km—high vert. res.	0.28	0.42	1.2	1.0	3.3	2.2	0.95	0.98
Nordenskiöldbreen	2.7 km	0.44	0.50	-0.1	0.0	3.1	2.7	0.99	0.68
	2.7 km—high vert. res.	0.46	0.48	0.5	0.4	3.0	2.8	0.94	0.70
	900 m	0.41	0.44	-0.6	-0.8	2.4	2.5	0.75	0.62

resolution as it makes it possible to find grid points with the correct terrain slope direction. In Figure 11 and comparing with the observations and with 2.7 km resolution in Figure 4 it is evident that the wind direction is very much improved even if the side winds are still slightly exaggerated compared to the observations. Even when only increasing the vertical resolution, the wind direction becomes less spread compared to the main runs but the principal direction is too easterly.

The improvement of the long-wave radiation in correlation, bias, and MAEs for higher vertical resolution can probably be traced back to better resolved cloud formation in the boundary layer (Table 15). Increased horizontal resolution does not improve the correlation in winter but otherwise the bias and errors are improved with this configuration. In Figure 12 time series in January and July of incoming long-wave radiation at Nordenskiöldbreen are shown. The simulated long-wave radiation relatively well follows the observed fluctuations but underestimates the radiation in periods with less than 50 W m^{-2} . These low values are associated with clear sky or missed clouds in the model. Also when the radiation is high in both observations and in simulations the long-wave radiation is somewhat underestimated, except in the end of July. Most of the time the difference is very small between the simulations, but occasionally either the higher vertical or the higher horizontal resolution captures the changes in incoming long-wave radiation. For instance, the increased vertical resolution captures the clear sky in the beginning of January and the low clouds on 12-13 July, whereas the 900 m resolution captures the clouds on 17-18 July. Incoming short-wave radiation (Table 16) is improved with the higher vertical resolution but not as significantly as the long-wave radiation. The correlation for the 900 m simulation decreases but the bias and errors are improved.

To summarize, the higher vertical resolution improves all the simulated parameters, except the distribution of temperature, wind speed, and direction. Regarding the latter the 900 m horizontal resolution performs best. The changes for the other parameters are though rather small and in view of CPU time the higher vertical resolution seems to be the most economic change of the grid resolution. The 10 m wind direction is slightly improved (less spread) also with the increased vertical resolution. This suggests to potentially use a grid point with a terrain slope reflecting the actual observation site. However, when testing surrounding grid points in the 2.7 km resolution none of them gave better wind directions compared to the grid point used in the investigation, based on the correlation to the wind speed. Further, we have used a rather modest increase of vertical resolution of the PBL. It is possible that there would be even better scores of the meteorological surface layer variables with finer vertical resolution. As mentioned in Section 3, Söderberg and Parmhed [70] used 2 m vertical resolution in the lowest 10 s of meters.

5. Discussion and Conclusions

Results are presented from simulations performed over Svalbard by the mesoscale climate model WRF 3.2.1 for 2 years from spring 2008 to spring 2010. The ERA-Interim reanalysis was dynamically downscaled with the WRF model using the physics setup used in Polar WRF. The polar-optimized WRF model simulated the climate in 3 domains with the resolutions 24 km, 8 km, and 2.7 km. The inner nest was only simulated for summer 2009 and winter 2009-2010. Also sensitivity simulations were performed with one alternative microphysics scheme, WRF6 (used in the Arctic

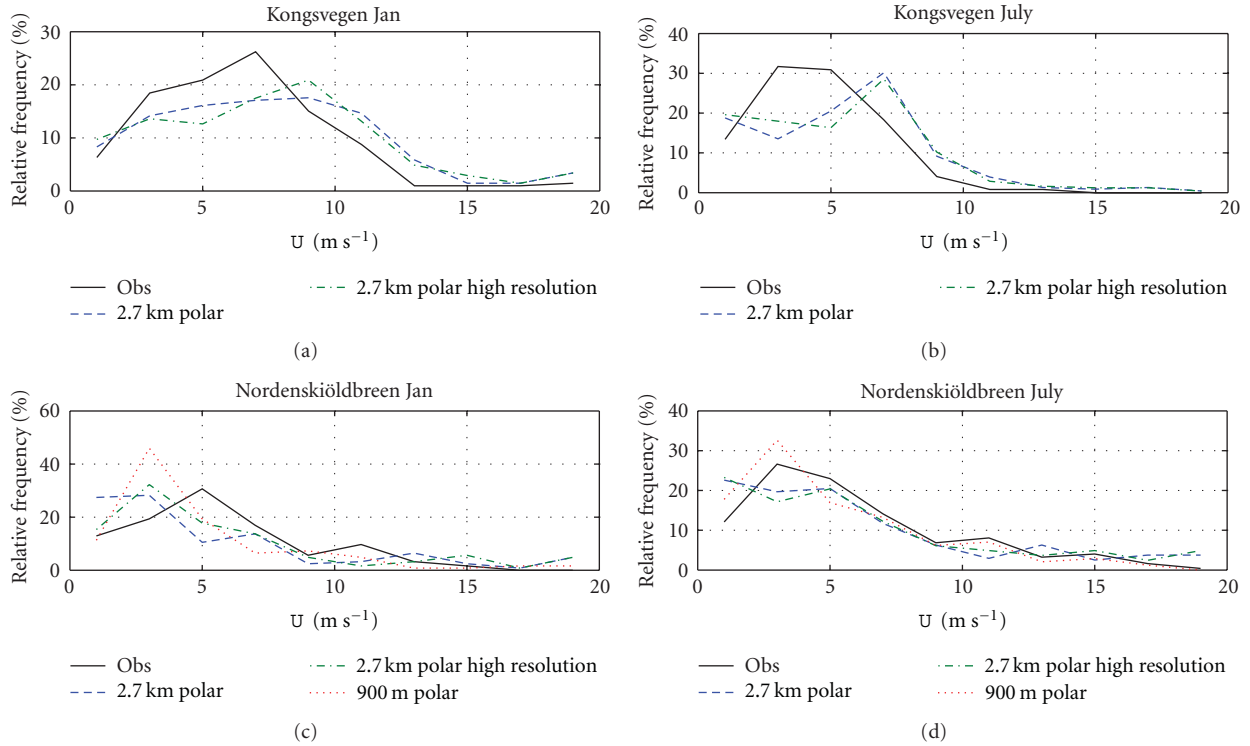


FIGURE 10: Frequency distribution of wind speed at Kongsvegen and Nordenskiöldbreen.

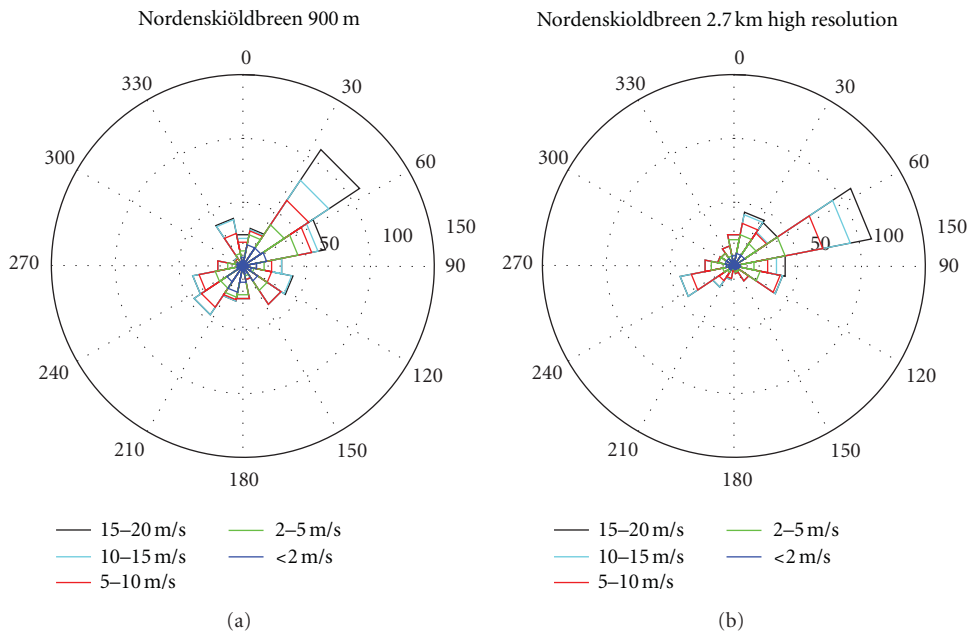


FIGURE 11: Wind roses of simulated wind at Nordenskiöldbreen in July together with January. Note that given frequency is absolute (hours).

Re-Analysis), and two PBL/surface layer schemes, QNSE (developed for very stable conditions) and MYNN2.5 (with turbulence interaction with clouds). Additional simulations were performed for July 2009 and January 2010 considering higher vertical resolution in the lowest 1.5 km and 900 m horizontal resolution, respectively. The investigation focuses

on validating the following surface variables: temperature, wind speed, specific humidity, and incoming short-wave and long-wave radiation. The WRF data are compared with observational data received from three automatic weather stations on Svalbard, Kongsvegen, Vestfonna, and Norden-skiöldbreen.

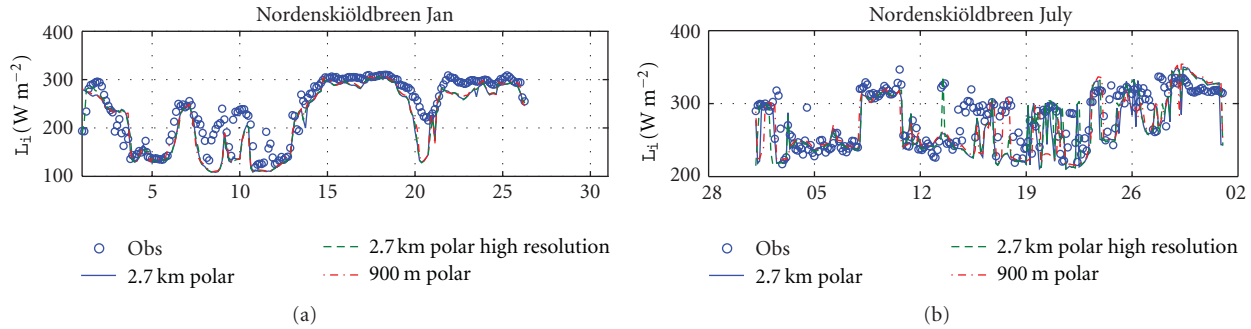


FIGURE 12: Time series of incoming long-wave radiation at Nordenskiöldbreen.

TABLE 15: Long-wave radiation statistics in summer and winter 2009-2010 in 2.7 km resolution, with and without increased vertical resolution in the boundary layer (high vert. res.), and in 900 m resolution. Bold numbers indicate the best result for each AWS. Vestfonna data are not used here because of the lack of data during the chosen period.

		R^2		Bias		MAE		SSC	
		Jan	Jul	Jan	Jul	Jan	Jul	Jan	Jul
Kongsvegen	2.7 km	0.73	0.40	-33	-8	36	22	0.74	0.58
	2.7 km—high vert. res.	0.75	0.42	-31	-5	35	22	0.71	0.56
Nordenskiöldbreen	2.7 km	0.79	0.39	-21	-14	27	25	0.43	0.72
	2.7 km—high vert. res.	0.81	0.44	-21	-12	26	24	0.42	0.67
	900 m	0.79	0.44	-19	-12	25	24	0.40	0.68

Downscaling the ERA-Interim analysis with the WRF model improved the simulated wind speed and to some extent the temperature. The correlation of the ERA-Interim temperature with the observations was from the beginning very high, R^2 being around 0.9, probably due to the assimilation of data from nearby SYNOP stations. Temperature changes are thus less sensitive to the topography than the wind speed.

Increased resolution did not always give better results, probably due to important unresolved topographic and heterogenic effects even for the 2.7 km resolution. The correlation of the wind speed in the 2.7 km resolution ranges between 0.32 in winter (Kongsvegen) and 0.55 in summer (Nordenskiöldbreen). The terrain is rather complex at both glaciers. It was examined if the lack of improvement from increasing the resolution from 8 km to 2.7 km may also be attributed to possible shortcomings with the downscaling method. The downscaling to the 24 km and 8 km grid is performed every time step (c. 7 min), meaning that every calculated field in the outer domain is used as boundary condition to the inner domain. The downscaling from 8 km to 2.7 km, done to reduce the CPU time, only provides boundary conditions each 3 h. Thus the 2.7 km nest lacks the transitional information between the 3 h inputs. However, a sensitivity study performed in the winter period showed however that this was of minor importance. The correlations for wind and temperature and the bias for wind at Vestfonna, with smoother topography, were higher than the other observations and improved with increased resolution. The radiation is very much influenced by clouds and at least the low-level clouds appear to be underestimated, leading

to periods of underestimated incoming long-wave radiation and overestimated incoming shortwave radiation. As a consequence the winter temperature was underestimated (when there is no short-wave radiation). During the summer months the bias was smaller or even positive due to the erroneous simulated shortwave radiation.

Higher vertical resolution in the boundary layer improved the simulations of radiation and wind speed, probably due to more correct vertical profiles of wind speed and moisture transport from the open sea. Temperature was not significantly improved. Higher horizontal resolution over Nordenskiöldbreen did surprisingly not improve the wind speeds, but the direction and also frequency distribution of temperature and wind. It requires more computer resources to increase the horizontal resolution in relation to the vertical. The room for improvement regarding resolution would thus favour the vertical. The vertical resolution may very well be increased more than 8 layers below 1500 m and would probably increase the scores.

The sensitivity study of the physics schemes revealed that for the Kongsvegen and Nordenskiöldbreen sites the Morrison microphysics scheme is recommended as is used in the Polar WRF. It is also more sophisticated than the WRF6 scheme giving improved incoming long-wave radiation, due to better cloud simulation. Both the QNSE and the MYNN2.5 schemes showed improvements compared to the Polar WRF scheme MYJ2.5. The QNSE scheme was slightly better than MYNN2.5 in winter and the opposite in the summer. When performing the high vertical resolution simulations it showed out that the model was suffering from numerical instability dependent on the PBL scheme. It might

TABLE 16: Short-wave radiation statistics in summer and winter 2009-2010 in 2.7 km resolution, with and without increased vertical resolution in the boundary layer (high vert. res.), and in 900 m resolution. Bold numbers indicate the best result for each AWS. Vestfonna data are not used here because of the lack of data during the chosen period.

		R^2	Bias	MAE	SSC
		Jul	Jul	Jul	Jul
Kongsvegen	2.7 km	0.71	35	75	0.49
	2.7 km—high vert. res.	0.71	34	74	0.49
Nordenskiöldbreen	2.7 km	0.62	86	109	0.65
	2.7 km—high vert. res.	0.62	79	106	0.63
	900 m	0.59	78	106	0.63

thus be crucial to use a certain PBL scheme when increasing the vertical resolution.

Overall, this investigation proves a good ability of the WRF model to simulate present climate on Svalbard glaciers, except for wind speed where correlations are as low as $R^2 = 0.3$. However, the importance of having physics schemes suitable for polar environments and fine vertical and horizontal resolution cannot be overemphasized. The study points out that simulations mainly could benefit from better descriptions of surface roughness length, and seasonal and shorter-term variation of glacier albedo (snow and ice), which is partly realized in Polar WRF already. Short fluctuations in the surface albedo are associated with new snow and high albedo, melting snow with lower albedo while even older snow or bare ice are strongly affected by dust deposition darkening the surface. In the measurements the albedo ranges between 0.2 and 0.95, whereas in Polar WRF it is varying between 0.5 and 0.82. Even though the 2 m temperature was proved to not be very sensitive to albedo it is of major importance for the glacier/snow surface energy balance.

Main conclusions regarding the WRF model performance based on observations at Kongsvegen and Vestfonna are as follows.

- (1) For future simulations with the WRF model over Svalbard glaciers,
 - (a) polar WRF physics should be used, except regarding the PBL scheme, where QNSE or MYNN2.5 better describes distribution of temperature and wind speed, the QNSE scheme being better in winter;
 - (b) 8 km resolution is not sufficient to model fine scale variations of the field but may be sufficient for Vestfonna due to a much simpler topography;
 - (c) finer vertical resolution in the lower part improves the model score, but probably there is need for even finer resolution than that used in this study (3 levels below 100 m and lowest at 11 m).
- (2) Improvements are needed regarding albedo, turbulence, and the related surface roughness.

Future possible investigations include precipitation validation and quantitative wind direction evaluation. The influence of terrain gives realistic enhancements of the precipitation in relation to the surrounding sea, but it remains to quantitatively evaluate the model with observations and whether the Morrison scheme outperforms the WRF6 scheme also for precipitation amount. Evaluating simulations with even finer vertical resolution and with the QNSE and MYNN2.5 scheme is also very interesting. Regarding observations there is firstly a need for more and consistent long-term meteorological observations at these glaciers. Secondly, alternative parameters may be considered. Thus turbulence measurements over glaciers would help to find out if the model performs well with respect to the turbulent flux components of the energy balance. Momentum flux measurements can also give information of surface roughness.

Acknowledgments

The authors thank their research groups and funding agencies for providing the observation data and related meta information. Thus, the Vestfonna data were acquired within IPY-KINNVKA project expeditions funded by the Swedish Research Council. The data were provided by Regine Hock (Geophysical Institute, University of Alaska), Rickard Pettersson, and Ulf Jonsell (Swedish Polar Research Secretariat, Stockholm, Sweden). Thanks are due to Ulf Jonsell also for comments on the paper. The Vestfonna data are also available through <http://www.smhi.se/ecds/Search-data>. The achievement of data from Nordenskiöldbreen station was financed by The Netherlands Organisation for Scientific Research (NWO) and the Swedish Science Council as part of the IPY-GLACIODYN project. The glacier field work at Vestfonna and Nordenskiöldbreen was partly supported by Norwegian Polar Institute (NPI). Kongsvegen data were collected within field work funded by ARCFAC V 2007 (EC Contract no. 026129-75). Fieldwork on Kongsvegen was partly supported by NPI (J. Kohler, Tromsø). Kongsvegen data analysis was supported by the Austrian Science Fund (FWF, Grant I 369-B17) and ESF, that is, the SvalGlac project (<http://svalglac.eu/>). NPI is acknowledged for the DEM data. The WRF simulations were performed on resources provided by the Swedish National Infrastructure for Computing (SNIC) at Uppsala Multidisciplinary Center for Advanced

Computational Science (UPPMAX). ECMWF ERA-Interim data used in this study have been obtained from the ECMWF data server. Work on the paper itself was a joint effort by ESF-SvalGlac members and thereby was also funded by the Nordic council of ministers (SVALI publication no. 6). The authors finally acknowledge two anonymous reviewers for their input to improve the original paper.

References

- [1] J. O. Hagen, J. Kohler, K. Melvold, and J. G. Winther, "Glaciers in Svalbard: mass balance, runoff and freshwater flux," *Polar Research*, vol. 22, no. 2, pp. 145–159, 2003.
- [2] P. Lemke, J. Ren, and R. B. Alley et al., "Observations: changes in snow, ice and frozen ground," in *Climate Change 2007: The Physical Science Basis. Contribution of Working Group I to the Fourth Assessment Report of the Intergovernmental Panel on Climate Change*, S. Solomon, D. Qin, M. Manning et al., Eds., Cambridge University Press, Cambridge, UK, 2007.
- [3] C. Nuth, G. Moholdt, J. Kohler, J. O. Hagen, and A. Kääb, "Svalbard glacier elevation changes and contribution to sea level rise," *Journal of Geophysical Research F*, vol. 115, no. 1, Article ID F01008, pp. 1–16, 2010.
- [4] G. Moholdt, J. O. Hagen, T. Eiken, and T. V. Schuler, "Geometric changes and mass balance of the Austfonna ice cap, Svalbard," *Cryosphere*, vol. 4, no. 1, pp. 21–34, 2010.
- [5] H. Svendsen, A. Beszczynska-Møller, J. O. Hagen et al., "The physical environment of Kongsfjorden-Krossfjorden, and Arctic fjord system in Svalbard," *Polar Research*, vol. 21, no. 1, pp. 133–166, 2002.
- [6] H. Hop, T. Pearson, E. N. Hegseth et al., "The marine ecosystem of Kongsfjorden, Svalbard," *Polar Research*, vol. 21, no. 1, pp. 167–208, 2002.
- [7] J. G. Winther, O. Bruland, K. Sand et al., "Snow research in Svalbard—an overview," *Polar Research*, vol. 22, no. 2, pp. 125–144, 2003.
- [8] J. Kohler and R. Aanes, "Effect of winter snow and ground-icing on a Svalbard reindeer population: results of a simple snowpack model," *Arctic, Antarctic, and Alpine Research*, vol. 36, no. 3, pp. 333–341, 2004.
- [9] S. Willmes, J. Bareiss, C. Haas, and M. Nicolaus, "Observing snowmelt dynamics on fast ice in Kongsfjorden, Svalbard, with NOAA/AVHRR data and field measurements," *Polar Research*, vol. 28, no. 2, pp. 203–213, 2009.
- [10] S. Westermann, J. Lüers, M. Langer, K. Piel, and J. Boike, "The annual surface energy budget of a high-arctic permafrost site on Svalbard, Norway," *Cryosphere*, vol. 3, no. 2, pp. 245–263, 2009.
- [11] AMAP Secretariat, "Snow, Water, Ice and Permafrost in the Arctic (SWIPA) 2011—Executive Summary," AMAP, Norway, 2011, <http://www.amap.no/swipa/>.
- [12] I. Hanssen-Bauer and E. J. Førland, "Temperature and precipitation variations in Norway and their links to atmospheric circulation," *International Journal of Climatology*, vol. 20, no. 14, pp. 1693–1708, 2000.
- [13] J. J. Cassano, J. E. Box, D. H. Bromwich, L. Li, and K. Steffen, "Evaluation of polar MM5 simulations of Greenland's atmospheric circulation," *Journal of Geophysical Research D*, vol. 106, no. 24, pp. 33867–33889, 2001.
- [14] H. Wei, W. J. Gutowski, C. J. Vorosmarty, and B. M. Fekete, "Calibration and validation of a regional climate model for pan-Arctic hydrologic simulation," *Journal of Climate*, vol. 15, no. 22, pp. 3222–3236, 2002.
- [15] J. A. Curry and A. H. Lynch, "Comparing arctic regional climate model," *EOS Transactions of the American Geophysical Union*, vol. 83, no. 9, pp. 83–87, 2002.
- [16] M. Tjernström, M. Žagar, G. Svensson et al., "Modelling the Arctic boundary layer: an evaluation of six ARCMIP regional-scale models using data from the SHEBA project," *Boundary-Layer Meteorology*, vol. 117, no. 2, pp. 337–381, 2005.
- [17] C. Jones, K. Wyser, A. Ullerstig, and U. Willen, "The Rossby-Centre Regional Atmospheric Climate model (RCA) Part II: application to the arctic climate," *AMBIO*, vol. 33, no. 4-5, pp. 261–266, 2004.
- [18] A. Rinke, K. Dethloff, J. J. Cassano et al., "Evaluation of an ensemble of Arctic regional climate models: spatiotemporal fields during the SHEBA year," *Climate Dynamics*, vol. 26, no. 5, pp. 459–472, 2006.
- [19] L. Rontu, F. Obleitner, S. Gollvik, C. Zingerle, and S. Tijm, "HIRLAM experiments on surface energy balance across Vatnajökull," *Meteorology and Atmospheric Physics*, vol. 103, no. 1–4, pp. 67–77, 2009.
- [20] J. J. Cassano, M. E. Higgins, and M. W. Seefeldt, "Performance of the weather research and forecasting (WRF) model for month-long pan-arctic simulations," *Monthly Weather Review*, vol. 139, no. 11, pp. 3469–3488, 2011.
- [21] D. K. Perovich, E. L. Andreas, J. A. Curry et al., "Year on ice gives climate insights," *EOS Transactions of the American Geophysical Union*, vol. 80, no. 41, p. 481, 1999.
- [22] P. Skeie and S. Grønas, "Strongly stratified easterly flows across Spitsbergen," *Tellus A*, vol. 52, no. 5, pp. 473–486, 2000.
- [23] D. H. Bromwich, J. J. Cassano, T. Klein et al., "Mesoscale modeling of katabatic winds over Greenland with the Polar MM5," *Monthly Weather Review*, vol. 129, no. 9, pp. 2290–2309, 2001.
- [24] A. D. Sandvik and B. R. Furevik, "Case study of a coastal jet at Spitsbergen—comparison of SAR- and model-estimated wind," *Monthly Weather Review*, vol. 130, no. 4, pp. 1040–1051, 2002.
- [25] H. Olafsson and H. Agustsson, "Gravity wave breaking in easterly flow over Greenland and associated low level barrier and reverse tip-jets," *Meteorology and Atmospheric Physics*, vol. 104, no. 3-4, pp. 191–197, 2009.
- [26] S. Grønas, "Mesoscale phenomena induced by mountains over Scandinavia and Spitsbergen," in *Proceedings of the Workshop on Orography*, pp. 165–182, ECMWF, Reading, UK, 1997.
- [27] A. Dörnbrack, I. S. Stachlewska, C. Ritter, and R. Neuber, "Aerosol distribution around Svalbard during intense easterly winds," *Atmospheric Chemistry and Physics*, vol. 10, no. 4, pp. 1473–1490, 2010.
- [28] K. Dethloff, M. Schwager, J. H. Christensen et al., "Recent greenland accumulation estimated from regional climate model simulations and ice core analysis," *Journal of Climate*, vol. 15, no. 19, pp. 2821–2832, 2002.
- [29] M. Bougamont, J. L. Bamber, and W. Greuell, "A surface mass balance model for the Greenland Ice Sheet," *Journal of Geophysical Research F*, vol. 110, no. 4, Article ID F04018, pp. 1–13, 2005.
- [30] J. E. Box, D. H. Bromwich, B. A. Veenhuis et al., "Greenland ice sheet surface mass balance variability (1988–2004) from calibrated polar MM5 output," *Journal of Climate*, vol. 19, no. 12, pp. 2783–2800, 2006.
- [31] J. Ettema, M. R. van den Broeke, E. van Meijgaard et al., "Higher surface mass balance of the Greenland ice sheet revealed by high-resolution climate modeling," *Geophysical Research Letters*, vol. 36, no. 12, Article ID L12501, pp. 1–5, 2009.

- [32] W. J. J. van Pelt, J. Oerlemans, C. H. Reijmer, V. A. Pohjola, R. Petterson, and J. H. van Angelen, "Simulating melt, runoff and refreezing on Nordenskiöldbreen, Svalbard, using a coupled snow and energy balance model," *The Cryosphere Discussions*, vol. 6, pp. 211–266, 2011.
- [33] W. C. Skamarock, J. B. Klemp, J. Dudhia et al., "A description of the advanced research WRF version 2," NCAR Technical Note TN-468 + STR, Boulder, Colo, USA, 2005.
- [34] W. C. Skamarock, J. B. Klemp, and J. Dudhia et al., "A description of the advanced research WRF version 3," NCAR Technical Note TN-475+STR, Boulder, Colo, USA, 2008.
- [35] K. M. Hines and D. H. Bromwich, "Development and testing of polar weather research and forecasting (WRF) model. Part I: greenland ice sheet meteorology," *Monthly Weather Review*, vol. 136, no. 6, pp. 1971–1989, 2008.
- [36] D. H. Bromwich, K. M. Hines, and L. S. Bai, "Development and testing of Polar Weather Research and Forecasting model: 2. Arctic Ocean," *Journal of Geophysical Research D*, vol. 114, no. 8, Article ID D08122, pp. 1–22, 2009.
- [37] K. M. Hines, D. H. Bromwich, L. S. Bai, M. Barlage, and A. G. Slater, "Development and testing of polar WRF. Part III: Arctic land," *Journal of Climate*, vol. 24, no. 1, pp. 26–48, 2011.
- [38] N. Mölders and G. Kramm, "A case study on wintertime inversions in Interior Alaska with WRF," *Atmospheric Research*, vol. 95, no. 2-3, pp. 314–332, 2010.
- [39] D. F. Porter, J. J. Cassano, and M. C. Serreze, "Analysis of the Arctic atmospheric energy budget in WRF: a comparison with reanalyses and satellite observations," *Journal of Geophysical Research*, vol. 116, Article ID D22108, pp. 1–20, 2011.
- [40] A. B. Wilson, D. H. Bromwich, and K. M. Hines, "Evaluation of polar WRF forecasts on the Arctic System Reanalysis domain: surface and upper air analysis," *Journal of Geophysical Research D*, vol. 116, no. 11, Article ID D11112, pp. 1–18, 2011.
- [41] T. Kilpeläinen, T. Vihma, and H. Ólafsson, "Modelling of spatial variability and topographic effects over Arctic fjords in Svalbard," *Tellus A*, vol. 63, no. 2, pp. 223–237, 2011.
- [42] S. Kirkwood, M. Mihalikova, T. N. Rao, and K. Satheesan, "Turbulence associated with mountain waves over Northern Scandinavia—a case study using the ESRAD VHF radar and the WRF mesoscale model," *Atmospheric Chemistry and Physics*, vol. 10, no. 8, pp. 3583–3599, 2010.
- [43] E. Mäkiranta, T. Vihma, A. Sjöblom, and E. M. Tastula, "Observations and modelling of the atmospheric boundary layer over sea-ice in a Svalbard Fjord," *Boundary-Layer Meteorology*, vol. 140, no. 1, pp. 105–123, 2011.
- [44] M. Reeve and E. Kolstad, "The spitsbergen south cape tip jet," *Quarterly Journal of the Royal Meteorological Society*, vol. 137, no. 660, pp. 1739–1748, 2011.
- [45] E. Stütz, *Dynamically and thermally driven flows over and around Svalbard, a case study based on numerical simulations and airborne measurements*, Diploma thesis, Institute of Meteorology and Geophysics, Innsbruck University, Innsbruck, Austria, 2010.
- [46] D. P. Dee, S. M. Uppala, A. J. Simmons et al., "The ERA-Interim reanalysis: configuration and performance of the data assimilation system," *Quarterly Journal of the Royal Meteorological Society*, vol. 137, no. 656, pp. 553–597, 2011.
- [47] U. Heikkilä, A. Sandvik, and A. Sorteberg, "Dynamical downscaling of ERA-40 in complex terrain using the WRF regional climate model," *Climate Dynamics*, vol. 37, no. 7-8, pp. 845–866, 2010.
- [48] M.-D. Chou and M. J. Suarez, "An efficient thermal infrared radiation parametrization for use in general circulation models," NASA Technical Memorandum 104606, 1994.
- [49] E. J. Mlawer, S. J. Taubman, P. D. Brown, M. J. Iacono, and S. A. Clough, "Radiative transfer for inhomogeneous atmospheres: RRTM, a validated correlated-k model for the longwave," *Journal of Geophysical Research D*, vol. 102, no. 14, pp. 16663–16682, 1997.
- [50] G. A. Grell and D. Devenyi, "A generalized approach to parameterizing convection combining ensemble and data assimilation techniques," *Geophysical Research Letters*, vol. 29, no. 14, article 1693, 2002.
- [51] H. Morrison, J. A. Curry, and V. I. Khvorostyanov, "A new double-moment microphysics parameterization for application in cloud and climate models. Part I: description," *Journal of the Atmospheric Sciences*, vol. 62, no. 6, pp. 1665–1677, 2005.
- [52] Z. I. Janjic, "The surface layer in the NCEP Eta Model," in *Proceedings of the 11th Conference on Numerical Weather Prediction*, pp. 354–355, American Meteorological Society, Norfolk, Va, USA, August 1996.
- [53] Z. I. Janjic, "Non singular Implementation of the Mellor–Yamada Level 2.5 Scheme in the NCEP Meso model," NCEP Office Note no. 437, 2002.
- [54] G. L. Mellor and T. Yamada, "Development of a turbulence closure model for geophysical fluid problems.," *Reviews of Geophysics & Space Physics*, vol. 20, no. 4, pp. 851–875, 1982.
- [55] A. S. Monin and A. M. Obukhov, "Basic laws of turbulent mixing in the surface layer of the atmosphere," *Trudy Geofizicheskogo Instituta, Akademiya Nauk SSSR*, vol. 24, no. 151, pp. 163–187, 1954.
- [56] F. Chen and J. Dudhia, "Coupling and advanced land surface-hydrology model with the Penn State-NCAR MM5 modeling system. Part I: model implementation and sensitivity," *Monthly Weather Review*, vol. 129, no. 4, pp. 569–585, 2001.
- [57] M. Möller, R. Möller, É. Beaudon et al., "Snowpack characteristics of Vestfonna and de Geerfonna (Nordaustlandet, Svalbard)—a spatiotemporal analysis based on multiyear snow-pit data," *Geografiska Annaler*, vol. 93A, no. 4, pp. 273–285, 2011.
- [58] S.-Y. Hong and J.-O. Lin, "The WRF single-moment 6-class microphysics scheme (WSM6)," *Journal of the Korean Meteorological Society*, vol. 42, no. 2, pp. 129–151, 2006.
- [59] S. Sukoriansky, B. Galperin, and V. Perov, "Application of a new spectral theory of stably stratified turbulence to the atmospheric boundary layer over sea ice," *Boundary-Layer Meteorology*, vol. 117, no. 2, pp. 231–257, 2005.
- [60] T. Kilpeläinen, T. Vihma, M. Manninen et al., "Modelling the vertical structure of the atmospheric boundary layer over Arctic fjords in Svalbard," *Quarterly Journal of the Royal Meteorological Society*. In press.
- [61] M. Nakanishi and H. Niino, "An improved Mellor-Yamada Level-3 model: its numerical stability and application to a regional prediction of advection fog," *Boundary-Layer Meteorology*, vol. 119, no. 2, pp. 397–407, 2006.
- [62] R. L. Hawley, O. Brandt, E. M. Morris, J. Kohler, A. P. Shepherd, and D. J. Wingham, "Techniques for measuring high-resolution firn density profiles: case study from Kongsvegen, Svalbard," *Journal of Glaciology*, vol. 54, no. 186, pp. 463–468, 2008.
- [63] M. A. G. den Ouden, C. H. Reijmer, V. Pohjola, R. S. W. van de Wal, J. Oerlemans, and W. Boot, "Stand-alone single-frequency GPS ice velocity observations on Nordenskiöldbreen, Svalbard," *Cryosphere*, vol. 4, no. 4, pp. 593–604, 2010.
- [64] M. Möller, R. Finkelnburg, M. Braun et al., "Climatic mass balance of the ice cap Vestfonna, Svalbard: a spatially distributed assessment using ERA-Interim and MODIS data,"

- Journal of Geophysical Research*, vol. 116, Article ID F03009, pp. 1–14, 2011.
- [65] V. A. Pohjola, P. Kankaanpää, J. C. Moore, and T. Pastusiak, “Preface: the international polar year project “Kinnvika”—arctic warming and impact research at 80° N,” *Geografiska Annaler*, vol. 93A, no. 4, pp. 201–208, 2011.
- [66] F. Obleitner and M. Lehning, “Measurement and simulation of snow and superimposed ice at the Kongsvegen glacier, Svalbard (Spitzbergen),” *Journal of Geophysical Research D*, vol. 109, no. 4, Article ID D04106, pp. 1–12, 2004.
- [67] G. König-Langlo and E. Augstein, “Parameterization of the downward long-wave radiation at the earth’s surface in polar regions,” *Meteorologische Zeitschrift*, vol. 3, no. 6, pp. 343–347, 1994.
- [68] C. R. Stearns, G. A. Weidner, and L. M. Keller, “Atmospheric circulation around the Greenland Crest,” *Journal of Geophysical Research*, vol. 102, no. D12, pp. 13801–13812, 1997.
- [69] V. A. Pohjola, J. C. Moore, E. Isaksson et al., “Effect of periodic melting on geochemical and isotopic signals in an ice core from Lomonosovfonna, Svalbard,” *Journal of Geophysical Research D*, vol. 107, no. 4, Article ID 4036, pp. 1–14, 2002.
- [70] S. Söderberg and O. Parmhed, “Numerical modelling of katabatic flow over a melting outflow glacier,” *Boundary-Layer Meteorol*, vol. 120, no. 3, pp. 507–543, 2006.
- [71] D. Wilks, *Statistical Methods in the Atmospheric Sciences*, Academic Press, 2006.
- [72] R. B. Stull, *An Introduction to Boundary Layer Meteorology*, Kluwer Academic Publishers, 1988.
- [73] F. Pellicciotti, T. Raschle, T. Huerlimann, M. Carezzo, and P. Burlando, “Transmission of solar radiation through clouds on melting glaciers: a comparison of parameterizations and their impact on melt modelling,” *Journal of Glaciology*, vol. 57, no. 202, pp. 367–381, 2011.
- [74] S. Forsström, J. Ström, C. A. Pedersen, E. Isaksson, and S. Gerland, “Elemental carbon distribution in Svalbard snow,” *Journal of Geophysical Research D*, vol. 114, no. 19, Article ID D19112, pp. 1–8, 2009.
- [75] B. Aamaas, C. E. Bøggild, F. Stordal, T. Berntsen, K. Holmén, and J. Ström, “Elemental carbon deposition to Svalbard snow from Norwegian settlements and long-range transport,” *Tellus B*, vol. 63, no. 3, pp. 340–351, 2011.

Research Article

Wind Climate in Kongsfjorden, Svalbard, and Attribution of Leading Wind Driving Mechanisms through Turbulence-Resolving Simulations

Igor Esau^{1,2} and Irina Repina³

¹Nansen Environmental and Remote Sensing Centre, G.C. Rieber Climate Institute, 5006 Bergen, Norway

²Centre for Climate Dynamics, 5020 Bergen, Norway

³Obukhov Institute for Atmospheric Physics, Russian Academy of Sciences, 119017 Moscow, Russia

Correspondence should be addressed to Igor Esau, igore@nersc.no

Received 31 October 2011; Revised 28 January 2012; Accepted 22 February 2012

Academic Editor: Anna Sjöblom

Copyright © 2012 I. Esau and I. Repina. This is an open access article distributed under the Creative Commons Attribution License, which permits unrestricted use, distribution, and reproduction in any medium, provided the original work is properly cited.

This paper presents analysis of wind climate of the Kongsfjorden-Kongsvegen valley, Svalbard. The Kongsfjorden-Kongsvegen valley is relatively densely covered with meteorological observations, which facilitate joint statistical analysis of the turbulent surface layer structure and the structure of the higher atmospheric layers. Wind direction diagrams reveal strong wind channeled in the surface layer up to 300 m to 500 m. The probability analysis links strong wind channeling and cold temperature anomalies in the surface layer. To explain these links, previous studies suggested the katabatic wind flow mechanism as the leading driver responsible for the observed wind climatology. In this paper, idealized turbulence-resolving simulations are used to distinct between different wind driving mechanisms. The simulations were performed with the real surface topography at resolution of about 60 m. These simulations resolve the obstacle-induced turbulence and the turbulence in the non-stratified boundary layer core. The simulations suggest the leading roles of the thermal land-sea breeze circulation and the mechanical wind channeling in the modulation of the valley winds. The characteristic signatures of the developed down-slope gravity-accelerated flow, that is, the katabatic wind, were found to be of lesser significance under typical meteorological conditions in the valley.

1. Introduction

Understanding of driving mechanisms shaping wind climate of the Arctic is important to a number of different research and applied problems, the regional weather forecast, planning of industrial activity, and better health care of the local population. In particular, strong and persistent surface winds in the western part of Svalbard can significantly alter ocean and sea ice processes [1] and climate of the larger region in the key Atlantic sector of the Arctic [2]. Unfortunately, the network of meteorological stations, which provide information to characterize the wind climate, is rather sparse in the Arctic. Therefore, the long-term, consistent, and relatively diverse observations in the Kongsfjorden-Kongsvegen valley (see Figure 1) are valuable for research on the detection and attribution of specific feature of the wind climate in a typical

Arctic fjord. Similar fjords with steep slopes and glaciers are found in Greenland and in many other places in the Arctic.

The major observed feature of the Arctic fjord wind climate can be described as surface winds, which blow along the axis of the fjord. The wind climate of the Kongsfjorden-Kongsvegen valley (hereafter referred to as the valley) exhibits this feature very clearly (e.g., [3–9]). Hanssen-Bauer et al. [3], Førland et al. [4], and Hartmann et al. [5] compiled a general description of the Svalbard wind climate on the basis of ground-born meteorological observations. They emphasized the typically observed wind channeling in the valley and other Arctic fjords but did not provide the details of the wind climate. Beine et al. [7] and Argentini et al. [9] studies are more specific as they were based on the results of field measurement campaigns. In particular, the wind roses for different months and for different elevations up to 500 m

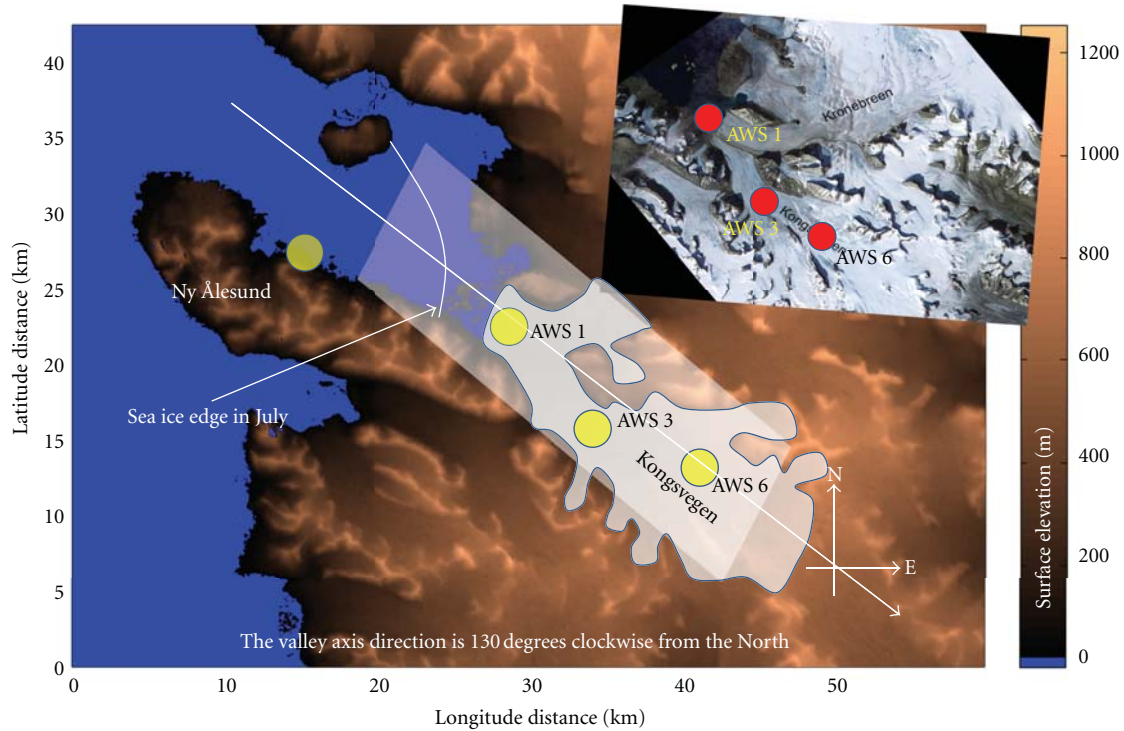


FIGURE 1: The scheme of the Kongsfjorden-Kongsvegen area with the research station Ny-Ålesund and the automatic weather station (AWS) sites on the glacier. The surface elevation is taken from the digital elevation model ASTER. The satellite image is courtesy of Andy Käab. The domain of PALM simulations is shown with the semitransparent rectangle.

(at Zeppelin Mountain) were presented. The wind channeling was found for all months and at all heights but during the summer months this channeling was less pronounced. Similar conclusions were drawn in Erath [10], Krismer [11], and Livik [12] studies based on analysis of the AWS data. The reviewed studies used different combinations of the available surface data sets, which were collected at different locations and heights and during different time periods. Despite those differences, the surface wind channeling and alignment with the valley axis remain the dominant wind features in the data.

The studies of the surface layer wind based on the high-quality but short-term observations are however not sufficient to characterize the wind climate, its vertical structure, and its driving mechanisms. Therefore, there were several modeling studies dealing with one or several aspects of the Svalbard regional climate. Here, we review only those studies where the model resolution was sufficiently fine to resolve some typical features of the Svalbard relief. Skeie and Grønås [6] simulated strongly stratified easterly flow across the Svalbard archipelago with a numerical model with a grid distance of 10 km. They found pronounced wind wakes with high velocity to downstream from the valleys. Later this feature was confirmed by simulations and satellite image analysis in Sandvik and Furevik [2]. The wind wakes were originated from the three resolved fjords Isfjorden, van Mijenfjorden, and Hornsund. The wind speed in the wakes was by factors of 1.7 to 2.2 higher than the wind speed in the undisturbed

flow. Skeie and Grønås [6] attributed this acceleration to the gravity wave activity and the large-scale left-right asymmetry induced by planetary rotation. The model resolution in Kilpeläinen et al. [13] study was significantly refined. The study did not aim to perform simulations of climatologically typical cases. Instead, ten real cases from winter and spring 2008 were simulated at 9, 3, and 1 km resolutions for 36 h each. Fairly good agreement with observations was demonstrated, although a systematic warm and moist bias and slightly overestimated wind speeds were found close to the surface. One should note that even the model resolution of 1 km does not represent properly the valley and steep surrounding mountains. Moreover, the model simulations included the complicated combinations of physical and advective driving factors, as it is usually found in the simulations of the realistic cases, which limit the extend of attribution studies. Nevertheless, Kilpeläinen et al. [13] concluded that the spatial variability of the surface fluxes of sensible and latent heat was mostly controlled by the air and sea surface temperatures instead of wind speed. The influence of the realistic topography on meteorological quantities was not systematic, except that a clear warming effect was seen in all the fjords studied. These conclusions are confirmed in Livik [12] simulations centered on the Kongsfjorden-Kongsvegen valley. Livik [12] model study is the attribution study with the Weather Research and Forecast model (WRF) run at resolution of 1 km. The simulations were performed for different flow regimes

assumably associated with the katabatic wind and the katabatic wind with different patterns of large-scale advection. This study includes also detailed comparisons between the model and observational results for the studied cases. Livik focused the discussion of the differences in the wind structures in topographically deflected flows and the pure katabatic flows. He concludes that the poor katabatic flows are the leading wind driving mechanism in the valley.

The aforementioned very brief review shows that there is a reasonable agreement between the surface data sets on the spatial and temporal structure of the valley winds. The consistent wind channeling features were clearly identified in all data sets. The attributions of the wind driving mechanisms in the model studies, however, diverged. The most detailed study by Livik [12] criticized the earlier intuitive attributions of the driving mechanisms. It compares the mechanical wind channeling of the flow and the katabatic flow mechanisms. Despite certain inconsistency of the model results with observations and the katabatic wind theory, it was concluded that the katabatic wind mechanism is the leading driving mechanism shaping the wind climate of the valley.

One should note that the reviewed studies are incomplete in two aspects. Firstly, the earlier studies were based on short data sets or even on a few specifically selected cases. Moreover, they did not consider the climatology of the wind and temperature vertical structures. Hence, they did not disclosed typical free atmosphere conditions associated with the observed combination of the meteorological parameters in the surface layer where the wind variability is naturally very limited. Secondly, the attribution studies did not consider one of the strongest thermal circulations, namely, the circulation caused by the horizontal difference in the land and sea surface temperatures. This difference will drive the valley wind even in the case of negligible surface vertical heat flux divergence.

In this study, we advance the description of the valley wind climate and the statistical detection of certain specific features in it. We use primarily the observations from the Integrated Global Radiosonde Archive (IGRA; available on <ftp://ftp.ncdc.noaa.gov/pub/data/igra/data-por>) made at the station Ny-Ålesund. The IGRA data analysis complements the previous studies, which have been based on the data collected by the automatic weather stations (AWS) on the glacier [10, 11] and along the fjord coast [12, 13]. The IGRA data also characterize the wind climate at higher elevations and over longer period of time than AWS and episodic field campaigns [9] do. In contrast to previous studies, our work includes also a composite analysis of the wind-temperature structure at different levels and for different seasons. It gives a chance to recognize specific signatures of one or another driving mechanism directly in the data statistics.

The wind field in the valley is likely created by a complex interplay of different mechanisms where the commonly accepted katabatic wind mechanism may not be leading or even important. Presence of large mountain glaciers in the valley is frequently referred to as one of the reasons to invoke the katabatic wind mechanism for explanation of observed

and simulated wind features [12, 15–19]. In particular, Oerlemans and Grisogono [18] analyzed different mounting glaciers in Switzerland, Iceland, and West Greenland to conclude that the katabatic wind is very common in all three valleys and rarely disrupted by the large-scale flow. Indeed, the observed vertical structure of the wind profiles looks similar to the structure predicted by the theory of the phenomenon of the equilibrium gravity-accelerated dense current over an infinite inclined surface (e.g., [20, 21]). However, winds in a valley are always channeled. Hence, the qualitative similarity is not sufficient for reliable attribution of the driving mechanisms. In fact the qualitative analogy to the katabatic winds in Greenland and Antarctica is deficient due to rather small length (just about 50 km) of the mountain glaciers. England and McNider [22] derived a quadratic asymptotic estimation of the maximum katabatic wind speed in the neutrally stratified atmosphere as function of the glacier length. The katabatic wind speed for the Svalbard glaciers according to the England and McNider [22] formula should be less than 5 m s^{-1} .

It is not only the down-slope gravity acceleration of an air mass cooled at the surface, that is, the katabatic wind mechanism, which can create strong surface winds in the valley. Another common mechanism, which has been missed in the Arctic studies, is the thermally driven land-sea breeze circulation. The breeze is created by the horizontal temperature difference between the open water fjord and the glacier. Kilpeläinen et al. [13] study indicates that the mountains increase this difference and therefore strengthen the breeze circulations. Furthermore, the topography can cause purely mechanical effects on the wind [6, 14, 23] like channeling, drainage, and gravity waves, which do not require the density difference to drive the flow.

In a series of publications, Doran with coauthors developed methodology of wind direction phase diagrams, which has been later successfully applied to attribute the mechanisms driving the valley flow under different climate conditions. Doran [14] numerical study demonstrated that the air forced into the valley by the mean pressure gradient (by the geostrophic wind) must induce the surface current in the opposite (down-slope) direction. Whiteman and Doran [24] applied the diagrams based on directions of the surface and the geostrophic winds to distinguish between four different mechanisms driving the valley flow. These authors studied the wind channeling in the Tennessee River valley, which is covered with observations much denser than the Arctic fjord valley under consideration. Cogliati and Mazzeo [25] applied the diagrams to study the valley wind climate utilizing only a limited number of observations. Recently, Nawri and Harstveit [26] have applied the diagrams to study the wind climate and to attribute the wind driving mechanisms in the Northern Norwegian fjords in Finnmark. In particular, they concluded that a clear separation between different prevailing surface wind directions in each season can be achieved based exclusively on the local mean sea level geostrophic wind direction. During the warm season, downward mixing of westerly overlying winds becomes more important as the stability of the boundary layer stratification decreases.

In this study, we advance the attribution of the revealed statistical features in the valley wind climate with fine resolution numerical simulations. We utilized the turbulence-resolving model Parallelized Atmospheric Large-eddy Model (PALM) described in Letzel et al. [27]. The PALM simulations are more suitable for the attribution studies than the regular WRF simulations as PALM is easy to set up for one particular driving mechanism at time. Moreover, PALM resolution is of two orders of magnitude finer than the achieved WRF resolution. Therefore not only the model topography is more realistic (especially slopes in the valley) but also the turbulence is partially resolved. We will elaborate this statement in the paper. The model topography with horizontal resolution of about 60 m is shown in Figure 1. The digital elevation model (DEM) is taken from the Advanced Spaceborne Thermal Emission and Reflection Radiometer (ASTER; available from <http://www.gdem.aster.ersdac.or.jp/>).

This paper consists of three research sections. Section 2 reports wind climatology based on the IGRA data and compares it with the published AWS data and results of field campaigns. This section constitutes the detection part of the study. Section 3 constitutes the attribution part of the study. This section describes the numerical experiments with PALM. It highlights specific features in the wind structure associated with different driving mechanisms. Section 4 concludes the study combining the results of the statistical analysis of the wind climatology with the model attribution study.

2. Wind Climatology

2.1. Wind Climatology from the Data Archive IGRA. The Kongsfjorden-Kongsvegen valley (see Figure 1) is relatively densely covered with observations, and therefore, the valley is one of a few well-studied places of the Svalbard archipelago as well as among other Arctic fjords. The longest atmospheric observations are provided by the radiosounding station in Ny-Ålesund. In order to establish the wind climatology in the valley, we utilized the observations from the Integrated Global Radiosonde Archive (IGRA; available on <ftp://ftp.ncdc.noaa.gov/pub/data/igra/data-por>). IGRA is a quality controlled archive [28] with data available at the standard pressure levels (1000, 925, 850, 700, 500, 400, 300, 250, 200, 150, 100 hPa), the surface, the tropopause, and several significant levels in the atmosphere. The available meteorological parameters are the temperature, the geopotential height, the dew point depression, and the wind direction and speed. The Ny-Ålesund station has the World Meteorological Organization identifier 01004. It is located at 78.9N and 11.9E. The archive contains 5396 soundings, which is 76.5% of the theoretically possible amount [29, 30]. Thus, the observational record is rather complete. The data are available for the period 1993–2008. In this study, we use only the data at the standard pressure levels and at the surface.

The Ny-Ålesund wind climatology computed for the period 1993–2008 is shown in Figure 2. The surface wind channeling is clearly seen on the plot where the median wind direction is shown by arrows. The wind directions at the surface level and, to some degree, at the 925 hPa pressure

level are limited to the sector 100–160 degrees (clockwise from the North). These directions correspond to the wind from the South-East along the major axis of the valley. On average, the summertime and wintertime wind directions are slightly different but remain within this sector. Wind directions at the higher pressure levels change dramatically. The most probable (median) wind directions at the 700 hPa pressure level become nearly 270 degrees, which correspond to the westerly winds. The mean surface pressure in Ny-Ålesund is 1009 hPa. The mean height of the 925 hPa surface is about 700 m. Thus, the layer of the strongly channeled winds is comparable in thickness with the height of the surrounding mountains (800 m to 1200 m). The wind channeling is persistent throughout the year. In wintertime, the significant change of the wind direction is found near the 850 hPa pressure level at about 1.5 km height. In summertime, the layer of the channeled winds is thinner. The wind direction changes already at 700 m. The obtained wind climatology is consistent with analysis of the short-term data sets for March–September 1998 during the Arctic Radiation and Turbulence Interaction Study (ARTIST) reported by Beine et al. [7] and Argentini et al. [9]. These authors also observed significant changes in the wind direction between 300 m and 500 m in the ARTIST data for April.

The more detailed analysis of the structural feature of the wind climatology is obtained through development of the wind diagram methodology previously utilized in Cogliati and Mazzeo [25] and Nawri and Harstveit [26]. Probabilities to find certain wind direction at two levels in the atmosphere are shown in Figure 3. The winds at the 700 hPa pressure level (at about 3 km above the sea level) have the maximum probability to blow from the western sectors. The surface winds are constrained by the valley and exhibit the much larger probabilities to blow along the valley. It is noteworthy that wind direction alignment throughout the entire 3 km layer of the atmosphere is the least probable for the directions close to the direction of the axis of the valley. Figure 4 discloses that strong winds are those channeled the most. As expected, the strongest winds at the surface are aligned with the valley axis. It is surprising, however, that the directions of the strong winds at the 700 hPa pressure level are opposite to the directions of the surface strong winds. Figure 5 complements this description. It shows the typical (mean) wind speed at the surface and at the 700 hPa pressure level as well as the median angle between the surface and the 700 hPa level wind directions for all four seasons. The channeled wind is stronger than the wind in other sectors for all seasons but summer. The strong surface winds do not necessarily correspond to the equally strong winds at higher elevations. Moreover, the surface winds are on average rotated by 90 to 120 degrees with respect to the winds in the free atmosphere.

The analysis given in Figures 2–5 supports the conclusion that the dominant surface winds in the valley are strongly channeled but not driven by the similar wind at higher altitudes. Contrary, the surface winds frequently blow in the opposite direction to the geostrophic winds in the free atmosphere. The 850 hPa pressure level does not have any dominant direction of the wind. It allows identification of this or adjacent levels as the top of the layer of channeled winds.

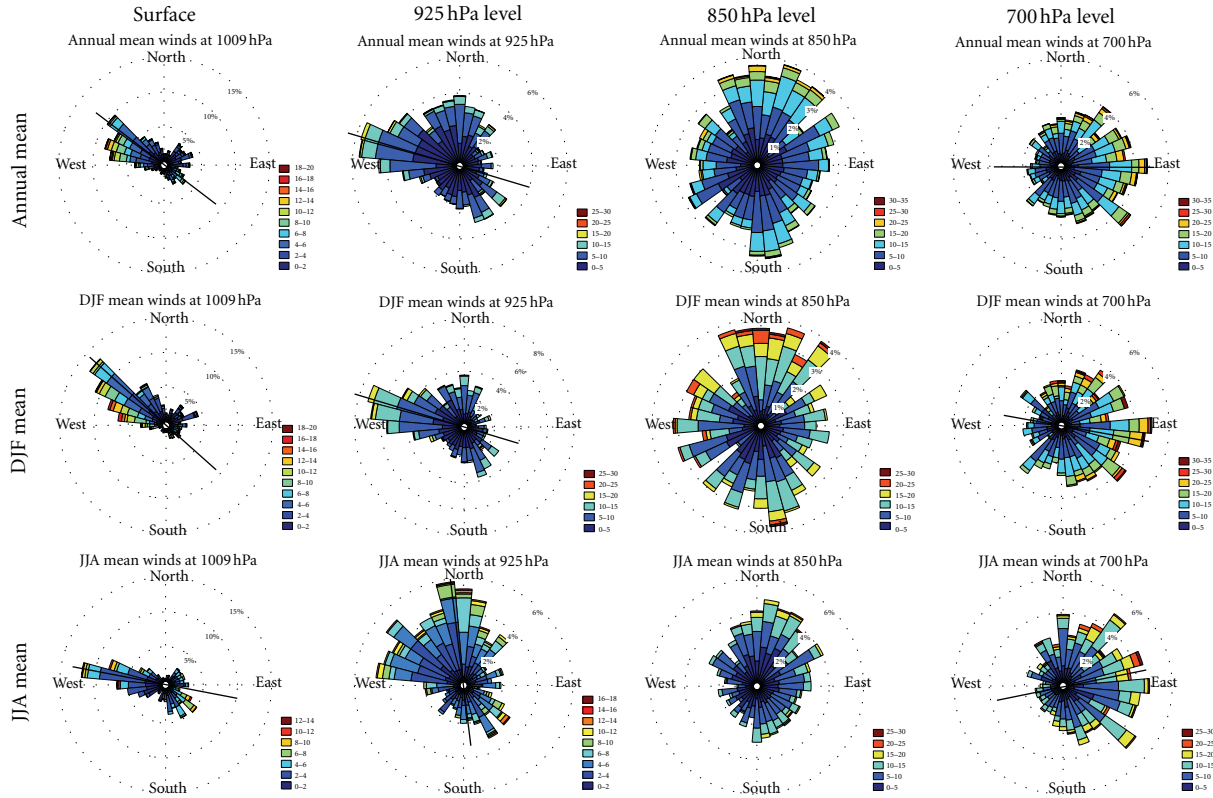


FIGURE 2: The wind climatology for the Ny-Ålesund station as obtained from the IGRA data archive for the period 1993–2008. The wind speed climatology is shown with color; wind direction, with the orientation of the bars; and probability, with the size of the bars. Arrows show the median wind vectors.

Hence, the wind channeling can be recognized up to 1000 m height.

To our opinion such a deep layer cannot be attributed to the effect of the katabatic winds. The theory of the katabatic wind [16–18, 21] suggests that the layer of significant katabatic wind should be rather shallow. Indeed, the katabatic wind mechanism implies that the dense air layer is created by the intense surface cooling, which means that this layer must be stably stratified. The vertical turbulent mixing in the stably stratified layers is suppressed (e.g., [31, 32]). Hence, the air is cooled significantly only in a thin (a few tens of meters) layer near the surface. On an inclined surface, this relatively dense but shallow layer will be accelerated down-slope by the gravity force. Above this surface layer, the air temperature is little affected by the cooling. Moreover, the weak turbulent friction cannot redistribute enough momentum from the accelerated layer below. Exactly this pattern is observed in Antarctica and Greenland where the katabatic wind is common (e.g., [33]). Hence, the air above a few tens of meters from the surface should not reveal significant movement, especially under the conditions of the opposite geostrophic wind.

2.2. Wind Climatology from Surface Layer Observations. The surface layer data sets are more diverse in the valley. The data sets include the regular observations in Ny-Ålesund available since 1974, several AWS in continues operation over several

years, and more short-term data sources operated during field campaigns, mostly during spring and summertime. Table 1 provides information about some of these data sources. There are also a number of short-term installations (Zeppelin, Pynten, Austre, Gåsebu, Brandal, Stupbekken; see [12]), which are not reviewed in this study. Our own analysis is focused on the AWS 3 and Ny-Ålesund data records, whereas AWS 1 and AWS 6 results are taken from Krismser [11]. The AWS 3 carried out the measurements on a flat surface with no obstacles nearby. The station instrumentation consisted of the Metek ultrasonic thermometer-anemometer (model USA-1) mounted on top of a 2 m mast, the Kipp&Zonen net radiometer (model CNR1), and the meteorological station.

The composite analysis of the surface meteorological data from Ny-Ålesund is shown in Figure 6. The diagram in the parameter phase space defines the position of each measurement through the triplet: the wind speed, U , the wind direction, D , and the temperature, T . The parameter phase space is then divided on $N = 20$ bins along each axis. Hence, the parameter phase space is covered with N by N squares. All data points inside each square are averaged to obtain the mean values of the triplets \bar{U} , \bar{D} , and \bar{T} . Then \bar{T} is shown in colors and \bar{U} and \bar{D} as two orthogonal axes. The contour lines show the relative number of measurements found in each square, that is, the relative probability to find the given combination of those three meteorological parameters in

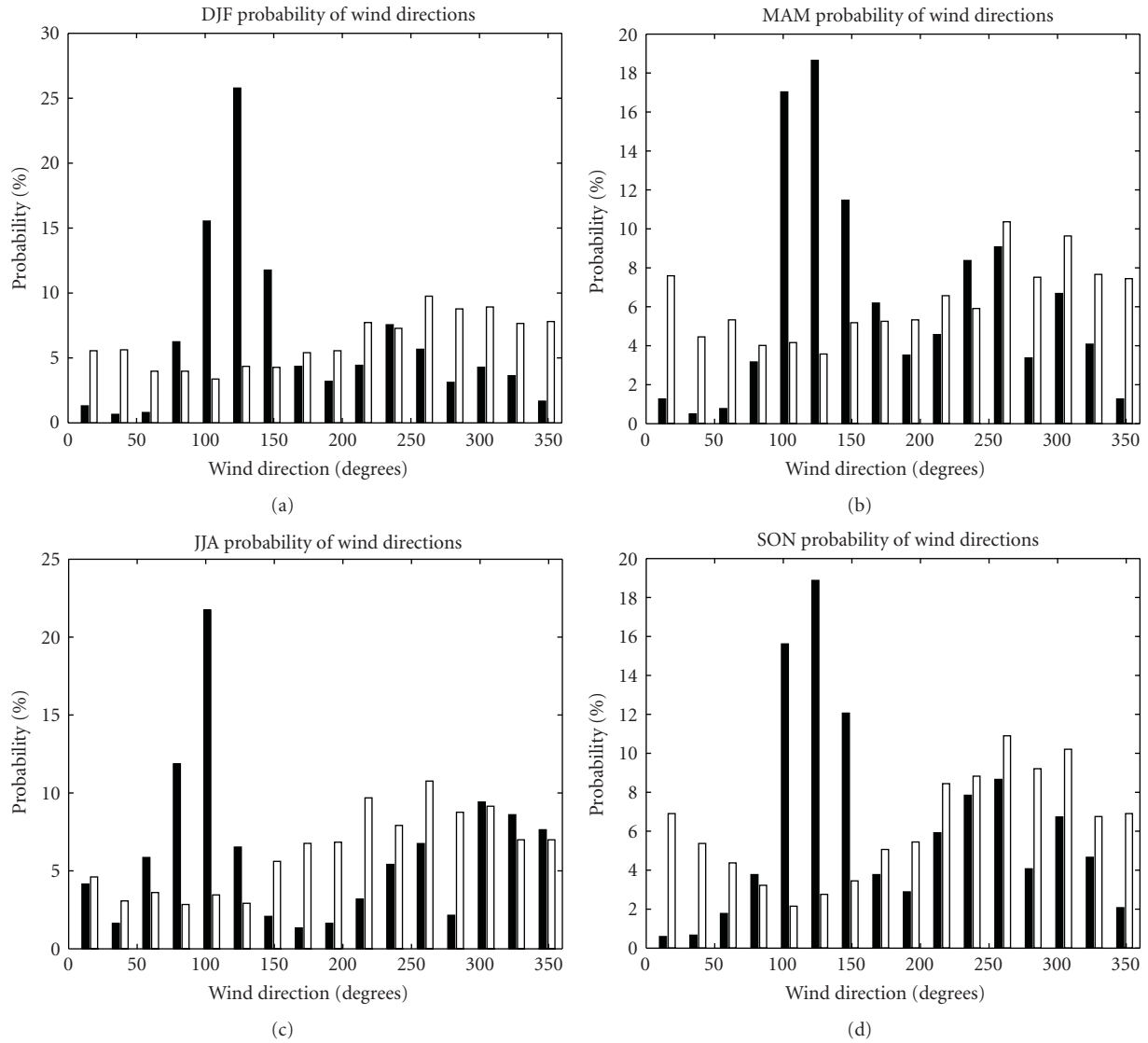


FIGURE 3: The climatological probability of wind directions in Ny-Ålesund from the IGRA data archive for four seasons: winter (a), spring (b), summer (c), and autumn (d). The black bars correspond to the probability of the surface winds, and the white bars to the winds at the 700 hPa pressure level.

TABLE 1: Sources of the meteorological data in the Kongsfjorden-Kongsvegen valley.

Station	Coordinates	Maintenance	Observations	Period
Ny-Ålesund	8 m a.s.l. 78.9230 N 11.9333 E	WMO station 99910 eKlima@met.no	Regular meteorological observations	06.1974–to date
AWS 1 (Glacier margin)	170 m a.s.l.	Institute of Meteorology and Geophysics Innsbruck (IMGI) and the Norwegian Polar Institute (NPI)	Temperature, wind speed and direction, relative humidity, global and reflected short-wave radiation, atmospheric and surface long-wave radiation	05.2007–06.2008
AWS 3	350 m a.s.l.	Obukhov Institute for Atmospheric Physics (IAP) and the Institute for Marine and Atmospheric Research, Utrecht University	The same; in addition 15 m gradient mast and a number of remote sensing instruments including SODAR were installed	05.2009–to date
AWS 6 (equilibrium altitude of the glacier)	550 m a.s.l.	Institute of Meteorology and Geophysics Innsbruck (IMGI) and the Norwegian Polar Institute (NPI)	The same	05.2000–02.2006 05.2007–to date

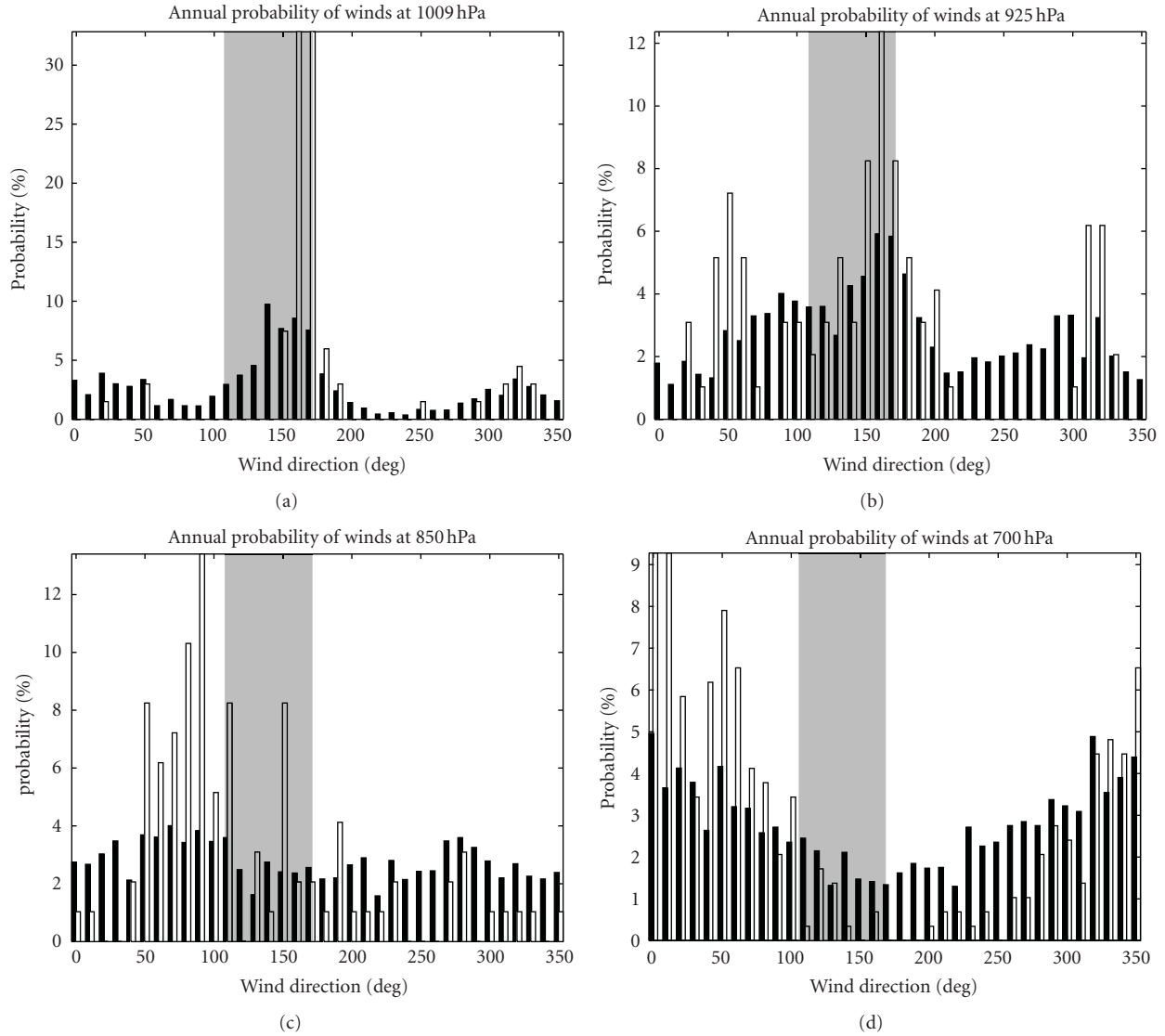


FIGURE 4: The annual climatological probability of the wind speed to be found within the given range of wind directions. The analysis is based on the IGRA data archive for the Ny-Ålesund stations. The probabilities are shown at four pressure levels: the surface (a), 925 hPa (b), 850 hPa (c), and 700 hPa (d). The black bars correspond to the total probability, and the white bars to the probability of the strongest winds (the wind speed belongs to the top quartile). The gray strips indicate the direction of the valley.

the observations. The probabilities are normalized by the maximum probability found on the plot, which therefore will be equal to 1. The contour lines of 0.25, 0.5, 0.75, and 0.9 of the maximum probability are shown. The composite analysis shows the mean properties of the channeled wind for the entire period of observations since 1974. In addition, we show such an analysis for all May months only and for the period between May 2nd and 13th 2009. The latter period is highlighted due to availability of turbulence and mast measurements for those days. The corresponding meteorological and turbulent characteristics measured by AWS 3 are shown in Figure 7.

The pattern of the temperature in the wind speed and direction phase space is very variable. However, the major part of this variability is associated with rare meteorological

events. It is worth to consider only the areas of the phase space, which are under the first contour line. As the katabatic wind is supposed to bring cold temperatures from the glacier, we expect to find a good association between the wind directions in the sector 100–160 degrees, the stronger than average wind speed of 5 to 10 m s^{-1} , and the lower temperatures. Although such combination of meteorological parameters could be found on the diagram, it is similarly likely to find the associated high temperatures as well. The high temperatures could indicate the adiabatic air subsidence in the valley due to the mechanical drainage or föhn mechanisms. The pattern of the diagram for May month is generally similar to the pattern on the climatologic diagram. However, May 2009 at the AWS 3 site was different. We found stronger winds and lower temperatures in the valley, which clearly

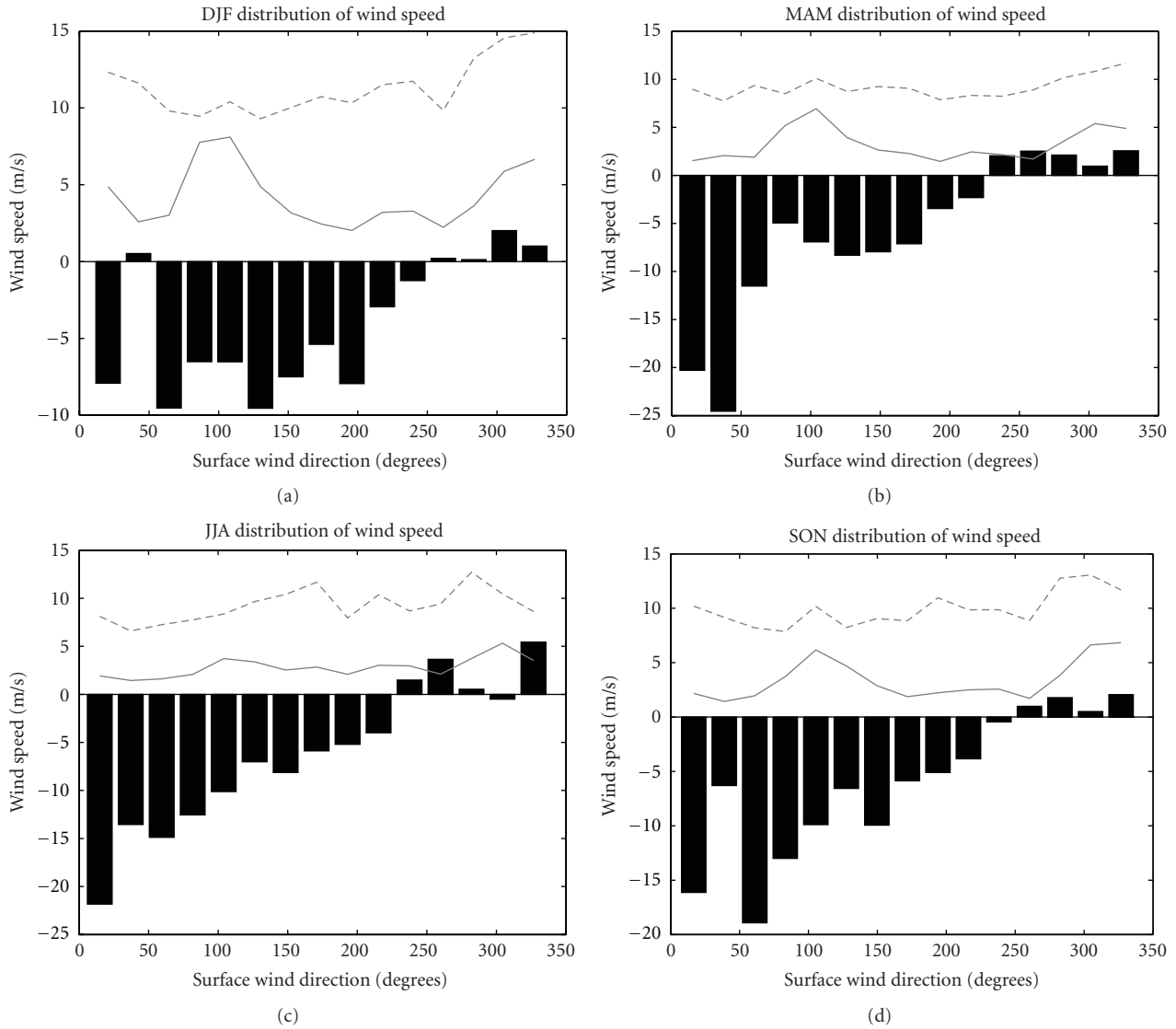


FIGURE 5: Composite plot of the wind speed at the surface (solid gray line), at the 700 hPa pressure level (dashed gray line), and the angle between wind directions at those surfaces (black bars). The wind speed is given in m s^{-1} ; the angle in degrees $\times 10^{-1}$. The IGRA data analysis for Ny-Ålesund is shown for four seasons: winter (a), spring (b), summer (c), and autumn (d).

indicate the development of the katabatic wind. Figure 7 confirms that the local meteorological conditions at the AWS 3 site and in Ny-Ålesund were often very different with the wind blowing in opposite directions. This observation may explain paradoxical lack of the katabatic winds in the Ny-Ålesund data. The katabatic wind could be simply too weak to reach this station.

The strongly channeled winds were found in records from other glacier AWSs as well. The highest station (AWS 6) observed the wind directions in the sector of 100° to 150° in 20% (summertime with the minimum in June) to 50% (springtime with the maximum in March) of cases [11]. The secondary maximum corresponding to the cases with the wind direction of about 300° could be also identified in the station records. The surface is typically colder than the air above it. At the glacier sites, the temperature difference is

usually 10 K to 20 K in the winter season and 0 K to 5 K in the summer season. By contrast, Oerlemans and Grisogono [18] study of midlatitude glaciers revealed the temperature deficit over the melting ice surface as large as 15 K. As the summertime temperature at Svalbard typically does not exceed 5°C , such a large temperature deficit is physically impossible. Recall that the asymptotic theory links the temperature deficit with the maximum katabatic wind speed. Thus, smaller temperature deficit on the Svalbard glacier implies much weaker katabatic winds in the valley.

3. Numerical Simulations of the Wind Patterns Induced by Different Driving Mechanisms

We established in the previous section, statistical significance, the vertical structure, and the parametrical composition of the winds in the valley. In this section, we will look

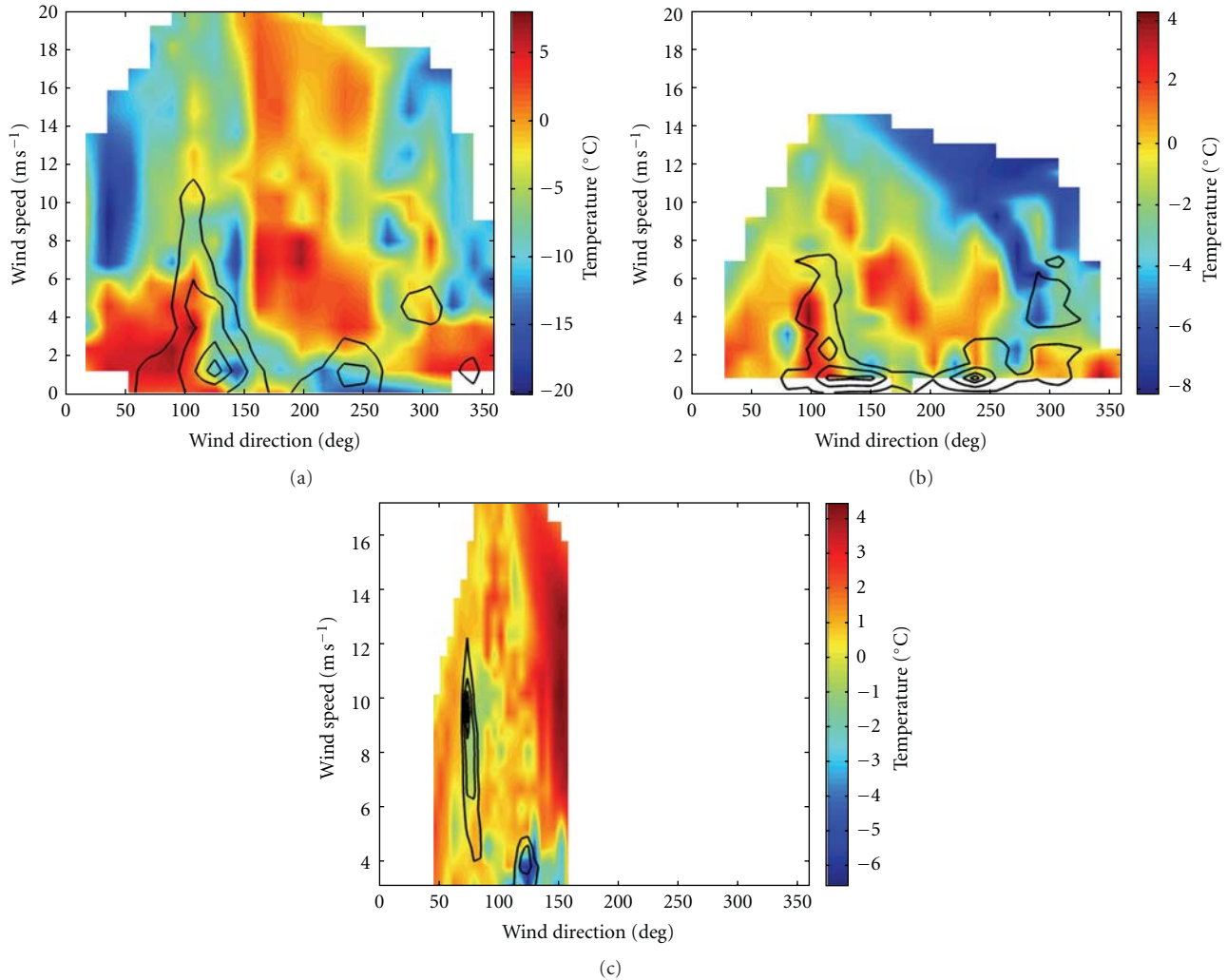


FIGURE 6: Composite representation of the surface layer meteorological conditions in Ny-Ålesund as observed between 1974 and 2011: (a) during the entire period; (b) during the all May months. (c) The same type of composite representation but for the AWS 3 data during the intensive observation period between May 2nd and 13th 2009. Colors show the mean temperature [$^{\circ}\text{C}$] at 2 m under the given wind direction and the wind speed. The contours show 0.25, 0.5, 0.75, and 0.9 relative probability levels to observe the given combination of the wind speed and direction and the wind speed. Detailed description of the procedure is given in the text.

at the structure of the wind and temperature fields obtained in idealized simulations with a fine resolution turbulence-resolving model. The simulations are aimed to distinct between the wind-temperature patterns generated by each of possible driving mechanisms. This distinction will hopefully improve the attribution of the wind driving mechanisms in the valley complementing previously published case studies where many of those mechanisms were acting simultaneously.

The Parallelized Atmospheric Large-eddy simulation Model (PALM) was utilized. The model was developed at the Institute for Meteorology and Climatology (IMUK) of the Leibniz University of Hannover. The version of PALM used in this study was described in details in Letzel et al. [27]. The model ability to work with stratified flows in complex surface geometry has been described in Castillo et al. [34]. PALM solves the Navier-Stokes and thermo-dynamic equations for

the Boussinesq incompressible fluid. PALM also solves the transport equations for a passive scalar or moisture. Further numerical details of PALM could be found in Raasch and Schröter [35] and Castillo et al. [34]. The model simulations were run for the part of the valley, which is shown by the light rectangle in Figure 1. The model resolution was 61 m in the direction along the valley and 56 m in the direction across the valley. Despite the fact that the model resolution of our runs is about 20 times finer than the simulations with WRF available to date, this resolution is probably too coarse to resolve the small-scale turbulence in the strongly stratified atmosphere near the surface. In this sense, the PALM simulations still rely on the Smagorinsky turbulent closure to parameterize the turbulent exchange. However, this parameterization deals with the full turbulent stress/diffusivity tensors, which makes it more adequate to the problem in question than the one-dimensional column-wise parameterizations in

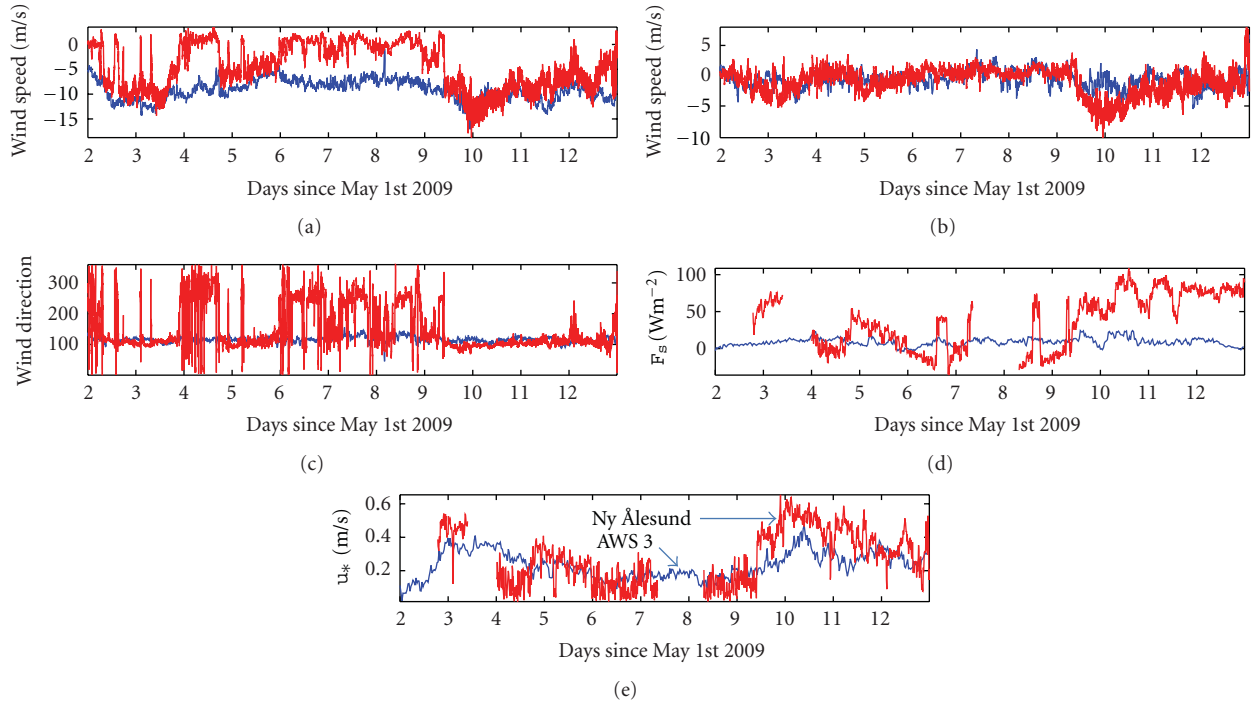


FIGURE 7: In situ meteorology at the surface layer between May 2nd and 13th 2009: the wind speed projected on the valley axis (a); the wind speed projected on the axis perpendicular to the valley (b); the meteorological wind direction (c); the surface sensible heat flux (d); the surface friction velocity (e). Blue curves: data from AWS 3 on the glacier; red curves: data from the Ny-Ålesund station.

the WRF model. Although the turbulent processes governed by the stable stratification of the surface atmosphere are not resolved, the simulations are still turbulence-resolving as the large-scale turbulence generated by topographical features is resolved. Thus, the model achieves a qualitative shift from the parameterized to resolved turbulence for a part of the turbulent spectra on scales larger than about 100 m. In this sense, PALM resolves the energy containing part of the turbulence spectrum [36]. To use this advantageous feature, turbulence-resolving simulations have been already applied in several katabatic wind studies (e.g., [37, 38]).

The model mesh in this study was chosen to be 2048 by 128 grid point. The selected domain occupied only 512 (along the valley) by 112 (across the valley) grid points within this mesh. The rest of the mesh is used to create periodic boundary conditions, which are at sufficient distance from the selected domain to minimize the effect of the flow recycling. This resolution is to be compared with the resolution in the WRF simulations where just 2–5 grid points were placed across the valley. The vertical resolution of the simulations was 10 m in the lowest 500 m of the domain and stretched to 60 m at the domain top. The total number of the vertical levels was 128. The initial potential temperature gradient was set to $6.3 K km^{-1}$ to be consistent with the climate data. It is important to bear in mind that the PALM model is incompressible and, therefore, calculates the potential temperature. The potential temperature, which is referred just as temperature, does not change in the adiabatic processes such as up- and down-ward motions. However, the initial potential temperature gradient implies that the higher potential

temperature can be entrained into the lower layers from the upper part of the domain. This entrainment will be clearly seen in the simulation results. Unresolved surface roughness was taken 0.01 m. Table 2 lists the other initial conditions of the runs.

To run the simulations, two sets of initial conditions were used. One set of runs had no background wind. Another set of runs was driven with the constant background wind of $U = 10 m s^{-1}$ and $V = 0 m s^{-1}$ where U and V are the velocity components along and across the valley with the positive sign corresponding to the wind from the fjord mouth towards the glacier. The surface kinematic heat flux over the open water area in the domain (the blue area in Figure 1) was set to $0.1 K m s^{-1}$, which roughly corresponds to the upward heat flux of $100 W m^{-2}$. The flux over the land surface was set either to $-0.02 K m s^{-1}$ or to $0.0 K m s^{-1}$. The model was integrated for 6 model hours. Due to very large amount of data produced by the model integration, only a limited sampling at selected vertical levels and along-valley slices was applied. The data were sampled every 30 min. Each run was initiated with slightly perturbed laminar flow. Therefore, runs undergo a spin-up period. The run post-processing revealed that the flow in the domain of interest is nearly statistically steady state already after 3 hours of simulations. Nevertheless, we used for this study the averaged meteorological fields sampled between hours 5 and 6 of simulations. As the flow in the valley is strongly channeled, this study is limited only to the analysis of the averaged circulation in the vertical plane aligned with the valley major axis. The data were averaged over 4 instant samplings and from

TABLE 2: The initial and boundary conditions of the numerical experiments with the PALM code.

Run	Symbol	Initial wind (U, V) [m s^{-1}]	Surface temperature flux (open water), [K m s^{-1}]	Surface temperature flux (land and ice), [K m s^{-1}]	Relief
R0SF	•	(0.0, 0.0)	0.1	-0.02	Yes
R0FF	○	(0.0, 0.0)	0.1	-0.02	No
R10SF	■	(10.0, 0.0)	0.1	-0.02	Yes
R10FF	□	(10.0, 0.0)	0.1	-0.02	No
R10S0	▲	(10.0, 0.0)	0.1	0.0	Yes
R10F0	△	(10.0, 0.0)	0.1	0.0	No
R10S00	▽	(10.0, 0.0)	0.0	0.0	Yes

three vertical slices along the valley. The slices are located at the valley central line and at the distance of about 2 km from the central line on each side of it.

The performed runs allow comparison of the mean wind-temperature patterns induced in the valley separately for three driving mechanisms: the mechanical forcing and drainage, the thermally forced land-sea breeze circulation, and the katabatic wind. Figure 8 shows wind and temperature anomalies obtained in four runs: R0SF and R0FF—two runs without the external mechanical forcing; and R10SF and R10S0—two runs with the strong external mechanical forcing pushing the air into the valley from open water. Other performed runs will not be shown here due to limited journal space. The temperature anomaly is defined as the difference between the temperature at given location and the temperature averaged over the open water part of the domain for the same height above the sea level. The obtained temperature anomalies were rescaled to be within the range $[-1 \text{ K}; -10 \text{ K}]$. This procedure makes the runs directly comparable to each other.

The run R0SF (Figure 8(a)) simulates the atmospheric circulation driven by the differential cooling of the realistic valley surface. Thus, the circulation in the R0SF is driven by the combined effect of the katabatic wind (due to the presence of the cooled slope) and the breeze (due to the horizontal thermal gradient between open water and the land in the domain). In the run R0FF (Figure 8(b)), however, the katabatic wind mechanism is absent as the simulations were performed with the flat surface domain. The run R0FF develops a typical sea breeze circulation pattern with the strong low-level flow directed from cold (land) to warm (open water) parts of the valley and the weak compensating high-level flow in the opposite direction. The maximum low-level wind speed reaches -8 m s^{-1} near the surface at the edge of open water. Arrows reveal significant vertical velocity at the sea breeze front. As it has been noted previously, the entrainment of the potentially warmer air from the upper levels in the down-draft branch of the circulation is clearly seen in the right part of the plots. The surface temperature over the land is about 5 K colder in this simulation than the open water temperature. Here, we probably see the model failure to produce turbulence in the stably stratified surface layer as the vertical temperature gradient at the surface is too sharp. The thickness of the layer affected by the surface cooling is about 100 m. But the circulation reverts at much higher elevation of

about 700 m. The considered details of the breeze circulation are in good correspondence to the theoretical expectations [39, 40].

The circulation in the run R0SF (Figure 8(a)) closely resembles the breeze circulation. The principal properties of the temperature and wind fields are very similar to the properties found in the R0FF. However, the circulation is intensified. The maximum low-level wind speed reaches -11 m s^{-1} near the surface at the open water edge. The nonflat surface generates significant turbulence, which mixes the temperature and disturbs the breeze circulation. The layer of cooled air is significantly thicker towards the end of the slope reaching 200 m to 300 m. Simultaneously the entrainment of higher potential temperature in the down-ward branch of the circulation has significantly increased. At the same time, the circulation reverts at about the same 700 m height. This comparison suggests that the effect of the slope does not play a leading role in driving of the circulation. The effect is relatively minor and only assists and, to some degree, amplifies the breeze circulation. The katabatic wind mechanism affects at the most the lowermost 50 m in the domain. Figure 9(a) compares the wind speed directly as it has been recalculated to obtain the heights above the inclined surface. In the lower layer (0 m to 50 m), the katabatic wind accelerates the flow between 2 km and 12 km and between 15 km and 25 km from the mouth of the fjord. At the distances between 12 km and 15 km, one can find some sort of obstacles (cliffs or islets) in the valley, which force the flow to move upward and above the 50 m layer. At the same time, the mean wind speed in the thicker 500 m layer is only marginally larger than the wind speed in the flat surface run R0FF. Thus, the acceleration is significant but seen only in the lowermost 100 m or less. The additional acceleration by the katabatic wind pushes the breeze front by just a few kilometers. This is consistent with the qualitative experience of observers that the glacier winds do not penetrate far over the open water part of the fjord.

Our statistical analysis has demonstrated that the mean background wind above the valley is about 10 m s^{-1} . The background wind can significantly modify circulations in the valley as it imposes additional mechanical forcing [14, 26]. According to Doran [14], the mechanical driving creates higher pressure in the valley. It causes air drainage along the slope in the lower layers, sometimes in the direction opposite to the background wind. To clarify the effect, five runs with the background wind were performed (see Table 2). The runs

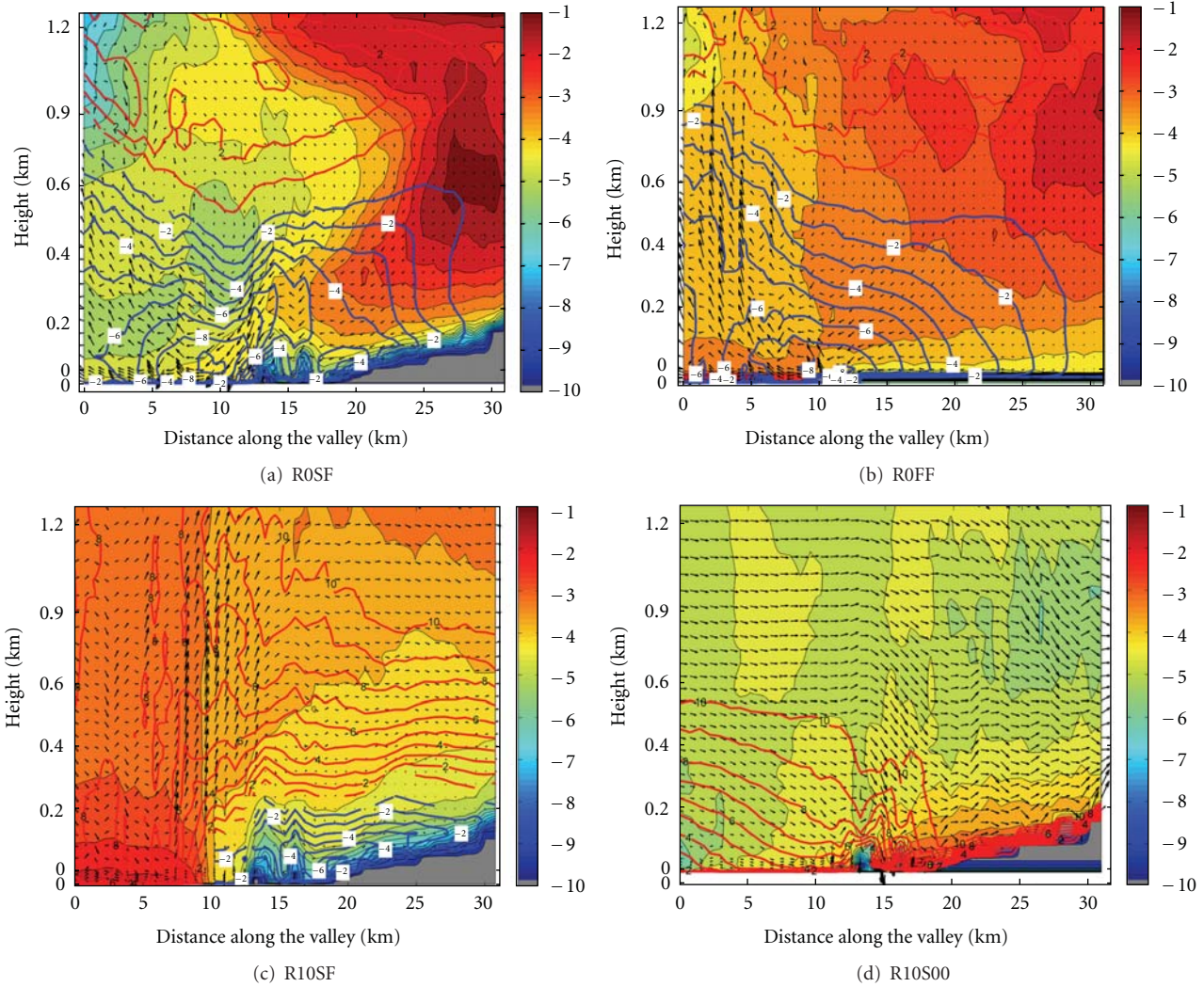


FIGURE 8: The averaged circulation in the vertical plane with orientation along the central axis of the valley. The velocity vectors represent the horizontal (along the valley) and vertical component of the wind. The wind speed (m s^{-1}) is shown by isolines. Winds down the valley are indicated with blue isolines; winds in the opposite direction, with red isolines. Temperature anomalies (see the text for details) are shown through color. The gray shading shows the surface elevation. Four runs are shown: (a) R0SF: the thermally driven breeze circulation over the realistic relief of the surface (b) R0FF: the thermally driven breeze circulation over flat but differentially cooled surface; (c) R10SF: the circulation over the cooled surface in presence of the strong westerly background wind; (d) R10S00: the circulation over the surface with no additional cooling in presence of the strong westerly background wind.

with the realistic topography (with and without land cooling) are shown in Figures 8(c) and 8(d). The runs R10SF and R10S00 have the background wind of 10 m s^{-1} in the valley direction. Comparison between runs R0SF (Figure 8(a)) and R10SF (Figure 8(c)) shows that the background on-slope wind strongly suppresses but not eliminates the surface layer with the down-slope winds. The breeze front becomes very sharp in this case. The upward motions at the front are strong (up to 1 m s^{-1}). The run R10S00 (Figure 8(d)) reveals that the down-slope winds does not develop in absence of the katabatic wind and the breeze mechanisms under the typical forcing conditions. Thus, the presence of the surface layer cooling or the horizontal temperature gradient is needed to

maintain the surface wind counter flow. Figures 9(b) and 9(c) reveal that the background wind shifts the breeze front and makes the additional effect of the katabatic wind mechanism insignificant.

The layer with such winds is also much thinner under the conditions with the background wind. In the run R10SF, thickness of this layer was just 150 m to 200 m. Detailed study of the effects of the background wind speed and direction on circulations in a valley has been published by Doran [14]. Figure 10 compares the results of Doran's simulations with the present simulations. The present simulations are in good agreement with the overall linear regression on the plot. This dependence needs more studies. In particular, it would be

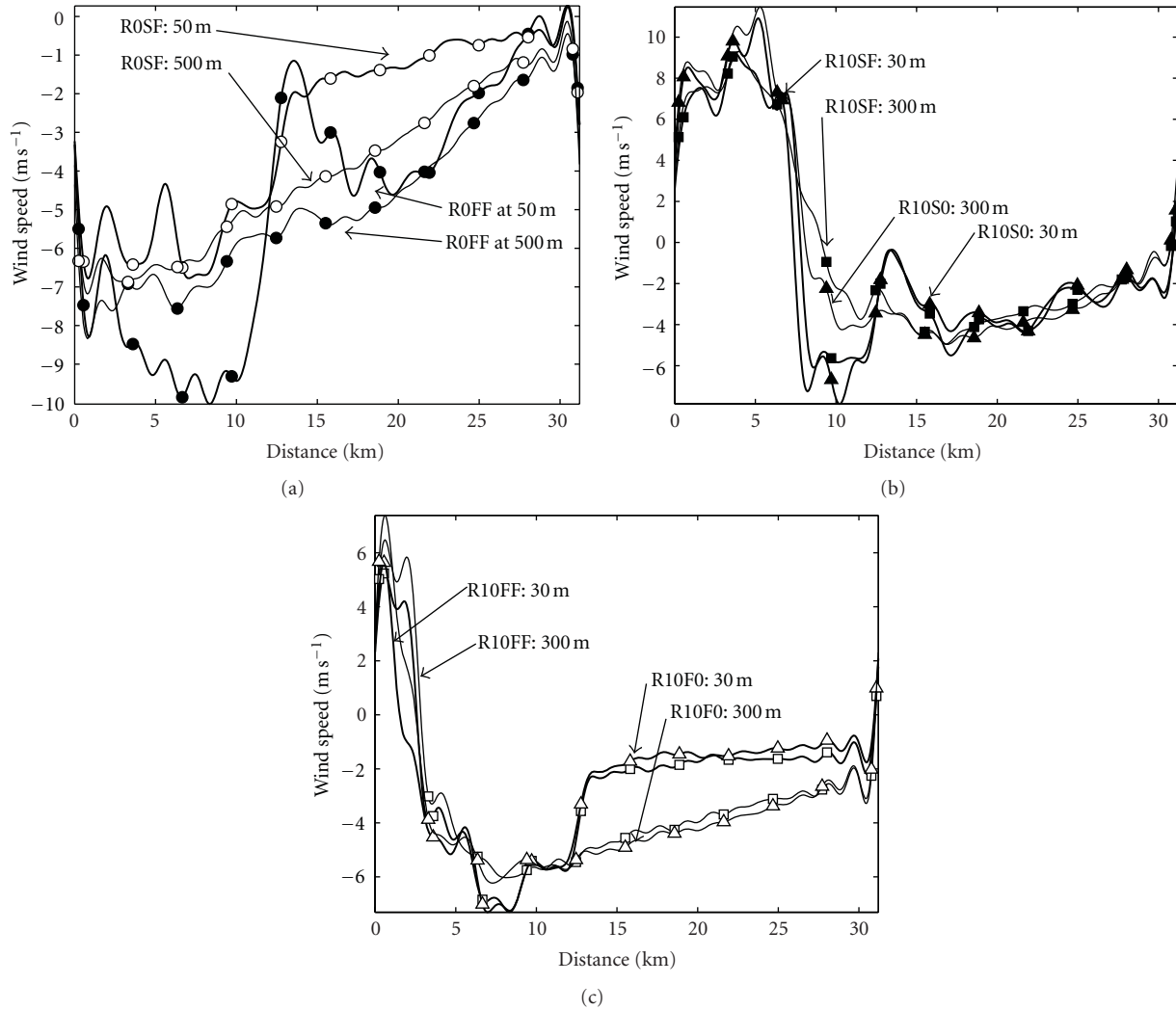


FIGURE 9: The averaged wind speed in the lower layer (thick lines) and in a thicker layer (thin lane) in the domain. The heights were recalculated relative to the inclined surface. (a) The runs R0SF (black circles) and R0FF (white circles); (b) the runs R10SF (black squares) and R10S0 (black triangles); (c) the runs R10FF (white squares) and R10F0 (white triangles).

interesting to find the combination of the wind speed and direction, the surface cooling rate, and the slope angle at which down-slope flows appear.

4. Attribution of Wind Driving Mechanisms to the Observed Wind Patterns

Strong and persistent channeled wind has been reported in several previous analyses of the surface layer observations in the valley. More detailed but short-term studies of the phenomenon during field observational campaigns (e.g., in ARTIST; [7]) disclosed that the thickness of the layer with persistent winds was just of 300 m to 500 m. The wind direction changed significantly above this layer. In this study, we completed those findings with the statistical analysis of the long-term radiosounding data archive IGRA. The previous observations were corroborated and extended. In particular, we presented the climatological analysis of the vertical

structure of the winds in the valley. We also linked this structure with the structure of temperature anomalies. We demonstrated that the channeled winds are typical for both winter and summer seasons. The thickness of the surface layer winds reveals significant seasonal variations. In the summer season, the layer is thinner. Although we did not have high-resolution vertical profiles for analysis, the wind rotation suggests that 500 m depth might be a reasonable estimation of the layer thickness. The winter season is characterized with thicker layer of about 1000 m depth, which is comparable with the height of the surrounding mountains.

The statistical analysis of the wind vertical structure has revealed that the surface winds frequently blow in the direction opposite to the direction of the geostrophic winds at higher atmospheric levels. This feature suggests an action of a specific driving mechanism, which reverts the background atmospheric winds. A number of studies refer to the katabatic wind mechanism. Indeed, some features of the surface

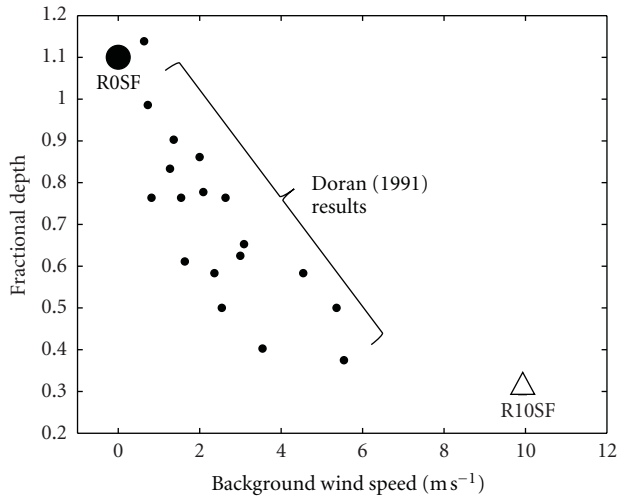


FIGURE 10: The thickness of the surface layer with winds directed to down slope in the valley. The thickness is normalized by valley depth. The small black dots represent data from Doran [14]. The present runs R0SF (black dot) and R10SF (triangle) are given by large symbols.

layer winds in the valley resemble the typical katabatic wind features. However, the channeled wind layer was found too deep as compared to the theoretical predictions [16, 17, 21]. The theories of the katabatic wind are of cause strongly simplified and linearized to be treated analytically. They parameterize suppression of the turbulence in the stably stratified layer and, therefore, the reduced transport of momentum from the accelerating surface layer air to higher layers of the atmosphere. Recent turbulence-resolving simulations by Axelsen and van Dop [38] and Largeron et al. [41] addressed the turbulence structure in the katabatic wind without simplifications imposed on the turbulence profile. In particular, Largeron et al. [41] found the thickness of the katabatic wind layer to be not deeper than 50 m. This is one order of magnitude less than the thickness found in our statistical analysis of the wind profile climatology. The simulations, however, were performed for a valley with featureless, smooth slopes.

The heterogeneity of the realistic relief can create additional turbulence due to the form drag of the resolved-scale obstacles (small valleys and islets in the fjord). Therefore, new turbulence-resolving simulations with the PALM code have been performed for this study with realistic topography taken from the ASTER digital elevation model. These simulations were not designed to mimic any observed meteorological situation because such a situation is unavoidably complicated by a superposition of different driving mechanisms and large-scale synoptic tendencies. Instead, we designed a set of simulations to single out particular driving mechanisms and to study the wind structure patterns corresponding to them.

Unfortunately, the pure katabatic wind mechanism can be simulated only in a model with infinite inclined slope. Such simulations cannot be performed with the realistic relief in the model domain. Therefore, we studied the effect of the katabatic wind driving mechanism through intercomparisons of simulations with and without the relief. The

simulations demonstrated that the major driving mechanism should be attributed to the land-sea breeze circulation driven by the horizontal temperature difference between the open water part of the fjord and the glacier. The katabatic wind mechanism strengthens this circulation significantly only in the lower 50 m–100 m. This circulation seems to be necessary to produce the near surface wind reversal in the meteorological situations with significant background winds. In turn, the background westerly winds are needed to produce the thickness of the surface layer-channeled winds of the order of observed 300 m. In the simulations with no background winds, the thickness of this layer was obtained deeper by a factor of two.

It is certain that our simulations could not explain all details of the observed climatological wind structure. Our simulations reveal that the breeze front moves only 5 km to 10 km off the oblation glacier edge. It is too short distance to explain persistent winds with vertical reversal of directions found in Ny-Ålesund data. As found by Skeie and Grønås [6], Sandvik and Furevik [2], Livik [12], and Kilpeläinen et al. [13], there are also regional circulations at larger scales, which can significantly influence the wind structure in the valley. In particular, the work of Livik [12] suggests that the simulations must also include the area of the adjacent Kronebreen glacier to be able to reproduce the circulations toward the mouth of the valley.

Finally, it has to be mentioned that the fjord may have own microclimate, which is different from the climate of the marine part of the region. Unfortunately, there are no long-term records for the latter part to estimate this difference. Nevertheless, close analogies can be drawn between the wind climate and its attribution to the wind driving mechanisms found in the statistical analysis of the northern Norwegian fjords by Nawri and Harstveit [26] and the wind climate and its attribution reported in this study for the Arctic fjord. Simulations by Kilpeläinen et al. [13] suggest that the difference in temperature could be as large as +3 K. The development of the breeze circulation in the valley can have such warming effect through frequent entrainment and recirculation of the warmer marine air in the valley. Attributing larger role in the Arctic fjord microclimate to the breeze circulation, we emphasize the difference between the Arctic and midlatitude mounting glacier conditions. As it has been described in Oerlemans and Grisogono [18], the midlatitude glaciers have stronger surface cooling due to higher ambient air temperature. Correspondingly, the large surface temperature deficit generates stronger katabatic winds. The high-latitude glaciers in Svalbard have typically much smaller deficit due to lower air temperatures, and therefore, the katabatic winds are not the primary driving mechanism of the circulation in the valley.

Acknowledgments

The authors thank for the support of the Norwegian Research Council bilateral collaboration projects: NERSC-IAP 196174/S30: The Atmospheric Boundary Layer Structure and Surface-Atmosphere Exchange in the Svalbard Area; PAACSIZ 178908/S30: Planetary Boundary Layer Feedbacks

Affecting the Polar Amplification of Arctic Climate Change in Seasonal Ice Zone; NERSC-IARC 196178/S30: Detailed Studies of the Bjerknes Compensation Mechanism. The work has been also supported by the grant of the Government of the Russian Federation designed to support scientific research projects implemented under the supervision of leading scientists at Russian institutions of higher learning (project code 11.G34.31.0048) and by the European Research Area Advanced Research Grant no. 227915 PBL-PMES.

References

- [1] F. Geyer, I. Fer, and L. H. Smedsrud, "Structure and forcing of the overflow at the Storfjorden sill and its connection to the Arctic coastal polynya in Storfjorden," *Ocean Science*, vol. 6, no. 1, pp. 401–411, 2010.
- [2] A. D. Sandvik and B. R. Furevik, "Case study of a coastal jet at Spitsbergen—comparison of SAR- and model-estimated wind," *Monthly Weather Review*, vol. 130, no. 4, pp. 1040–1051, 2002.
- [3] I. Hanssen-Bauer, M. K. Solas, and E. L. Stefensen, "The climate of Spitsbergen," Den Norske Meteorologiske Institutt report, Oslo, Norway, DMNI, 39/90 KLIMA, 1990.
- [4] E. J. Forland, I. Hansen-Bauer, and P. Ø. Nordli, "Climate statistics and long-term series of temperature and precipitation at Svalbard and Jan Mayen," Den Norske Meteorologiske Institutt report, Oslo, Norway, DNMI Report 21/97 KLIMA, 1997.
- [5] J. Hartmann, F. Albers, S. Argentini et al., "Arctic radiation and turbulence interaction study (ARTIST)," Report on Polar Research 305/1999, 81 pp., 1999.
- [6] P. Skeie and S. Grønås, "Strongly stratified easterly flows across Spitsbergen," *Tellus A*, vol. 52, no. 5, pp. 473–486, 2000.
- [7] H. J. Beine, S. Argentini, A. Maurizi, G. Mastrantonio, and A. Viola, "The local wind field at Ny-Ålesund and the Zeppelin mountain at svalbard," *Meteorology and Atmospheric Physics*, vol. 78, no. 1-2, pp. 107–113, 2001.
- [8] H. Svendsen, A. Beszczynska-Møller, J. O. Hagen et al., "The physical environment of Kongsfjorden-Krossfjorden, and Arctic fjord system in Svalbard," *Polar Research*, vol. 21, no. 1, pp. 133–166, 2002.
- [9] S. Argentini, A. P. Viola, G. Mastrantonio, A. Maurizi, T. Georgiadis, and M. Nardino, "Characteristics of the boundary layer at Ny-Ålesund in the Arctic during the ARTIST field experiment," *Annali di Geofisica*, vol. 46, no. 2, pp. 185–196, 2003.
- [10] S. Erath, *Simulation of the mass and energy balance at Kongsvegen 2001–2003*, M.S. thesis, University Innsbruck, 2005.
- [11] Th. Krismer, *Local and Spatial Mass Balance Modelling on an Arctic Glacier Kongsvegen, Spitzbergen*, University of Innsbruck, 2009.
- [12] G. Livik, *An Observational and Numerical Study of Local Winds in Kongsfjorden, Spitsbergen*, M.S. thesis, Geophysical Institute, University of Bergen, 2011.
- [13] T. Kilpeläinen, T. Vihma, and H. Ólafsson, "Modelling of spatial variability and topographic effects over arctic fjords in svalbard," *Tellus A*, vol. 63, no. 2, pp. 223–237, 2011.
- [14] J. C. Doran, "The effects of ambient winds on valley drainage flows," *Boundary-Layer Meteorology*, vol. 55, no. 1-2, pp. 177–189, 1991.
- [15] L. Prandtl, *Fuhrer durch die Stroemungslehre*, Vieweg, Braunschweig, Germany, 1949.
- [16] L. N. Gutman, "On the theory of the katabatic slope wind," *Tellus, Series A*, vol. 35, no. 3, pp. 213–218, 1983.
- [17] A. M. J. Davis and R. T. McNider, "The development of antarctic katabatic winds and implications for the coastal ocean," *Journal of the Atmospheric Sciences*, vol. 54, no. 9, pp. 1248–1261, 1997.
- [18] J. Oerlemans and B. Grisogono, "Glacier winds and parameterisation of the related surface heat fluxes," *Tellus A*, vol. 54, no. 5, pp. 440–452, 2002.
- [19] E. J. Klok, M. Nolan, and M. R. Van Den Broeke, "Analysis of meteorological data and the surface energy balance of McCall Glacier, Alaska, USA," *Journal of Glaciology*, vol. 51, no. 174, pp. 451–461, 2005.
- [20] B. Grisogono and J. Oerlemans, "A theory for the estimation of surface fluxes in simple katabatic flows," *Quarterly Journal of the Royal Meteorological Society*, vol. 127, no. 578, pp. 2725–2739, 2001.
- [21] L. K. Ingel, "Toward a nonlinear theory of katabatic winds," *Fluid Dynamics*, vol. 46, no. 4, pp. 505–513, 2011.
- [22] D. E. England and R. T. McNider, "Concerning the limiting behavior of time-dependent slope winds," *Journal of the Atmospheric Sciences*, vol. 50, no. 11, pp. 1610–1613, 1993.
- [23] R. G. Barry, *Mountain Weather and Climate*, Cambridge University Press, Cambridge, UK, 2008.
- [24] C. D. Whiteman and J. C. Doran, "The relationship between overlying synoptic-scale flows and winds within a valley," *Journal of Applied Meteorology*, vol. 32, no. 11, pp. 1669–1682, 1993.
- [25] M. G. Cogliati and N. A. Mazzeo, "Air flow analysis in the upper Río Negro Valley (Argentina)," *Atmospheric Research*, vol. 80, no. 4, pp. 263–279, 2006.
- [26] N. Nawri and K. Harstveit, "Variability of surface wind directions over Finnmark, Norway, and coupling to the larger-scale atmospheric circulation," *Theoretical and Applied Climatology*, vol. 107, no. 1-2, pp. 15–33, 2012.
- [27] M. O. Letzel, M. Krane, and S. Raasch, "High resolution urban large-eddy simulation studies from street canyon to neighbourhood scale," *Atmospheric Environment*, vol. 42, no. 38, pp. 8770–8784, 2008.
- [28] I. Durre, R. S. Vose, and D. B. Wuertz, "Overview of the integrated global radiosonde archive," *Journal of Climate*, vol. 19, no. 1, pp. 53–68, 2006.
- [29] I. Esau and S. Sorokina, "Climatology of the arctic planetary boundary layer," in *Atmospheric Turbulence, Meteorological Modeling and Aerodynamics*, P. R. Lang and F. S. Lombargo, Eds., pp. 3–58, Nova Science Publishers, 2010.
- [30] S. Sorokina and I. Esau, "Meridional energy flux in the Arctic obtained from data of the IGRA radio sounding archive," *Izvestiya, Atmospheric and Oceanic Physics*, vol. 47, no. 5, pp. 572–583, 2011.
- [31] S. S. Zilitinkevich and I. N. Esau, "Similarity theory and calculation of turbulent fluxes at the surface for the stably stratified atmospheric boundary layer," *Boundary-Layer Meteorology*, vol. 125, no. 2, pp. 193–205, 2007.
- [32] S. S. Zilitinkevich, T. Elperin, N. Kleerorin et al., "Turbulence energetics in stably stratified geophysical flows: strong and weak mixing regimes," *Quarterly Journal of the Royal Meteorological Society*, vol. 134, no. 633, pp. 793–799, 2008.
- [33] B. S. Gera, S. Argentini, G. Mastrantonio, A. Viola, and A. Weill, "Characteristics of the boundary layer thermal structure at a coastal region of Adelie Land, East Antarctica," *Antarctic Science*, vol. 10, no. 1, pp. 89–98, 1998.

- [34] M. C. L. Castillo, M. Kanda, and M. O. Letzel, "Heat ventilation efficiency of urban surfaces using large-eddy simulation," *Annual Journal of Hydraulic Engineering*, vol. 53, pp. 175–180, 2009.
- [35] S. Raasch and M. Schröter, "PALM—a large-eddy simulation model performing on massively parallel computers," *Meteorologische Zeitschrift*, vol. 10, no. 5, pp. 363–372, 2001.
- [36] I. Esau, "Large-eddy simulations of geophysical turbulent flows with applications to planetary boundary layer research," in *Proceedings of the 5th Conference on Computational Mechanics (MekIT '09)*, B. Skallerud and H. I. Andersson, Eds., pp. 7–37, Tapir Academic Press, 2009.
- [37] C. M. Smith and E. D. Skyllingstad, "Numerical simulation of katabatic flow with changing slope angle," *Monthly Weather Review*, vol. 133, no. 11, pp. 3065–3080, 2005.
- [38] S. Axelsen and H. van Dop, "Katabatic flow—the great Large-Eddy Simulation challenge," *Geophysical Research Abstracts*, vol. 8: 02696, 2006.
- [39] R. Rotunno, "On the linear theory of the land and sea breeze," *Journal of the Atmospheric Sciences*, vol. 40, no. 8, pp. 1999–2009, 1983.
- [40] G. A. Dalu and R. A. Pielke, "An analytical study of the sea breeze," *Journal of the Atmospheric Sciences*, vol. 46, no. 12, pp. 1815–1825, 1989.
- [41] Y. Largeron, C. Staquet, and C. Chemel, "Turbulent mixing in a katabatic wind under stable conditions," *Meteorologische Zeitschrift*, vol. 19, no. 5, pp. 467–480, 2010.

Research Article

Estimate of the Arctic Convective Boundary Layer Height from Lidar Observations: A Case Study

L. Di Liberto,¹ F. Angelini,¹ I. Pietroni,¹ F. Cairo,¹ G. Di Donfrancesco,² A. Viola,¹ S. Argentini,¹ F. Fierli,¹ G. Gobbi,¹ M. Maturilli,³ R. Neuber,³ and M. Snels¹

¹*Institute for Atmospheric Sciences and Climate, CNR, 00133 Rome, Italy*

²*ENEA UTA, Santa Maria di Galeria, 00123 Rome, Italy*

³*Alfred Wegener Institute for Polar and Marine Research, 14473 Potsdam, Germany*

Correspondence should be addressed to L. Di Liberto, l.diliberto@isac.cnr.it

Received 16 November 2011; Revised 18 January 2012; Accepted 19 January 2012

Academic Editor: Igor N. Esau

Copyright © 2012 L. Di Liberto et al. This is an open access article distributed under the Creative Commons Attribution License, which permits unrestricted use, distribution, and reproduction in any medium, provided the original work is properly cited.

A new automated small size lidar system (microlidar or MULID) has been developed and employed to perform aerosol measurements since March 2010 at Ny Ålesund (78.9°N, 11.9°E), Svalbard. The lidar observations have been used to estimate the PBL height by using the gradient method based on abrupt changes in the vertical aerosol profile and monitor its temporal evolution. The scope of the present study is to compare several approaches to estimate the PBL height, by using lidar observations, meteorological measurements by radio soundings, and a zero-order one-dimensional model based on a parameterization of the turbulent kinetic energy budget within the mixing layer, under the assumptions of horizontal homogeneity, and neglecting radiation and latent heat effects. A case study is presented here for a convective PBL, observed in June 2010 in order to verify whether the Gradient Method can be applied to lidar measurements in the Arctic region to obtain the PBL height. The results obtained are in good agreement with the PBL height estimated by the analysis of thermodynamic measurements obtained from radio sounding and with the model.

1. Introduction

There is no region on Earth where the climate is changing faster than in the Arctic. Recent studies show that processes in the lower atmosphere are critical for a proper understanding and modelling of Arctic climate change [1–3]. The reliability of climate models is often poor in Arctic regions because the parameterizations of the planetary boundary layer (PBL) are mainly based on observations at lower latitudes.

A proper characterization of the Arctic PBL processes, including the exchange of momentum, heat, moisture, and chemical species between the surface and the free troposphere, is needed for a better understanding of the forcings that drive the changes going on in these regions.

In this context the PBL height is an important parameter as it allows to define a scale on which several processes in the Arctic PBL occur.

In spite of the importance of proper monitoring the vertical development of the PBL (which is also a key parameter

in mesoscale climate models), no unique method exists to determine its height [4]. In fact, the evaluation of the PBL height can be performed by using a variety of methods, based on the analysis of thermodynamic variables, on turbulence-related parameters or by measuring concentrations of tracers. According to [4], the measurement of tracers concentration is the only direct method allowing the estimate of the PBL height under stable conditions as in such conditions the thermodynamic approach is neither reliable nor well defined.

Atmospheric aerosols represent often a good tracer for this purpose. It is produced at ground and mixed within the PBL through turbulence processes. If no advection/removal of aerosol occurs in the PBL, the concentration profile of aerosols can be assumed as a reliable proxy for the PBL height.

The evaluation of the aerosol burden in the Arctic PBL is not only useful to provide an estimation of PBL dynamics, but also valuable in itself since the presence of aerosol in the planetary boundary layer influences the energy budget and hence the climate in several ways.

It is widely accepted that the aerosol concentrations in Arctic are lower than at midlatitude, thereby making the system more sensitive to climate changes; due to a low background concentration, even a small increase can be observed and is significant in terms of climate change [5, 6]. There are indications of important local sources inside the pack ice that rely on biogenic processes in the ice and in open leads. These may be very susceptible to change through a global warming. Moreover, transport of aerosols from the midlatitudes has been observed in the Arctic in the last 10 years, and its impact has been investigated [7].

According to recent calculations using Global Circulation Models (e.g., [8]), aerosol particles may have a cooling effect at the Earth surface, smaller but possibly comparable to the warming effect due to the increased concentration of anthropogenic greenhouse gases in the atmosphere. However, in the case of snow-covered surfaces, the effect of black carbon deposited on the surface may counteract the predicted cooling through a reduction of the surface albedo [9]. These opposite effects make the arctic changes an extremely unpredictable scenario [10].

The structure and dynamics of the majority of the aerosols present in the PBL are strongly influenced by the surface energy fluxes. Especially in snow-covered regions, the deposition of aerosol on the surface primarily leads to a reduction of the albedo, and consequently to the heat amount absorbed by the soil. The concentration of aerosols may also affect the melting/freezing of the Arctic sea ice ([11, 12]).

To provide both a characterization of PBL dynamics and a monitoring of aerosol burden in the Arctic lower troposphere, a microlidar has been installed in Ny Ålesund (78.9°N, 11.9°E), Svalbard, Norway, in 2010 and has been operating since then, in the framework of a collaboration between the Italian Consiglio Nazionale delle Ricerche (CNR) and the German Alfred Wegener Institute (AWI). Ny Ålesund represents a unique site where a large international cooperation granted the deployment of an ample set of instruments for monitoring a large number of key parameters of the Arctic system. Ny Ålesund is situated on the south side of the deep and sheltered *Kongsfjord* on the west coast of the Svalbard archipelago. The fjord is enclosed by glaciers on one side and by the Zeppelin mountain (473 m a.s.l.) south of the town.

In the framework of the Climate Change Tower-Integrated Project (CCT-IP), an instrumented meteo-tower (32 m high) has been deployed in Ny Ålesund in the year 2009, complemented by a number of other in situ and remote sensing devices for the characterization of the Arctic surface and lower troposphere. The small-sized, portable, and automated micro-LIDAR (Light Detection And Ranging), MULID, has been installed at the AWI Koldewey station and has been providing high-resolution profiles of the aerosol vertical distribution and optical properties from the ground up to about 3000 m, since March 2010. The system is a zenith-pointing Rayleigh (elastic) lidar, operating at 532 nm, providing also the volume depolarization that gives qualitative information on the shape of the scattering particles [13, 14].

In the present work we analyse a case study in order to test the applicability of the aerosol vertical profiles as tracers

in the determination of the PBL height at the Svalbard site. The chosen case (14 June 2010) is characterised by low wind speed, and the PBL shows evident convective characteristics. The method is inadequate when the PBL height is extremely low (below 50 m), or when the PBL is not well mixed, as occurs in strong wind conditions.

Furthermore, both LIDAR profiles and ancillary data are available for the whole day, and the aerosol concentration is large enough to allow the use of the aerosol backscatter profiles to estimate the PBL height. The PBL height is also determined by using meteorological measurements from collocated simultaneous radio sounding, and by applying the zero-order one-dimensional model proposed by Gryning [15]. The aim of this work is to understand to what extent the lidar-based technique can be adopted in future campaigns, combining the lidar technique with other complementary methods such as SODAR RASS, Models, Soundings, Wind-Profiling Radars in order to obtain reliable values for the PBL height in this region. Some techniques are described in [16–18].

The paper is organized as follows: in Section 2, the instruments and methods used in our work are presented. A discussion of the results is presented in Section 3, and the comparison between observations and the 1D prognostic model is shown in order to evaluate the accuracy of the PBL height obtained from the lidar data. Finally, in Section 4 conclusions will be drawn.

2. Instruments and Methods

2.1. Micro-Lidar (MULID). The lidar system has been developed in the laboratories of the Institute of Atmospheric Science and Climate of CNR, (ISAC-CNR). It is contained inside a thermally insulated, fiberglass, and polystyrene box. The temperature in the box is controlled by three 30 W heaters, and two fans mainly dedicated to keep the system temperature at operating conditions. An external blower with a laminar diffuser continuously cleans the glass window on the top of the system. The Lidar system [19] is shown in Figure 1.

The laser source is a compact size, low-weight diode pumped Nd:YAG laser (Laser-Compact group), with second-harmonic generation and active Q switching. The laser pulse duration is less than 10 ns and the output energy is $29 \mu\text{J}$ /pulse at 532 nm and $25 \mu\text{J}$ /pulse at 1064 nm. The pulse repetition rate is 1 kHz, with a beam divergence at 532 nm of less than 1.5 mrad which is reduced by a beam expander to 0.2 mrad. The laser system has a maximum power consumption of 100 W (60 W Laser Head and 40 W Power Supply Unit).

The receiving optics is composed of a Newtonian 20 cm diameter $f/1.5$ telescope, with a full Field of View (FOV) of 1.3 mrad set by a field stop of 400 micron. The laser is mounted in a quasiparallel geometry, causing intersection with the telescope FOV at about 50 m reaching full overlap at 150 m. A polarizing beam-splitter cube is used to separate the 532 nm signal collected by the telescope into two polarized components, respectively, parallel and perpendicular to the laser emission. The radiation is then focused onto miniaturized

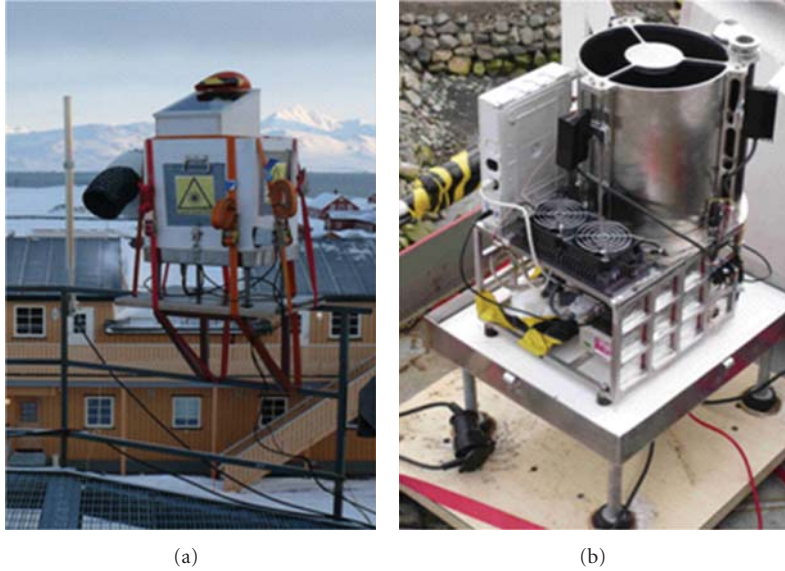


FIGURE 1: In (a) the micro-lidar (MULID) on the roof of the AWI station at Ny Ålesund (78.9°N, 11.978.9°E, 11.9°E), Svalbard. In (b) the optical and electronic components of the system.

photomultiplier modules (Hamamatsu 5783P) with very low thermal noise (below 10 counts/s at 25°C). The PMT signal is recorded both in current mode and in photon counting mode. In the current mode the time resolution of the AD (80 MHz) converter allows a vertical resolution of 1.875 m over a 1.875 km range, while in photon counting mode the time resolution (100 ns) allows a vertical resolution of 15 m and a range of 15 km. These parameters can be varied to reduce the vertical resolution to 15 m and 75 m, respectively, and to increase the range to 15 km and 75 km, respectively, in case a coarser and more extended profile reconstruction is needed.

The system capability to work unattended for long periods has allowed continuous operation (24/24) delivering 5-minute averaged profiles every half hour. In special observing periods, like in the springtime, when vertical profiles of meteorological parameters were simultaneously obtained by using different sondes operated from a tethered balloon by AWI, a higher temporal resolution has been set, providing continuous time series of profiles.

2.1.1. Gradient Method. The height of the PBL may be estimated by lidar measurements by investigating the vertical profile of the aerosol backscatter signal. Several approaches have been proposed in the literature for determining the PBL height from Rayleigh-Mie lidar measurements. One method which is frequently used with low power lidars is based on the determination of the inflection points of the profile. The aerosol backscatter signal depends on the aerosol numerical concentration, and in a rather complicated way also on aerosol size, shape, and composition. If the size, shape, and composition can be considered uniform in space, the volume aerosol backscatter coefficient, determined from the lidar measurements can be considered linearly proportional to the aerosol number concentration. Generally the aerosol

concentration decreases sharply at the transition between the PBL and the free troposphere. This variation, observed as a sharp decrease of the aerosol backscatter cross section, may be used to determine the PBL height. The amount of the variation depends on the aerosol type, concentration, and the wavelength employed [20]. Since this approach is based on finding the maxima of the first derivative of the signal, this method, described by Endlich et al. [21], is called “gradient method.” Other approaches employ the absolute value of the aerosol cross-section [22] and define the top of the PBL as the lowest point where the backscatter ratio falls below a threshold value. This is based on the assumption that in the free troposphere the aerosol concentration is very low. The main drawback of this method is that the inversion of the lidar profile is required, and a high signal-to-noise ratio is necessary to avoid false attributions. A third method, the so-called variance method, is based on the analysis of the temporal behaviour of the variance of the signal at each altitude. It represents a very powerful approach to detect the convective boundary layer, since the turbulence inside the mixing layer and the entrainment zone leads to very variable concentration of tracers, resulting in a highly variable aerosol cross-section. On the other hand, stable boundary layers are not easy to detect in this way thus restricting most of these studies to the daytime observations [23–26]. Obviously, all these methods are valid under the assumption that no aerosol advection or removal from the PBL is occurring.

The appeal of the gradient method resides in the fact that it neither requires to perform a full inversion of the profile, nor does it take into account corrections for beam-FOV overlap [27, 28]. Often inflection points are determined in the background subtracted range corrected signal (RCS), or, in alternative, its logarithm.

In order to find the inflection points, which are needed while using the gradient method, two different strategies are

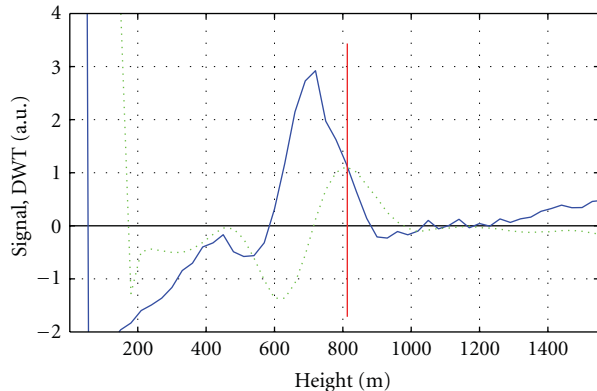


FIGURE 2: The logarithmic Range-Corrected Signal (blue) and its Discrete Wavelet Transform (green) of the profile around 9:00 UTC. The DWT is calculated with a Haar function of 150 m width. The red line is set at the height corresponding to the first maximum of the DWT exceeding the threshold of 0.5 and represents the estimate of the PBL height at that moment. This threshold is the only parameter to be tuned in the wavelet analysis.

possible: the first is based on the direct numerical differentiation, while the second employs the so-called Discrete Wavelet Transform (DWT), using a zero-order wavelet (Haar function). This DWT consists in the convolution product of the signal (either range-corrected or logarithmic range-corrected) with a finite-size step function. The method is well described, for example, in [29, 30].

Where the signal is “in phase” with the Haar wavelet, the convolution product shows a maximum, and an inflection point is found. The maxima of this DWT can then be used to determine the inflection points of the RCS. The advantage of the DWT is that, being based on an integral quantity instead of a derivative, it is much less prone to noise-induced detections than the numerical differentiation. Another advantage of the DWT technique is that, changing the dilation of the Haar function, a multiscale analysis [31] can be easily performed. On the other hand, it should be stressed that the width of the Haar function affects the minimum height at which the retrieval of inflection points is possible. In fact, the DWT is only defined above the centre of the wavelet. Hence, it is fundamental to choose the dilation of the wavelet coherently with the scale of the structures we expect to observe. This is visible in Figure 2, where the logarithmic RCS (blue) and its DWT (green) are shown for one lidar profile. There, the red line is set at the height where the first maximum of the DWT has exceeded a threshold value of 0.5. That height in fact represents the estimate of the PBL height. The threshold value is the only parameter to be tuned in the wavelet analysis; its value in the present analysis has been chosen according to Haij et al. [31].

Once the aerosol layers have been identified with the gradient method (by DWT or direct differentiation), a problem of attribution still remains, since multiple aerosol layers can simultaneously be present in the vertical profile [20] leaving the correct identification of the actual PBL height still an open task. A very popular criterion is to choose the lowest

maximum whose first derivative is above the threshold ([31] and reference there in).

2.2. PBL Height from Radiosonde Data. Atmospheric soundings by Vaisala RS92 radio sondes are carried out at Ny Ålesund once a day at 12 UTC, providing profiles of pressure, temperature, relative humidity, wind speed, and wind direction from ground to about 30 km, with a vertical resolution of a few metres depending on the balloon ascending speed.

The sondes are carried by helium-filled balloons (TOTEX TX600, or TX800), and data reception and evaluation are provided by a DigiCora System (VAISALA). The data is coded (FM35-Temp) and transferred to the Global Telecommunication System (GTS).

2.2.1. Lapse Rate Method and Richardson Bulk Method. Since the convective PBL is characterised by deep mixing of thermodynamic quantities, their gradients are expected to be very small. The inversion present on top of the convective PBL shows significant gradients in potential temperature and relative humidity, towards the warmer and drier free atmosphere. A method for the determination of the PBL height from radiosonde or balloon observations is based on the computation of the vertical gradients in potential temperature and/or relative humidity [32]. The algorithm of Hayden et al. [33] detects PBL height as the first level at which the vertical gradient in potential temperature exceeds 2 K/km and the vertical gradient in RH < 0%/km. This kind of method is commonly called the lapse rate method, because the PBL height is defined when a determined value or a combination of determined values of lapse rates in atmospheric variables is met.

Another commonly used method which is suitable for stable as well as for unstable conditions is the Richardson bulk method [23, 34–36]. The Richardson number is a scaling parameter that indicates the ratio of thermal and mechanical production of turbulence. It has a characteristic behaviour for the mixing layer and the free atmosphere on top of it.

The Richardson bulk number R_{ib} is calculated as

$$R_{ib}(z) = g \frac{(z - z_0)[\vartheta(z) - \vartheta(z_0)]}{\vartheta(z)[u^2(z) - v^2(z)]} \quad (1)$$

with g the gravity constant of 9.81 m/s², z and z_0 represent altitude and the lowest level of observation, respectively. Furthermore, $\vartheta = T(P_0/P)^{R_d/c_p}$ denotes potential temperature and $u(z)$ and $v(z)$ are the zonal and meridional components of the wind vector, respectively. The numerator represents the buoyancy term, in which the rising of the thermal potential is described. The denominator contains information about wind shear. Here it is assumed that the wind speed at z_0 is zero.

The PBL height can be defined as the height of the first level at which the Richardson bulk number exceeds a certain threshold value, such that $R_{ib} > R_{ibc}$ [36, 37]. A common value for R_{ibc} reported in the literature is 0.21. Beyond this critical value of R_{ib} the atmosphere can be considered fully

decoupled from the PBL. In other studies reported by Troen and Mahrt [38], R_{ibc} reaches the critical value of 0.25.

2.3. Batcharova and Gryning Model. Several models have been proposed to estimate the PBL height under convective conditions. Among these a simple one-dimensional prognostic model proposed by Gryning and Batcharova [15] was used in various studies both in mid and high latitudes. The results obtained in harsh climate [39] encouraged the use of this model for the Ny Ålesund dataset. The model is based on a parametrization of the turbulent kinetic energy budget within the mixing layer, assuming horizontal homogeneity, and neglecting radiation and latent heat effects [40]. In the derivation of the model the entrainment zone is idealized as infinitesimally thin (zero order scheme). The final practical and prognostic equation for the height evolution is the following [15, 40]:

$$\left\{ \left(\frac{h^2}{(1+A)h - 2BkL} \right) + \frac{Cu_*^2 T}{\gamma g [(1+A)h - BkL]} \right\} \left(\frac{dh}{dt} - w_s \right) = \frac{(\overline{w'\vartheta'})_s}{\gamma}, \quad (2)$$

where h is the PBL height, k is the von Karman constant ($k = 0.41$), L is the Obukhov length, u_* is the friction velocity, T is the surface temperature, g is the acceleration due to gravity, $(\overline{w'\vartheta'})_s$ is the kinematic heat flux at the surface, γ is the potential temperature gradient in the free atmosphere, w_s is the negative of the subsidence velocity, and A , B , and C are empirical constants set to 0.2, 2.5 and 8, respectively [41].

The first two terms on the left side of (2) represent the entrainment due to buoyancy and mechanical turbulence, and the so-called spin-up effect, respectively. The latter is active during the morning, when the PBL height is small and its growth rate is controlled by the friction velocity. In the central part of the day this contribution decreases and the turbulent flux influences the development of the PBL [15].

Equation (2) was solved numerically with an initial guess value of h set at 30 m and a time step of 10 minutes.

The turbulent parameters, namely, u_* , $(\overline{w'\vartheta'})_s$ and L , were derived from the sonic anemometer (Gill R50 Solent) data using the eddy covariance technique [42]. Two rotations have been applied to correct the measurements for possible sensor tilt errors.

The two external parameters γ , and w_s present in (2) have been estimated as described in Section 3.

The subsidence w_s represents the mean vertical motion of the air at the top of the boundary layer. It can be estimated if the horizontal divergence of the large-scale flow is known as function of height. When the horizontal divergence is constant with height, the subsidence is proportional to the divergence. The latter can be estimated if wind measurements from a network of meteorological stations are available [15].

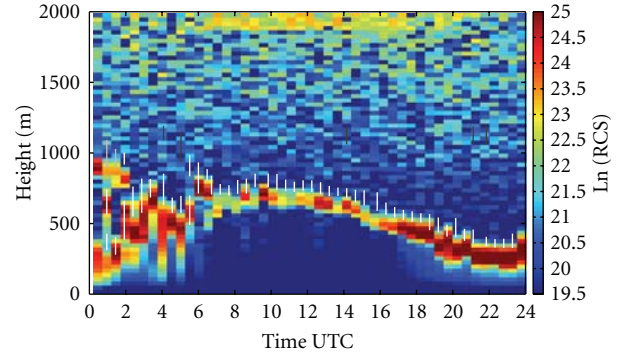


FIGURE 3: The natural logarithm of the RCS at 532 nm (parallel polarization). The higher the $\ln(\text{RCS})$, the larger the aerosol cross-section. This can be due to larger particles (i.e., cloud droplets or rain) as well as higher numerical particle concentration. Gray and white bars represent the top of aerosol stratifications. The PBL height can be assigned to one of these aerosol layers. The length of the lines represent their indetermination.

3. Discussion

The lidar observations can be used to obtain the boundary layer height, in convective conditions.

During summer, the wind speed reaches a minimum value in the free lower troposphere. The average speed in June from 0 to 3 km is less than 4 m/s, while during winter it is about 12 m/s. At the selected day, the wind speed was close to the corresponding monthly average. Consequently, the advection of air masses over the observation site is reduced, and the aerosol concentration can thus be considered a good indicator of the PBL dynamics.

Figure 3 shows the logarithm of the lidar range corrected signal, observed on June 14th; 2010, demonstrating how, even at low aerosol concentrations, the lidar observations allow to determine the layered structure of the boundary layer.

The aerosol distribution clearly shows the temporal evolution of a convective PBL, and the formation of a thin haze layer due to enhanced condensation at its top.

On June 14, the sun never sets at this site, reaching a minimum elevation angle of 12.4° at 23.12 UTC and a maximum of 34.3° at 11.12 UTC. In the early hours of the day (00 UTC–07 UTC) lidar profiles show the presence of haze and thin stratiform cloud layers in the first km, while in the central part of the day the sun radiation reaches the ground through a broken layer and heats the surface. This is also confirmed by the net radiative balance at the surface, which reaches peaks of 700 W/m^2 around noon, a value compatible with clear sky conditions at that latitude and season. This heat flux determines thus the convective structure observed for the PBL.

After noon, the weakened solar radiance causes the thinning of the mixed layer, which falls under 300 m at midnight. Low clouds are formed again after 16 UTC, likely due to radiative cooling.

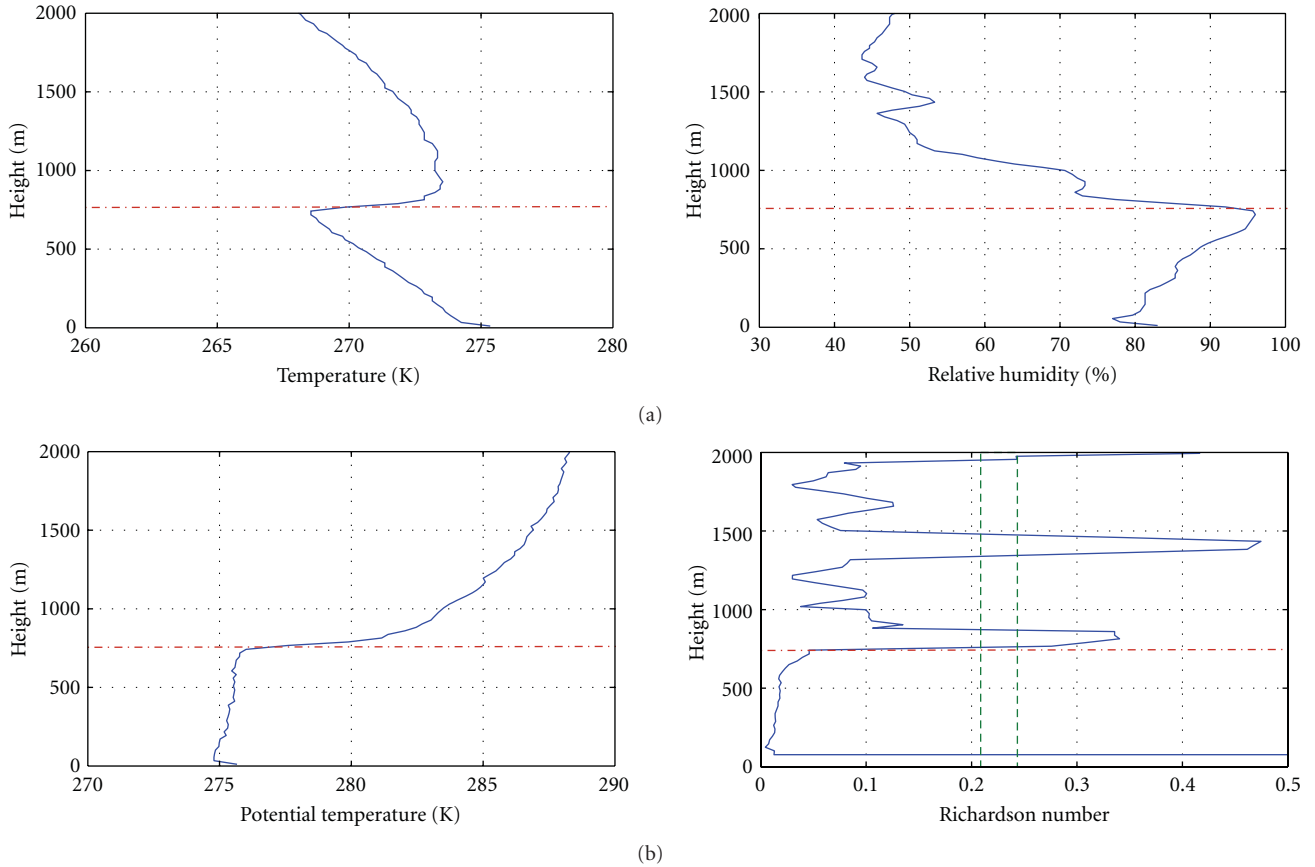


FIGURE 4: Determination of PBL height from thermodynamic values obtained by a VAISALA RS92 radiosonde. The radiosonde was launched at 12 UTC of the June 14th 2010 from the AWIPEV station of Ny Ålesund. In blue in the upper panel temperature and relative humidity while in the lower panel potential temperature and Richardson number. In dashed red the height of the PBL calculated for potential temperature with the Lapse Rate Method while the vertical green dashed lines on the fourth panel show the range of Richardson numbers between 0.21 and 0.25.

Figure 4 shows the vertical profiles of temperature, relative humidity, potential temperature, and Richardson number obtained from the 12 UTC radio sounding. The Richardson number is calculated using (1), and a green dotted box identifies the region where the R_{ib} is in the range between 0.21 and 0.25. The altitude identified with the values between 0.21 and 0.25 is shown as red-dotted line and represents the PBL height.

In Figure 4 in the upper panel temperature and relative humidity profiles are presented, and the relative inflection points are shown. In the lower panel, the potential temperature and the Richardson bulk number profiles are presented as well, together with the PBL height retrieved using these two quantities. These four different estimates are within 20 m, leading to an unambiguous determination of the PBL height by radio sounding. Considering the mean of these four values, the PBL height at 12 UTC can be set to 767 m above sea level (Figure 5).

This value is consistent with lidar and model estimates, as shown in Figure 5. However, it must be noted that, as explained in Section 2, the attribution of the PBL height to the lidar-derived estimations is still open to question. In fact, it

has to be noted that the analysis of lidar produces several layers, which should be interpreted by a visual comparison with the radio sonde measurements and the model output.

The convective behavior of the PBL is confirmed by the model simulation, as will be illustrated below. Because of the difficulties in estimating the subsidence, the w_s parameter is often neglected in formula (2). In the shallow mixed layers, the omission of w_s is of minor importance in the entire range of meteorological conditions. However, during a high pressure regime, characterized by positive horizontal divergence, the downward directed subsidence velocity increases as the mixed layer evolves and could be comparable in size to the rate at which the mixed layer entrains into the air aloft [40]. In these cases, w_s is negative and of the order of some cm s^{-1} [41]. Because of the difficulty in estimating w_s , three values between 3 and 4 cm s^{-1} have been employed. Comparable values were derived for the Antarctica PBL and can be found in the literature [43]. The value of γ was derived from the temperature profiles measured by the radio soundings at 12 UTC, obtained in a 100 m layer above the entrainment layer. The value has been kept constant during the day and equals 0.0025 K m^{-1} .

TABLE 1: Comparison between the advantages and drawbacks of the three approaches to determinate the PBL height.

	Advantages	Disadvantages
Lidar-based gradient method	High vertical resolution Continuous measurements Opportunity to observe aerosol layers	Lack of overlap at low altitudes sets a lower limit for PBL height determination Needs well-mixed aerosol. Problems of interpretation with advected layers
Radiosonde-based LR and RB methods	Large dataset over the world since radiosondes are routinely operated Can be used also in adverse meteorological conditions	Determination of the PBL height only in coincidences of the balloon launch In case of stable PBL methods based on potential temperature are not applicable (or reliable)
Batchvarova and Gryning model	Provides continuous estimate of the PBL height Employs only ground based measurements	Good results only under convective regimes and clear sky conditions Estimate of initialization values and uncertainties on estimates of parameters Turbulent flux measurements are required Many approximations in the physics of PBL processes make the estimate subject to large uncertainties

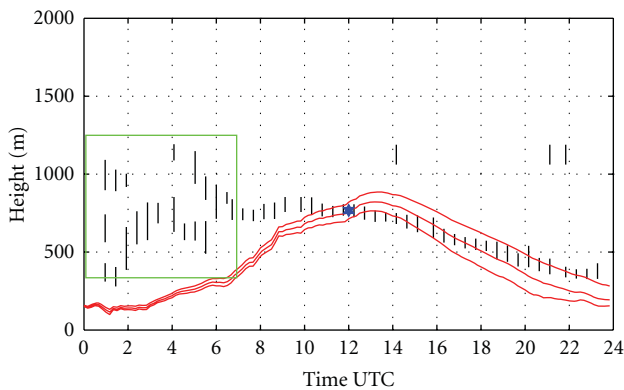


FIGURE 5: The PBL height as obtained from the Batchvarova and Gryning model (red line) and radiosonde (blue star) for 14 June 2010. The three red lines correspond to different w_s values, as discussed in the text. Black lines indicate the top of the aerosol layers, as detected by the DWT on lidar data, showing the associated indetermination. The aerosol layers enclosed in the green box are associated to hazy layers that likely do not mark off the PBL.

In Figure 5, the behaviour of the PBL height computed using the model for 14 June 2010 is shown as a red line, for the values of 3.0, 3.5, and 4.0 cm s^{-1} . The maximum value (always reached at 1330 UTC) ranges between 885 m and 750 m, depending on the value of w_s .

The early morning haze does not permit to identify the PBL height by the gradient method with accuracy, since the large aerosol backscatter cross section relative to such layers usually masks the weaker gradients connected to changes in

the aerosol vertical distribution. As shown in Figure 5, the Batchvarova and Gryning model predicts a PBL height between 150 m and 300 m while the lidar observations show clouds up to 1 km (green box).

Considering the sensitivity of the model to the values of w_s , during the evening (19 UTC–24 UTC), the PBL height obtained by the model presents a substantial agreement with the aerosol layer between 400 and 500 m ASL. Moreover, the wavelet method detects the top of the PBL aerosol/haze, while the model considers the entrainment zone as a null thickness layer.

Considering that the PBL heights determined by the specific methods are based on a different definition of PBL, the comparison of the results obtained, presented in Figure 5, is satisfying.

Table 1 resumes the advantages and drawbacks of each of the three techniques presented in this study, depending on the different meteorological conditions or due to different spatial and temporal resolutions which can be achieved. An integration of the three techniques would provide an accurate determination of the PBL height in different meteorological conditions.

During the spring-summer season, when convective structures of the PBL are frequently observed, the aerosol represents a good tracer to estimate the PBL height. The availability of the lidar data during the day allows to study the daily evolution of the PBL height, while the radio sonde provides only one (or few) measurements per day.

The analysis showed that under suitable conditions the gradient method allows the determination of aerosol layers

over the Svalbard region. Nevertheless, in case of multiple layers, the attribution of the PBL top still remains uncertain with automated algorithms, and physical constraints have to be applied to determine the PBL height. A methodology to routinely take into account the physics behind the PBL dynamics, assimilating the model prediction in the retrieval algorithm is under development. An example of such approach is described in di Giuseppe et al. [44]. This will likely allow to automatically use Lidar to determine the PBL height and build an extensive data base of PBL height, determined from lidar observations at this site.

4. Conclusions

Lidar observations have been used to determine the PBL height at the Arctic site of Ny Ålesund, Svalbard, Norway. The gradient method has been applied to a dataset covering one day (June 14, 2010) with a convective PBL, typically occurring in the spring early summer season in the Arctic. The logarithm of the range-corrected signal collected by the lidar was processed by a Discrete Wavelet Transform method to determine the inflection points in the aerosol backscatter profile. The aerosol layers found in such way have been compared with radiosonde-based estimate of the PBL height and with the one dimensional zero order Batchvarova and Gryning model.

The results showed a good agreement, considering the differences among the various methods involving several observables and instruments, and different approaches based on distinct physical processes. In favourable cases the gradient method may work automatically providing reliable results, as in the midday period, while more sophisticated algorithms are being developed to deal with more complex conditions.

In spite of the drawbacks inherent to the gradient method and the difficulties in comparing estimates from different approaches, the results obtained encourage to apply this method to a wider data set. A future measurement campaign is planned for 2012, in order to perform an analysis by using the different methods on an extended set of data covering various boundary layer conditions.

Acknowledgments

The authors wish to thank the station team in Ny Ålesund (AWIPEV) and the logistical support provided by the Department of Earth and Environment of the Italian National Research Council (DTA-CNR). The work was in part funded by the Italian Project PRIN 2007.

References

- [1] J. E. Kay, K. Raeder, A. Gettelman, and J. Anderson, "The boundary layer response to recent arctic sea ice loss and implications for high-latitude climate feedbacks," *Journal of Climate*, vol. 24, no. 2, pp. 428–447, 2011.
- [2] C. Deser, R. Tomas, M. Alexander, and D. Lawrence, "The seasonal atmospheric response to projected Arctic sea ice loss in the late twenty-first century," *Journal of Climate*, vol. 23, no. 2, pp. 333–351, 2010.
- [3] J. Boé, A. Hall, and X. Qu, "Current GCMs' unrealistic negative feedback in the arctic," *Journal of Climate*, vol. 22, no. 17, pp. 4682–4695, 2009.
- [4] P. Seibert, F. Beyrich, S. E. Gryning, S. Joffre, A. Rasmussen, and P. Tercier, "Review and intercomparison of operational methods for the determination of the mixing height," *Atmospheric Environment*, vol. 34, no. 7, pp. 1001–1027, 2000.
- [5] D. S. Covert, A. Wiedensohler, P. Aalto, J. Heintzenberg, P. H. McMurry, and C. Leck, "Aerosol number size distributions from 3 to 500 nm diameter in the arctic marine boundary layer during summer and autumn," *Tellus, Series B*, vol. 48, no. 2, pp. 197–212, 1996.
- [6] J. Heintzenberg, C. Leck, W. Birmili, B. Wehner, M. Tjernström, and A. Wiedensohler, "Aerosol number-size distributions during clear and fog periods in the summer high Arctic: 1991, 1996 and 2001," *Tellus, Series B*, vol. 58, no. 1, pp. 41–50, 2006.
- [7] T. J. Garrett and C. Zhao, "Increased Arctic cloud longwave emissivity associated with pollution from mid-latitudes," *Nature*, vol. 440, no. 7085, pp. 787–789, 2006.
- [8] S. Solomon, D. Qin, M. Manning et al., Eds., *The Physical Science Basis. Contribution of Working Group I to the Fourth Assessment Report of the Intergovernmental Panel on Climate Change*, Cambridge University Press, New York, NY, USA, 2007.
- [9] J. R. McConnell, R. Edwards, G. L. Kok et al., "20th-Century industrial black carbon emissions altered arctic climate forcing," *Science*, vol. 317, no. 5843, pp. 1381–1384, 2007.
- [10] M. C. Serreze, M. M. Holland, and J. Stroeve, "Perspectives on the Arctic's shrinking sea-ice cover," *Science*, vol. 315, no. 5818, pp. 1533–1536, 2007.
- [11] M. Z. Jacobson, "Climate response of fossil fuel and biofuel soot, accounting for soot's feedback to snow and sea ice albedo and emissivity," *Journal of Geophysical Research D*, vol. 109, no. 21, Article ID D21201, 15 pages, 2004.
- [12] J. Hansen and L. Nazarenko, "Soot climate forcing via snow and ice albedos," *Proceedings of the National Academy of Sciences of the United States of America*, vol. 101, no. 2, pp. 423–428, 2004.
- [13] F. Cairo, G. Di Donfrancesco, A. Adriani, L. Pulvirenti, and F. Fierli, "Comparison of various linear depolarization parameters measured by lidar," *Applied Optics*, vol. 38, no. 21, pp. 4425–4432, 1999.
- [14] L. Liu and M. I. Mishchenko, "Constraints on PSC particle microphysics derived from lidar observations," *Journal of Quantitative Spectroscopy and Radiative Transfer*, vol. 70, no. 4–6, pp. 817–831, 2001.
- [15] S. E. Gryning and E. Batchvarova, "Analytical model for the growth of the coastal internal boundary layer during onshore flow," *Quarterly Journal*, vol. 116, no. 491, pp. 187–203, 1990.
- [16] S. Emeis, K. Schäfer, and C. Münkel, "Surface-based remote sensing of the mixing-layer height—a review," *Meteorologische Zeitschrift*, vol. 17, no. 5, pp. 621–630, 2008.
- [17] F. Beyrich, "Mixing height estimation from sodar data—a critical discussion," *Atmospheric Environment*, vol. 31, no. 23, pp. 3941–3953, 1997.
- [18] S. A. Cohn and W. M. Angevine, "Boundary layer height and entrainment zone thickness measured by lidars and wind-profiling radars," *Journal of Applied Meteorology*, vol. 39, no. 8, pp. 1233–1247, 2000.
- [19] F. Cairo, G. Di Donfrancesco, L. Di Liberto, and M. Viterbini, "The RAMNI airborne lidar for cloud and aerosol research,"

- Atmospheric Measurement Techniques Discussions*, vol. 5, pp. 1253–1292, 2012.
- [20] M. Haeffelin, F. Angelini, Y. Morille et al., “Evaluation of mixing height retrievals from automatic profiling lidars and ceilometers in view of future integrated networks in Europe,” *Boundary-Layer Meteorology*, pp. 1–27, 2011.
- [21] R. M. Endlich, F. L. Ludwig, and E. E. Uthe, “An automatic method for determining the mixing depth from lidar observations,” *Atmospheric Environment*, vol. 13, no. 7, pp. 1051–1056, 1979.
- [22] S. H. Melfi, J. D. Spinhirne, S. H. Chou, and S. P. Palm, “Lidar observations of vertically organized convection in the planetary boundary layer over the ocean,” *Journal of Climate & Applied Meteorology*, vol. 24, no. 8, pp. 806–821, 1985.
- [23] B. Hennemuth and A. Lammert, “Determination of the atmospheric boundary layer height from radiosonde and lidar backscatter,” *Boundary-Layer Meteorology*, vol. 120, no. 1, pp. 181–200, 2006.
- [24] A. Lammert and J. Bösenberg, “Determination of the convective boundary-layer height with laser remote sensing,” *Boundary-Layer Meteorology*, vol. 119, no. 1, pp. 159–170, 2006.
- [25] S. Pal, A. Behrendt, and V. Wulfmeyer, “Elastic-backscatter-lidar-based characterization of the convective boundary layer and investigation of related statistics,” *Annales Geophysicae*, vol. 28, no. 3, pp. 825–847, 2010.
- [26] A. Behrendt, S. Pal, F. Aoshima et al., “Observation of convection initiation processes with a suite of state-of-the-art research instruments during COPS IOP 8b,” *Quarterly Journal of the Royal Meteorological Society*, vol. 137, supplement 1, pp. 81–100, 2011.
- [27] U. Wandinger and A. Ansmann, “Experimental determination of the lidar overlap profile with Raman lidar,” *Applied Optics*, vol. 41, no. 3, pp. 511–514, 2002.
- [28] G. Biavati, G. Di Donfrancesco, F. Cairo, and D. G. Feist, “Correction scheme for close-range lidar returns,” *Applied Optics*, vol. 50, no. 30, pp. 5872–5882, 2011.
- [29] I. M. Brooks, “Finding boundary layer top: application of a wavelet covariance transform to lidar backscatter profiles,” *Journal of Atmospheric and Oceanic Technology*, vol. 20, pp. 1092–1105, 2003.
- [30] K. J. Davis, N. Gamage, C. R. Hagelberg, C. Kiemle, D. H. Lenschow, and P. P. Sullivan, “An objective method for deriving atmospheric structure from airborne lidar observations,” *Journal of Atmospheric and Oceanic Technology*, vol. 17, no. 11, pp. 1455–1468, 2000.
- [31] M. Haij, W. Wauben, and K. Baltink, “Continuous mixing layer height determination using the LD-40 ceilometer: a feasibility study,” KNMI Scientific Report, 2007.
- [32] A. J. Garrett, “Comparison of observed mixed-layer depths to model estimates using observed temperatures and winds, and MOS forecasts,” *Journal of Applied Meteorology*, vol. 20, no. 11, pp. 1277–1283, 1981.
- [33] K. L. Hayden, K. G. Anlauf, R. M. Hoff et al., “The vertical chemical and meteorological structure of the boundary layer in the Lower Fraser Valley during Pacific ’93,” *Atmospheric Environment*, vol. 31, no. 14, pp. 2089–2105, 1997.
- [34] D. H. P. Vogelesang and A. A. M. Holtslag, “Evaluation and model impacts of alternative boundary-layer height formulations,” *Boundary-Layer Meteorology*, vol. 81, no. 3-4, pp. 245–269, 1996.
- [35] L. Menut, C. Flamant, J. Pelon, and P. H. Flamant, “Urban boundary-layer height determination from lidar measurements over the Paris area,” *Applied Optics*, vol. 38, no. 6, pp. 945–954, 1999.
- [36] M. Sicard, C. Pérez, A. Comerón, J. M. Baldasano, and F. Rocadenbosch, “Determination of the mixing layer height from regular lidar measurements in the Barcelona Area,” in *Remote Sensing of Clouds and the Atmosphere VIII*, vol. 5235 of *Proceedings of SPIE*, Barcelona, Spain, 2004.
- [37] G. Martucci, R. Matthey, V. Mitev, and H. Richner, “Lidar determination of mixing layer height with high resolution,” in *Remote Sensing of Clouds and the Atmosphere X*, vol. 5979 of *Proceedings of SPIE*, Brugge, Belgium, 2005.
- [38] I. B. Troen and L. Mahrt, “A simple model of the atmospheric boundary layer; sensitivity to surface evaporation,” *Boundary-Layer Meteorology*, vol. 37, no. 1-2, pp. 129–148, 1986.
- [39] J. C. King, S. A. Argentini, and P. S. Anderson, “Contrasts between the summertime surface energy balance and boundary layer structure at Dome C and Halley stations, Antarctica,” *Journal of Geophysical Research D*, vol. 111, no. 2, Article ID D02105, 13 pages, 2006.
- [40] E. Batchvarova and S. E. Gryning, “An applied model for the height of the daytime mixed layer and the entrainment zone,” *Boundary-Layer Meteorology*, vol. 71, no. 3, pp. 311–323, 1994.
- [41] E. Batchvarova and S. E. Gryning, “Applied model for the growth of the daytime mixed layer,” *Boundary-Layer Meteorology*, vol. 56, no. 3, pp. 261–274, 1991.
- [42] X. Lee, W. Massman, and B. Law, *Handbook of Micrometeorology*, Kluwer Academic, Dordrecht, The Netherlands, 2004.
- [43] S. Argentini, A. Viola, A. M. Sempreviva, and I. Petenko, “Summer boundary-layer height at the plateau site of Dome C, Antarctica,” *Boundary-Layer Meteorology*, vol. 115, no. 3, pp. 409–422, 2005.
- [44] F. Di Giuseppe, A. Riccio, L. Caporaso, G. Bonafè, G. P. Gobbi, and F. Angelini, “Automatic detection of atmospheric boundary layer height using ceilometer backscatter data assisted by a boundary layer model,” *Quarterly Journal of the Royal Meteorological Society*, In press.

Research Article

Distribution, Composition, and Vertical Fluxes of Particulate Matter in Bays of Novaya Zemlya Archipelago, Vaigach Island at the End of Summer

N. V. Politova, V. P. Shevchenko, and V. V. Zernova

Departments of Marine Geology and Ecology of Seas and Oceans, P. P. Shirshov Institute of Oceanology RAS, 36 Nakhimovskii prospect, 117997 Moscow, Russia

Correspondence should be addressed to N. V. Politova, politova@ocean.ru

Received 15 September 2011; Revised 9 January 2012; Accepted 19 January 2012

Academic Editor: Igor N. Esau

Copyright © 2012 N. V. Politova et al. This is an open access article distributed under the Creative Commons Attribution License, which permits unrestricted use, distribution, and reproduction in any medium, provided the original work is properly cited.

An analysis of suspended particulate matter (SPM) and phytoplankton distribution, composition and vertical particle fluxes in Russkaya Gavan' Bay (Northern Island of the Novaya Zemlya), Bezymyannaya Bay (Southern Island of the Novaya Zemlya), Dolgaya Bay (northwestern part of the Vaigach Island) in comparison with the data from the Svalbard Archipelago is presented. Field studies were carried out by the authors during the 9th expedition of the RV "Professor Logachev" in September 1994, the 11th, 13th, and 14th expeditions of the RV "Akademik Sergey Vavilov" in September-October 1997 and August-September 1998. The data about Spitsbergen fjords are from literature. Our results show that, on the bays of the Barents Sea islands, most SPM stays in the bays (fjords) and only small part of it reaches the open sea. This is due to the hydrodynamic conditions in the bays, the large size of the particles, flocculation, and often to the morphological barriers in the relief at the bay entrances. It is important for ecological purposes to map out migration pathways of the SPM with pollutants from bays to the open sea. Results of our investigation indicate that the western bays of the Novaya Zemlya act as traps for SPM derived from glaciers and coastal abrasion.

1. Introduction

The suspended particulate matter (SPM) is an important link in the natural cycle of matter. Its study in the Ocean is necessary for understanding modern sedimentation processes and for the ecological assessment of the state of the environment [1, 2]. Currently, SPM in the Arctic is studied insufficiently in order to receive the complete picture of the sedimentation process in the severe polar conditions [3, 4].

The fjords of the archipelagos and islands are one of sediment sources for the Barents Sea [5]. The intensive glacial meltwater discharge and riverine runoff occur on the Novaya Zemlya and Svalbard archipelagos [6–9]. Studies in fjords receiving glacial meltwater show diversity of biogeochemical and sedimentological processes taking place there [10–14]. SPM in glacier-influenced fjords of western coast of the northern Novaya Zemlya was studied by Medvedev and Potekhina [6] using filtration through the old type filters (nitrocellulose membrane), which increased the values of

SPM concentration because of the colmatage [15]. Since 1996 SPM in fjords of the northern Novaya Zemlya was studied by modern methods [16–20]. SPM in fjords of the Svalbard was studied by scientists from different countries [5, 9, 12–14, 21].

Some fjords of the Novaya Zemlya Archipelago are also the damping places of the nuclear waste. It is important for ecological purposes of the region monitoring to map out migration pathways of the SPM with pollutants from bays to the open sea [22].

Particle fluxes have been studied in detail in the western Barents Sea, the Norwegian Sea, the Greenland Sea, and in the Fram Strait [23–30]. The first studies of particle fluxes in the Kara Sea and in the eastern Barents Sea were carried out in September 1993 during the 49-th cruise of the RV "Dmitry Mendeleev" [31] and in August-September 1994 during the 9-th cruise of the RV "Professor Logachev" [32–34].

We have carried out a comparative analysis of SPM and phytoplankton distribution and composition and of

TABLE 1: Coordinates, dates, and concentrations of the SPM in the bays of the Barents Sea.

Cruise, year	Station	Date-Time	Coordinates		Level, m	SPM concentrations, mg/L
			N	E		
PL-9	103	26.09-08.35	72°57,51'	53°01,76'	0	0.37
1994	104	26.09-09.35	72°55,31'	53°03,07'	0	1.67
	105	26.09-11.00	72°56,60'	53°03,19'	0	1.27
	106	26.09-12.24	72°55,53'	52°56,79'	0	1.28
	107	26.09-12.37	72°54,49'	53°01,22'	0	2.29
	108	26.09-13.41	72°54,45'	53°01,21'	0	2.07
	109	26.09-14.25	72°54,05'	53°07,86'	0	3.32
	110	26.09-14.47	72°54,48'	53°04,34'	0	3.30
	111	26.09-15.39	72°54,45'	53°04,28'	0	2.07
	112	26.09-16.03	72°54,94'	53°05,82'	0	3.28
	113	26.09-16.56	72°54,13'	53°07,94'	0	2.79
	114	26.09-17.40	72°54,25'	53°10,29'	0	2.38
	ASV-11 1997	985	22.09-12.10	76°12.3'	62°37.7'	0
10						3.53
25						1.71
50						0.68
60						0.49
988		22.09-20.00	76°11.7'	62°28.3	0	13.51
					10	10.11
					25	3.09
					50	1.00
					85	0.51
989a		22.09-23.20	76°13.5'	62°27.4'	0	2.88
					10	2.14
	25				1.25	
	50				0.45	
	75				0.33	
989b	23.09-06.35	76°13.5'	62°27.4'	0	1.17	
				10	1.26	
				25	0.56	
				50	0.32	
				75	1.68	
990	23.09-09.15	76°15.7'	62°37.6'	0	5.41	
				10	1.13	
				25	4.99	
				50	1.18	
				95	0.92	
991	23.09-12.00	76°15.3'	62°29.2'	0	1.83	
				10	1.37	
				25	1.32	
				50	1.21	
				80	1.58	

TABLE 1: Continued.

Cruise, year	Station	Date-Time	Coordinates		Level, m	SPM concentrations, mg/L
			N	E		
	992	23.09-15.45	76° 15.2'	62° 33.4'	0	2.15
					10	1.38
					25	0.96
					50	1.39
					120	1.29
	1000	24.09-01.05	76° 17.7'	62° 19.0'	0	1.83
					10	4.75
					25	1.25
					40	1.06
					55	1.71
	1001	24.09-02.45	76° 17.6'	62° 25.8'	0	1.81
					10	1.90
					25	1.67
					50	1.48
					75	1.31
					100	0.96
	1002	24.09-04.30	76° 17.7'	62° 33.4'	0	1.81
					10	1.51
					25	1.41
					50	1.33
					75	1.05
					125	1.08
	1003	24.09-06.25	76° 17.8'	62° 43.5'	0	1.96
					10	1.60
					25	1.21
					50	1.18
					75	1.10
					120	1.08
	1004	24.09-08.15	76° 17.9'	62° 49.8'	0	1.51
					10	1.51
					25	1.18
					50	4.48
					75	1.08
					140	0.76
Sampling	41	22.09			0	358.50
near the	42				0	271.50
Shokal'sky	43				0	273.75
glacier	44				0	212.75
	45				0	209.50
	46				0	8.33
	47				0	65.75
	48				0	42.80
	49				0	27.10
	50				0	20.50
	1018	30.09-12.00	70° 15.1'	58° 39.0'	0	1.29
					8	0.72
					12	0.61
	1019	30.09-13.00	70° 15.9'	58° 32.3'	0	0.77
					10	1.39
					23	2.26

TABLE 1: Continued.

Cruise, year	Station	Date-Time	Coordinates		Level, m	SPM concentrations, mg/L
			N	E		
	1020	30.09-14.40	70° 17.1'	58° 25.1'	0	1.14
					10	1.81
					25	1.61
	1021	30.09-16.00	70° 18.4'	58° 18.1'	0	0.96
					10	1.31
					40	1.06
	1022	30.09-20.00	70° 19.7'	58° 24.8'	0	0.97
					10	1.11
					30	1.28
	1023	30.09-21.15	70° 16.8'	58° 15.1'	0	0.83
					10	1.92
					50	0.62

TABLE 2: Coordinates, dates of deployment, and recovery of sedimentological mooring stations and vertical particle fluxes in the Barents Sea [33, 44].

Station	Coordinates		Date		Depth m	Level m	Flux mg m ⁻² d ⁻¹	POC mg m ⁻² d ⁻¹	
	N	E	Deployment	Recovery					
PL-3	79 23.4'	69 58.4'	10.08.1994	20.08.1994	515	55	23.0	4.65	
						205	19.7	2.28	
						405	19.5	1.68	
						465	27.9	2.67	
PL-5	72 56.8'	51 26.9'	24.09.1994	30.09.1994	35	62.9	7.61	12.1	
						95	4.05	9.5	
PL-6	73 01.2'	52 53.9'	25.09.1994	30.09.1994	15	314	34.8	11.1	
						20	656	55.2	8.4
						70	9.8	1.59	
ASV-11-3	78° 05.0'	60° 00.2'	9/14/1997	9/19/1997	380	130	17.7	0.98	
						360	62.9	4.63	
ASV-11-5	76° 16.0'	62° 27.1'	9/22/1997	9/24/1997	104	70	346	8.53	
						85	7660	185	
						80	212	4.15	
ASV-11-7	70° 18.1'	57° 58.2'	9/29/1997	10/3/1997	190	120	3500	86.8	
						165	2040	18.4	
ASV-11-8	70° 17.8'	58° 11.15'	10/5/1997	10/7/1997	230	55	256	8.27	
ASV-13-2	69° 43.6'	51° 03.2'	8/12/1998	8/30/1998	82	40	99	29.9	
ASV-14-3	75° 59.2'	44° 08.3'	9/17/1998	9/29/1998	255	80	23.5	7.72	

the vertical particle fluxes in Russkaya Gavan' Bay (Northern Island of the Novaya Zemlya), Bezymyannaya Bay (Southern Island of the Novaya Zemlya), Dolgaya Bay (northwestern part of the Vaigach Island), and in the fjords of the Svalbard Archipelago.

2. Materials and Methods

Field studies were carried out during the 9th expedition of the RV "Professor Logachev" in September 1994, the 11th,

13th, and 14th expeditions of the RV "Akademik Sergey Vavilov" in September-October 1997 and August-September 1998 (Figures 1–3; Tables 1 and 2).

For SPM studies the filtration of water samples was carried out through Nuclepore membrane filters 47 mm in diameter (pore size 0.45 μm). For vertical particle flux studies, we used small cylindrical sediment traps (vinyl plastic cylinders, 118 mm in diameter, with a 490 mm high working part and baffled grid installed in the upper part to avoid washing out of the sediments). Prior to sediment trap

TABLE 3: Granulometric composition of the particulate matter in the bays of the Novaya Zemlya Archipelago and Vaigach Island (sizes of particles are in μm).

Area	St.	Depth m	Fractions, %					Mean size, μm
			Sand 1000–100	Aleurite 100–10	10–5	Pelite 5–1	<1	
Russkaya Gavan' near the Shokal'sky glacier	41	0	0	32	15	49	4	1.07
	42	0	0	0	20	75	5	1.16
	43	0	0	16	24	54	6	1.10
	44	0	0	4	23	65	8	1.05
	45	0	0	4	37	56	3	1.18
	46	0	0	0	8	82	10	1.03
	47	0	0	0	18	76	6	1.13
	48	0	0	1	26	69	4	1.16
	49	0	0	0	34	62	4	1.15
	50	0	0	0	36	60	4	1.21
Russkaya Gavan'		0	0	0	19	73	9	1.08
		10	0	0	10	79	11	1.02
	985	25	0	0	20	68	12	1.00
		50	0	0	10	82	8	1.12
		60	0	0	7	83	10	1.06
		0	0	4	33	60	3	1.31
		10	0	0	28	66	6	1.12
	988	25	0	0	26	68	6	1.13
		50	0	49	19	30	2	1.19
		85	0	0	8	85	7	1.17
		0	0	0	20	72	8	1.08
		10	0	0	0	87	13	1.00
	989a	25	0	0	0	62	28	0.91
		50	0	0	0	40	60	0.82
		75	0	0	10	81	8	1.06
		0	0	0	22	71	7	1.09
		10	0	0	31	63	6	1.13
	989b	25	0	0	5	85	10	1.05
		50	0	0	0	89	11	1.04
		75	0	2	36	58	4	1.21
990	0	0	0	17	75	8	1.05	
991	0	0	0	11	80	9	1.06	
	0	0	0	19	74	7	1.10	
	10	0	0	21	71	8	1.10	
992	25	0	0	10	81	9	1.06	
	50	0	0	8	83	9	1.08	
	120	0	0	10	82	8	1.12	
1000	0	0	0	5	83	12	1.00	
1001	0	0	0	6	82	12	1.00	
1002	0	0	0	8	83	9	1.05	
1003	0	0	0	7	84	9	1.05	
1004	0	0	0	0	88	12	1.01	
Dolgaya Bay		0	0	0	6	86	8	1.09
	1018	8	0	0	10	85	5	1.12
		12	0	0	9	84	7	1.12
		0	0	0	19	78	3	1.2
	1019	10	0	0	15	82	3	1.17
	23	0	17	37	45	1	1.3	

TABLE 3: Continued.

Area	St.	Depth m	Fractions, %					Mean size, μm
			Sand 1000–100	Aleurite 100–10	10–5	Pelite 5–1	<1	
Dolgaya Bay	1020	0	0	0	12	83	5	1.18
		10	0	0	0	93	7	1.12
		25	0	0	18	74	8	1.08
		0	0	0	20	75	5	1.09
	1021	10	0	0	11	82	7	1.08
		40	0	0	19	76	5	1.17
		0	0	0	11	82	7	1.11
	1022	10	0	0	14	79	7	1.09
		30	0	0	27	68	5	1.13
		0	0	0	24	70	6	1.09
	1023	10	0	0	28	69	3	1.25
50		0	0	6	85	9	1	

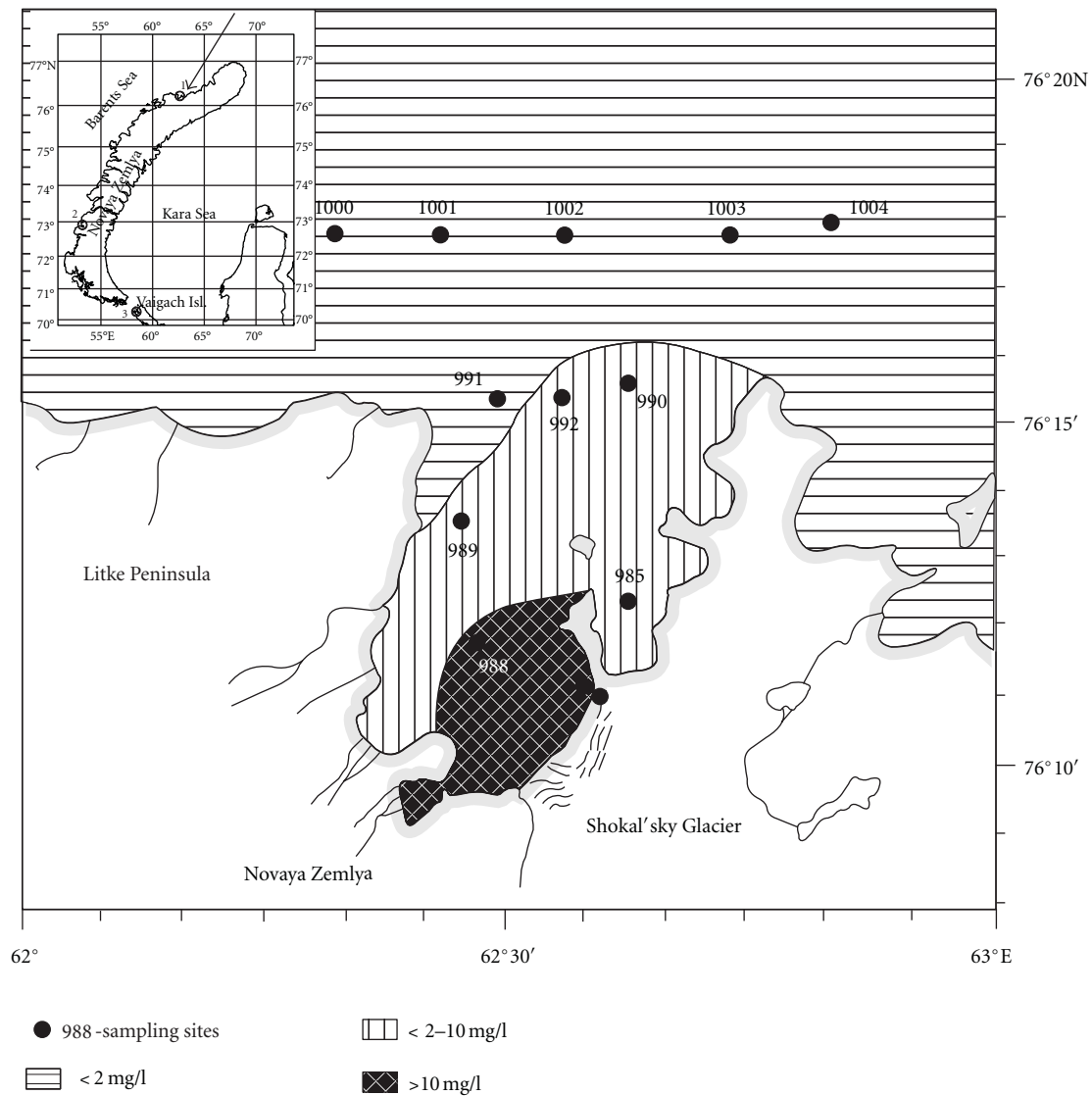


FIGURE 1: Distribution of SPM (mg/L) in the surface layer of Russkaya Gavan' Bay, Novaya Zemlya on 22.09–24.09.97: 1: station number; concentration of SPM: 2: <2 mg/L; 3: 2–10 mg/L; 4: >10 mg/L [36].

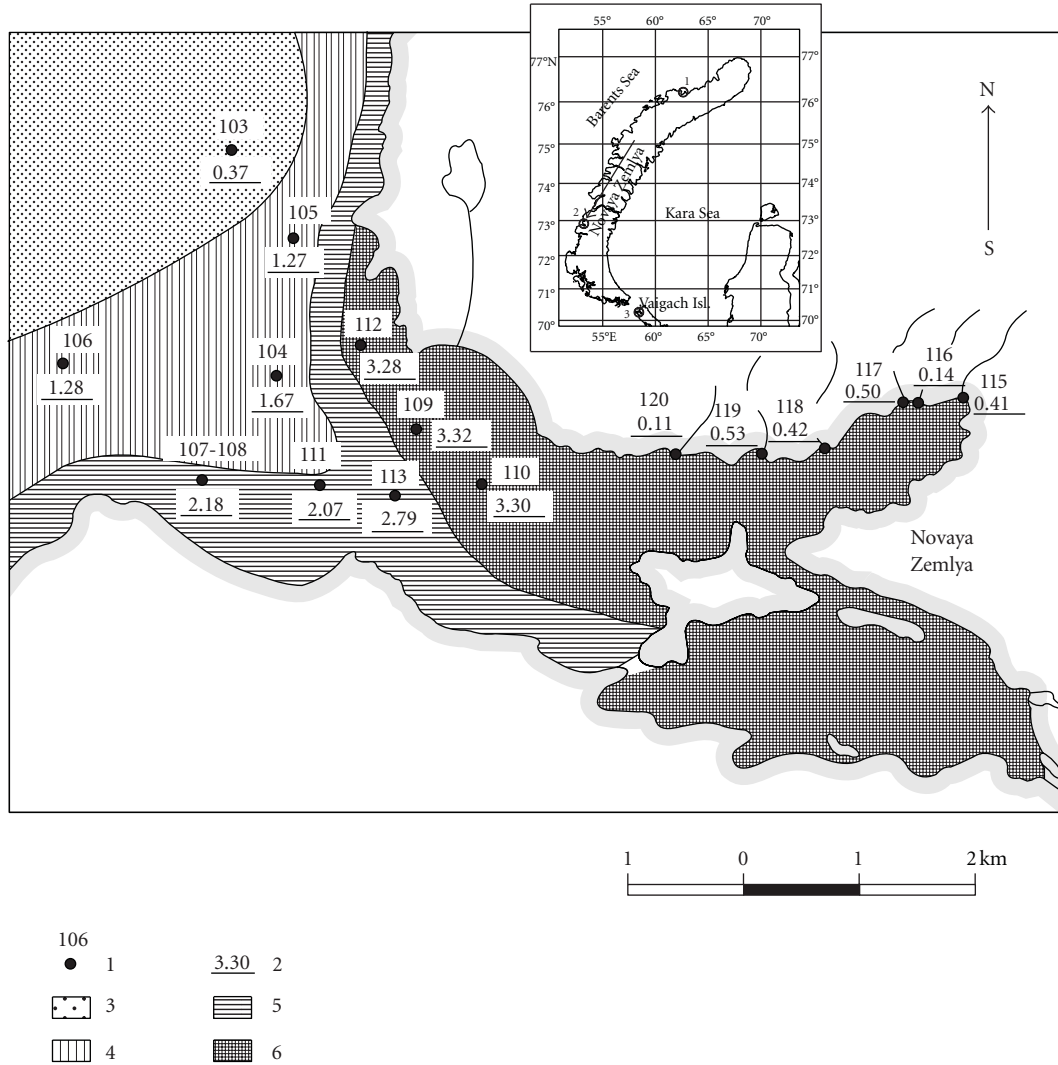


FIGURE 2: Distribution of suspended particulate matter (SPM) in the surface layer (0-1 m) of the Bezymyannaya Bay, Novaya Zemlya Archipelago, in September 1994: 1: station number; 2: concentration of SPM; 3: <1 mg/L; 4: 1-2 mg/L; 5: 2-3 mg/L; 6: >3 mg/L [18].

deployment, we poured into the flasks 5 mL 40% formalin to eliminate bacterial activity and to prevent the settled particles from being eaten by zooplankton.

For studying the SPM distribution and to establish the correlation between the SPM concentration and the beam attenuation coefficient, we used “Del’fin” transparency probe. Its measurement range is 0.01–8.00 m^{-1} with absolute accuracy 0.005 m^{-1} on the 555 nm wave length [3]. Spatial distribution of SPM in the surface waters of the Barents Sea was assessed using the data of the ocean color scanner SeaWiFS (data of the second and third levels were verified by the measurements in situ in time of satellite passing; the algorithm was modified for the Barents Sea) [35].

For plankton studies, we used method of reverse filtration (1–6 L of the water) through the membrane nuclear filter (the pore size was 1 μm), then the sample was concentrated again up to the volume 5–6 mL. The counting and determination of algae and microzooplankton were carried out in the

counting camera with volume 0.05 mL by microscope MBI-3 with magnification of 210–420 times.

We used laser-optical counter of the particles CIS-1 (Galai, Israel) in Alfred-Wegener Institute of Polar and Marine Researchers (Bremerhaven, Germany) for granulometric studies of the SPM from the filters in the range 0.5–100 μm . Filters were also studied in the scanning electron microscope JSM-U3 (Jeol, Japan).

In more details the methods of SPM and particle flux studies are described elsewhere [18, 31, 33, 34].

3. Results and Discussion

3.1. Quantitative Distribution of the SPM in the Bays. In the Russkaya Gavan’ Bay, it was the period of active melting of the glacier. The SPM concentration in the surface layer in the inner part of the bay was >10 mg/L, reaching value of 265 mg/L near the Shokalsky Glacier edge (Figure 1). In the

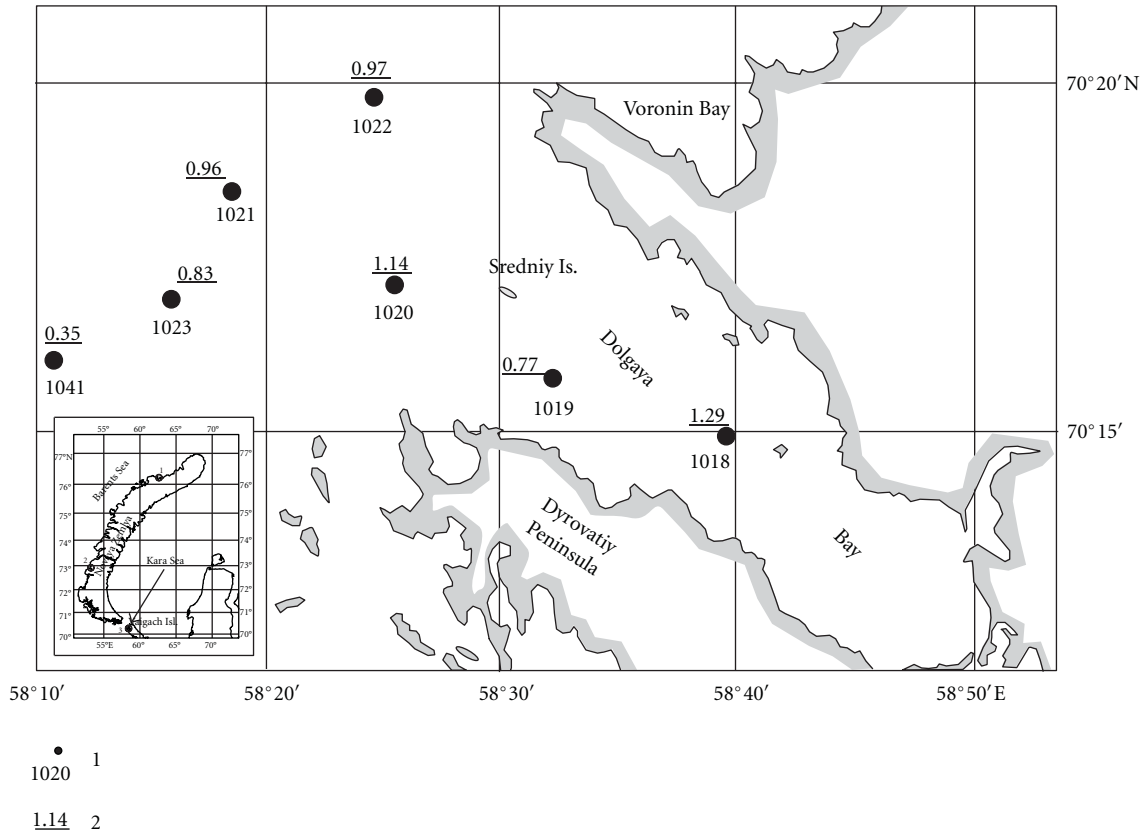


FIGURE 3: Distribution of SPM in the surface layer of Dolgaya Bay, Vaigach Island: 1: station number; 2: concentration of SPM (mg/L).

outer part of the bay, SPM concentration in the surface layer was from 2 to 10 mg/L, and in adjacent Barents Sea it was <2 mg/L [36]. The concentration of SPM decreases under the pycnocline.

On September 26-27, 1994 in the inner part of the Bezymyannaya Bay, SPM concentration (Figure 2) was >3 mg/L, decreasing towards the open sea, where concentration is <1 mg/L [18]. We could assume that suspended matter mostly deposits in the outer part of the bay. The SPM concentrations in the area of the river tributary were relatively low, so the influence of the river was insignificant and the abrasion prevailed as the source of the suspended matter during the period of our investigations.

In the Dolgaya Bay of Vaigach Island, the SPM concentration was relatively low (0.15–2.58 mg/L). The decreasing of SPM concentration occurs also from inner part of the bay to the open sea (Figure 3).

The high concentrations of the SPM were observed in the other bays of the Novaya Zemlya Archipelago. For example, in the Inostrantsev Bay, the SPM concentrations were 13.05 mg/L in the surface waters, decreasing under the pycnocline and towards the open sea [20].

The SPM concentrations of such degree were observed in the fjords of the Svalbard Archipelago too; in the Kongsfjorden in 1999, the concentrations on the surface were more than 400 mg/L near the glacier edge and 2-3 mg/L in

the outer part of the bay [13], in the Hornsund Bay in July 2002 the values were 12.1–19.5 mg/L [37], and in the Grøn fjorden in 2001-2002 summers they reached 25.4 mg/L [12]. In the Adventfjorden tidal flat, the SPM concentration in the July 2002 was 911.3 mg/L, and it decreased sharply as the distance from the river mouth increased [9]. The distribution on the surface of the area and on the vertical is similar to the Novaya Zemlya bays.

The investigations have shown a good comparability between the optical measurements and data on natural SPM concentration. The spatial distribution of SPM on the sea surface obtained from the data of the SeaWiFS ocean color scanner agrees with the field in situ data (the correlation coefficient is equal to 0.91) [35]. The regression equation was calculated as

$$C_{\text{spm}} = 73.5b_{\text{bp}}(550) + 0.016, \quad (1)$$

where C_{spm} is SPM concentrations (mg/L), b_{bp} is index of backscattering by the suspended matter (m^{-1}), calculated using the algorithm [35].

For vertical distribution of SPM in the Arctic, the presence of two maximums is typical: in the surface and (not always) in near-bottom (nepheloid) layers [3], but in our investigations in the bay the appreciable increasing was not observed in the bays (Figure 4). We have added the optical

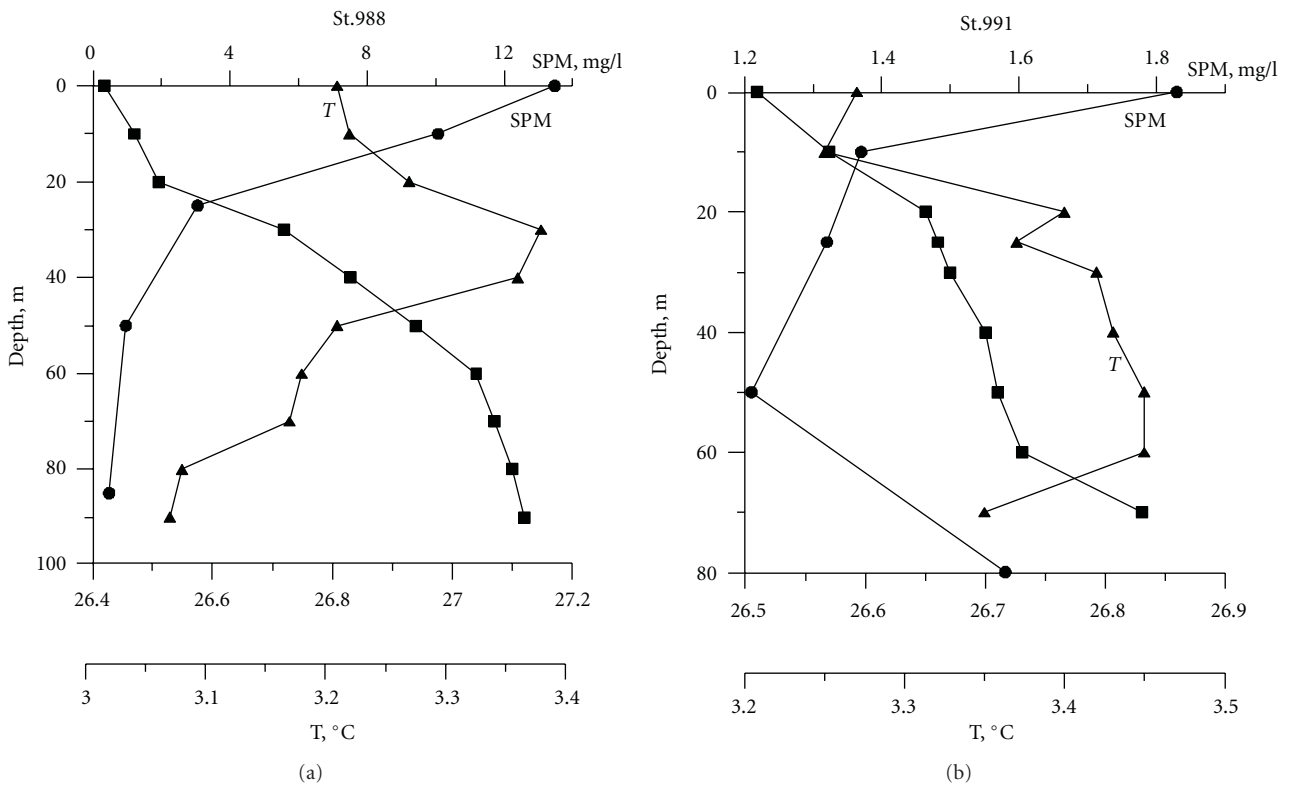


FIGURE 4: Vertical distribution of parameters of the water column on some stations in Russkaya Gavan' bay: SPM: concentration of the suspended particulate matter, mg/L (circles); T: temperature (triangles), °C; σ : water density (square box).

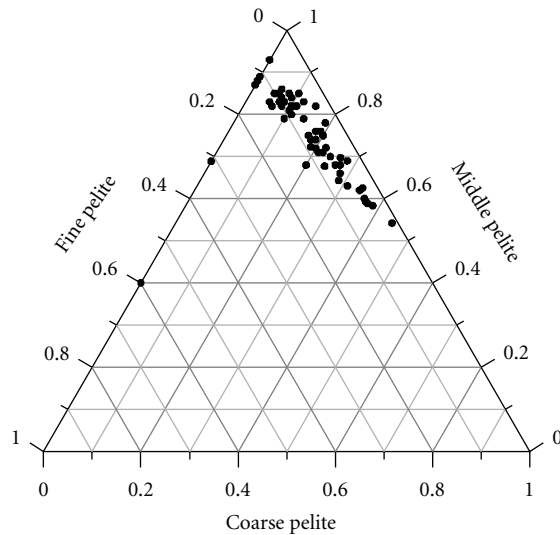


FIGURE 5: Granulometric composition of the pelitic fraction of SPM in the Russkaya Gavan' Bay (Table 3): fine pelite ($<1 \mu\text{m}$), middle pelite (5– $1 \mu\text{m}$) and coarse pelite (10– $5 \mu\text{m}$).

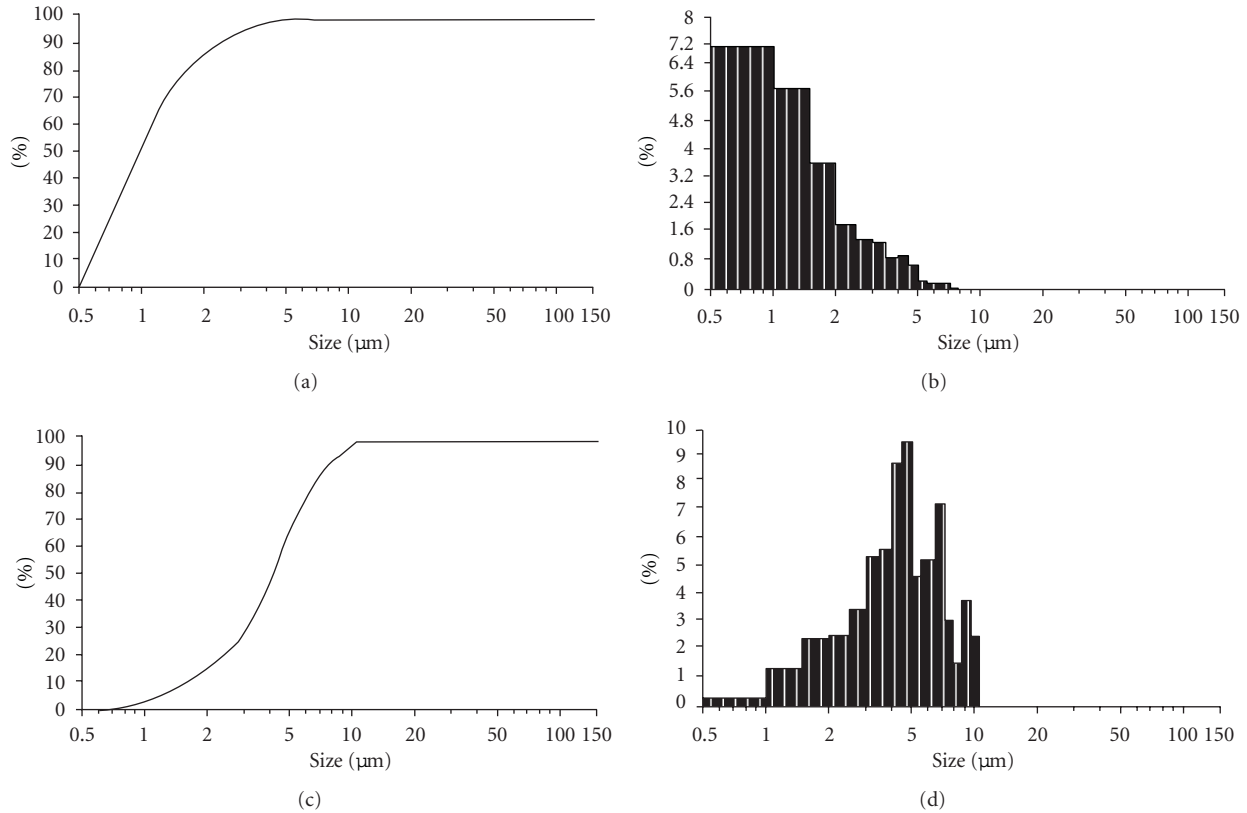


FIGURE 6: Granulometric composition of the surface SPM on the st. 985 (Russkaya Gavan' Bay): (a) accumulation curve of the counting concentration of the particles; (b) histogram of the counting concentration of the particles; (c) accumulation curve of the particle's volume distribution; (d) histogram of the particle's volume distribution.

scanning of the water column to the sampling on the definite depths, and the regression equation was calculated as

$$C_{\text{spm}} = 1.66\varepsilon - 0.145, \quad (2)$$

where C_{spm} is SPM concentrations (mg/L), ε is attenuation coefficient (m^{-1}) [36]. The correlation between SPM concentration and beam attenuation coefficient was 0.94 for more than 100 measurements.

3.2. Composition of the SPM. The granulometric composition of the suspended matter is mainly pelitic. The size of the particles is 1–5 μm (middle pelitic fraction) (Figures 5 and 6, Table 3). In the outer parts of the bays, the size of the particles has grown probably because of the increase of the biogenic component of the suspended matter.

The lithogenic particles prevailed in the composition of the suspended matter in the coastal zone and in the bays (Figure 7(a)). In the direction to the open sea, the role of the biogenic component of the suspended matter (phytoplankton—such as diatoms, dinoflagellates) increases (Figure 7(b)) [38, 39]. Surface phytoplankton in the Russkaya Gavan' Bay was very poor (average numbers concentration was 365 cells/L and biomass -4.2 mg/m^3), and it had gone to the autumn stage of development

[40]. Dinoflagellates were the most numerical group (46%), and diatoms had only 18%. Only some cells had chromatophores (*Chaetoceros decipiens*, *Pterosperma undulata*, *Protoperdinium bipes*, and *P. brevipes*). The concentration of diatom cells with chromatophores ("living cells") was equal to the number of empty valves (65–50 cells/L). Conditions for algae life are bad here because high contents of mineral suspended matter coming from glaciers. Similar situations with the plankton impoverishment of the water in the fjords with glaciers were described in the Spitsbergen fjords [41–43].

3.3. Vertical Particle Fluxes. The location of the mooring stations with the sediment traps is shown on Figure 8. Low values of the particle fluxes (from 5.8 to $17.7 \text{ mg m}^{-2} \text{ d}^{-1}$) and particulate organic carbon fluxes (from 0.5 to $1.59 \text{ mg C m}^{-2} \text{ d}^{-1}$) from the euphotic zone were measured in the open sea, which is evidence for an ultraoligotrophic character of the studied area [44] during the time of expedition. Much higher particle fluxes were registered in the outer part of Russkaya Gavan' Bay, Novaya Zemlya Archipelago (up to $7660 \text{ mg m}^{-2} \text{ d}^{-1}$), and in the Karskie Vorota Strait (up to $2040 \text{ mg m}^{-2} \text{ d}^{-1}$).

Particle flux at the station ASV-5 in the Russkaya Gavan' Bay ($76^\circ 16' \text{N}$, $62^\circ 27.1' \text{E}$, water depth 104 m) at 70 m was

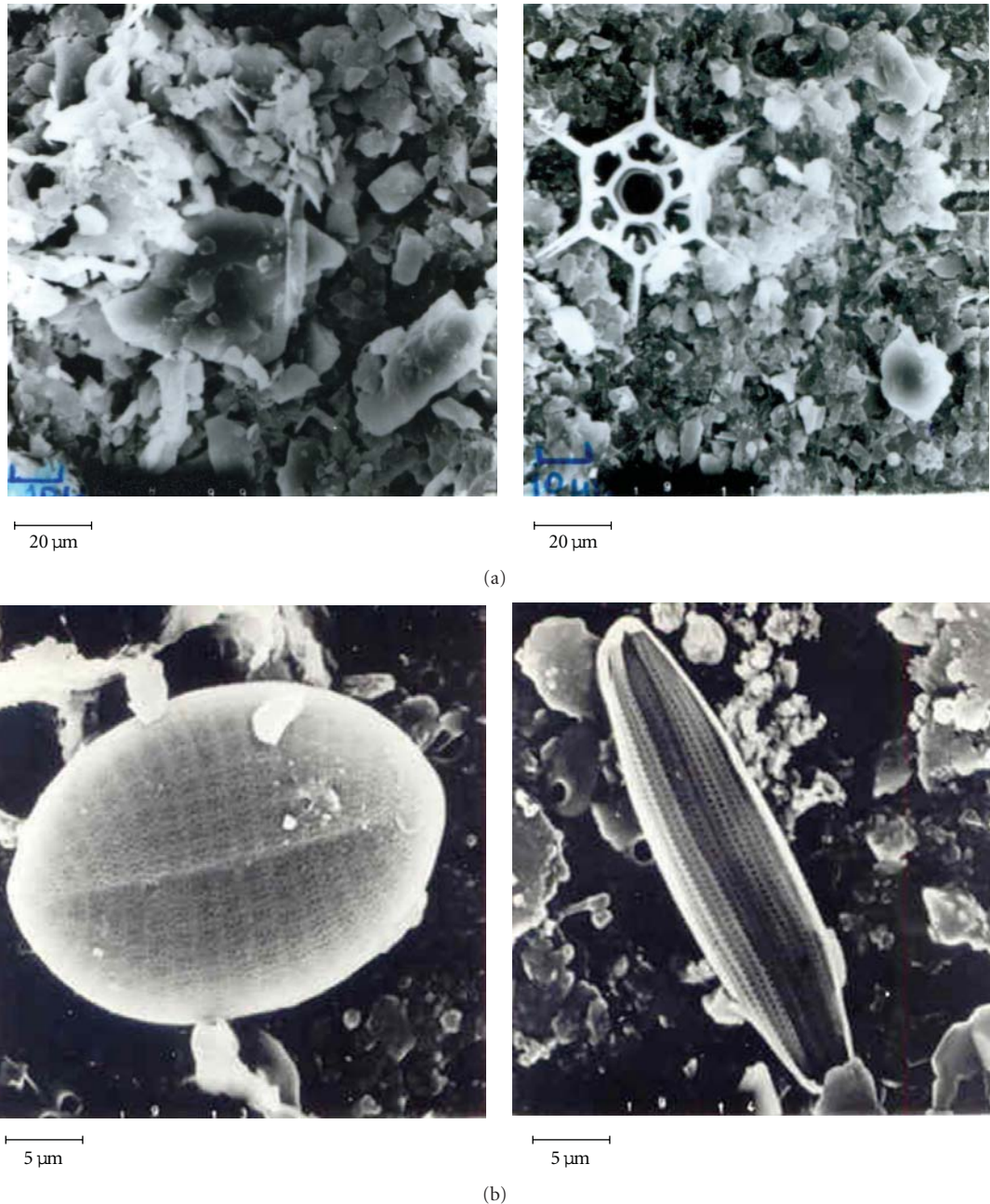


FIGURE 7: The composition of the suspended matter: (a) lithogenic part; (b) biogenic part.

$346 \text{ mg m}^{-2} \text{ d}^{-1}$, and organic carbon flux was 2.47% . Particle flux at 85 m depth (19 m above the sea bottom) at this station was $7660 \text{ mg m}^{-2} \text{ d}^{-1}$. Particulate matter collected by sediment traps in the open sea areas consisted mainly of amorphous aggregates (“marine snow”) and pellets of Crustacea (Figure 9). In the bays sedimentary matter consisted mainly of mineral grains, only few empty diatom valves were found here. Conditions for algae life is bad here because of the high contents of mineral suspended matter coming from the land.

The high values of the vertical particle fluxes were described in fjords of Spitsbergen: Kongsbreene (933000

$\text{mg m}^{-2} \text{ d}^{-1}$) near the melting glacier [45], Adventfjorden (over $1000000 \text{ mg m}^{-2} \text{ d}^{-1}$) at the front of the river mouth [9], and Greenfjorden $-180000 \text{ mg m}^{-2} \text{ d}^{-1}$ in 2005–2009 summers [14, 46]. The high rates of the sedimentation were marked in the fjords of the polar archipelagoes [47]. So, the suspended matter of the fjords is mainly deposited in the bay or near the outlet. The investigations in similar fjords of Alaska [48] showed that the sedimentation of the mainly volume of the suspended matter from the glaciers is occurred in the fjord or not far from the bay, only occasionally the undercooled near-bottom waters bring them into the deeper areas.

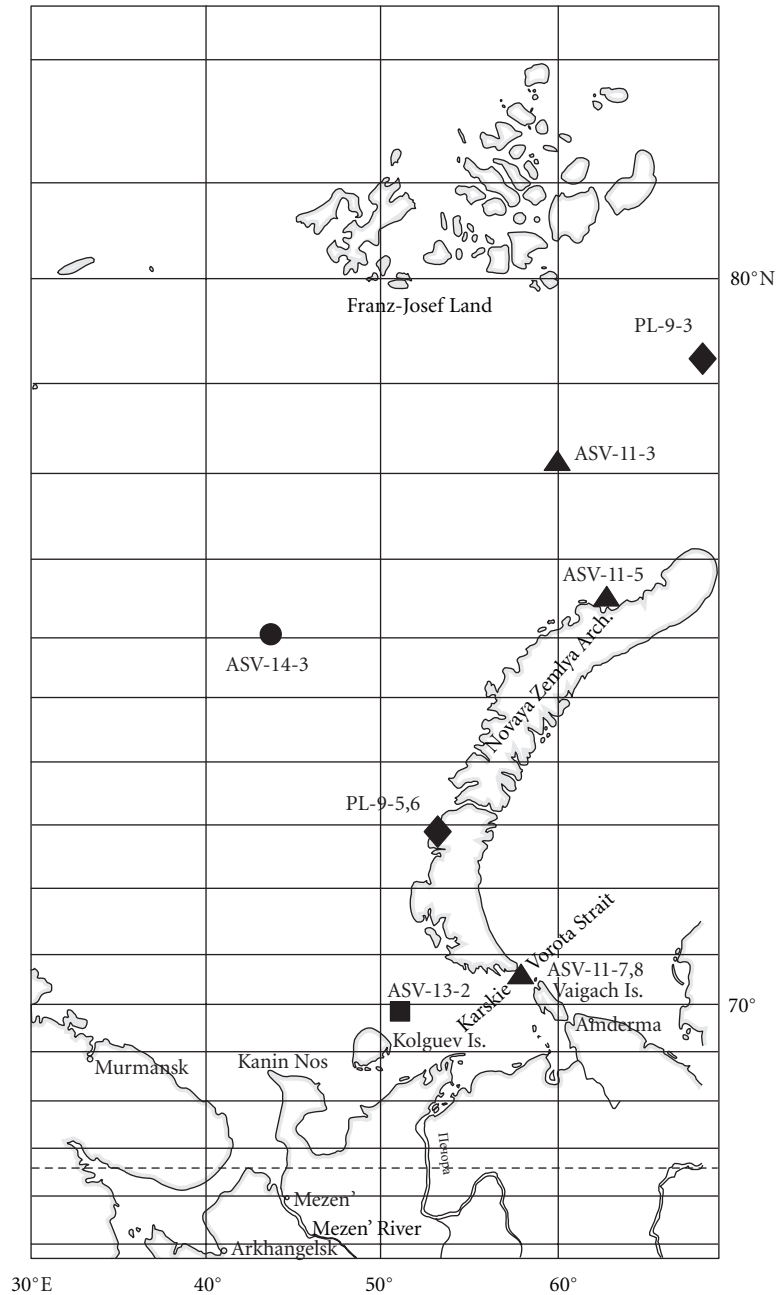


FIGURE 8: The location of the mooring stations with sediment traps: rectangle: 9th cruise of RV “Professor Logachev,” 1994; triangles: 11th cruise of RV “Akademik Sergey Vavilov,” 1997; square: 13th cruise of RV “Akademik Sergey Vavilov,” 1998; circle: 14th cruise of RV “Akademik Sergey Vavilov,” 1998 (Table 2).

4. Conclusions

In general, on the archipelagos and islands of the Barents Sea SPM mostly deposits in bays (fjords), and only small part of it is delivered to the open sea because of the hydrodynamic conditions in the bays, the large size of the particles, flocculation, and morphological barriers in the relief on the enter of the bays [49]. It is important for ecological purposes to know the ways of migration of the SPM with pollutants from bays to the open sea. Our investigations allowed us to

say that the bays of the Novaya Zemlya Archipelago are the traps for the suspended matter from the glaciers and coast abrasion, and the pollutants from the Novaya Zemlya will stay in the bays.

Acknowledgments

The studies were supported by Russian Fund of Basic Research (Grant 11-05-00087), Russian Ministry for the

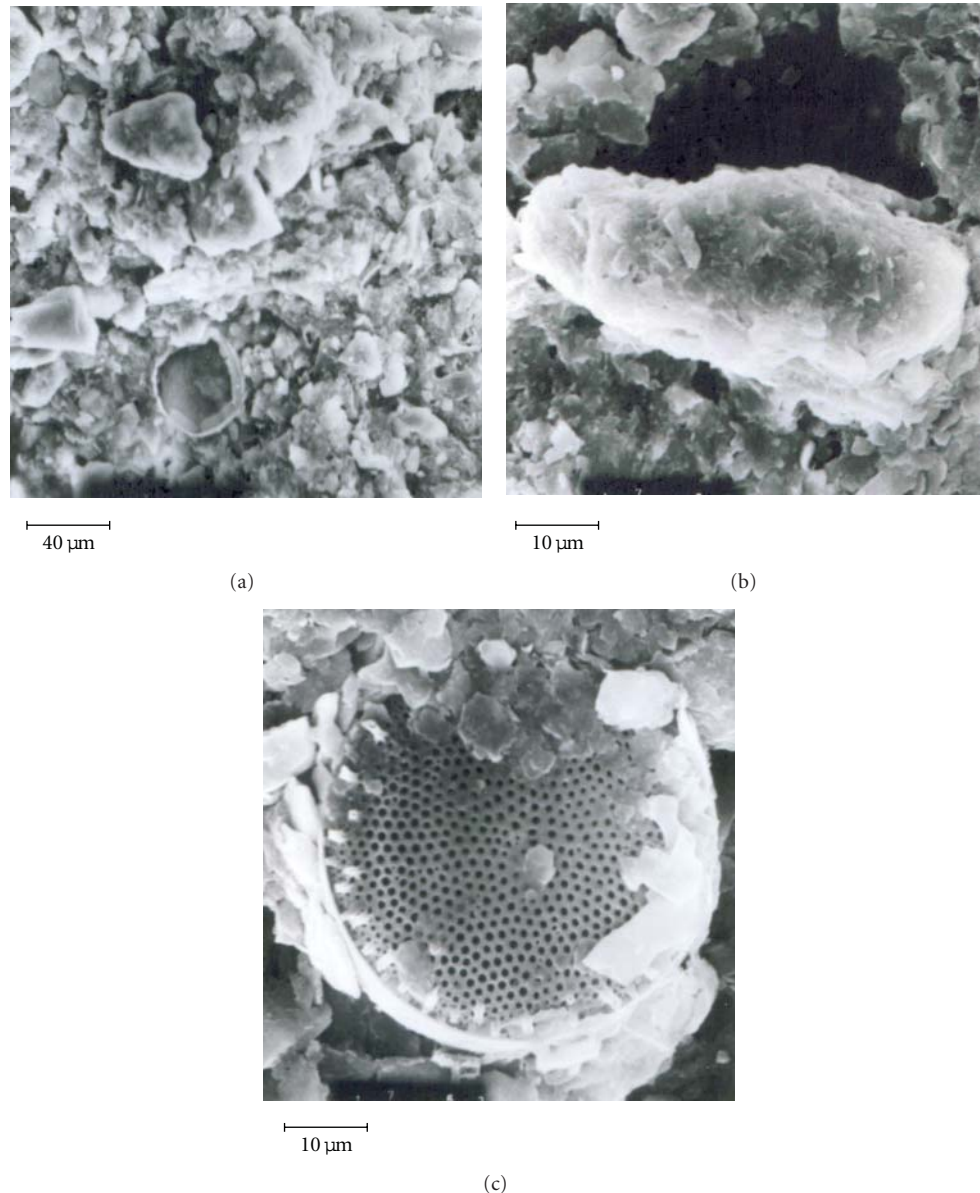


FIGURE 9: The composition of the particulate matter in the sediment trap collected in Russkaya Gavan' Bay: (a) general view; (b) pellet; (c) diatom debris.

Education and the Science (Grant NSh-3714.2010.5), and the Earth Sciences Department of Russian Academy of Sciences (Project "Nanoparticles in the Earth's geospheres"). The practical help of masters and crews of the RV "Professor Logachev" and "Akademik Sergey Vavilov" is acknowledged. The authors are grateful to Academician A. P. Lisitzin, G. I. Ivanov, N. A. Aibulatov, R. Stein, and P. V. Boyarsky for support.

References

- [1] N. A. Aibulatov, *Dynamics of the Particulate Matter in the Shelf Zone*, Hydrometeoizdat, Leningrad, Russia, 1990.
- [2] A. P. Lisitzin, *Oceanic Sedimentation. Lithology and Geochemistry*, American Geophysical Union, Washington, DC, USA, 1996.
- [3] A. P. Lisitzin, V. P. Shevchenko, and V. I. Burenkov, "Hydrooptics and suspended matter of Arctic Seas," *Atmospheric and Oceanic Optics*, vol. 13, pp. 61–71, 2000.
- [4] N. A. Aibulatov, *Geoecology of Shelf and Coasts of Russian Seas*, Noosphera, Moscow, Russia, 2001.
- [5] A. Elverhøi, S. L. Pfirman, A. Solheim, and B. B. Larssen, "Glaciomarine sedimentation in epicontinental seas exemplified by the northern Barents Sea," *Marine Geology*, vol. 85, no. 2–4, pp. 225–250, 1989.
- [6] V. S. Medvedev and E. M. Potekhina, "Export of terrigenous suspended material by Novaya Zemlya glaciers into the

- Barents Sea,” in *Modern Sedimentogenesis in Shelves of the World Ocean*, N. A. Aibulatov, Ed., pp. 103–110, Nauka, Moscow, Russia, 1990.
- [7] G. G. Matishov, *Environment and Ecosystems of Novaya Zemlya*, The Archipelago and the Shelf, Kola Science Centre Publication, Apatity, Russia, 1995.
- [8] R. Hodgkins, “Glacier hydrology in Svalbard, Norwegian High Arctic,” *Quaternary Science Reviews*, vol. 16, no. 9, pp. 957–973, 1997.
- [9] M. Zajaczkowski and M. Włodarska-Kowalczyk, “Dynamic sedimentary environments of an Arctic glacier-fed river estuary (Adventfjorden, Svalbard). I. Flux, deposition, and sediment dynamics,” *Estuarine, Coastal and Shelf Science*, vol. 74, no. 1-2, pp. 285–296, 2007.
- [10] J. P. M. Syvitski and J. W. Murray, “Particle interaction in fjord suspended sediment,” *Marine Geology*, vol. 39, no. 3-4, pp. 215–242, 1981.
- [11] A. G. Lewis and J. P. M. Syvitski, “The interaction of plankton and suspended sediment in fjords,” *Sedimentary Geology*, vol. 36, no. 2–4, pp. 81–92, 1983.
- [12] M. V. Mityaev, I. A. Pogodina, and M. V. Gerasimova, “Facies variability of recent sediments in the Hornsund Fjord, western Spitsbergen,” *Lithology and Mineral Resources*, vol. 40, no. 5, pp. 401–407, 2005.
- [13] B. V. Ivanov, A. K. Pavlov, and J.-B. Orbaek, “Investigations of concentration of the suspended particles in the Kongsfjorden, Spitsbergen Archipelago,” in *Multidisciplinary Investigations of the Spitsbergen Nature*, Proceedings of VII International Conference, pp. 156–164, Apatity, Russia, 2007.
- [14] G. A. Tarasov and O. V. Kokin, “On the investigation of the particle fluxes in the Gronfjord,” in *Marine Investigations of the Polar regions of the Earth in the International Polar Year 2007/08*, Proceedings of International conference, pp. 84–85, St.-Petersburg, Russia, 2010.
- [15] L. L. Demina, “Methods of the suspended particle matter separation,” in *Modern Methods of the Hydrochemical Investigations of the Ocean*, O. K. Bordovskii and A. M. Chernyakova, Eds., pp. 7–13, Moscow, Russia, 1992.
- [16] S. A. Korsun, *Scientific Report of MMBI Expedition “Yasnogorsk’95”*, Marine Biological and Geological Studies off Novaya Zemlya Glaciers and in St. Anna Trough, Kola Science Centre Publication, Apatity, Russia, 1996.
- [17] V. P. Shevchenko, M. V. Gerasimova, S. A. Korsun, V. V. Serova, G. A. Tarasov, and A. A. Filippova, “Quantitative distribution and composition of water suspension in the impact area of glaciers of Novaya Zemlya, Northern Island,” in *Biological Processes and Evolution of Marine Ecosystems under Conditions of Oceanic Periglacial*, Abstracts of International Conference, p. 71, Murmansk, Russia, October 1996.
- [18] V. P. Shevchenko, G. I. Ivanov, S. S. Shanin, and E. A. Romankevich, “The distribution of total suspended matter and particulate organic carbon in the St. Anna Trough and in the Barents Sea,” *Berichte zur Polarforschung*, vol. 342, pp. 55–67, 1999.
- [19] V. P. Shevchenko, N. V. Politova, G. I. Ivanov et al., “Suspended sediment distribution and vertical particle fluxes in western bays of the Novaya Zemlya archipelago and Vaigach Island,” *Berichte zur Polar- und Meeresforschung*, no. 482, pp. 134–141, 2004.
- [20] S. Korsun and M. Hald, “Modern benthic foraminifera off Novaya Zemlya tidewater glaciers, Russian Arctic,” *Arctic and Alpine Research*, vol. 30, no. 1, pp. 61–77, 1998.
- [21] K. Gorlich, J. M. Weslawski, and M. Zajaczkowski, “Suspension settling effect on macrobenthos biomass distribution in the Hornsund fjord, Spitsbergen,” *Polar Research*, vol. 5, no. 2, pp. 175–192, 1987.
- [22] N. A. Aibulatov, *An Ecological Response of the Cold War’s Impact in the Russian Arctic Seas*, GEOS, Moscow, Russia, 2000.
- [23] S. Honjo, “Particle fluxes and modern sedimentation in the polar oceans,” in *Polar Oceanography. Part B: Chemistry, Biology and Geology*, W. O. Smith, Ed., pp. 687–739, 1990.
- [24] P. Wassmann, R. Martinez, and M. Vernet, “Respiration and biochemical composition of sedimenting organic matter during summer in the Barents Sea,” *Continental Shelf Research*, vol. 14, no. 1, pp. 79–90, 1994.
- [25] P. Wassmann, E. Bauerfeind, M. Fortier et al., “Particulate organic carbon flux to the Arctic Ocean sea floor,” in *The Organic Carbon Cycle in the Arctic Ocean*, R. Stein and R. W. Macdonald, Eds., pp. 101–138, Springer, Berlin, Germany, 2004.
- [26] B. von Bodungen, A. Antia, E. Bauerfeind et al., “Pelagic processes and vertical flux of particles: an overview of a long-term comparative study in the Norwegian Sea and Greenland Sea,” *Geologische Rundschau*, vol. 84, no. 1, pp. 11–27, 1995.
- [27] I. Andreassen, E. M. Nothig, and P. Wassmann, “Vertical particle flux on the shelf off northern Spitsbergen, Norway,” *Marine Ecology Progress Series*, vol. 137, no. 1–3, pp. 215–228, 1996.
- [28] V. N. Lukashin, M. E. Vinogradov, V. Yu. Gordeev, and V. Yu. Rusakov, “Sedimentary material streams in the Norwegian Sea: data from the year-round sediment-trapping station,” *Transactions (Doklady) of the Russian Academy of Sciences. Earth Science Sections*, vol. 349, no. 5, pp. 844–847, 1996.
- [29] E. Bauerfeind, C. Garrity, M. Krumbholz, R. O. Ramseier, and M. Voß, “Seasonal variability of sediment trap collections in the Northeast Water Polynya. Part 2. Biochemical and microscopic composition of sedimenting matter,” *Journal of Marine Systems*, vol. 10, no. 1–4, pp. 371–389, 1997.
- [30] M. Reigstad, C. Wexels Riser, P. Wassmann, and T. Ratkova, “Vertical export of particulate organic carbon: attenuation, composition and loss rates in the northern Barents Sea,” *Deep-Sea Research II*, vol. 55, no. 20-21, pp. 2308–2319, 2008.
- [31] A. P. Lisitsyn, V. P. Shevchenko, M. E. Vinogradov, O. V. Severina, V. V. Vavilova, and I. N. Mitskevich, “Particle fluxes in the Kara Sea and Ob and Yenisey estuaries,” *Oceanology*, vol. 34, no. 5, pp. 683–693, 1995.
- [32] G. I. Ivanov, V. P. Shevchenko, E. E. Musatov, T. V. Ponomarenko, A. A. Svertilov, and A. V. Nesheretov, “Multidisciplinary research on the Svyataya Anna Trough (the Kara Sea),” *Oceanology*, vol. 37, pp. 632–634, 1997.
- [33] V. P. Shevchenko, G. I. Ivanov, A. A. Burovkin et al., “Sedimentary material flows in the St. Anna Trough and eastern Barents Sea,” *Doklady Earth Sciences*, vol. 359, no. 3, pp. 400–403, 1998.
- [34] V. P. Shevchenko, G. I. Ivanov, and V. V. Zernova, “Vertical particle fluxes in the St. Anna Trough and in the Eastern Barents Sea in August-September 1994,” *Berichte zur Polarforschung*, vol. 342, pp. 46–54, 1999.
- [35] V. I. Burenkov, S. V. Ershova, O. V. Kopelevich, S. V. Sheberstov, and V. P. Shevchenko, “An estimate of the distribution of suspended matter in the Barents Sea waters on the basis of the SeaWiFS satellite ocean color scanner,” *Oceanology*, vol. 41, no. 5, pp. 622–628, 2001.
- [36] N. A. Aibulatov, V. A. Matyushenko, V. P. Shevchenko, N. V. Politova, and E. M. Potekhina, “New data on the transverse structure of lateral suspended matter fluxes along the margins of the Barents Sea,” *Geoecologiya*, vol. 6, pp. 526–540, 1999 (Russian).

- [37] M. V. Mityaev and M. V. Gerasimova, "Facies variability of recent sediments in the Hornsunn fjord (Western Spitsbergen)," in *Multidisciplinary Investigations of the Spitsbergen Nature*, Proceedings of III International conference, pp. 99–108, Apatity, Russia, 2003.
- [38] V. V. Zernova, V. P. Shevchenko, and N. V. Politova, "Features of the phytoecene structure of the Barents Sea over a meridional section at 37°–40°E (September 1997)," *Oceanology*, vol. 43, no. 3, pp. 395–403, 2003.
- [39] V. Y. Rusakov, A. P. Lisitsyn, S. S. Izotova, A. S. Moskalev, A. O. Gizenko, and F. Rahold, "Distribution and mineral composition of particulate matter in the Franz Victoria Trough (Northern Barents Sea)," *Oceanology*, vol. 44, no. 2, pp. 247–256, 2004.
- [40] V. V. Zernova, V. P. Shevchenko, and N. V. Politova, "Phytoplankton and vertical microalgae fluxes in the north-eastern part of the Barents Sea in September 1997," in *Experience of System Oceanologic Studies in the Arctic*, Lisitzin A. P., Vinogradov M. E., and Romankevich E. A., Eds., pp. 301–316, Scientific World, Moscow, Russia, 2001.
- [41] A. Keck, J. Wiktor, R. Hapter, and R. Nilsen, "Phytoplankton assemblages related to physical gradients in an Arctic, glacier-fed fjord in summer," *ICES Journal of Marine Science*, vol. 56, pp. 203–214, 1999.
- [42] Y. B. Okolodkov, B. Yu, R. Hapter, and S. V. Semovski, "Phytoplankton in Kongsfjorden, Spitsbergen, July 1996," *Sarsia*, vol. 85, no. 4, pp. 345–352, 2000.
- [43] J. Wiktor and K. Wojciechowska, "Differences in taxonomic composition of summer phytoplankton in two fjords of West Spitsbergen, Svalbard," *Polish Polar Research*, vol. 26, no. 4, pp. 259–268, 2005.
- [44] V. P. Shevchenko, A. P. Lisitzin, V. V. Zernova et al., "Vertical particle fluxes in seas of the western Russian Arctic," in *Proceedings of the Humanity and the World Ocean: Interdependence at the Dawn of the New Millennium (PACON '99)*, pp. 239–249, Moscow, Russia, June 2000.
- [45] M. Zajackowski, "On the use of sediment traps in sedimentation measurements in glaciated fjords," *Polish Polar Research*, vol. 23, no. 2, pp. 161–174, 2002.
- [46] G. A. Tarasov, "New data on the particle fluxes in the Gronfjord (Western Spitsbergen)," in *Complex Investigation of the Spitsbergen Nature*, Abstracts of IV International Conference, pp. 151–159, Apatity, Russia, 2004.
- [47] A. Elverhoi, O. Lonne, and R. Seland, "Glaciomarine sedimentation in a modern fjord environment, Spitsbergen," *Polar Research*, vol. 1, no. 2, pp. 127–150, 1983.
- [48] R. A. Feely, G. D. Cline, G. J. Massoth et al., "Composition, transport and deposition of suspended matter in lower Cook inlet and Shelikof Strait, Alaska," *Environmental Assessment of the Alaskan Continental Shelf Annual Report*, vol. 5, pp. 195–263, 1979.
- [49] N. N. Dunaev, O. V. Levchenko, L. R. Merklin, and Yu. A. Pavlidis, "The Novaya Zemlya shelf in the late Quaternary," *Oceanology*, vol. 35, no. 3, pp. 407–416, 1995.

Research Article

Climatology of Total Cloudiness in the Arctic: An Intercomparison of Observations and Reanalyses

Alexander Chernokulsky and Igor I. Mokhov

*A.M. Obukhov Institute of Atmospheric Physics, Russian Academy of Sciences,
3 Pyzhevsky, Moscow 119017, Russia*

Correspondence should be addressed to Alexander Chernokulsky, chern_av@ifaran.ru

Received 15 September 2011; Revised 25 December 2011; Accepted 10 January 2012

Academic Editor: Irina Repina

Copyright © 2012 A. Chernokulsky and I. I. Mokhov. This is an open access article distributed under the Creative Commons Attribution License, which permits unrestricted use, distribution, and reproduction in any medium, provided the original work is properly cited.

Total cloud fraction over the Arctic (north of 60°N) has been evaluated and intercompared based on 16 Arctic cloud climatologies from different satellite and surface observations and reanalyses. The Arctic annual-mean total cloud fraction is about 0.70 ± 0.03 according to different observational data. It is greater over the ocean (0.74 ± 0.04) and less over land (0.67 ± 0.03). Different observations for total cloud fraction are in a better agreement in summer than in winter and over the ocean than over land. An interannual variability is higher in winter than in summer according to all observations. The Arctic total cloud fraction has a prominent annual cycle according to most of the observations. The time of its maximum concurs with the time of the sea ice extent minimum (early summer–late autumn) and vice versa (late spring). The main reason for the discrepancies among observations is the difference in the cloud-detection algorithms, especially when clouds are detected over the ice/snow surface (during the whole year) or over the regions with the presence of strong low-tropospheric temperature inversions (mostly in winter). Generally, reanalyses are not in a close agreement with satellite and surface observations of cloudiness in the Arctic.

1. Introduction

The Arctic is a very sensitive region to the global climate change [1–4]. As pointed out in the Intergovernmental Panel on Climate Change Fourth Assessment Report [2], surface air temperature in the Arctic increased in the beginning of the 21st century by 1.0–1.5 K compared to 1970s. This rate is approximately twice that of the entire Earth. According to the estimations with the global climate models (GCMs), the Arctic surface temperature may increase by 4–7 K to the end of the 21st century compared with the end of the 20th century [1, 2]. An increase of air temperature is accompanied by changes in other climate variables [1, 4, 5], particularly, a decrease of the Arctic sea ice extent [1, 6, 7] and cloud cover changes [8–10].

Clouds play the key role in the Earth's climate system by regulating the radiation budget of the planet through reflecting shortwave radiation coming from the sun and redistributing longwave radiation coming from the Earth

surface [11, 12]. Clouds of different layers have different influence on the radiation budget. High- and mid-level cloudiness tend to warm the atmosphere by strengthening and greenhouse effect, and low-level cloudiness tends to cool atmosphere by the increase of the albedo. Additionally, cloud radiative forcing (the difference between radiation fluxes in clear sky and cloudy conditions, CRF) strongly depends on season and the time of day. Generally, in the extratropical latitudes, CRF is positive in winter (at night) and negative in summer (during the daytime). The regional magnitude of CRF can reach 100 W/m^2 [13–15]. As a whole, cloudiness has a global cooling effect [11], but in the Arctic region, clouds slightly enhance surface cooling only for a few weeks in the midsummer and have a warming effect in the rest of the year [14, 16–18].

The sensitivity of CRF is about 1 W/m^2 per 1% of cloud cover in the Arctic [18]. Thus, relatively a small percentage of changes in cloud cover or cloud properties could result in an anomalous climate forcing of several

W/m². By using model simulations, Vavrus [19] showed that the positive cloud feedback may enhance the Arctic warming up to 40% under CO₂ doubling. This result is partially corroborated by the observations [20]. Cloud amount has increased in the Arctic during spring, summer, and autumn in the last decades according to satellite [8, 9] and surface [10, 21] observations, which can be indicated on a small positive feedback. However, satellite and surface observations disagree on winter cloudiness trends. According to model simulations, cloudiness will increase in high latitudes in the 21st century [22, 23].

Considering the importance of clouds in the Arctic, it is crucial to know exactly when and where clouds exist. However, the detection of clouds in the Arctic is intrinsically difficult. Clouds in the Arctic are mostly optically thin and low-lying [10, 16], and they have a little thermal and visible contrast with the underlying surface, which makes them hard to be observed from satellite mostly in winter [7, 24, 25]. The main obstacle to reliable surface observations in the Arctic is a very sparse network of ground-based observations especially over Greenland and over the Arctic Ocean [26]. In addition, visual observations are more reliable during daytime than during nighttime [27]. Several studies on an intercomparison of cloud climatologies indicate the polar regions as the regions with the largest discrepancies among observational data [28–33]. Similar conclusions were done for reanalyses and GCMs simulations [15, 34–39].

Major research programs such as Atmospheric Radiation Measurement program (ARM) [40], yearlong Surface Heat Budget of the Arctic (SHEBA) program, and, associated with it, First International Satellite Cloud Climatology Program (ISCCP) Regional Experiment (FIRE) [41–43] aimed to improve our knowledge about the Arctic atmosphere and climate and to help optimize satellite retrievals for the Arctic. Particularly, comparisons between data from these programs and satellite-derived or reanalyses data were performed in a number of studies (e.g., [15, 44, 45]). Additionally, satellites with active sensors like lidar on CALIPSO and ICESat [46, 47] and radar on CLOUDSAT and EarthCARE [48] have been launched in the recent years. Data provided with these satellites (or merged products like GeoPROF [49]) can improve our understanding of cloud vertical structure. However, these data are limited by 82°N and still too short (especially compared to an extremely narrow swath) for obtaining an adequate cloud climatology in the Arctic.

Here, we intercompare 16 cloud climatologies based on up-to-date satellite and surface observations and modern reanalyses in the Arctic region north of 60°N. Description of datasets is given in the Section 2. We present the results of a comparative analysis in Section 3 and discuss these results in Section 4.

2. Data

In this study, we used cloud information from up-to-date satellite and surface observations and global reanalyses data. These data are described in Sections 2.1, 2.2, and 2.3, respectively. Brief information on data is given in Table 1.

2.1. Satellite Observations

2.1.1. APP-x. The Advanced Very High Resolution Radiometer (AVHRR) Polar Pathfinder product (APP) was performed specially for polar regions [50, 51]. Cloudiness is derived from the Cloud And Surface Parameter Retrieval (CASPR) system [52] based on twice-a-day measurements in 5 spectral channels (with the central wavelengths of 0.63, 0.86, 3.75, 10.8, and 12 μm) by the AVHRR sensors which are flown on-board NOAA polar-orbiting (Low Earth Orbit) satellites (LEO). The combination of spectral and temporal uniformity tests is used in cloud mask algorithm [52]. According to several studies [44, 51], APP data has a good agreement with data from the SHEBA and FIRE field experiments. The extended version of APP (APP-x) was used in this study. Data provide information on polar cloudiness from January 1982 to December 2004 at a 25 km spatial resolution.

2.1.2. CERES. The main aim of the Clouds and Earth's Radiant Energy System (CERES) is an examination of the role of the cloud-radiation feedbacks in the climate system [53] by providing the simultaneous retrievals of cloud properties and broadband radiative fluxes from the instruments on two LEOs, Terra and Aqua, from the Earth Observing System. Terra satellite was launched in December 1999 and has a 10:30/22:30 local time (LT) equatorial crossing. Aqua satellite provides information from early summer 2002 and crosses the equator at 01:30/13:30 LT. Cloud properties are determined using measurements by the Moderate Resolution Imaging Spectroradiometer (MODIS). MODIS provides measurements in 36 spectral channels [54]. Five of them (with the central wavelengths of 0.64, 1.6 (Terra) or 2.1 (Aqua), 3.7, 11, and 12 μm) are used in the CERES cloud mask [55]. Series of the spectral threshold tests (different between night and day) are used to determine cloudiness. In this study, the Single Scanner Footprint (SSF) product edition 2.5 was used. Data span the period from February 2000 (July 2002) to February 2010 for Terra (Aqua) satellite and come gridded on a regular 1-degree grid.

2.1.3. ISCCP. The International Satellite Cloud Climatology Project (ISCCP) was established in 1982 to collect and to analyze satellite radiance measurements for inferring spatial and temporal structure of clouds [56]. ISCCP involves measurements from weather geostationary satellites (GEO) (like GMS, GOES East, GOES West, Meteosat, MTSAT, and INSAT) and NOAA LEO satellites. Radiance data from a visible (0.8 μm) and infrared (11 μm) channels were obtained every 3 hours and then performed by the ISCCP Global Processing Center [57]. Data are intercalibrated between GEO and LEO satellites. Information on cloudiness characteristics is derived by using the spectral threshold test and a combination of the spatial and temporal uniformity tests [57]. We used the D2 product in this study [58]. Data are presented on a regular 2.5-degree grid and available from July 1983 to June 2008.

2.1.4. MODIS. A complete description of the MODIS cloud mask algorithm is given by Ackerman et al. [59]. Instead of

TABLE 1: Cloudiness data information.

Short name	Dataset Full name	Time period	Data resolution
<i>Satellite observations</i>			
APP-x	Extended Advanced very high-resolution radiometer (AVHRR) Polar Pathfinder Product	01/1982–12/2004	25 km
CERES Terra CERES Aqua	Clouds and the Earth’s Radiant Energy System SSF Product Edition 2.5 (board on Terra and Aqua)	02/2000–02/2010 07/2002–02/2010	1°
ISCCP	International Satellite Cloud Climatology Project D2 Product	07/1983–06/2008	2.5°
MODIS Terra MODIS Aqua	Moderate-Resolution Imaging Spectroradiometer series 5 product (board on Terra and Aqua)	02/2000–12/2009 07/2002–12/2009	1°
PATMOS-x	AVHRR Pathfinder Atmosphere extended (version 5)	01/1982–12/2009	1°
<i>Surface observations</i>			
EECRA	Extended Edited Cloud Report Archive	01/1971–12/1996	5°
<i>Reanalyses data</i>			
ERA-40 ERA-Interim	European Centre for Medium-Range Weather Forecasts (ECMWF) Reanalyses	01/1979–08/2002 01/1989–12/2009	2.5° 1.5°
JRA-25	Japan Meteorological Agency Reanalysis	01/1979–12/2009	2.5°
NASA-MERRA	National Aeronautics and Space Administration (NASA) Modern Era Reanalysis for Research and Applications	01/1979–03/2009	0.5°
NCEP-CFSR	National Centers for Environmental Prediction (NCEP) Climate Forecast System Reanalysis	01/1979–12/2009	0.5°
NCEP/DOE	NCEP/Department of Energy	01/1979–01/2008	~1.9° (Gaussian)
NCEP/NCAR	NCEP/National Center for Atmospheric Research	01/1979–12/2008	~1.9° (Gaussian)
NOAA-CIRES 20CR	National Oceanic and Atmospheric Administration-Cooperative Institute for Research in Environmental Sciences (NOAA-CIRES) 20th Century Reanalysis	01/1979–12/2008	~1.9° (Gaussian)

the CERES algorithm, 14 of 36 spectral channels of MODIS instruments are used to derive cloudiness characteristics (2 visible, 4 near infrared, and 8 infrared channels). The MODIS cloud mask algorithm includes series of the spectral threshold tests and a combination of the spatial and temporal uniformity tests. Additional tests are applied specially for the polar regions [25]. Cloud data from the collection 5 [60] were used in this study. These data are in a good agreement with active lidar and radar observations [61]. Data span the period from February 2000 (July 2002) to December 2009 for Terra (Aqua) satellite and come gridded on a regular 1-degree grid.

2.1.5. PATMOS-x. The Pathfinder Atmosphere extended (PATMOS-x) cloudiness dataset is the longest one that based on satellite measurements (AVHRR sensors on NOAA LEO). We used the PATMOS-x version 5 in this study [62]. Data are presented on a regular 1-degree grid and available from January 1982 to December 2009. The Naive Bayesian methodology has been applied in the PATMOS-x version 5. Under this methodology, the cloud mask tests were reformulated as the Bayesian classifiers. An analysis of collocated LEO NOAA-18 and CALIPSO observations [47]

was used to automatically and globally derive 6 Bayesian classifiers. They are computed separately for 7 surface types used in the final algorithm. These classifiers come from the clouds from AVHRR extended (CLAVR-x) cloud mask algorithm [63] based on series of spectral threshold tests. A complete description of these data is given by Heidinger et al. [62].

Table 2 presents summarized information on the satellite observations and the cloud mask algorithms.

2.2. Surface Observations

2.2.1. EECRA. The Extended Edited Cloud Report Archive (EECRA) is a global cloud climatology derived from surface synoptic weather reports based on visual observations from ships and land meteorological stations [64]. Cloudiness observations are made visually by human observers every three or six hours. In this study, we used data from EECRA E-series, which are presented on a regular 5-degree grid [26] and cover the period from January 1972 to December 1996. These data include only weather reports which passed a series of quality-control checks, like the “moonlight criterion” [26, 65], the data homogeneity, and so forth.

TABLE 2: Satellite-based datasets information.

Dataset	Satellite	Spectral channels(visible (VIS), near infrared (NIR), infrared (IR))	Time of observations (local time)	Instrument resolution / swath (km)	Cloud detection algorithm
APP-x	LEO (NOAA)	1 VIS + 1 NIR + 3 IR	~14:00, 2:00	1–4 / ~3000	A combination of the spectral and temporal uniformity tests which are tuned specially for the polar regions [52].
CERES	LEO (Terra, Aqua)	1 VIS + 1 NIR + 3 IR	10:30, 22:30 (Terra) 01:30, 13:30 (Aqua)	0,25–1 / 2330	Series of the spectral threshold tests (different between night and day) [55].
ISCCP	GEO + LEO (NOAA)	1 VIS + 1 IR	every 3 hour	4–7 / —	The spectral threshold test and a combination of the spatial and temporal uniformity tests [57].
MODIS	LEO (Terra, Aqua)	1 VIS + 1 NIR + 3 IR	10:30, 22:30 (Terra) 01:30, 13:30 (Aqua)	0,25–1 / 2330	Series of the spectral threshold tests and a combination of the spatial and temporal uniformity tests. Special tests for the polar regions [59, 60].
PATMOS-x	LEO (NOAA)	1 VIS + 1 NIR + 3 IR	14:00, 2:00	1–4 / ~3000	CLAVR-x (series of the spectral threshold tests) + Naïve Bayesian methodology [62].

2.3. Reanalyses Data. Reanalyses are a synthesis of the observations and model physics. Reanalyses assimilate different observations of the key atmospheric variables and provide historical gridded fields for the whole atmosphere state at any given time (usually every 6 hours). We used information on cloudiness from 8 global reanalyses in our intercomparison (Tables 1 and 3). The following observations are assimilated in the majority of reanalyses: surface pressure from weather stations reports; surface pressure, temperature, humidity and wind from ship and buoys; upper-air wind, temperature and humidity from radiosondes, dropsondes, and balloons; temperature- and humidity-sensitive radiance from satellite-borne instruments; wind and temperature from aircrafts; cloud-tracked winds from geostationary satellites [66, 67]. New reanalyses (like NASA-MERRA, NCEP-CFSR, and ERA-Interim) assimilate additional satellite-derived information like ozone profiles or oceanic wave height [68, 69], whilst the NOAA-CIRES 20CR reanalysis is based only on pressure data [70].

Different reanalyses have different cloud prediction schemes. In particular, a diagnostic scheme where clouds are parameterized based on an empirical relationship with relative humidity is used in NCEP/NCAR and NCEP/DOE reanalyses. Convective cloudiness is derived from the convective precipitation rate [66, 71, 72]. In JRA-25 reanalysis, cloud fraction is estimated diagnostically from total water mixing ratio and liquid water potential temperature [73, 74]. In NCEP-CFSR, NASA-MERRA, and NOAA-CIRES 20CR reanalyses, cloud cover is derived from cloud condensate which is a prognostic variable with a simple cloud microphysics [69, 70, 75, 76]. A fully prognostic approach for cloud fraction due to the mass balance equations for cloud water/ice and cloud air is applied only in the European reanalyses [15, 67, 68, 77]. The method of the cloud overlap assumption is an additional factor that contributes

to differences in the cloud representations in different reanalyses [15]. For instance, the random cloud overlap is used in NCEP/NCAR reanalysis, while the maximum/random overlap is used in NCEP-CFSR reanalysis [69]. It should have noted that none of the reanalyses assimilate cloud fraction directly from observations.

Table 3 presents summarized information about reanalyses data.

Here, we analyzed monthly means of total cloud fraction with annual and seasonal averaging. All individual climatologies were obtained by averaging for time periods that are pointed out in Table 1.

3. Results

3.1. Annual and Seasonal Means Total Cloud Fraction. Annual and seasonal means total cloud fraction (TCF) from different data over the Arctic is shown in Figure 1. According to observations, the annual-mean TCF (Figure 1(a)) varies between 0.67 ± 0.01 for CERES Aqua and 0.73 ± 0.03 for APP-x data. According to all observations, the annual mean TCF is greater over the ocean (between 0.70 ± 0.02 for CERES Terra and 0.78 ± 0.03 for PATMOS-x) than over land (between 0.64 ± 0.01 for CERES Aqua and 0.70 ± 0.03 for APP-x data). According to reanalyses, the annual mean TCF varies in wider range from 0.48 ± 0.01 for NCEP/NCAR to 0.88 ± 0.01 for 20CR. NASA-MERRA reanalysis has the best fit to observations with annual mean TCF equal to 0.71 ± 0.01 . In general, reanalyses have lower value of the interannual standard deviation of TCF than observations, which indicate to lower interannual variability in reanalyses compared to observations.

In winter (Figure 1(b)), observations demonstrate worse agreement among each other. Winter mean TCF varies from

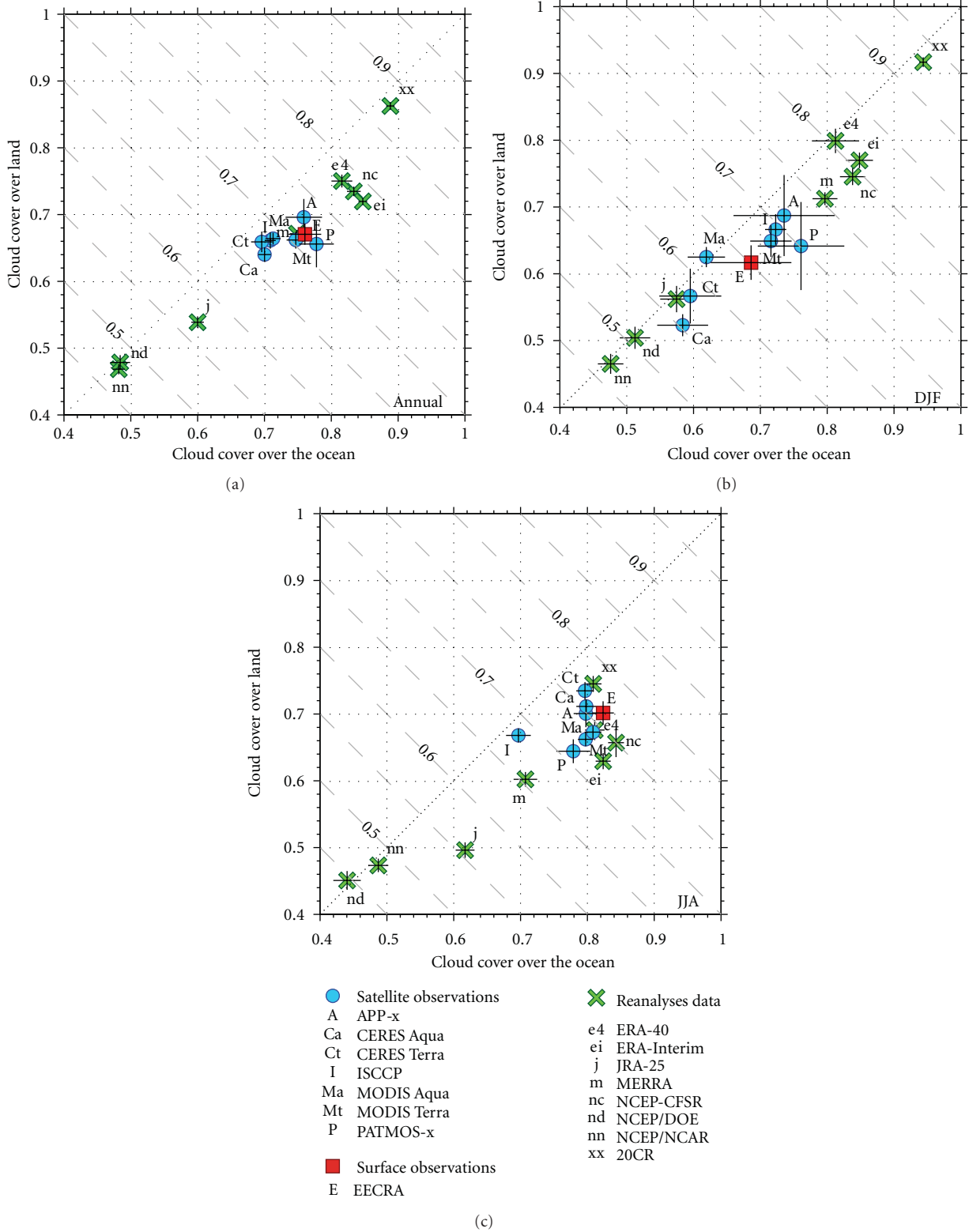


FIGURE 1: Annual (a), December-January-February (b), and June-July-August (c) mean of TCF over the Arctic (north of 60° N) from different data. The error bars correspond to the standard deviation (in the interannual variability) of each data (separately for land and the ocean). The abscissa corresponds to TCF over the ocean, and the ordinate corresponds to TCF over land. The inclined long-dashed lines correspond to TCF over land and the ocean (their slope is equal to the land-ocean ratio in the Arctic).

TABLE 3: Reanalyses information.

Dataset	Atmospheric model and its resolution/data assimilation method/reanalysis features	Predictors for cloud fraction
ERA-40 [67]	ECMWF cy13r4 T159 (80 km) L60 6 hr/3D VAR	Cloud fraction is fully prognostic (due to the mass balance equations for cloud water/ice and cloud air) [77]
ERA-Interim [68]	ECMWF cy29r1 T255 (50 km) L60 6 hr/4D VAR/weather station observations and new satellite data are assimilated	The same as for ERA-40 with several important modifications [68]
JRA-25 [74]	JMA/CRIEPI T160 (120 km) L40 6 hr/3D VAR	Water mixing ratio and the liquid water potential temperature [73]
NASA-MERRA [76]	GEOS-5 50 km L72 6 hr/3D VAR/new satellite data are assimilated	Prognostic cloud and a single-phase condensate with two species of condensate: “anvil” (originating from detraining convection) and large scale [78]
NCEP-CFSR [69]	NCEP GSI T382 (32 km) L64 6 hr/3D VAR/atmospheric model is coupled with the ocean, land, and sea ice analysis	Prognostic cloud condensate, water mixing ratio, and the liquid water potential temperature [73, 78]
NCEP/DOE [72] NCEP/NCAR [66]	NCEP T62 (210 km) L28 6hr / 3D VAR	Relative humidity (empirical relationship), prognostic convective precipitation rate [71]
NOAA-CIRES 20CR [70]	NCEP GFS T62 (210 km) L28 6 hr/ensemble Kalman filter/only surface pressure is assimilated	Prognostic cloud condensate, water mixing ratio, and the liquid water potential temperature [73, 78]

0.55 ± 0.02 for CERES Aqua to 0.71 ± 0.07 for APP-x. MODIS Aqua is only the one dataset that shows more TCF over land than over the ocean. In general, TCF over land is between 0.52 ± 0.02 (for CERES Aqua) and 0.68 ± 0.06 (for APP-x), and TCF over the ocean is between 0.58 ± 0.04 (for CERES Aqua) and 0.76 ± 0.06 (for PATMOS-x). According to JRA-25 reanalysis, TCF fits this range. It is less (about 0.5) according to NCEP/NCAR and NCEP/DOE and greater according to other reanalyses (up to 0.93 ± 0.01 for NOAA-CIRES 20CR). The reverse is true for summer (Figure 1(c)) when reanalyses show less TCF than observations (or equal to them). Observations are in a better agreement in summer than in winter, especially over the ocean where TCF is close to 0.8 except for ISCCP (0.7 ± 0.02). Over land, summer mean TCF varies from 0.64 ± 0.02 (for PATMOS-x) to 0.82 ± 0.02 (for EECRA). Over the entire Arctic, summer mean TCF is between 0.68 ± 0.01 (for ISCCP) and 0.76 ± 0.01 (for CERES Terra).

Interannual variability is higher in winter (its standard deviation is up to 0.07 over land and up to 0.08 over the ocean) than in summer (its interannual standard deviation does not exceed 0.3) according to all observation-derived data. However, the interannual variability almost does not depend on season according to reanalyses, which may indicate that high winter variability of observation-derived TCF is partly associated with uncertainties in observations [8, 79].

3.2. Annual Cycle of Total Cloud Fraction. Figure 2 shows annual cycle of TCF over the Arctic. The maximum of TCF is noted at the end of polar day (August–September), and its time concurs with the time of the minimum of the sea ice extent in the Arctic [45, 51]. The minimum of TCF is noted at the end of polar night (February–April) (Figure 2(a)).

According to the most of observations, the Arctic land-mean TCF has a prominent annual cycle (Figure 2(b)) with the maximum in August–October (0.64–0.78) and the minimum in December–March (0.50–0.68). According to CERES Aqua, land-mean TCF has the highest amplitude of annual cycle (close to 0.3). Annual cycle of cloudiness over the ocean (Figure 2(c)) is also prominent. High values of ocean-mean TCF are noted from May to October (about 0.8 excluding ISCCP). Low values are noted from November to April (0.55–0.75). However, months with the maximum (or the minimum) varied between different data. For instance, it is June for APP-x, July for CERES Terra, August for MODIS (Terra and Aqua), and September for EECRA (Figure 2(c)). According to Curry et al. [16], the summer maximum is associated with low-level stratiform cloudiness, while in winter cyclones-induced upper-level clouds dominate (see also [10]).

Meanwhile, the annual cycle of TCF according to PATMOS-x and ISCCP data is not revealed clearly. According to PATMOS-x, it has two maximums (in May and in September) and two minimums (in July and in December–March). Presumably, this may be associated with an overestimation of stratiform clouds (as shown in [10], these clouds also have the annual distribution with two minimums and two maximums) and an underestimation of the other cloud types. According to ISCCP, land-mean TCF is 0.66, and ocean-mean TCF is 0.71 during the whole year. As pointed out by Schweiger et al. [80], ISCCP is in a better agreement with surface observations in summer (with 10–20% underestimation) and in a worse agreement in winter mostly because of a systematic positive bias in surface temperature retrieval.

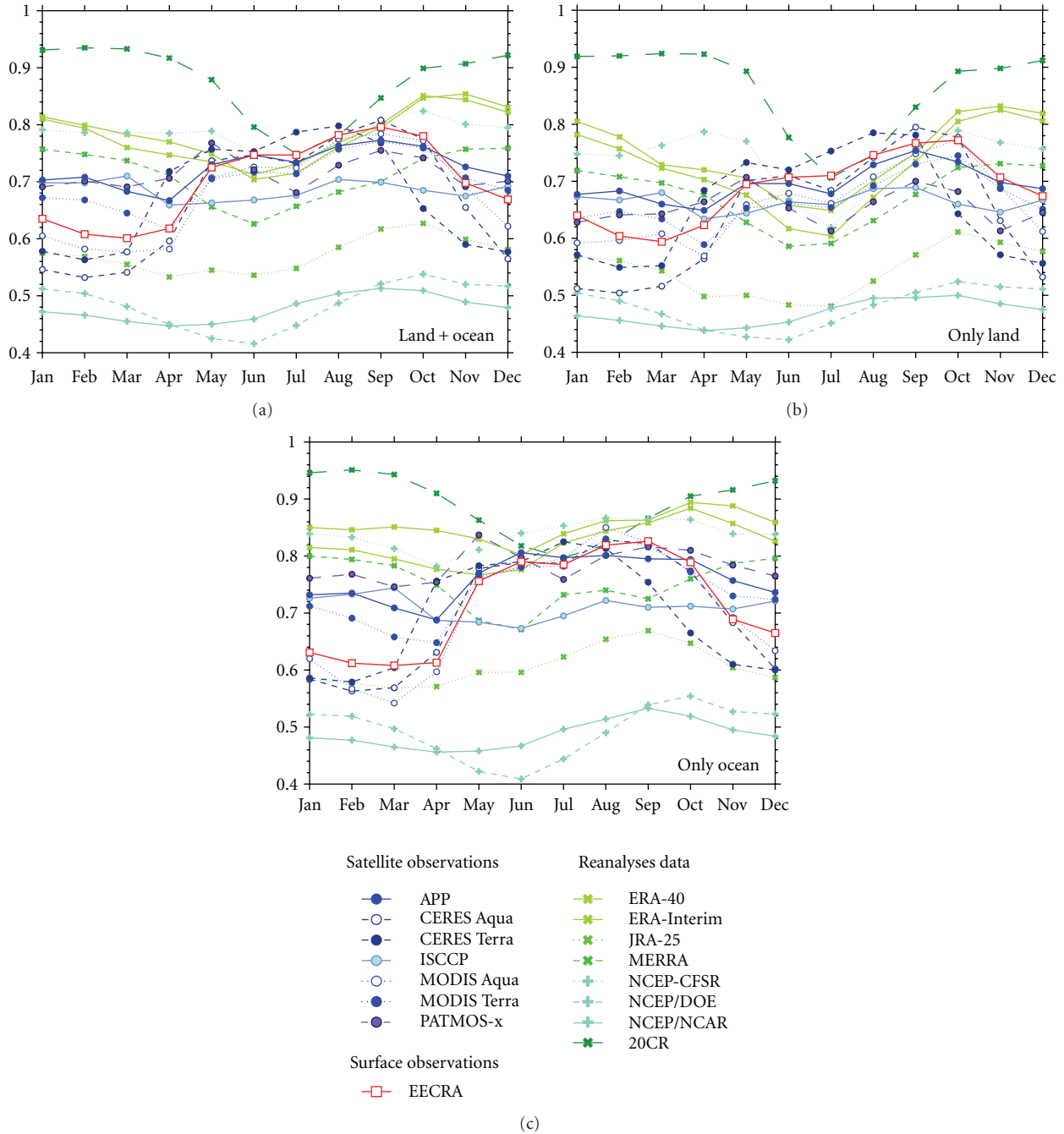


FIGURE 2: The annual cycle of TCF averaging over the entire Arctic (a), only over land (b), and over the ocean (c).

According to reanalyses, the annual cycle of TCF does not match well with the observational one. Closer agreement between most of reanalyses and observations in TCF values is noted during the sunlit part of the year (see also Figure 1(c)). NCEP/NCAR, NCEP/DOE, and JRA-25 reanalyses show lower values of TCF during the whole year. In general, according to reanalyses, the annual cycle of TCF is shifted by 1-2 months compared to observations. It has the minimum in early summer (June-July) and reaches the maximum in late autumn-early winter (from

October to January). NOAA-CIRES 20CR reanalysis (which is based on pressure data only [70]) shows the worst agreement with observations.

3.3. *Intercomparison of Total Cloud Fraction Spatial Distribution.* Spatial distribution of the annual mean TCF (not shown) is associated with the spatial distribution of the annual mean surface skin temperature. According to all observations, the annual mean TCF minimum occurs over the northeastern part of Greenland (it varies from 0.4 for

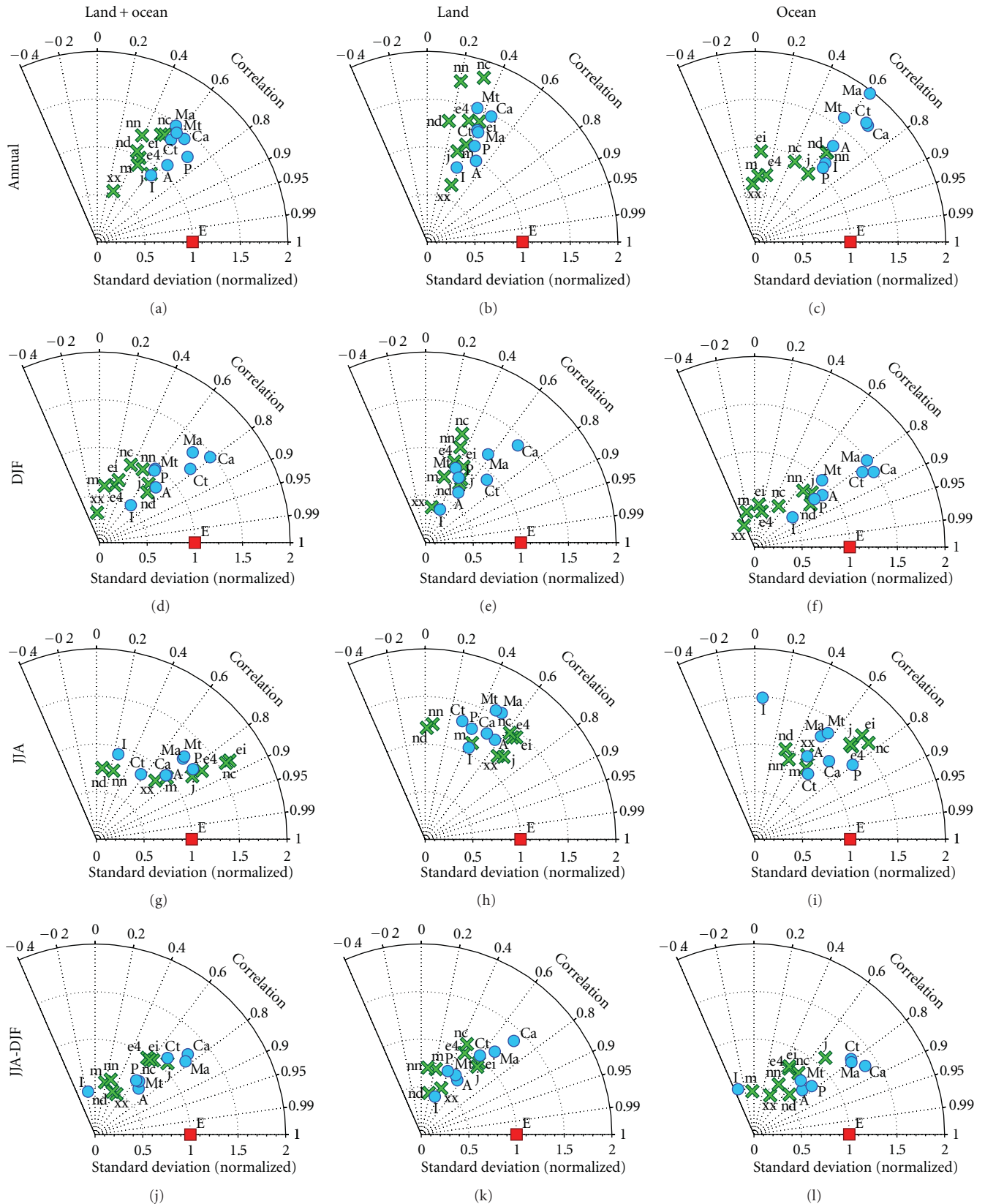


FIGURE 3: Normalized pattern statistics showing differences among different observational and reanalyses TCF spatial distribution (the reference data is surface-derived data EECRA) over the entire Arctic (a, d, g, j), only land (b, e, h, k), and only the ocean (c, f, i, l) for annual means (a, b, c), December-January-February (DJF) means (d, e, f), June-July-August (JJA) means (g, h, i), and seasonal differences (JJA-DJF) (j, k, l). The radial distances from the origin are proportional to the spatial standard deviation (SSTD) of each data (normalized to EECRA SSTD). The spatial correlation between EECRA and other data is given by the azimuthal position. Acronyms are the same as for Figure 1.

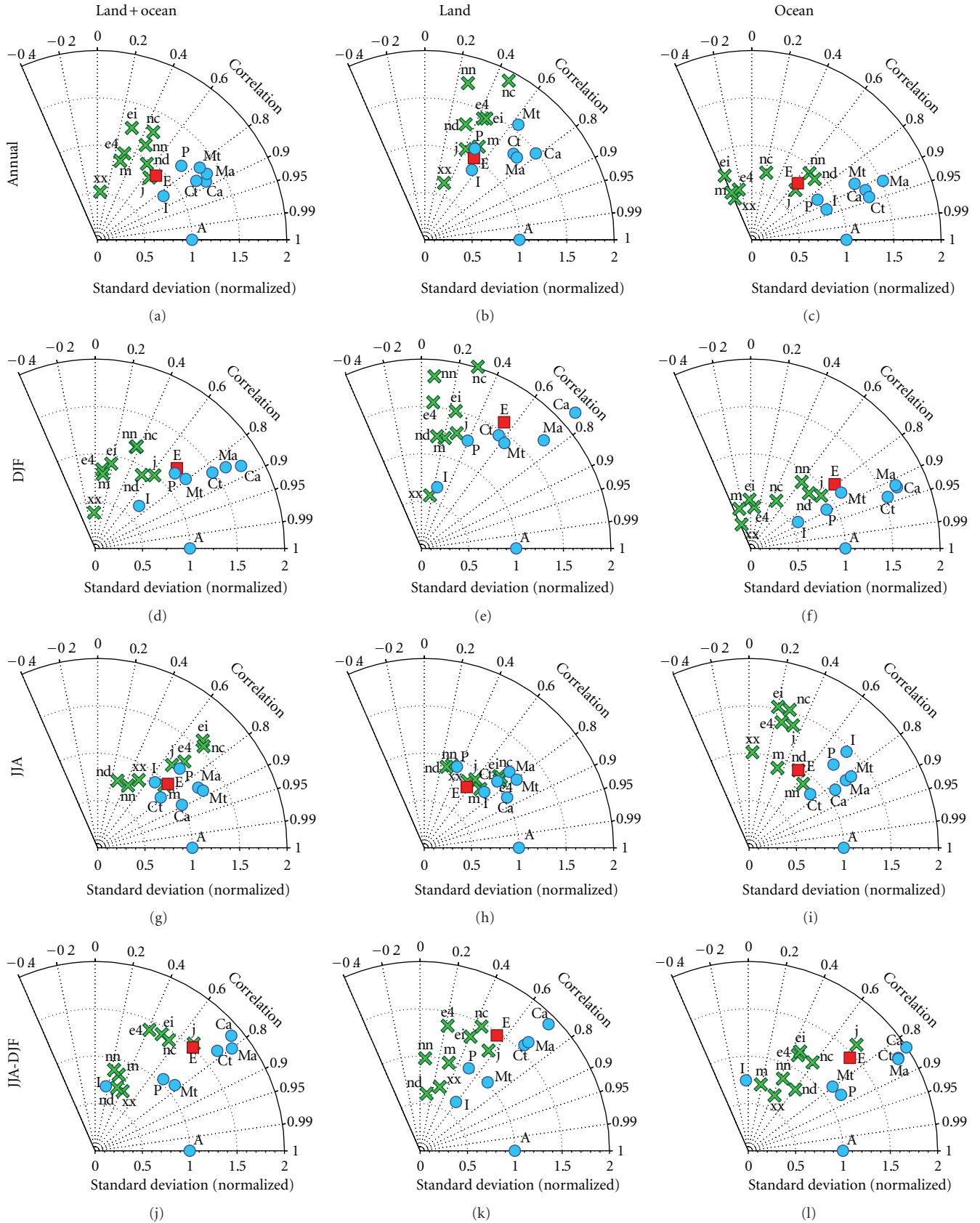


FIGURE 4: The same as Figure 3 but with satellite-derived APP-x as the reference data.

MODIS Terra to 0.6 for APP-x) and collocates with the skin surface temperature minimum (it is down to -30°C [51]). Reanalyses also show the minimum of TCF over Greenland (it varies from 0.2 for NCEP/NCAR to 0.8 for NOAA CIRES 20CR). The highest value of the annual mean TCF is over the warmest part of the Arctic (The Norwegian and Barents Sea). It is from 0.8–0.85 for EECRA and ISCCP to 0.9–1.0 according to other data. This high value of TCF is somewhat captured in reanalyses. They produce low values of the annual mean TCF over northern Eurasia, the Canadian Arctic archipelago, Alaska, and the Canadian part of the Arctic Ocean (particularly, over the Beaufort Sea) and high values over northern Europe, the Baffin Sea, and the central part of the Arctic Ocean. ERA-40, ERA-Interim, NASA-MERRA, and NOAA-CIRES 20CR reanalyses show the highest values of TCF over the central part of the Arctic Ocean but not over the Norwegian and Barents Sea as observations do.

To make a simultaneous intercomparison of the TCF spatial distribution from all data, we apply an approach that was introduced by Taylor [81]. All data were bilinearly interpolated to the uniform grid (EECRA grid with 5-degree resolution was chosen). In this approach, different data are spatially correlated with the particular data that are presupposed to be the reference data. EECRA (Figure 3) and APP-x (Figure 4) data were chosen as the reference data for this analysis which was performed separately for annual and seasonal means, for the entire Arctic, only for the ocean, and only for land.

In general, satellite data show a closer agreement with each other than with surface observations. Coefficient of spatial correlation (R) between EECRA data and others (RE) varies from 0.5 to 0.7 for the annual mean TCF. RE is higher over the ocean (0.5–0.8) than over land (0.3–0.7) and nearly the same for different seasons. The coefficient of spatial correlation between APP-x data and others (RA) varies from 0.7 to 0.9. RA for the annual mean TCF is higher over the ocean than over land (as well as RE). Over the ocean, RA is 0.6 for EECRA and 0.85–0.95 for satellite-derived data. It is from 0.5 to 0.8 over land. Besides, RA for TCF over the ocean is higher in winter, and RA for TCF over land is higher in summer. This is presumably due to a mosaic structure of the underneath surface which depends on the season in an opposite manner for land and for the ocean. The ocean is covered by the ice during winter and is partially open in summer. In contrast, land is free from snow in summer (excluding Greenland) and is partially covered by snow in winter.

ISCCP has the worst agreement with other observations. Particularly RE for ISCCP is negative for seasonal difference over land and over the ocean. RA for ISCCP is negative over the ocean and close to zero over land. However, ISCCP shows nearly the same values of spatial standard deviation (SSTD) of TCF as EECRA and APP-x. In general, short-period datasets like CERES and MODIS show higher SSTD than long-period datasets.

Reanalyses reproduce SSTD of TCF comparable to observations during summer over the entire Arctic. However, reanalyses show lower values of SSTD of ocean-mean TCF

than observations during the winter. The values of RE and RA for reanalyses are between 0.2 and 0.4 over land. This range is wider over the ocean (from 0 to 0.6). The European reanalyses and NOAA-CIRES 20CR have negative values of RA and RE over the ocean. During winter, RE and RA are also negative for NASA-MERRA reanalysis. Generally, reanalyses and observations are in closer agreement on the spatial distribution of TCF in summer than in winter. JRA-25 reanalysis shows the best agreement with observations on the spatial distribution of TCF among all reanalyses.

3.4. Reasons for Data Discrepancies. Differences among various observations may be due to several reasons. First of all, these are differences in instruments and in cloud detection algorithms. Especially these differences are crucial under harsh arctic conditions where the snow/ice surface and the presence of low-troposphere inversions lead to very low thermal and radiance contrasts between clouds and underneath surface. Liu et al. [79] compared arctic cloudiness from MODIS and GeoPROF data (based on simultaneous lidar and radar observations from A-Train satellites CALIPSO and CloudSat) and found out that passive satellite observations can underestimate cloudiness by 10–20% over the snow/ice surface under nighttime conditions. Thus, a decrease of the sea ice extent could lead to an appearance of an instrumental cloudiness trend in long-term datasets. Alongside with real cloudiness trends, it also can contribute to differences obtained in our analysis because of the different averaging period chosen for different data (Table 1). Due to diurnal cycle of cloudiness, different time of observations may also influence data discrepancies [33, 82]. According to [82], the differences between only-noon observations and four-times-a-day observations can reach 10% in tropics and do not exceed 5% in the Arctic. Differences in reanalyses mostly depend on different cloud prediction schemes, and methods of cloud overlap assumption [15].

To elucidate the main reason for data discrepancies, it is crucial to single out the regions with poor agreement among data. To reveal these regions, we interpolated all observations to the uniform grid (the robust EECRA grid was chosen). Annual and seasonal means of TCF were calculated for each observation-derived data and after that inter-data means and inter-data standard deviations of these individual means were obtained in each grid cell. Reanalyses were excluded from this analysis. Resulting values of the inter-data standard deviation (ISTD) in each grid cell are depicted in Figure 5.

We found the highest annual mean ISTD over Greenland and over the Arctic Ocean (particularly over the Canadian part) (Figure 5(a)). Meanwhile, over northern Eurasia and North America, ISTD is low, which indicates a good agreement among different data. In addition, ISTD is, respectively, low in regions with the dramatic sea ice extent loss such as the Beaufort Sea and Baffin Sea and the western part of the Greenland Sea [7].

For wintertime and for seasonal difference (Figures 5(b) and 5(d)), the highest values of ISTD are over the Canadian part of the Arctic Ocean and northeastern Eurasia (up to 0.2). According to Liu et al. [83] and Devasthale et al. [84],

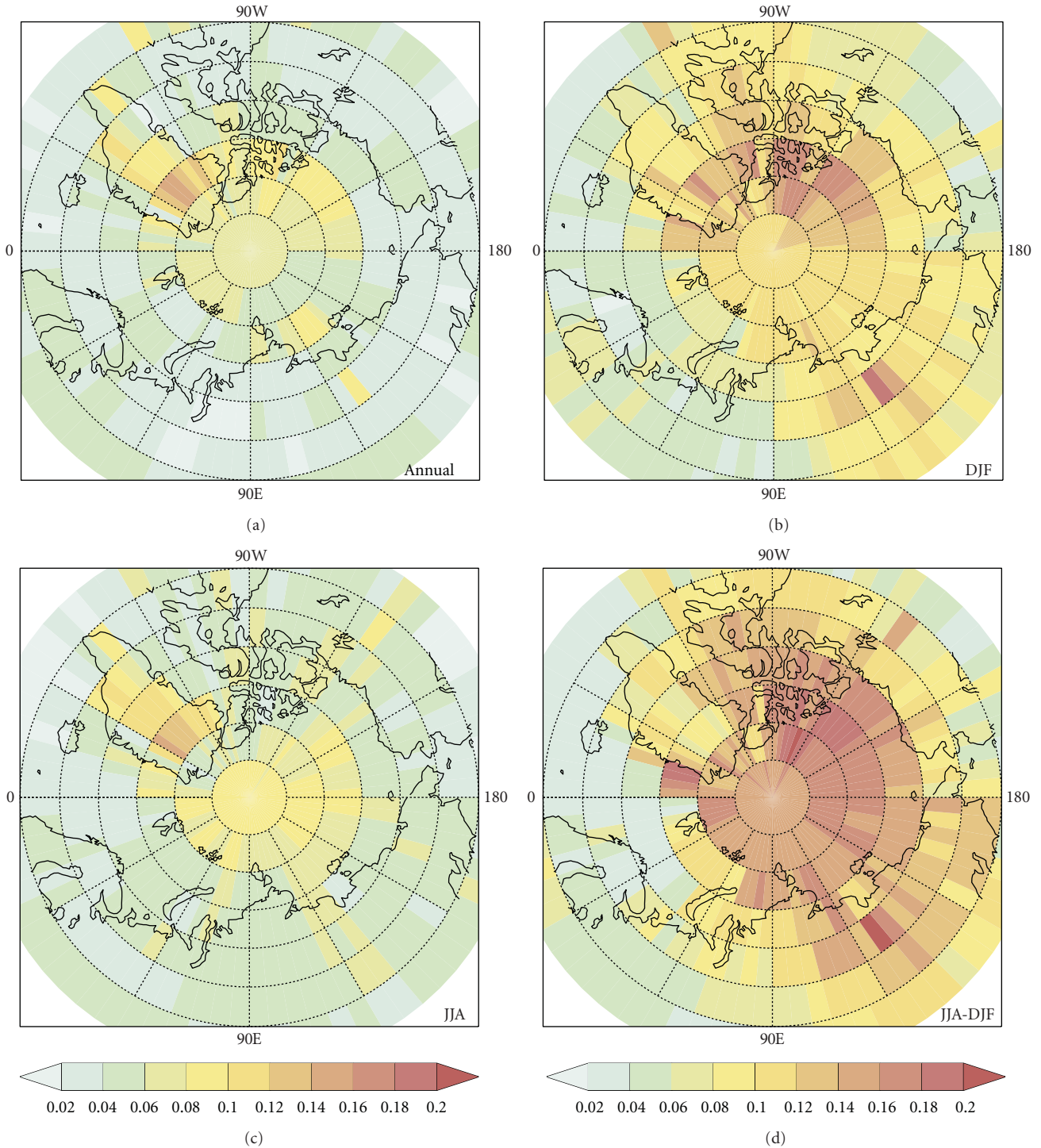


FIGURE 5: Distribution of inter-data standard deviation of TCF (reanalyses are excluded) for annual mean (a), December-January-February mean (DJF) (b), June-July-August mean (JJA) (c), and differences between JJA and DJF (d).

the strongest low-tropospheric temperature inversions occur in these regions. Relatively high ISTD over the Arctic Ocean in winter is mostly associated with ISCCP data, whose algorithm erroneously detects clear-sky ice crystal precipitation as cloudiness [16] and has a systematic positive bias in the

surface temperature retrieval [80]. In general, other satellite-derived datasets also have lower cloud detection capabilities during nighttime than daytime and over surfaces covered with the sea ice [79]. Ship observations from EECRA data also cannot provide suitable information over the central

part of the Arctic Ocean in winter due to a small number of observations [26]. In summer (Figure 5(c)), ISTD is smaller than in winter. The highest values of ISTD are noted over the ice surface of Greenland. Thus, we speculate that the main reason for observations discrepancies is differences in the cloud-detection algorithms, especially when clouds are detected over the ice/snow surface (during the whole year) or over regions with the presence of the strong low-tropospheric temperature inversions (mostly in winter).

4. Discussion and Conclusions

The Arctic annual mean TCF is 0.70 ± 0.03 according to different observations. It is greater over the ocean (0.74 ± 0.04) than over land (0.67 ± 0.03). Different observations are in a better agreement in summer than in winter and over the ocean than over land for the Arctic mean TCF as well as for the spatial distribution of TCF. The interannual variability is higher in winter than in summer according to all observation-derived data, which may be associated with uncertainties in observations that are greater in winter than in summer. Total cloud fraction in the Arctic has the prominent annual cycle according to all observations excluding PATMOS-x and ISCCP. The time of TCF maximum corresponds with the time of the sea ice extent minimum (early summer–late autumn) and vice versa (late spring) (see also [16]). This correspondence is also found in an interannual variability. Eastman and Warren [10] and Palm et al. [85] showed that TCF is greater during the years with the low sea ice extent and vice versa according to satellite data [85] and surface observations [10]. In general, reanalyses do not capture this feature of TCF annual cycle. According to most of the reanalyses, the maximum of TCF is shifted to October–November. NCEP/NCAR, NCEP/DOE, and JRA-25 reanalyses show less TCF than observations during the whole year. Other reanalyses are in a close agreement with observations during summer, while in wintertime, they show noticeably higher values of TCF than observations.

Spatial distribution of the annual mean TCF collocates with the spatial distribution of the annual mean surface skin temperature. The annual mean TCF minimum occurs over the northeastern part of Greenland and collocates with the minimum of the skin surface temperature, whilst the annual mean TCF maximum is noted over the warmest part of the Arctic (the Norwegian and Barents Sea). Reanalyses capture the position of the TCF minimum correctly, but some of them erroneously show the highest values of TCF over the central part of the Arctic Ocean but not over the Norwegian and Barents Sea as observations do. In addition, reanalyses show higher spatial correlation of TCF with observations in summer than in winter and over the ocean than over land. The spatial distributions of TCF from different satellite observations are in a closer agreement over the ocean in winter and over land in summer. The presumable reason for this peculiarity is the mosaic structure of the underneath surface which depends on season in an opposite manner for land and for the ocean. This feature is not revealed when

satellite data are compared with surface observations which do not depend on surface characteristics.

For the whole year, the greatest disagreement among observations was revealed in regions with the ice/snow surface. Furthermore, we found that agreement in winter is poor in regions with the presence of strong low-tropospheric temperature inversions. This can indicate the difference in the cloud-detection algorithms as the main reason for data discrepancies. Nonetheless, other reasons should also be taken into account (diurnal cycle, differences in averaging period). We should emphasize that we do not estimate here the quantitative input from different reasons into resulting discrepancies.

It is worth noting that surface and satellite observations and reanalyses define clouds slightly different. Particularly, human observers detect bases of the clouds, while satellite sensors observe tops of the clouds. Clouds are water condensates (water or ice) that are visible for human observers on surface or detectable for passive sensors on satellites. Thus, human observers as well as passive sensors can miss some small or semitransparent clouds, which are undetectable for them. Contrastingly, reanalyses define clouds independently for each model level and do not have a threshold on minimal amount of condensate that can be considered as cloud. These qualitative differences among different observational approaches should also be taken into account.

To determine real values of TCF over the Arctic in different seasons more evaluations are needed. Active sensors like radar and lidar have a potentially great capability to improve our knowledge about Arctic cloudiness especially during the cold portion of the year. However, these observations are still too short. Additionally, lidar could erroneously detect a thick Arctic haze layer as a cloud [79] and radar-derived cloudiness strongly depends on the applied thresholds [86].

At present, it is hard to distinguish the best observational dataset for the Arctic cloudiness. Further analyses should be carried out for the specific regions with the greatest disagreement among cloudiness datasets, particularly Greenland, the Canadian Arctic Archipelago, and the northern part of East Siberia.

Acknowledgments

The authors thank three anonymous reviewers for their helpful comments. They acknowledge the mission scientists and principal investigators who provided the data used in this research. APP-x and PATMOS-x data were obtained from the Cooperative Institute for Meteorological Satellite Studies, University of Wisconsin websites (<http://stratus.ssec.wisc.edu/projects/app/app.html> and <http://cimss.ssec.wisc.edu/patmosx/>). CERES data were obtained from the NASA Langley Research Center, Atmospheric Science Data Center. The ISCCP DX data are from the International Satellite Cloud Climatology Project data archives at NOAA/NESDIS/NCDC Satellite Services Group. MODIS data were obtained from Level 1 and Atmospheric Archive and Distribution System. EECRA data were obtained from Carbon Dioxide Information

Analysis Center website (<http://cdiac.ornl.gov/>). ERA-40 and ERA-Interim data have been provided by ECMWF. JRA-25 data have been provided by JMA. MERRA data have been provided by NASA through Goddard Earth Sciences Data Information Services Center. The NCEP/NCAR, NCEP/DOE, NCEP-CFSR, and 20CR data are from the Research Data Archive (RDA), which is maintained by CISL at NCAR. Support for this research was provided by The Research Council of Norway under the YGGDRASIL mobility programme, the Russian Foundation for Basic Research under Grants 11-05-01139 and 11-05-00579, by the Grant of the RF President SS-3301.2010.5, by Russian Ministry of Education and Science under contracts 14.740.11.1043 and 11.519.11.5004, and by programs of The Russian Academy of Sciences.

References

- [1] *Arctic Climate Impact Assessment*, Cambridge University Press, Cambridge, UK, 2005.
- [2] S. Solomon, D. Qin, M. Manning et al., *Climate Change 2007a: The Physical Science Basis. Contribution of Working Group I to the Fourth Assessment Report of the Intergovernmental Panel on Climate Change*, Cambridge University Press, Cambridge, UK, 2007.
- [3] M. L. Parry, O. F. Canziani, J. P. Palutikof et al., *Climate Change 2007b: Impacts, Adaptation and Vulnerability. Contribution of Working Group II to the Fourth Assessment Report of the Intergovernmental Panel on Climate Change*, Cambridge University Press, Cambridge, UK, 2007.
- [4] V. P. Meleshko and S. M. Semenov, "Russian Assessment Report on climate change and its impact on the Russian territory," Technical summary, 2008.
- [5] M. C. Serreze, J. E. Walsh, F. S. Chapin et al., "Observational evidence of recent change in the northern high-latitude environment," *Climatic Change*, vol. 46, no. 1-2, pp. 159–207, 2000.
- [6] J. Stroeve, M. M. Holland, W. Meier, T. Scambos, and M. Serreze, "Arctic sea ice decline: faster than forecast," *Geophysical Research Letters*, vol. 34, no. 9, Article ID L09501, 2007.
- [7] Y. Liu, J. R. Key, and X. Wang, "Influence of changes in sea ice concentration and cloud cover on recent Arctic surface temperature trends," *Geophysical Research Letters*, vol. 36, no. 20, Article ID L20710, 2009.
- [8] X. Wang and J. R. Key, "Arctic surface, cloud, and radiation properties based on the AVHRR polar pathfinder dataset. Part II: recent trends," *Journal of Climate*, vol. 18, no. 14, pp. 2575–2593, 2005.
- [9] Y. Liu, J. R. Key, J. A. Francis, and X. Wang, "Possible causes of decreasing cloud cover in the Arctic winter, 1982–2000," *Geophysical Research Letters*, vol. 34, no. 14, Article ID L14705, 2007.
- [10] R. Eastman and S. G. Warren, "Interannual variations of arctic cloud types in relation to sea ice," *Journal of Climate*, vol. 23, no. 15, pp. 4216–4232, 2010.
- [11] V. Ramanathan, R. D. Cess, E. F. Harrison et al., "Cloud-radiative forcing and climate: results from the earth radiation budget experiment," *Science*, vol. 243, no. 4887, pp. 57–63, 1989.
- [12] B. A. Wielicki, R. D. Cess, M. D. King, D. A. Randall, and E. F. Harrison, "Mission to Planet Earth: role of clouds and radiation in climate," *Bulletin of American Meteorological Society*, vol. 76, no. 11, pp. 2125–2154, 1995.
- [13] E. F. Harrison, P. Minnis, B. R. Barkstrom, V. Ramanathan, R. D. Cess, and G. G. Gibson, "Seasonal variation of cloud radiative forcing derived from the Earth Radiation Budget Experiment," *Journal of Geophysical Research*, vol. 95, no. 11, pp. 18687–18703, 1990.
- [14] J. M. Intrieri, C. W. Fairall, M. D. Shupe et al., "An annual cycle of Arctic surface cloud forcing at SHEBA," *Journal of Geophysical Research C*, vol. 107, no. 10, pp. 1–14, 2002.
- [15] J. E. Walsh, W. L. Chapman, and D. H. Portis, "Arctic cloud fraction and radiative fluxes in atmospheric reanalyses," *Journal of Climate*, vol. 22, no. 9, pp. 2316–2334, 2009.
- [16] J. A. Curry, W. B. Rossow, D. Randall, and J. L. Schramm, "Overview of arctic cloud and radiation characteristics," *Journal of Climate*, vol. 9, no. 8, pp. 1731–1764, 1996.
- [17] X. Wang and J. R. Key, "Recent trends in arctic surface, cloud, and radiation properties from space," *Science*, vol. 299, no. 5613, pp. 1725–1728, 2003.
- [18] M. D. Shupe and J. M. Intrieri, "Cloud radiative forcing of the Arctic surface: the influence of cloud properties, surface albedo, and solar zenith angle," *Journal of Climate*, vol. 17, no. 3, pp. 616–628, 2004.
- [19] S. Vavrus, "The impact of cloud feedbacks on Arctic climate under Greenhouse forcing," *Journal of Climate*, vol. 17, no. 3, pp. 603–615, 2004.
- [20] Y. Liu, J. R. Key, and X. Wang, "The influence of changes in cloud cover on recent surface temperature trends in the Arctic," *Journal of Climate*, vol. 21, no. 4, pp. 705–715, 2008.
- [21] A. V. Chernokulsky, O. N. Bulygina, and I. I. Mokhov, "Recent variations of cloudiness over Russia from surface daytime observations," *Environmental Research Letters*, vol. 6, no. 3, Article ID 035202, 2011.
- [22] S. Vavrus, D. Waliser, A. Schweiger, and J. Francis, "Simulations of 20th and 21st century Arctic cloud amount in the global climate models assessed in the IPCC AR4," *Climate Dynamics*, vol. 33, no. 7-8, pp. 1099–1115, 2009.
- [23] I. I. Mokhov, A. V. Chernokul'skii, M. G. Akperov, J. L. Dufresne, and H. Le Treut, "Variations in the characteristics of cyclonic activity and cloudiness in the atmosphere of extratropical latitudes of the Northern Hemisphere based from model calculations compared with the data of the reanalysis and satellite data," *Doklady Earth Sciences*, vol. 424, no. 1, pp. 147–150, 2009.
- [24] D. Lubin and E. Morrow, "Evaluation of an AVHRR cloud detection and classification method over the central arctic ocean," *Journal of Applied Meteorology*, vol. 37, no. 2, pp. 166–177, 1998.
- [25] Y. Liu, J. R. Key, R. A. Frey, S. A. Ackerman, and W. P. Menzel, "Nighttime polar cloud detection with MODIS," *Remote Sensing of Environment*, vol. 92, no. 2, pp. 181–194, 2004.
- [26] C. J. Hahn and S. G. Warren, *A Gridded Climatology of Clouds over Land (1971–96) and Ocean (1954–97) from Surface Observations Worldwide (NDP-026E)*, Carbon Dioxide Information Analysis Center, Oak Ridge, Tenn, USA, 2007.
- [27] S. G. Warren, R. M. Eastman, and C. J. Hahn, "A survey of changes in cloud cover and cloud types over land from surface observations, 1971–96," *Journal of Climate*, vol. 20, no. 4, pp. 717–738, 2007.

- [28] N. A. Hughes, "Global cloud climatologies: a historical review," *Journal of Climate & Applied Meteorology*, vol. 23, no. 5, pp. 724–751, 1984.
- [29] I. I. Mokhov and M. E. Schlesinger, "Analysis of global cloudiness: 1. Comparison of Meteor, Nimbus 7, and International Satellite Cloud Climatology Project (ISCCP) satellite data," *Journal of Geophysical Research*, vol. 98, no. 7, pp. 12849–12868, 1993.
- [30] I. I. Mokhov and M. E. Schlesinger, "Analysis of global cloudiness 2. Comparison of ground-based and satellite-based cloud climatologies," *Journal of Geophysical Research*, vol. 99, no. 8, pp. 17045–17065, 1994.
- [31] C. J. Hahn, W. B. Rossow, and S. G. Warren, "ISCCP cloud properties associated with standard cloud types identified in individual surface observations," *Journal of Climate*, vol. 14, no. 1, pp. 11–28, 2001.
- [32] S. M. Thomas, A. K. Heidinger, and M. J. Pavolonis, "Comparison of NOAA's operational AVHRR-derived cloud amount to other satellite-derived cloud climatologies," *Journal of Climate*, vol. 17, no. 24, pp. 4805–4822, 2004.
- [33] A. V. Chernokulsky and I. I. Mokhov, "Intercomparison of global and zonal cloudiness characteristics from different satellite and ground-based data," *Earth's Research from Space*, vol. 3, pp. 12–29, 2010.
- [34] B. C. Weare, "Evaluation of total cloudiness and its variability in the atmospheric model intercomparison project," *Journal of Climate*, vol. 8, no. 9, pp. 2224–2238, 1995.
- [35] A. V. Eliseev, H. Le Treut, I. I. Mokhov, M. Doutriaux-Boucher, and A. V. Chernokulsky, "Validation of TOA radiation and clouds simulated by different versions of the LMD general circulation model in comparison to satellite and ground-based data," *Izvestiya, Atmospheric and Ocean Physics*, vol. 39, pp. S15–S26, 2003.
- [36] M. H. Zhang, W. Y. Lin, S. A. Klein et al., "Comparing clouds and their seasonal variations in 10 atmospheric general circulation models with satellite measurements," *Journal of Geophysical Research D*, vol. 110, no. 15, pp. 1–18, 2005.
- [37] J. A. Griggs and J. L. Bamber, "Assessment of cloud cover characteristics in satellite datasets and reanalysis products for greenland," *Journal of Climate*, vol. 21, no. 9, pp. 1837–1849, 2008.
- [38] A. V. Chernokulsky and I. I. Mokhov, "Comparison of global cloud climatologies," *Current Issues of Remote Sensing of Earth from Space*, vol. 6, no. 2, pp. 235–243, 2009.
- [39] J. Karlsson and G. Svensson, "The simulation of Arctic clouds and their influence on the winter surface temperature in present-day climate in the CMIP3 multi-model dataset," *Climate Dynamics*, vol. 36, no. 3, pp. 623–635, 2011.
- [40] G. M. Stokes and S. E. Schwartz, "The Atmospheric Radiation Measurement (ARM) Program: programmatic background and design of the cloud and radiation test bed," *Bulletin of American Meteorological Society*, vol. 75, no. 7, pp. 1201–1221, 1994.
- [41] D. Randall, J. Curry, D. Battisti et al., "Status of and outlook for large-scale modeling of atmosphere-ice-ocean interactions in the arctic," *Bulletin of the American Meteorological Society*, vol. 79, no. 2, pp. 197–219, 1998.
- [42] J. A. Curry, P. V. Hobbs, M. D. King et al., "FIRE arctic clouds experiment," *Bulletin of the American Meteorological Society*, vol. 81, no. 1, pp. 5–29, 2000.
- [43] T. Uttal, J. A. Curry, M. G. McPhee et al., "Surface heat budget of the arctic ocean," *Bulletin of the American Meteorological Society*, vol. 83, no. 2, pp. 255–275, 2002.
- [44] J. A. Maslanik, J. Key, C. W. Fowler, T. Nguyen, and X. Wang, "Spatial and temporal variability of satellite-derived cloud and surface characteristics during FIRE-ACE," *Journal of Geophysical Research D*, vol. 106, no. 14, pp. 15233–15249, 2001.
- [45] S. Kato, N. G. Loeb, P. Minnis et al., "Seasonal and interannual variations of top-of-atmosphere irradiance and cloud cover over polar regions derived from the CERES data set," *Geophysical Research Letters*, vol. 33, no. 19, Article ID L19804, 2006.
- [46] B. E. Schutz, H. J. Zwally, C. A. Shuman, D. Hancock, and J. P. DiMarzio, "Overview of the ICESat mission," *Geophysical Research Letters*, vol. 32, no. 21, Article ID L21S01, pp. 1–4, 2005.
- [47] D. M. Winker, W. H. Hunt, and M. J. McGill, "Initial performance assessment of CALIOP," *Geophysical Research Letters*, vol. 34, no. 19, Article ID L19803, 2007.
- [48] G. L. Stephens, D. G. Vane, R. J. Boain et al., "The cloudsat mission and the A-Train: a new dimension of space-based observations of clouds and precipitation," *Bulletin of the American Meteorological Society*, vol. 83, no. 12, pp. 1771–1742, 2002.
- [49] G. G. Mace, Q. Zhang, M. Vaughan et al., "A description of hydrometeor layer occurrence statistics derived from the first year of merged Cloudsat and CALIPSO data," *Journal of Geophysical Research D*, vol. 114, no. 8, Article ID D00A26, 2009.
- [50] J. Key and R. G. Barry, "Cloud cover analysis with Arctic AVHRR data 1. Cloud detection," *Journal of Geophysical Research*, vol. 94, no. 15, pp. 18521–18535, 1989.
- [51] X. Wang and J. R. Key, "Arctic surface, cloud, and radiation properties based on the AVHRR polar pathfinder dataset. Part I: spatial and temporal characteristics," *Journal of Climate*, vol. 18, no. 14, pp. 2558–2574, 2005.
- [52] J. R. Key, *The Cloud and Surface Parameter Retrieval (CASPR) System for Polar AVHRR*, Cooperative Institute for Meteorological Satellite Studies, University of Wisconsin-Madison, 2002.
- [53] B. A. Wielicki, B. R. Barkstrom, E. F. Harrison, R. B. Lee, G. L. Smith, and J. E. Cooper, "Clouds and the earth's radiant energy system (CERES): an earth observing system experiment," *Bulletin of the American Meteorological Society*, vol. 77, no. 5, pp. 853–868, 1996.
- [54] M. D. King, Y. J. Kaufman, W. P. Menzel, and D. Tanre, "Remote sensing of cloud, aerosol, and water vapor properties from the moderate resolution imaging spectrometer (MODIS)," *IEEE Transactions on Geoscience and Remote Sensing*, vol. 30, no. 1, pp. 2–27, 1992.
- [55] P. Minnis, D. Young, S. Sun-Mack, P. W. Heck, D. R. Doelling, and Q. Z. Trepte, "CERES cloud property retrievals from imagers on TRMM, Terra, and Aqua," in *Proceedings of the Remote Sensing of Clouds and the Atmosphere VIII*, vol. 5235 of *Proceedings of SPIE*, pp. 37–48, Barcelona, Spain, September 2003.
- [56] R. A. Schiffer and W. B. Rossow, "The International Satellite Cloud Climatology Project (ISCCP): the first project of the World Climate Research Programme," *Bulletin of American Meteorological Society*, vol. 64, no. 7, pp. 779–784, 1983.
- [57] W. B. Rossow and L. C. Garder, "Cloud detection using satellite measurements of infrared and visible radiances for ISCCP," *Journal of Climate*, vol. 6, no. 12, pp. 2341–2369, 1993.

- [58] W. B. Rossow and R. A. Schiffer, "Advances in understanding clouds from ISCCP," *Bulletin of the American Meteorological Society*, vol. 80, no. 11, pp. 2261–2287, 1999.
- [59] S. A. Ackerman, K. I. Strabala, W. P. Menzel, R. A. Frey, C. C. Moeller, and L. E. Gumley, "Discriminating clear sky from clouds with MODIS," *Journal of Geophysical Research D*, vol. 103, no. 24, pp. 32141–32157, 1998.
- [60] R. A. Frey, S. A. Ackerman, Y. Liu et al., "Cloud detection with MODIS. Part I: improvements in the MODIS cloud mask for Collection 5," *Journal of Atmospheric and Oceanic Technology*, vol. 25, no. 7, pp. 1057–1072, 2008.
- [61] S. A. Ackerman, R. E. Holz, R. Frey, E. W. Eloranta, B. C. Maddux, and M. McGill, "Cloud detection with MODIS. Part II: validation," *Journal of Atmospheric and Oceanic Technology*, vol. 25, no. 7, pp. 1073–1086, 2008.
- [62] A. K. Heidinger, M. J. Foster, and A. T. Evan, "A naive bayesian cloud detection scheme derived from CALIPSO and applied within PATMOS-x," *Journal of Applied Meteorology and Climatology*. In press.
- [63] A. K. Heidinger, *CLAVR-x Cloud Mask Algorithm Theoretical Basis Document (ATBD)*, NOAA/NESDIS/Office of Research and Applications, Washington, DC, USA, 2004.
- [64] C. J. Hahn and S. G. Warren, *Extended Edited Synoptic Cloud Reports from Ships and Land Stations Over the Globe, 1952–1996. NDP-026C*, CDIAC, Oak Ridge, Tenn, USA, 1999.
- [65] C. J. Hahn, S. G. Warren, and J. London, "The effect of moonlight on observation of cloud cover at night, and application to cloud climatology," *Journal of Climate*, vol. 8, no. 5, pp. 1429–1446, 1995.
- [66] R. Kistler, E. Kalnay, W. Collins et al., "The NCEP-NCAR 50-year reanalysis: monthly means CD-ROM and documentation," *Bulletin of the American Meteorological Society*, vol. 82, no. 2, pp. 247–267, 2001.
- [67] S. M. Uppala, P. W. Källberg, A. J. Simmons et al., "The ERA-40 re-analysis," *Quarterly Journal of the Royal Meteorological Society*, vol. 131, no. 612, pp. 2961–3012, 2005.
- [68] D. P. Dee, S. M. Uppala, A. J. Simmons et al., "The ERA-Interim reanalysis: configuration and performance of the data assimilation system," *Quarterly Journal of the Royal Meteorological Society*, vol. 137, no. 656, pp. 553–597, 2011.
- [69] S. Saha, S. Moorthi, H. L. Pan et al., "The NCEP climate forecast system reanalysis," *Bulletin of the American Meteorological Society*, vol. 91, no. 8, pp. 1015–1057, 2010.
- [70] G. P. Compo, J. S. Whitaker, P. D. Sardeshmukh et al., "The twentieth century reanalysis project," *Quarterly Journal of the Royal Meteorological Society*, vol. 137, no. 654, pp. 1–28, 2011.
- [71] K. A. Campana, Y.-T. Hou, K. E. Mitchell et al., "Improved diagnostic cloud parameterization in NMC's global model," in *Proceedings of the 10th Conference on Numerical Weather Prediction*, pp. 324–325, Portland, Ore, USA, 1994.
- [72] M. Kanamitsu, W. Ebisuzaki, J. Woollen et al., "NCEP-DOE AMIP-II reanalysis (R-2)," *Bulletin of the American Meteorological Society*, vol. 83, no. 11, pp. 1631–1559, 2002.
- [73] K. M. Xu and D. A. Randall, "Evaluation of statistically based cloudiness parameterizations used in climate models," *Journal of the Atmospheric Sciences*, vol. 53, no. 21, pp. 3103–3119, 1996.
- [74] K. Onogi, J. Tsutsui, H. Koide et al., "The JRA-25 reanalysis," *Journal of the Meteorological Society of Japan*, vol. 85, no. 3, pp. 369–432, 2007.
- [75] S. Moorthi, H.-L. Pan, and P. Caplan, "Changes to the 2001 NCEP operational MRF/AVN global analysis/forecast system," *NWS Technical Procedures Bulletin*, vol. 484, 14 pages, 2001.
- [76] M. M. Rienecker, M. J. Suarez, R. Gelaro et al., "MERRA: NASA's modern-era retrospective analysis for research and applications," *Journal of Climate*, vol. 24, no. 14, pp. 3624–3648, 2011.
- [77] M. Tiedtke, "Representation of clouds in large-scale models," *Monthly Weather Review*, vol. 121, no. 11, pp. 3040–3061, 1993.
- [78] J. T. Bacmeister, M. J. Suarez, and F. R. Robertson, "Rain reevaporation, boundary layer-convection interactions, and pacific rainfall patterns in an AGCM," *Journal of the Atmospheric Sciences*, vol. 63, no. 12, pp. 3383–3403, 2006.
- [79] Y. Liu, S. A. Ackerman, B. C. Maddux, J. R. Key, and R. A. Frey, "Errors in cloud detection over the arctic using a satellite imager and implications for observing feedback mechanisms," *Journal of Climate*, vol. 23, no. 7, pp. 1894–1907, 2010.
- [80] A. J. Schweiger, R. W. Lindsay, J. R. Key, and J. A. Francis, "Arctic clouds in multiyear satellite data sets," *Geophysical Research Letters*, vol. 26, no. 13, Article ID 1999GL900479, pp. 1845–1848, 1999.
- [81] K. E. Taylor, "Summarizing multiple aspects of model performance in a single diagram," *Journal of Geophysical Research D*, vol. 106, no. 7, pp. 7183–7192, 2001.
- [82] D. Wylie, "Diurnal cycles of clouds and how they affect polar-orbiting satellite data," *Journal of Climate*, vol. 21, no. 16, pp. 3989–3996, 2008.
- [83] Y. Liu, J. R. Key, A. Schweiger, and J. Francis, "Characteristics of satellite-derived clear-sky atmospheric temperature inversion strength in the Arctic, 1980–96," *Journal of Climate*, vol. 19, no. 19, pp. 4902–4913, 2006.
- [84] A. Devasthale, U. Willén, K. G. Karlsson, and C. G. Jones, "Quantifying the clear-sky temperature inversion frequency and strength over the Arctic Ocean during summer and winter seasons from AIRS profiles," *Atmospheric Chemistry and Physics*, vol. 10, no. 12, pp. 5565–5572, 2010.
- [85] S. P. Palm, S. T. Strey, J. Spinhirne, and T. Markus, "Influence of Arctic sea ice extent on polar cloud fraction and vertical structure and implications for regional climate," *Journal of Geophysical Research D*, vol. 115, no. 21, Article ID D21209, 2010.
- [86] E. W. Eloranta, J. P. Garcia, I. A. Razenkov et al., "Cloud fraction statistics derived from 2-years of high spectral resolution lidar data acquired at Eureka, Canada," in *Proceedings of the 24th International Laser Radar Conference*, vol. 555–558, Boulder, Colo, USA, 2008.

Research Article

Solar Activity and Svalbard Temperatures

Jan-Erik Solheim,¹ Kjell Stordahl,² and Ole Humlum^{3,4}

¹Department of Physics and Technology, University of Tromsø, 9037 Tromsø, Norway

²Finance, Telenor Norway, Snarøyveien 30, 1331 Fornebu, Norway

³Department of Geosciences, University of Oslo, P.O. Box 1047 Blindern, 0316 Oslo, Norway

⁴Department of Geology, University Centre in Svalbard, Pb. 156, 9171 Longyearbyen, Norway

Correspondence should be addressed to Jan-Erik Solheim, janesol@online.no

Received 14 September 2011; Revised 23 November 2011; Accepted 29 November 2011

Academic Editor: Stefania Argenti

Copyright © 2011 Jan-Erik Solheim et al. This is an open access article distributed under the Creative Commons Attribution License, which permits unrestricted use, distribution, and reproduction in any medium, provided the original work is properly cited.

The long temperature series at Svalbard (Longyearbyen) show large variations and a positive trend since its start in 1912. During this period solar activity has increased, as indicated by shorter solar cycles. The temperature at Svalbard is negatively correlated with the length of the solar cycle. The strongest negative correlation is found with lags 10–12 years. The relations between the length of a solar cycle and the mean temperature in the following cycle are used to model Svalbard annual mean temperature and seasonal temperature variations. Residuals from the annual and winter models show no autocorrelations on the 5 per cent level, which indicates that no additional parameters are needed to explain the temperature variations with 95 per cent significance. These models show that 60 per cent of the annual and winter temperature variations are explained by solar activity. For the spring, summer, and fall temperatures autocorrelations in the residuals exist, and additional variables may contribute to the variations. These models can be applied as forecasting models. We predict an annual mean temperature decrease for Svalbard of $3.5 \pm 2^\circ\text{C}$ from solar cycle 23 to solar cycle 24 (2009–20) and a decrease in the winter temperature of $\approx 6^\circ\text{C}$.

1. Introduction

The question of a possible connection between solar activity and the Earth's climate has received considerable attention in the last 200 years [1, 2]. It may therefore be of interest to investigate if part of the temperature increase and large variations in Arctic temperatures may be attributed to solar influence.

One of the longest Arctic temperature series is from Svalbard. It started in 1912 and is discussed and analysed by Humlum et al. [3] (called HSS12 in the following). Their analysis of the temperature record identified a linear trend of $0.023^\circ\text{C yr}^{-1}$, in addition to cyclic variations. The strongest cyclic variations have periods 62–68, 26, and 15–17 years. HSS12 also finds lower amplitude variations with periods 11–12 years, which may be related to the solar activity cycle.

Solar activity can be described by the following proxies described by Gray et al. [2, Figures 1 and 2]: the sunspot number R ; the 10.7 cm solar radio flux, $F_{10.7}$; the

chromospheric Mg II line; the open solar flux near the Earth F_s ; galactic cosmic ray neutron counts; the total solar irradiance (TSI); variations in the geomagnetic field (the aa index); counts of low-latitude aurora; the radioactive ^{10}Be isotope. Most attention has been paid to the number of sunspots, which varies with a period of 9–13 years. Also the length of the sunspot cycle is known to vary with the solar activity, in the sense that high activity is related to short cycles and low activity to long cycles. The length is shown to vary in a systematic way in a cycle of length of 80–90 years, named after Gleissberg [4].

The length of a solar cycle can be determined from the appearance of the first spot in a cycle at high solar latitude, to the disappearance of the last spot in the cycle near solar equator. However, before the last spot in a cycle disappears, the first spot in the next cycle appears at high latitude, and there is normally a two-year overlap [5]. The time of minimum is defined as the central time of overlap between the two cycles [5], and the length of a cycle can be measured between successive minima or maxima.

It was for a long time thought that the appearance of a solar cycle was a random event, that is, each cycle's length and amplitude were independent of the previous. However, Dicke [6] showed already in 1978 that an internal chronometer has to exist inside the Sun, which, after a number of short cycles, reset the cycle length so the average length of 11.2 years is kept.

Comparing sunspot numbers with the Northern Hemisphere land temperature anomaly, Friis-Christensen and Lassen [7] found a better correlation between the solar cycle length (SCL) and the temperature anomaly than with the number of sunspots, in the sense that shorter sunspot cycles indicated higher temperatures. They used a smoothed value for SCL over 5 solar cycles. This resulted in good correlations when the SCL on average decreased, indicating that solar activity was the dominant contributor to the NH-land temperature increase in their period of investigation (1860–1990).

However, at the turn of the millennium, inconsistency with this relation was found [8–10] because of the sudden lengthening of the solar cycle (see Figure 1) while the NH-land temperature anomaly remained positive.

Solanki and Krivova [11] showed by cross-correlations between time series of solar cycle length and sunspot number maxima (R_{\max}) that the length precedes the amplitude, in the sense that short cycles preceded strong cycles. A test of the back time showed that a lag of one period of 11 years or one solar cycle gave highest correlation after SC10. Before SC10 a lag of 3 cycles dominated. They interpreted this as the solar dynamo has a memory of the length of previous cycles and suggested an empirical model based on lag one and three cycles for predicting the amplitude of the following cycle.

Butler [12] proposed that a well-observed temperature series as the one at Armagh Observatory might be a better indicator for NH temperature anomaly than the HadCRUT3 average, which has a variable number of stations and includes large cities with urban heating. He found good correlations between the temperature measured at Armagh Observatory in the period 1844–1992 and the number of sunspots smoothed with the 1-2-2-2-1 filter. He concluded that solar activity, or something closely related to it, had dominating influence on the lower atmosphere temperature at Armagh in this period. Butler and Johnston [13] studied the same data and noticed a delay of about one solar cycle (10–12 yrs) between the shortest solar cycles and temperature peaks at Armagh. Archibald [14] proposed that this delay could be used to predict a cooling during the present solar cycle 24, which follows the longest in a century solar cycle 23, for certain locations in Europe and the East Coast of the USA where he found correlations between SCL and the temperature in the following cycle.

A systematic study by Solheim et al. [15] (called SSH12 in the following) of the correlation between SCL and temperature lags in 11-year intervals, for 16 data sets, revealed that the strongest correlation took place 10–12 years after the midtime of a solar cycle, for most of the locations included. In this study the temperature series from Svalbard (Longyearbyen) was included, and a relation between the previous sunspot cycle length (PSCL) and the temperature in

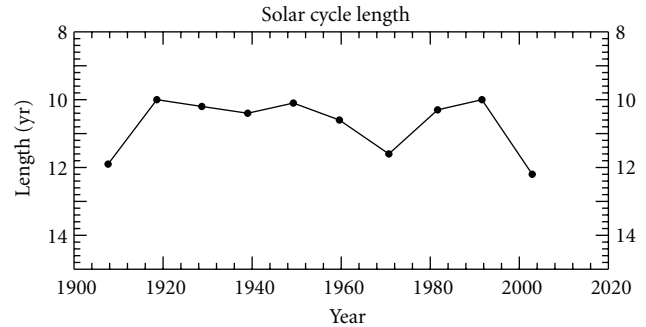


FIGURE 1: Length of solar cycles (inverted scale) since 1900. The black dots are the midtime for each cycle.

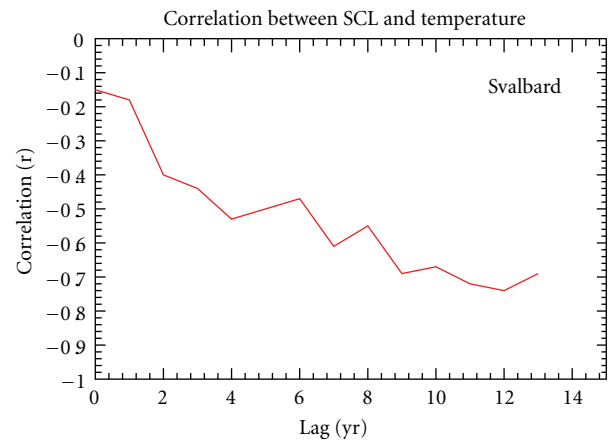


FIGURE 2: Correlation r between the length of a solar cycle and 11-year running mean of the Svalbard (Longyearbyen) temperature record, with different lags.

the following cycle was determined. This relation was used to predict that the yearly average temperature, which was -4.2°C in sunspot cycle (SC) 23, was estimated to decrease to -7.8°C in SC24, with a 95% confidence interval of -6.0 to -9.6°C [15]. SSH12 [15] found that stations in the North Atlantic (Torshavn, Akureyri, and Svalbard) had the highest correlations between the length of a solar cycle and the temperature in the next cycle, showing correlation coefficient r from 0.79 to 0.86

In Figure 2, we show the correlation r between the solar cycle length and an 11-year running mean temperature, with zero to 13 years lag for the Svalbard temperature series. The correlation is always negative and has a maximum absolute value between 10- and 13-year lag. This indicates that a lag of one solar cycle may give the highest correlation.

In the following we will discuss the Svalbard temperature series in more detail and investigate how this correlation is related to seasons. We will also investigate how other variables may contribute to temperature variations at Svalbard.

2. Svalbard Temperature Series and Solar Cycle Relations

2.1. The Svalbard Temperature Record. The modern official Svalbard meteorological station is located near the main settlement in Svalbard, Longyearbyen ($78^{\circ} 13'N$, $15^{\circ} 33'E$, about 2000 inhabitants), in central Spitsbergen. The station is located at the Svalbard Airport (24 m asl.), about 3 km NW of Longyearbyen, near the shore of the large fjord Isfjorden. Monthly temperature data were obtained from the *eKlima* portal run by the Norwegian Meteorological Institute. MAAT and seasonal temperature (DJF, MAM, JJA, and SON) values 1912–2011 were calculated from this.

The Svalbard meteorological record is a composite record, representing homogenized observations originally made at 4 different stations, located along the shore of the fjord Isfjord, extending from the west coast to the interior of the main island Spitsbergen. A survey of meteorological statistics for the Norwegian Arctic is described by Førland et al. [16], and the individual Spitsbergen meteorological stations are described by Hanssen-Bauer et al. [17]. The Standard Normal Homogeneity Test [18, 19] was applied on the series, and the results were validated by a study of the stations history by Nordli et al. [20]. The absence of visible irregularities in the record itself (Figure 3) as well as in wavelet diagrams [3], corresponding to the timing of known station changes, testifies to the quality of the homogenization carried out.

Comparing the Svalbard MAAT record with average Arctic temperature development since 1912 [21, 22] there are both similarities and differences. The Arctic temperature increase around 1920 lasting to about 1940 is recognised in the Svalbard record, although this increase apparently began about 5 years before 1920. The general Arctic temperature decrease from about 1940 lasting to about 1970 is clearly visible in the Svalbard record also. Finally, the general Arctic temperature increase since 1980, until now, is also expressed by the Svalbard record, although with an apparent delay of 5–10 years.

2.2. Svalbard Temperatures in Solar Cycles. The Svalbard temperature series starts in 1912. The starting dates (in decimal years) and the length of solar cycles after 1900 are given in Table 1 which is obtained from the National Geophysical Data Center (NGDC): ftp://ftp.ngdc.noaa.gov/STP/SOLAR_DATA/SUNSPOT_NUMBERS/INTERNATIONAL/maxmin/MAXMIN.

Solar cycle 14 (SC14) began in 1901 and was nearly finished when the Svalbard temperature observations started. Our analysis therefore starts with SC15 which began in 1914. Table 1 gives the mean temperature in each solar cycle, based on yearly temperatures in the range of years given in column 5.

We have also calculated mean temperatures for four seasons as given in the table. Figure 3 shows the yearly temperatures and the solar cycle mean temperatures with standard errors (σ_i). Weighted linear least square fits to the solar cycle mean temperature values on the form $y = \beta x + \alpha$

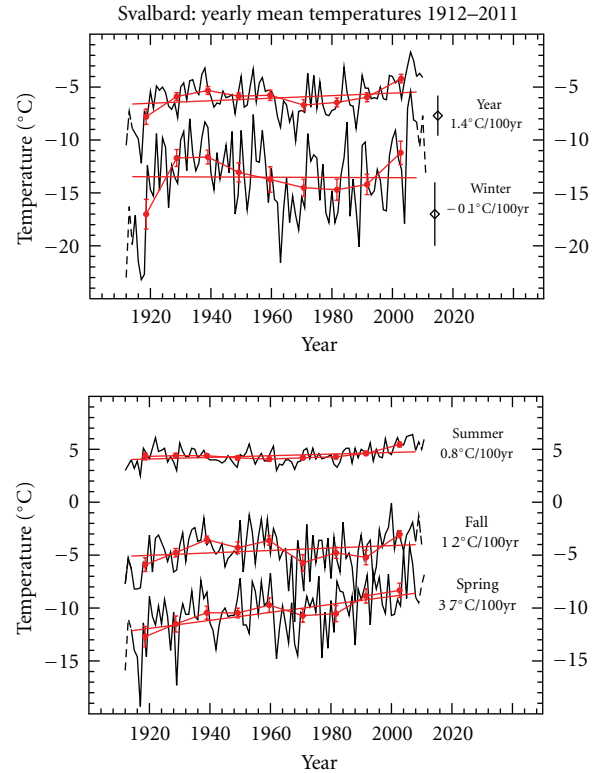


FIGURE 3: The mean yearly (MAAT) temperatures at Svalbard (Spitzbergen)—for the year and the four seasons. The red circles are the mean temperatures in sunspot cycles with standard error bars, also used for the correlation analysis. The red thick lines are weighted linear least square fits to the solar cycle mean temperatures, with the trends for the period 1914–2008 (β_1) indicated. The black dashed curves are data before 1914 and after 2008, corresponding to incomplete solar cycles, and not used in the averaging. Forecasts for SC24 temperatures based on length of SC23 are given with 95% confidence intervals (diamonds with bars) for the year and winter temperatures.

gave the trends β_1 shown in Figure 3 and in Table 2. As weight for the observation i we used

$$w_i = \frac{N/\sigma_i}{\sum_i(1/\sigma_i)}, \quad \text{for } i = 1 \dots N, \quad (1)$$

where $N = 9$ is the number of cycles.

The calculated linear trend is given by

$$\beta = \sum_i \frac{(x_i - x_{\text{mean}})(y_i - y_{\text{mean}})w_i}{(x_i - x_{\text{mean}})^2 w_i}, \quad (2)$$

where σ_i is the standard deviation of the mean value of the temperature in cycle i .

The number of observations in the regression analysis is 9. Usually the degree of freedom is the number of observations minus the number of parameters in the model. However, analysis of the sunspot length effect on different lags of delayed temperature has been performed on beforehand, which resulted in a model where the previous sunspot cycle period explains the temperature in the next

TABLE 1: Svalbard: Mean temperatures in sunspot cycles.

Cycle no.	Minimum yr	R_{\max} no.	Length yr	Years temp.	Year MAAT °C	Winter DJF °C	Spring MAM °C	Summer JJA °C	Fall SON °C
14	1901.7	64.2	11.9						
15	1913.6	105	10.0	1914–23	−7.80	−17.01	−12.70	4.32	−5.90
16	1923.6	78.1	10.2	1924–33	−5.89	−11.70	−11.51	4.40	−4.77
17	1933.8	119	10.4	1924–43	−5.32	−11.61	−10.44	4.39	−3.53
18	1944.2	152	10.1	1944–53	−5.86	−13.06	−10.47	4.19	−4.30
19	1954.3	201	10.6	1954–64	−5.77	−13.73	−9.72	4.07	−3.62
20	1964.9	111	11.6	1965–76	−6.70	−14.51	−10.72	4.20	−5.73
21	1976.5	165	10.3	1977–86	−6.45	−14.70	−10.53	4.29	−4.78
22	1986.8	159	10.0	1987–96	−5.96	−14.24	−8.85	4.61	−5.22
23	1996.9	121	12.2	1997–2008	−4.20	−11.20	−8.33	5.45	−3.03
24	2008.9								

TABLE 2: Statistics on Svalbard temperature series.

	Model 1		Model PSCL		Bootstrap (1000 samples)	
	β_1 °C(100 yr) ^{−1}	r_1	β_{PSCL} °Cyr ^{−1}	r_{PSCL}	r'_{PSCL}	95% confidence limit
Year	1.4 ± 1.1	0.43	−1.05 ± 0.35	0.75	0.79	0.54 : 0.96
Winter	−0.1 ± 2.4	0.02	−2.25 ± 0.59	0.82	0.81	0.52 : 0.97
Spring	3.9 ± 0.9	0.85	−1.09 ± 0.59	0.57	0.57	0.04 : 0.93
Summer	0.8 ± 0.4	0.54	−0.17 ± 0.22	0.28	0.33	0.02 : 0.70
Fall	1.1 ± 1.2	0.33	−0.98 ± 0.44	0.65	0.60	0.15 : 0.94

sunspot cycle. Hence, the regression model is reduced with one additional degree of freedom which results in $9 - 2 - 1 = 6$ degrees of freedom.

The lengths of solar cycles since 1900 are shown with an inverted scale in Figure 1 and can be compared with the Svalbard temperatures in Figure 3.

We recognize some qualitative similarities: the SCL shortened in 1910–20, while the average temperature, and in particular the winter temperature, increased until about 1935. When the SCL became longer around 1970 a temperature minimum appeared a few years later. The short period SC22 which ended early in 1996 was followed by a temperature maximum around 2005.

Correlating the 11-year averaged Svalbard MAAT with the lengths of the solar cycles shows that the correlation (r) increases in absolute value from 0.15 to 0.74 with increasing lags from 0 to 12 years (Figure 2). The correlation increases to $r = 0.79$ for the Svalbard yearly average temperature when the length of the previous solar cycle (PSCL) is correlated with the temperature in the next cycle, that is, observed solar cycles are used instead of 11-year intervals [3].

This motivates our choice of comparing the temperature in one solar cycle with the length of the previous cycle.

2.3. Correlations between the Length of a Solar Cycle and the Temperature in the Next Cycle. Linear least square fits between the length of a solar cycle and the average temperature in the next cycle (weighted with w_i) were done for the yearly and seasonal Svalbard mean temperature series

(Table 1). The resulting trends (β_{PSCL}) are shown in Table 2, and the linear fits obtained are shown in Figure 4.

Table 2 shows results of the model fitting for winter, spring, summer, fall, and the whole year temperatures for the following models:

- (i) temperatures explained as a function of time (secular trend) (Model 1),
- (ii) temperatures explained by the previous solar cycle (Model PSCL).

Analytical correlations coefficients (r) are calculated for Model 1 and Model PSCL, also shown in Table 2. There is no analytical expression to estimate the error in the correlation coefficient r .

We have therefore determined a correlation coefficient r' by the so-called “bootstrap method.” This is done by 1000 regression calculations on the N observations, by drawing sets of N observations (pairs of x_i, y_i) from the sample, and after each drawing return the observation to the sample. A regression coefficient is calculated for each new set, and the distribution of these regression coefficients is then analyzed. The mean value is the estimated nonparametric regression constant r' , and the 95% confidence interval is defined as the interval spanning from the 2.5th to the 97.5th percentile of the resampled r -values (r').

Comparing r and r' , we find they are on average 6% and maximum 18% different. The coefficient of determination r'^2_{PSCL} is a measure of the contribution of the PSCL model to the temperature variations. For the Svalbard year and

the winter mean temperatures $r^2_{\text{PSCL}} = 0.62 \pm 0.35$ within 95% confidence interval, which means that the Sun may contribute more than half to the temperature variations at Svalbard.

2.4. Examination of Correlations in the Residuals. The model fitting is not complete without examining the residuals. We have performed a Durbin-Watson (DW) statistical test [23–25] for serial correlation in the residuals—investigating if a positive error for one observation increases the chances of a positive error for another observation. The result is given in Table 3.

For two of the series, the yearly average and the winter temperatures, we find no autocorrelations in the residuals, which means that the model can be accepted by using the traditional statistical tests and confidence limits estimation without reduction of degrees of freedom. Then the β_{PSCL} parameter gives a complete description. This is also supported by the strong correlations $r_{\text{PSCL}} \approx 0.80$ for these series.

For the three other series: spring, summer, and fall, the DW test gives positive or negative autocorrelations, indicating that the linear relation found is not a complete description. These series should be further analyzed for development of better models. The Durbin-Watson tables [26] show lower and upper limits (D(L) and D(U)) based on number of observations and number of parameters excluding the intercept in the regression model.

The residuals from the PSCL-model are shown in Figure 5. For the winter temperatures the trend in the residuals $\beta_2 = -0.5^\circ\text{C}/100\text{ yr}$. The spring residuals show $\beta_2 = 3.2^\circ\text{C}/100\text{ yr}$, which is a small reduction from β_1 (Table 1). For the year mean residuals we get $\beta_2 = 1.1^\circ\text{C}/100\text{ yr}$.

2.5. Predictions for Mean Temperatures in Sunspot Cycle 24. Of the 5 series investigated, the yearly mean and the winter mean temperatures are completely described by the PSCL-model. This model can be used to give forecasts for SC24 based on SCL23. The resulting forecasts show that the mean yearly temperature will decrease from -4.2°C in SC23 to -7.8°C , with a 95% confidence interval $[-5.8; -9.6]^\circ\text{C}$ in SC24. This is the same result as with unweighted relations in SSH11 [15]. For the winter temperature the forecasts show a decrease from -11.2 in SC23 to -17.2°C with a 95% confidence interval $[-14; -20.5]$. These predictions are shown as diamonds in Figure 3. For the other series: spring, summer, and fall, the DW test and the less significance of the β_{PSCL} values make less confident predictions. They are shown as diamonds in Figure 4.

3. Discussion

Our main result is a strong correlation between the mean air temperature at Svalbard in a solar cycle and the length of the previous solar cycle. The relation is highly significant for the yearly and winter mean temperatures. This is documented by stringent statistical tests showing no significant autocorrelations in the residuals, and small standard deviations in

TABLE 3: Durbin Watson test on the autocorrelations in the PSCL model residuals.

Series	DW	Level result	Result
Year	2.10	4-D(U) > DW > D(U)	No autocorrelation
Winter	2.44	4-D(U) > DW > D(U)	No autocorrelation
Spring	0.56	DW < D(L)	Positive autocorrelation
Summer	0.64	DW < D(L)	Positive autocorrelation
Fall	3.24	DW > 4-D(L)	Negative autocorrelation

The number of observations in each series is 9. Because of inspection of the data on beforehand one degree of freedom has been subtracted which corresponds to 8 instead of 9 “effective” observations. The model has one parameter in addition to the intercept. Then the 5% significance levels for the DW test are $D(L) = 0.763$ and $D(U) = 1.332$. The DW test is considered to have no significant autocorrelations if $D(U) < DW < 4-D(U)$, indifferent if $D(L) < DW < D(U)$ and $4-D(L) > DW > 4-D(U)$, positive autocorrelations if $DW < D(L)$, and negative autocorrelations if $DW > 4-D(L)$.

the β_{PSCL} values, giving relations significant on the 95% level. For the spring and fall series the β_{PSCL} values are significant at about 80% level, depending on how the autocorrelations reduce the degrees of freedom. For the summer temperatures there is no significant PSCL relation. The differences through the seasons may partly be explained by local conditions.

The yearly and winter solar influence on the Svalbard temperature is estimated to $\approx 60\%$. The fact that there appears to be a clear solar influence on the air temperature in Svalbard during the winter may come as a surprise, as the Sun at $78^\circ 13' \text{N}$ is below the horizon from October 28 to February 14. Consequently, there is very little incoming solar radiation during the period December–February. Most likely, the explanation should be sought in the recurrent advection of warm air masses from lower latitudes across the North Atlantic towards Svalbard. This usually happens several times each winter and often results in marked temperature increases within few hours. In this way a solar temperature signal originating at lower latitudes may be recorded at Svalbard, even during the winter.

In the spring (MAM) the landscape at Svalbard is almost completely snow covered, which means that most of the incoming short wave radiation from the Sun will be reflected, which results in little direct solar warming in the spring. On the other hand spring is normally the driest period of the year and dominated by an Arctic anticyclone, which prohibits warm air advection from lower latitudes. Here is a marked difference between winter (DJF) and spring (MAM). The spring relation is modulated by ice or no ice in the fjord. In the summer, fall, and winter the fjord has been ice-free since 1912, but ice usually appears some times in the spring months (MAM). The increasing spring temperatures may be related to less ice in the fjord and the general reduction of the Arctic ice.

The summer air temperature recorded at Svalbard Airport is highly influenced by local wind conditions, partly controlled by a land-sea breeze effects because of relatively small regional air pressure differences during the summer. By this the summer air temperature is controlled mainly by local conditions in the neighbourhood of the meteorological station (topography, land surface characteristics, and surface

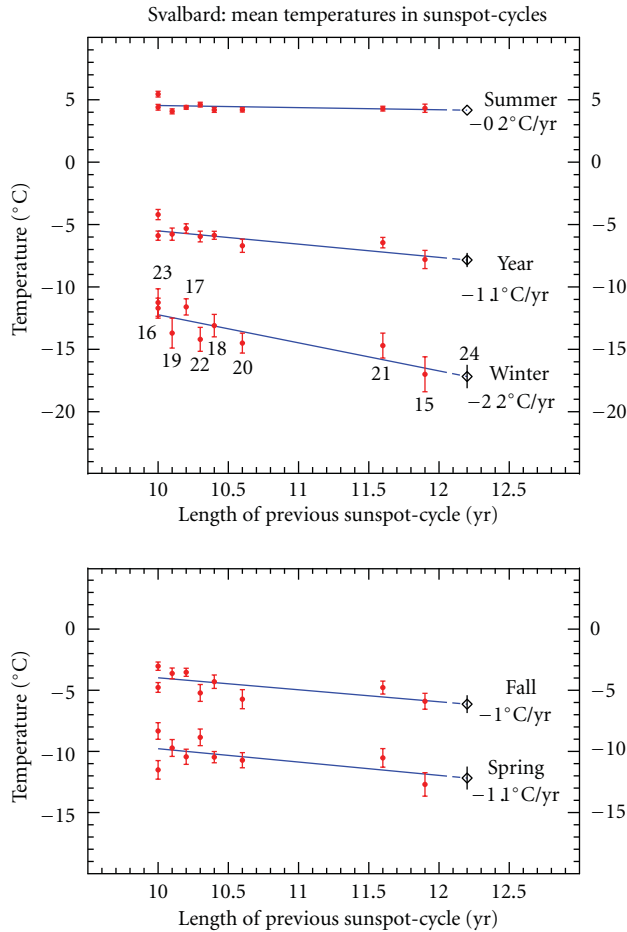


FIGURE 4: Residuals from PSCL model for the Svalbard temperature series and the seasonal series. The sunspot-cycle number is shown by the winter series.

temperature in the adjoining fjord), which are relatively stable from summer to summer.

Looking at the observed and averaged temperatures in Figure 3, we get the impression of a periodic variation with a period of about 70 years. This may be the low-frequency oscillation in the Arctic temperatures as determined by Polyakov et al. [22]. However, if we study the residuals in Figure 5, these oscillations have more or less disappeared. We may then speculate if they are related to solar variability described by the PSCL model. The remaining trend for the MAAT: $\beta_2 = 1.1^\circ\text{C}/100\text{ yrs}$ agrees with the trend $0.9 \pm 0.3^\circ\text{C}/100\text{ yrs}$, determined by Polyakov et al. [22] for the Arctic poleward of 62 N.

The strong trend in the spring residuals of $3.2^\circ\text{C}/100\text{ yrs}$ may be explained as a Polar amplification as described by Bekryaev et al. [27], who find stronger trends in Polar spring warming than for the other seasons. For the period 1901–2008, they find for the Northern Polar Area trends for the annual, winter, and fall temperatures, in agreement with our results (β_2). For the spring and summer they find trends of 1.6 and $0.88^\circ\text{C}/100\text{ years}$, which is in agreement with our summer residuals trend, but about one half of our spring

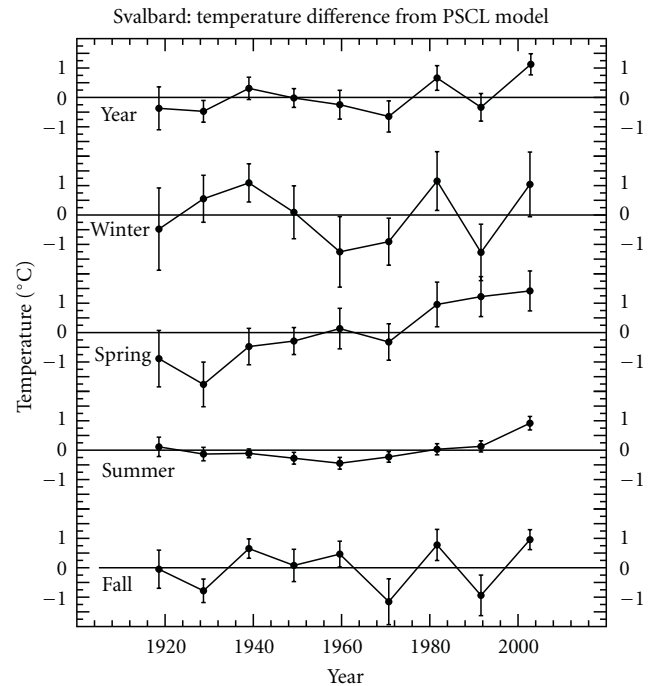


FIGURE 5: The average temperature during a solar cycle as a function of the length of the previous cycle for Svalbard yearly and seasonal mean temperatures 1914–2008. Trends (β_{PSCL}) are shown for each line. Solar cycle numbers are given for the winter series.

trend of $3.2^\circ\text{C}/100\text{ yrs}$. They find an increasing trend (Polar amplification) when they determine trends for recent periods 1959–2008 and 1979–2008, the latter with an annual trend of $6.4^\circ\text{C}/100\text{ yrs}$ [27]. We cannot confirm this result in our residual series, but agree to a possible explanation of the stronger amplification of the spring trends by an albedo-ice effect.

The result of our PSCL model, explaining more than 60% of the temperature variance for annual and winter temperatures for Svalbard, can be compared with a solar forcing well over 75% of the variance for the decadal smoothed Arctic mean or spring temperatures as determined by Soon [28]. His analysis is based on decadal and multidecadal reconstruction of Arctic, North of 62 N, temperatures from wavelet analysis and correlation of the reconstructed temperatures with solar TSI variations.

The lag of one solar cycle for the temperature response may have two explanations. The first is a relation between solar cycle length and the amplitude (R_{max}) of the next cycle as found by Solanki and Krivova [11], assuming a relation between R_{max} and temperature. This effect should be global. The other factor is the transport time of a solar signal with the Atlantic currents from the warm Caribbean to the West Coast of Svalbard. Analyzing sea temperatures in the Faroe-Shetland Channel and the Kola Section, Yndestad et al. [29] find a phase delay of 2 years for a lunar-tide signal. A solar irradiation signal from the Caribbean may therefore take several years to reach the Svalbard region. Increased sea temperature will also reinforce the advective fall and

winter warm air flows and explain seasonal differences at Svalbard. Additional arguments for this interpretation are the higher PSCL correlations found at the North Atlantic stations (Torshavn, Akureyri, Svalbard) than in coastal and inland regions of Norway by SSH11 [15].

Based on the PSCL relation we predict a temperature decrease at Svalbard of about $\approx 3.5^\circ\text{C}$ [$\pm 2^\circ\text{C}$ —95% confidence interval] in the period 2009–20 compared with the previous SC23. This drop is of the same order as a forecast based on the strongest temperature cycles in HSS12 [3]. For the average winter temperatures a temperature drop of $\approx 6^\circ\text{C}$ is estimated and shown in Figure 3 as a diamond with bars indicating the 95% confidence interval. In this figure also observed temperatures 2009–2011 are shown as broken lines, giving an impression that at least the winter temperature has decreased substantially already.

4. Conclusions

- (i) A linear relation exists in the temperature series from Svalbard between the length of a solar cycle and the average temperature in the next solar cycle.
- (ii) The yearly average and the winter temperatures can be modelled as a function of the length of the previous solar cycle, with highly significant negative trends. We call this the PSCL regression model.
- (iii) The residuals from the PSCL model show no positive autocorrelation using the Durbin Watson test. The estimated correlation coefficients between the observed temperatures and the temperature from the fit to the regression models are reasonably high for yearly average and winter temperatures. Also the uncertainty levels of the estimated correlations coefficients calculated by Bootstrap analysis are on an acceptable level. Hence, the winter model and the yearly average model are considered to be acceptable, which means that no additional variables are needed.
- (iv) A measure of the solar contribution is the coefficient of determination $r^2 \approx 0.6$ for the PSCL year and winter models. This indicates that about 60% of the temperature variation can be attributed to solar activity for the yearly average and the winter average temperatures.
- (v) For the average winter temperature the residuals show a negative linear trend, which indicates that cooling might have taken place the last 100 years if the solar activity did not increase as observed by the shortening of the solar cycle.
- (vi) The solar cycle/temperature relation (our Model PSCL) can, when a sunspot cycle is finished, be used to predict the temperature in the next solar cycle. For Svalbard it means an estimated cooling of $\approx 3^\circ\text{C}$ for the yearly average temperature from SC23 to the present SC24, which will last at least until 2020. The winter cooling will be $\approx 6^\circ\text{C}$. These predictions can test a possible solar-climate connection.

- (vii) This regression forecasting model benefits, as opposed to the majority of other regression models with explanatory variables, to use an explanatory variable—the previous sun cycle length—nearly without uncertainty. Usually the explanatory variables have to be forecasted, which of course induce significant additional forecasting uncertainties.
- (viii) The negative trends in the spring and fall PSCL models are significant on 80% level. With positive and negative autocorrelations in the residuals, one may expect also other variables could be present for these series. The spring model residuals show a significant secular trend of $0.032^\circ\text{C}/\text{yr}$, which indicates an amplification of some kind, probably related to diminishing Arctic and local ice cover in the spring season with an albedo effect. The residuals from the fall series show no significant trend. This may be explained by the nearby fjord (Isfjord) which never has been frozen in the fall and winter seasons since the start of the temperature series in 1912.

Acknowledgments

The Svalbard temperature data series used in this study was obtained from the *eKlima* Internet data portal run by the *Norwegian Meteorological Institute*. Håkon Stordahl is thanked for help with the Bootstrap programming and an anonymous referee for suggestions that helped the authors to improve the paper considerably.

References

- [1] G. Bond, B. Kromer, J. Beer et al., “Persistent solar influence on north atlantic climate during the Holocene,” *Science*, vol. 294, no. 5549, pp. 2130–2136, 2001.
- [2] L. J. Gray, J. Beer, M. Geller et al., “Solar influences on climate,” *Reviews of Geophysics*, vol. 48, no. 4, article RG4001, 2010.
- [3] O. Humlum, J.-E. Solheim, and K. Stordahl, “Spectral analysis of the Svalbard temperature record,” Submitted to *Advances in Meteorology*. In press.
- [4] W. Gleissberg, “A table of secular variations of the solar cycle,” *Terrestrial Magnetism and Atmospheric Electricity*, vol. 49, no. 4, pp. 243–244, 1944.
- [5] M. Waldmeier, “Die zonenwanderung der sonnenflecken,” *Astronomische Mitteilungen der Eidgenössischen Sternwarte Zürich*, vol. 14, no. 138, pp. 470–481, 1939.
- [6] R. H. Dicke, “Is there a chronometer hidden deep in the Sun?” *Nature*, vol. 276, no. 5689, pp. 676–680, 1978.
- [7] E. Friis-Christensen and K. Lassen, “Length of the solar cycle: an indicator of solar activity closely associated with climate,” *Science, New Series*, vol. 254, no. 5032, pp. 698–700, 1991.
- [8] P. Laut and J. Gundermann, “Solar cycle length hypothesis appears to support the IPCC on global warming,” *Journal of Atmospheric and Solar-Terrestrial Physics*, vol. 60, no. 18, pp. 1719–1728, 1998.
- [9] P. Thejll and K. Lassen, “Solar forcing of the Northern hemisphere land air temperature New data,” *Journal of Atmospheric and Solar-Terrestrial Physics*, vol. 62, no. 13, pp. 1207–1213, 2000.

- [10] P. Thejll, “Danish climate centre report,” Tech. Rep. 09-01, 2009.
- [11] S. K. Solanki, N. A. Krivova, M. Schüssler, and M. Fligge, “Search for a relationship between solar cycle amplitude and length,” *Astronomy and Astrophysics*, vol. 396, no. 3, pp. 1035–1029, 2002.
- [12] C. J. Butler, “Maximum and minimum temperatures at armagh observatory, 1844–1992, and the length of the sunspot cycle,” *Solar Physics*, vol. 152, no. 1, pp. 35–42, 1994.
- [13] C. J. Butler and D. J. Johnston, “A provisional long mean air temperature series for Armagh Observatory,” *Journal of Atmospheric and Terrestrial Physics*, vol. 58, no. 15, pp. 1657–1672, 1996.
- [14] D. Archibald, “Solar Cycle 24: Implications for the United States,” <http://www.davidarchibald.info/>, 2008.
- [15] J.-E. Solheim, K. Stordahl, and O. Humlum, “The long sunspot cycle 23 predicts a significant temperature decrease in cycle 24,” Submitted to *Journal of Atmospheric and Solar-Terrestrial Physics*, 2011. In press.
- [16] E. J. Førland, I. Hanssen-Bauer, and P. Ø. Nordli, “Climate statistics and long-term series of temperature and precipitation at Svalbard and Jan Mayen,” Tech. Rep. 21/97, The Norwegian Meteorological Institute, Norway, Oslo, 1997.
- [17] I. Hanssen-Bauer, M. Kristensen Solås, and E. L. Steffensen, “The climate of Spitsbergen,” Tech. Rep. 39/90, Norwegian Meteorological Institute, Norway, Oslo, 1990.
- [18] H. Alexandersson, “A homogeneity test applied to precipitation data,” *Journal of Climatology*, vol. 6, no. 6, pp. 661–675, 1986.
- [19] I. Hanssen-Bauer and J. Førland, “Homogenizing long Norwegian precipitation series,” *Journal of Climate*, vol. 7, no. 6, pp. 1001–1013, 1994.
- [20] P. Ø. Nordli, I. Hanssen-Bauer, and E. Førland, “Homogeneity analyses of temperature and precipitation series from Svalbard and Jan Mayen,” Tech. Rep. 16/96, The Norwegian Meteorological Institute, Norway, Oslo, 1996.
- [21] P. Frich, H. Alexandersson, J. Ashcroft et al., “North atlantic climatological dataset (NACD Version 1)—final report,” Tech. Rep. 96-1, Danish Meteorological Institute, 1996.
- [22] I. V. Polyakov, R. V. Bekryaev, G. V. Alekseev et al., “Variability and trends of air temperature and pressure in the maritime Arctic, 1875-2000,” *Journal of Climate*, vol. 16, no. 12, pp. 2067–2077, 2003.
- [23] J. Durbin and G. S. Watson, “Testing for serial correlation in least squares regression. I,” *Biometrika*, vol. 37, no. 3-4, pp. 409–428, 1950.
- [24] J. Durbin and G. S. Watson, “Testing for serial correlation in least squares regression. II,” *Biometrika*, vol. 38, no. 1-2, pp. 159–178, 1951.
- [25] J. Durbin and G. S. Watson, “Testing for serial correlation in least squares regression III,” *Biometrika*, vol. 58, pp. 1–19, 1951.
- [26] N. E. Savin and K. J. White, “The Durbin-Watson Test for Serial Correlation with Extreme Sample Sizes or Many Regressors,” *Econometrica*, vol. 45, pp.1989-1996, 1977. http://www.eco.uc3m.es/~ricmora/ecii/materials/durbin_watson_tables.pdf.
- [27] R. V. Bekryaev, I. V. Polyakov, and V. A. Alexeev, “Role of polar amplification in long-term surface air temperature variations and modern arctic warming,” *Journal of Climate*, vol. 23, no. 14, pp. 3888–3906, 2010.
- [28] W. Soon, “Variable solar irradiance as a plausible agent for multidecadal variations in the Arctic-wide surface air temperature record of the past 130 years,” *Geophysical Research Letters*, vol. 32, no. 16, article L16712, pp. 1–5, 2005.
- [29] H. Yndestad, W. R. Turell, and V. Ozhigin, *Deep Sea Research Part I: Oceanographic Research Papers*, vol. 55, 2008.

Research Article

Temperature and Precipitation Development at Svalbard 1900–2100

**Eirik J. Førland,¹ Rasmus Benestad,¹ Inger Hanssen-Bauer,^{1,2}
Jan Erik Haugen,¹ and Torill Engen Skaugen¹**

¹Norwegian Meteorological Institute, P.O. Box 43 Blindern, 0313 Oslo, Norway

²Telemark University College, P.O. Box 203, 3901 Porsgrunn, Norway

Correspondence should be addressed to Eirik J. Førland, eirik.forland@met.no

Received 26 September 2011; Revised 6 December 2011; Accepted 20 December 2011

Academic Editor: Stefania Argentini

Copyright © 2011 Eirik J. Førland et al. This is an open access article distributed under the Creative Commons Attribution License, which permits unrestricted use, distribution, and reproduction in any medium, provided the original work is properly cited.

Substantial variations in temperature and precipitation have been observed since the first permanent weather station was established in the Svalbard region in 1911. Temperature and precipitation development are analysed for the longest observational series, and periods with positive and negative trends are identified. For all temperature series, positive linear trends are found for annual values as well as spring, summer, and autumn series. A very strong winter warming is identified for the latest decades. Evaluation of temperature trends downscaled from global climate models forced with observed greenhouse gas emissions suggests that the downscaled results do span the observation-based trends at Svalbard Airport 1912–2010. Novel projections focussing on the Svalbard region indicate a future warming rate up to year 2100 three times stronger than observed during the latest 100 years. The average winter temperature in the Longyearbyen area at the end of this century is projected to be around 10°C higher than in present climate. Also for precipitation, the long-term observational series indicate an increase and the projections indicate a further increase up to year 2100.

1. Introduction

The Arctic land areas have over the last 2-3 decades experienced more warming than any other region on earth [1, 2]. This “Arctic amplification” may be due to feedback mechanisms from loss of sea ice [3] or changes in atmospheric and oceanic circulation [4]. Similarly, Serreze et al. [5] interpret the Arctic temperature anomalies for the most recent decade 2000–2009 as reflecting the combined effects of (1) a general background warming which is part of the planet’s response to positive radiative forcing, (2) anomalies in the atmospheric circulation, and (3) changes in characteristics of the surface, in particular, reduced sea ice extent and higher sea surface temperatures compared to climatology. Climate models [1, 2, 6] furthermore indicate that anthropogenic global warming also in the future will be enhanced in the northern high latitudes by complex feedback mechanisms in the atmosphere-ocean-ice system.

The most sophisticated tools for describing future long-term climate development are the atmosphere ocean general circulation models (AOGCMs). These models include a description of physical processes associated with the atmosphere, oceans, sea ice, and often land surface processes. The resolution in the AOGCMs is presently sufficient for modelling most of the large-scale features in the atmosphere, but in general still too coarse for reproducing the climate on regional or local scale.

For most studies of impacts of climate change, detailed scenarios are needed for specific locations, that is, with a much more detailed spatial resolution than the present simulations with global climate models. To get more site-specific climate projections for the Svalbard region, different downscaling techniques (dynamical and empirical-statistical) were used to “downscale” results from global climate models to regional and local scales. A large variety of national and international global climate model results (incl.

the CMIP3 ensemble [7]) were in this study downscaled for the Svalbard region and particularly for the Longyearbyen area.

In regional attribution studies for the Arctic, the importance of natural variability must be recognized. In climate model simulations, the Arctic signal resulting from human-induced warming is large but the variability (noise) is also large. As the signal-to-noise-ratio may be lower in the Arctic than at lower latitudes [8], most of the projections in this study are focussing on the end of the 21st century. In the Arctic, data scarcity and measuring problems are other important issues. To monitor the long-term variations of climate conditions in the Svalbard region, it is important to make optimal use of observational series from the region.

This paper describes the observed variations in temperature and precipitation during the latest 100 years (Section 2), methods and background data for applying AOGCMs to provide regional and local climate information (Section 3), projections of climate development in the Svalbard region up to year 2100 (Section 4), and examples of projected changes in daily temperatures in the Longyearbyen (Svalbard Airport) area (Section 5).

2. Observed Climate Development at Svalbard during the Last 100 Years

2.1. Temperature. The first permanent weather station at Svalbard was established in Green Harbour in 1911 [9]. During the last century, there have been several relocations of the different weather station in the Svalbard region (Figure 1) [10]. Because of large climate gradients and the harsh weather conditions, even small changes at Arctic measuring sites may cause substantial changes in measuring conditions. Identification of inhomogeneities in Arctic series is also complicated by the sparse station network. The present temperature measurements at Svalbard Airport and Ny-Ålesund have been performed at the same sites since 1975, but by combining several series, homogenised, composite temperature series are established for the Longyearbyen/Svalbard Airport area back to 1911 and for Ny-Ålesund back to 1934 [9–11].

Table 1 shows that the average annual temperature in the “standard normal period 1961–90” [12] range from -2.4°C for Bjørnøya to -6.7°C at Svalbard Airport, and with average winter temperatures of -15 to -13°C for the Spitsbergen stations. Up to the most recent normal period 1981–2010 [12], Table 1 shows an increase in average annual temperatures of $1\text{--}2^{\circ}\text{C}$. The average winter temperatures have increased by 3.5°C at both Hopen and Svalbard Airport, while the summer increases at all stations are between $0.5\text{--}1.0^{\circ}\text{C}$.

The time series of annual mean temperatures for the stations in the Svalbard region show a quite similar long-term pattern (Figure 2). The temperature has increased in all seasons (cf. Table 2) with the strongest increase in winter and spring. The smoothed graphs indicate that there is variability on a multidecadal scale, leading to mainly positive temperature trends before the 1930s, then a relatively warm period during the subsequent two decades, a temperature

decrease from the 1950s to the 1960s, and thereafter a general temperature increase. These features are discussed by Hanssen-Bauer [13] and are also seen for other parts of the Arctic (e.g., [14]). Although data coverage was limited in the Arctic in the first half of the 20th century, the spatial pattern of the earlier warm period in the 1930s and 1940s appears to have been different from that of the current warm anomaly. In particular, the current warm period is partly linked to the Northern Annual Mode and affects a broader region [14].

While the dynamics of the warming in Svalbard prior to the 1930s is still not fully understood, the warming from the 1960s to the mid 1990s is clearly linked to atmospheric circulation patterns favouring increased southerly and south-westerly winds in the Svalbard area [15]. This agrees well with Rigor et al. [16] who state that more than half the warming over the eastern Arctic Ocean and the cooling over the Labrador Sea from the 1970s to the 1990s is accounted for by the Arctic Oscillation (AO), and Polyakov et al. [14] who state that the Northern Annual Mode is partly responsible for the Arctic warming in this period. The latest decade, however, show rather different patterns. While 5 of the 10 warmest winters in the Svalbard Airport composite series occurred after 2000 (2005, 2006, 2007, 2008, and 2010), several of these winters were characterised by average or even low AO mode. Recently it is suggested [17, 18] that the recent loss of Arctic sea ice is responsible for the high Arctic temperatures these later years, not only by directly contributing to altering the heat budget of the atmosphere in the area, but also by leading to a modification of large scale atmospheric circulation towards the “Warm Arctic-Cold Continents” wind pattern.

Linear trends (Table 2) were used to quantify the temperature development in Svalbard, even though there is certain scepticism against using linear trends as a measure for climate change, because such changes not necessarily occur linearly [19]. Also, linear trends for short time series are sensitive to the start and ending points. Earlier studies (e.g., [1]) have shown that the longest Arctic series by optimal choice of breaking points can be divided into three periods where the first and the last show statistically significant warming, while the middle period shows statistically significant cooling, cf. Figure 2. In order to make the trends for the stations in the Svalbard region directly comparable in different periods, the present study does not use these “optimal periods,” but rather linear trends for four ~ 23 -year periods where several stations were running simultaneously (1920–1942, 1943–1965, 1966–1988, and 1989–2011), Table 2.

In the first period (1920–1942), the composite Svalbard Airport series show a warming (annually and during autumn and winter). The huge warming of the Arctic in the decades before the 1940s is often called “early 20th century warming” and is one of the most spectacular climate events of the twentieth century [20]. In the next period (1943–1965), all stations tend to show negative trends in annual temperatures. The cooling was particularly strong ($1.5\text{--}1.8^{\circ}\text{C}$ per decade in the composite Ny-Ålesund and Svalbard Airport series) during the winter season. For the last two periods (1966–1988 and 1989–2011), there has been a warming at all stations and during all seasons, except for a minor cooling at

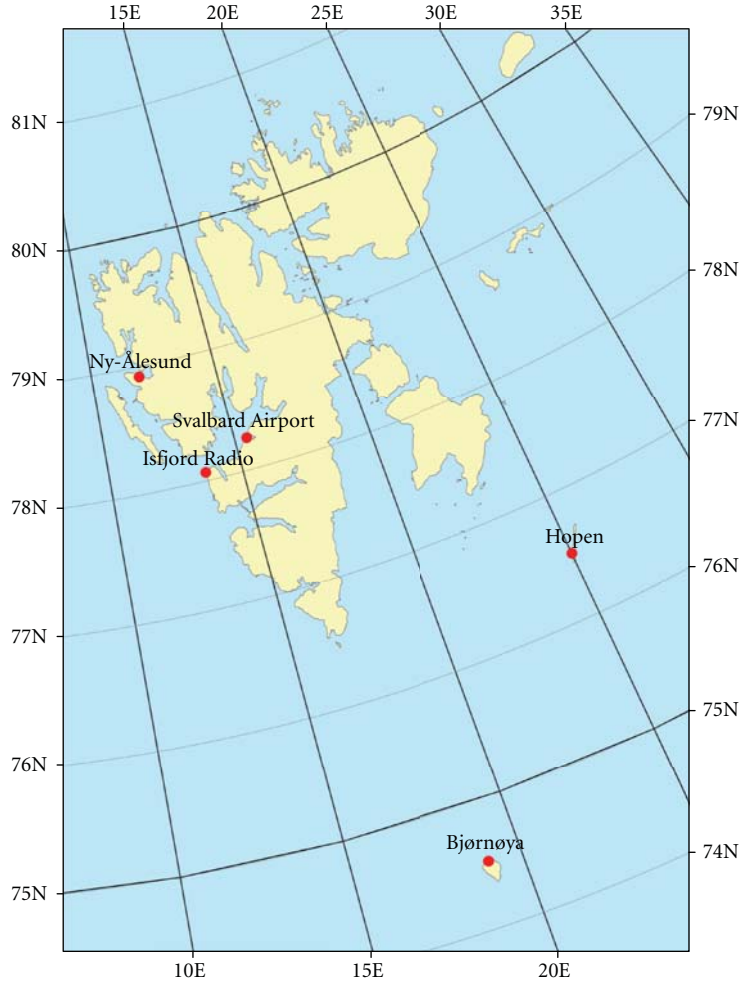


FIGURE 1: Map of the Svalbard region including weather stations used in the analysis.

TABLE 1: Average annual and seasonal temperatures (°C) during 1961–90 and 1981–2010.

Station	1961–1990					1981–2010				
	Annual	Winter	Spring	Summer	Autumn	Annual	Winter	Spring	Summer	Autumn
Ny-Ålesund	-6.3	-13.8	-9.8	3.4	-5.3	-5.2	-12	-8.5	3.8	-4.4
Svalbard Airport	-6.7	-15.1	-10.8	4.2	-5.2	-4.6	-11.7	-8.3	5.2	-3.5
Hopen	-6.4	-13.4	-9.9	1.3	-3.8	-4.3	-9.9	-7.6	2.3	-1.9
Bjørnøya	-2.4	-7.6	-4.8	3.5	-0.5	-0.9	-5.1	-3.4	4.4	0.6

Bjørnøya during summer 1966–88. The annual temperature increase at Svalbard Airport and Hopen during the latest two decades is close to 1.2°C per decade, and the warming during the winter season (2–3°C per decade) is substantially higher than during the “early 20th century warming.”

The trends for the optimal series (Table 2, bottom) show that the annual mean temperature has increased significantly in the Svalbard Airport/Longyearbyen area since 1912. The linear trend indicates an increase in mean annual temperature of 2.5°C during the latest 100 years, which is about three times the estimated global warming [2] during the

same period. The warming has also accelerated considerably since the increase of 0.14°C per decade from 1912 to 2000 reported by Hanssen-Bauer [13]. Also at Bjørnøya and Hopen, there are statistically significant positive trends in annual temperatures for the optimal series. The composite Ny-Ålesund series starts in the relatively warm 1930s, and thus there is no statistically significant warming in the optimal annual series from this station.

For the optimal series, all stations have statistically significant warming trends (0.27–0.46°C per decade) during spring. This reflects the fact that spring temperatures have

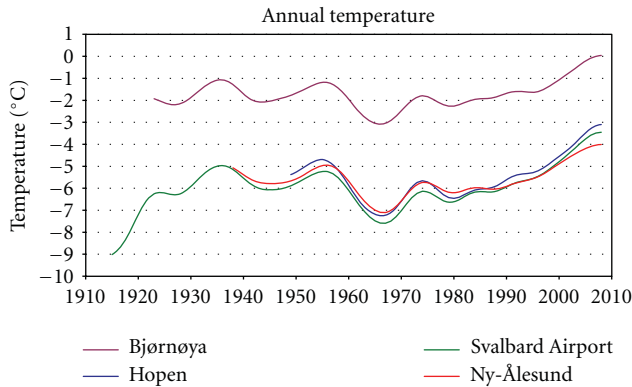


FIGURE 2: Annual temperature development at weather stations in the Svalbard region. The lowpass filtered series are smoothed by Gaussian weighting coefficients and show variability on a decadal time scale. The curves are cut three years from start and end.

increased more evenly throughout the century than, for example, the winter temperature. During 1912–2011 pronounced warming (statistically significant at the 5% level) at Svalbard Airport has occurred in spring, summer, and autumn.

For the period 1975–2011, it is possible to compare recent trends when all stations were running at the present sites. The linear trends in Table 2 indicate that during this 37-year period, the annual temperature at the four stations has increased by 2.7–4.0°C, and the winter temperature by 4.8–6.5°C.

2.2. Precipitation. Observations suggest that total annual precipitation has increased by roughly 14% in the Arctic north of 60°N over the past century [1]. The greatest increases were observed in autumn and winter. However, uncertainties in measuring precipitation in the harsh Arctic environment [22] and the sparseness of data in parts of the region limit confidence in these results. There are large regional variations in precipitation across the Arctic, and also large regional variations in the changes in precipitation. According to ACIA [1], the precipitation increased by about 2% per decade during the Arctic warming in the first half of the 20th century (1900–1945), with significant trends in the Nordic region. During the two decades of Arctic cooling (1946–1965), the high latitude precipitation increase was roughly 1% per decade. Since 1966, annual precipitation has increased at about the same rate as during the first half of the 20th century. Also, IPCC [2] states that there has been a widespread increase in precipitation over northernmost Europe during 1900–2005.

The harsh weather conditions (e.g., blowing and drifting snow, undercatch in precipitation gauges during snowfall, and high wind speeds) complicate precipitation measurements in the Arctic [10, 13, 22]. To reduce inhomogeneities because of instrumental changes, manual precipitation measurements are still performed at the stations used in this paper. Studies of long-term precipitation variability in the Svalbard region are hampered by several relocations of

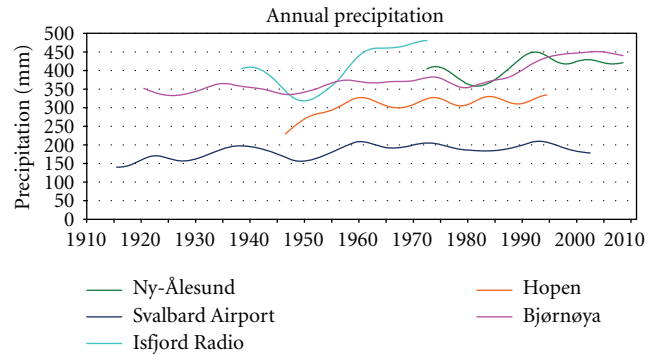


FIGURE 3: Annual precipitation development at weather stations in the Svalbard region. The lowpass filtered series are smoothed by Gaussian weighting coefficients and show variability on a decadal time scale. The curves are cut three years from start and end.

gauges. The precipitation gauge in Longyearbyen was moved to Svalbard Airport in 1975, but based on measurements at several sites, a composite, homogenised precipitation series back to 1912 was established by Nordli et al., 1996 [11]. However, this series is not homogenised after a new relocation in 2005. Also the Hopen series are not homogenised after relocation of the precipitation gauge in 1997.

The average annual precipitation at Ny-Ålesund is more than twice as high as at Svalbard Airport (Table 3). At Svalbard Airport and Ny-Ålesund, the recent average spring and summer precipitation is slightly lower than during the standard normal period 1961–1990, while there is an increase during autumn and winter. For Ny-Ålesund and Bjørnøya, the average annual precipitation during 1981–2010 is 10%, respectively, 20% higher than during 1961–1990.

The precipitation series from the Norwegian high-Arctic stations show quite different individual long-term patterns both on an annual as well as a decadal timescale (Figure 3). This is in contrast to the quite similar development for temperature, and the main reason is that precipitation varies locally on a smaller spatial scale than air temperature. However, the series have one common feature: all series show a positive trend in annual precipitation throughout the period of observations (cf. Table 4). Hanssen-Bauer and Førland [15] showed that the precipitation trend at Svalbard Airport from 1912 to the 1990s to a large degree could be explained by variations in the atmospheric circulation in the same period. The trends in annual precipitation at Svalbard Airport and Bjørnøya are statistically significant even at the 1% level. At Svalbard Airport, the annual measured precipitation has in average increased by 2% per decade, while the increase at Bjørnøya and Ny-Ålesund is 3–4% per decade. At Svalbard Airport, the summer and autumn precipitation show a pronounced increase (statistically significant at the 5% level), while on Bjørnøya, a marked increase has taken place during winter, spring, and autumn, (Table 4). During 1975–2011 when the measurements at Bjørnøya and Ny-Ålesund were performed at the present sites; positive trends are found for annual, autumn, and winter precipitation (Table 4, bottom).

TABLE 2: Linear temperature trends ($^{\circ}\text{C}$ per decade) in different time periods for stations in the Svalbard region. Trends significant at the 5% level are bold (Mann-Kendall nonparametric test [21]).

	Location	Annual	Winter	Spring	Summer	Autumn
1920–1942	Svalbard Airport*	0.34	1.23	0.09	−0.28	0.47
	Bjørnøya	0.14	−0.55	−0.35	0.18	0.66
1943–1965	Ny-Ålesund*	−0.26	−1.48	0.07	0.04	0.39
	Svalbard Airport*	−0.35	−1.76	−0.22	−0.00	0.58
	Bjørnøya	−0.33	−0.91	−0.19	−0.29	0.14
1966–1988	Ny-Ålesund*	0.38	0.54	0.73	0.10	0.51
	Svalbard Airport*	0.52	0.72	0.96	0.27	0.48
	Hopen	0.26	0.00	0.49	0.14	0.57
	Bjørnøya	0.34	0.53	0.71	−0.03	0.36
1989–2011	Ny-Ålesund	0.99	2.52	0.46	0.50	0.78
	Svalbard Airport	1.25	2.88	0.60	0.76	1.14
	Hopen	1.21	2.89	0.46	0.18	1.50
	Bjørnøya	0.91	2.01	0.86	0.32	1.14
1975–2011	Ny-Ålesund	0.73	1.36	0.60	0.33	0.53
1975–2011	Svalbard Airport	1.04	1.66	0.98	0.55	0.86
1975–2011	Hopen	1.10	1.76	1.02	0.43	1.00
1975–2011	Bjørnøya	0.76	1.30	0.59	0.39	0.62
1935–2011	Ny-Ålesund*	0.11	−0.02	0.27	0.09	0.07
1912–2011	Svalbard Airport*	0.25	0.25	0.46	0.11	0.19
1946–2011	Hopen	0.31	0.31	0.44	0.22	0.23
1920–2011	Bjørnøya	0.11	0.02	0.29	0.08	0.05

*The Svalbard Airport and Ny-Ålesund series are homogenised composites from other sites before 1975, respectively, 1969 [11].

TABLE 3: Average precipitation totals (in millimetres) during 1961–90 and 1981–2010.

Station	1961–1990					1981–2010				
	Annual	Winter	Spring	Summer	Autumn	Annual	Winter	Spring	Summer	Autumn
Ny-Ålesund	385	99	86	84	116	427	132	78	82	136
Svalbard Airport*	190	52	40	51	49	191	55	31	47	58
Hopen	476	135	97	104	140	NA	NA	NA	NA	NA
Bjørnøya	369	92	67	89	121	442	135	94	78	136

*The relocation of the gauge at Svalbard Airport in 2005 has minor influence on the 30-year average 1981–2010.

Though the long-term trends in annual precipitation tend to be positive at the Svalbard stations, the precipitation level seems to have been rather constant during the latest two decades (Figure 3), in spite of the fact that temperatures have continued to rise. This may have connection with the regime shift in the large-scale atmospheric circulation in the area, suggested by Overland and Wang [17].

3. Downscaling of Global Climate Models in the Norwegian Arctic

The comprehensive atmosphere ocean general circulation models (AOGCMs) are the most sophisticated tools available for projecting global climate development. These models provide a description of atmospheric, oceanic, sea ice, and often land surface processes in terms of a set of equations describing the essential physics and dynamics.

Different AOGCMs give differences in climate projections, and the major reason for this is different initial conditions, resolutions, and differences in parameterizations [2]. At higher latitudes, the natural variability is large and can explain much of the differences in AOGCM simulations [23]; however, the differences between different models can partly be attributed to the earth's geometry, lower degrees of freedom, and sampling fluctuations [24]. Another reason for the high climate variability in the Arctic is feed-back mechanisms connected to snow and ice.

The resolution in the AOGCMs is presently probably sufficient for modelling most of the large-scale features, but in general still too coarse to enable these models to reproduce the climate on regional or local scale. When more detailed climate data are needed, for example for impact studies, output from AOGCMs can be downscaled by dynamical or statistical techniques. An important (though not the only)

TABLE 4: Linear precipitation trends (% per decade) in the Svalbard region. Trends significant at the 5% level are bold. The statistical significance of the trends was tested by the Mann-Kendall nonparametric test [21]. The trend analysis for Svalbard Airport and Hopen do not include the latest years because of relocation of gauges. Absolute trends in millimetres may be deduced by combining with the 1961–1990 averages in Table 3.

Station	Period	Annual	Winter	Spring	Summer	Autumn
Ny-Ålesund	1969–2011	4.2	8.9	0.2	−3.6	9.1
Svalbard Airport*	1912–2005	1.9	−0.3	1.5	3.1	3.4
Isfjord Radio	1935–1975	8.0	11.2	8.4	8.5	9.6
Hopen	1946–1997	4.6	7.1	7.2	2.9	1.3
Bjørnøya	1920–2011	3.3	4.6	5.6	0.8	2.7
Ny-Ålesund	1975–2011	5.4	15.6	−2.7	−5.1	10.9
Bjørnøya	1975–2011	9.4	13.3	15.1	2.0	8.8

*The Svalbard Airport series is a homogenised composite from other locations before 1975 [11].

condition for making realistic local climate projections, is that the AOGCM used for downscaling gives a reasonably good description of the present climate in the Arctic. Though no single AOGCM can be said to be “best” to use in an assessment of the Arctic, Walsh et al. [25] have evaluated and ranked 15 of the IPCC [2] models according to their ability to reproduce the observed sea level pressure, temperature, and precipitation.

3.1. Regional Climate Models (Dynamical Downscaling). Output from AOGCMs can be used to drive regional climate models (RCMs) that have more detailed process representations compared to AOGCMs in addition to a much higher spatial resolution. The regional climate model HIRHAM has earlier been applied over the Nordic region [26] and in a transient climate simulation over Greenland and adjacent seas [27]. Successful implementation of an RCM depends on a number of conditions, for example, nesting strategy, domain size, difference in resolution between the AOGCM and RCM, the physical parameterisations, quality of the driving data, and spinup time. Generally, an RCM cannot be expected to improve errors in the AOGCM results on a large scale but should be able to develop small-scale features, at least due to more realistic surface forcing. As for its global counterpart, it is certainly necessary to realistically simulate present climate. Observed data can then be used for validation, as a first attempt to trust the output from climate change experiments.

Most European and Nordic RCM simulations do not cover the Norwegian Arctic, for example, in the large European ENSEMBLES project (www.ensembles-eu.org), the northern border for the domain was just north of the Norwegian mainland. A new regional climate model (NorACIA-RCM, spatial resolution 25×25 km) focussing on the Svalbard region was therefore established [28]. To evaluate whether the NorACIA-RCM gave a realistic description of the climate within the model domain, the RCM was run with input from a reanalysis dataset (ERA40) covering the period 1958–2002 [29]. The conclusion of comprehensive NorACIA-validations was that the present-day simulations gave a reasonable description of the observed

daily precipitation and temperature climate in the region [28]. It is worth mentioning that the climate signal around Svalbard is highly sensitive to the seasonal cycle in sea surface temperature and ice cover. In the NorACIA-RCM, this was specified from the global coupled ECHAM4/OPYC sea-ice module but modified around Svalbard due to more realistic representation of land-sea mask in the RCM.

The spatial resolution of RCMs is too coarse to provide representative information on a local scale. Empirically adjustment of the RCM output is therefore necessary to obtain site-specific projections. Different methods are available, for example, delta change methods, transformation of distribution functions, and so forth. In this study, local series of daily temperature and precipitation were derived from the RCMs as described by Engen-Skaugen [30]. This method applies monthly adjustment factors for the mean value and variance based on differences between daily values from RCM control runs and observations of temperature and precipitation for “the control period” (1961–1990).

3.2. Empirical/Statistical Downscaling. Empirical-Statistical downscaling (ESD) identifies empirical links between large-scale patterns of climate elements (predictors) and local climate (predictands), which are then used to predict local changes from the output from global or regional climate models. Successful downscaling depends on the following conditions: (1) the climate model should reproduce the large-scale predictor fields realistically, (2) the predictors should account for a major part of the variance in the predictands, (3) the links between predictors and predictands should be stationary, and (4) when applied in a changing climate, predictors that “carry the climate signal” should be included [31].

The philosophy behind empirical downscaling is that the local climate partly is a result of local conditions that are quite constant (e.g., topography and vegetation), and partly of large-scale weather patterns. In a comparison of results from empirical downscaling and regional climate modelling for Scandinavia, Hanssen-Bauer et al. [32] concluded that there were few statistically significant differences between the results. Empirical downscaling may catch several local

features that are not “resolved” in the present regional climate models. On the other hand, the regional climate models provide better temporal resolution as well as a number of climate variables which the empirical downscaling is not able to reproduce. Another limitation is that basically the empirical downscaling may just be used for localities with observational time series long enough to develop robust relationships between local climate and large-scale patterns. However, it is possible to add information in space through geographical interpolation based on ESD results for single sites [33]. Description of methodology and results for the empirical-statistical downscaling for the Norwegian Arctic are published in Benestad [34, 35] and Førland et al. [28, 36].

The ESD analysis for the Norwegian Arctic incorporated multimodel dataset (MMD) ensembles based on 48 integrations for temperature and 43 for precipitation. This model ensemble includes both simulations for the 20th century (20C3M) and scenario runs for the 21st century following the emission scenarios A1B [37]. The analysis performed by Benestad [34] involved new ways of combining observations from the 20th century with projections for the 21st century, and a quality control was used to “weed out” global climate models with a poor reproduction of present climate. The results were found to be sensitive to the choice of predictor domain, but smaller domains were taken to be more reliable. Some of the AOGCMs have been used to make several parallel runs, differing only by using different initial conditions (starting point). The ESD was applied to the MMD ensemble for both the 20th century and the 21st century simulations separately.

4. Climate Projections for the 21st Century

4.1. Air Temperature. Earlier temperature projections for the Arctic [1] indicate that by the end of the 21st century, Arctic mean annual temperature increases are 7°C and 5°C for the A2 and B2 emission scenarios [37], respectively, compared to the present climate. The multimodel dataset used in the regional climate projections for IPCC [2] projected an annual warming of the Arctic of 5°C at the end of the 21st century, but with a considerable across-model range of 2.8°C to 7.8°C. Over both ocean and land, the largest warming is projected in winter, and the smallest in summer. By the end of the century, the mean warming in the IPCC [2] projections ranges from 4.3°C to 11.4°C in winter and from 1.2°C to 5.3°C in summer under the A1B emission scenario.

The NorACIA-RCM was run for the Norwegian Arctic with input from six AOGCM simulations (cf. Table 5), while ca. 50 ESD projections [35] were performed for the weather stations in the Svalbard region based on the CMIP3 ensemble of global model runs [7]. Figure 4(a) shows projected spatial changes in mean annual temperature for the MPIB2 simulation. The results in Figure 5 demonstrate that this simulation is close to the median value for the 50 ESD-integrations. Figure 4(a) indicates that up to the end of this century, there will be an increase in annual temperature of 1.5–2.0°C southwest of Spitsbergen. The largest increase (6–8°C) is projected for the north-eastern parts of Svalbard, and between Spitsbergen and Novaja Zemlja. The smallest

seasonal changes (not shown) are projected for the mean summer temperature. For autumn, winter, and spring, a large increase is projected east and northeast of Svalbard. The projected decrease in sea-ice coverage will largely influence the temperature in the lower atmosphere, and this is the main reason for the large gradient in temperature increase from south-western to north-eastern parts of the Svalbard region.

For comparison with the station-based ESD-values, the results from the six RCM-simulations (Table 5) were interpolated to the locations of the Svalbard weather stations [36]. The quality of the ESD-results for the Arctic depends on the realism both in the re-analysed datasets and in the AOGCMs [35]. The climate description in the re-analyses may be misleading because of the scarcity in observations from the Arctic [38].

For most of the stations analysed in the Svalbard region, there was good accordance between the ESD and RCM-simulations [28, 36]. Combined results from the ESD and RCM simulations are shown in Figure 5 for Svalbard Airport/Longyearbyen. The thick line represents the ensemble median for the 48 ESD simulations. The coloured symbols indicate that most of the median values based on interpolated RCM values are quite close to the ESD median. The vertical bars give a measure for how the year-to-year variability is reproduced in the RCM simulations. The pink region indicates the 5–95 percentile range of the intermodel and internal variations in the ESD simulations. The large spread is mostly due to the pronounced interannual variability that characterises the Arctic and also reflects intermodel (AOGCM) differences. These results provide a basis for describing uncertainties associated with the projections [33]. The figure also illustrates that temperatures which in present climate would have been characterised as “extremely high” will according to these results be found in the lower part of the temperature distribution for the end of this century.

The ESD simulations for the period 1900–2000 are carried out for historical runs (20C3M) where the AOGCMs have been forced with observed emissions. As the RCM and ESD results are presented as 5–95% intervals, it should be expected that about 90% of the observation-based values (black dots) should be inside the hatched area if the models are able to reproduce the variance realistically. For Svalbard Airport (Figure 5), this mostly seems to be the case. However, it seems as if the ESD models are not able to reproduce the warmest winters during the 1930s to 1950s, nor the coldest seasons.

To compare modelled and observed historical trends, a linear trend fit was carried out for each realisation of the downscaled CMIP3 run that had results for both the 20th and 21st centuries. The trends associated with the ESD results were estimated for the same time interval as the optimal observational series from Svalbard Airport/Longyearbyen (Table 2). The CMIP3 trend distribution was approximately normally distributed according to a normal quantile-quantile plot, and a normal probability distribution function (PDF) was, therefore, used to estimate the similarity between the observed linear trends and corresponding downscaled trends. The PDFs are shown in Figure 6, together with the observed trend. The probabilities shown under each

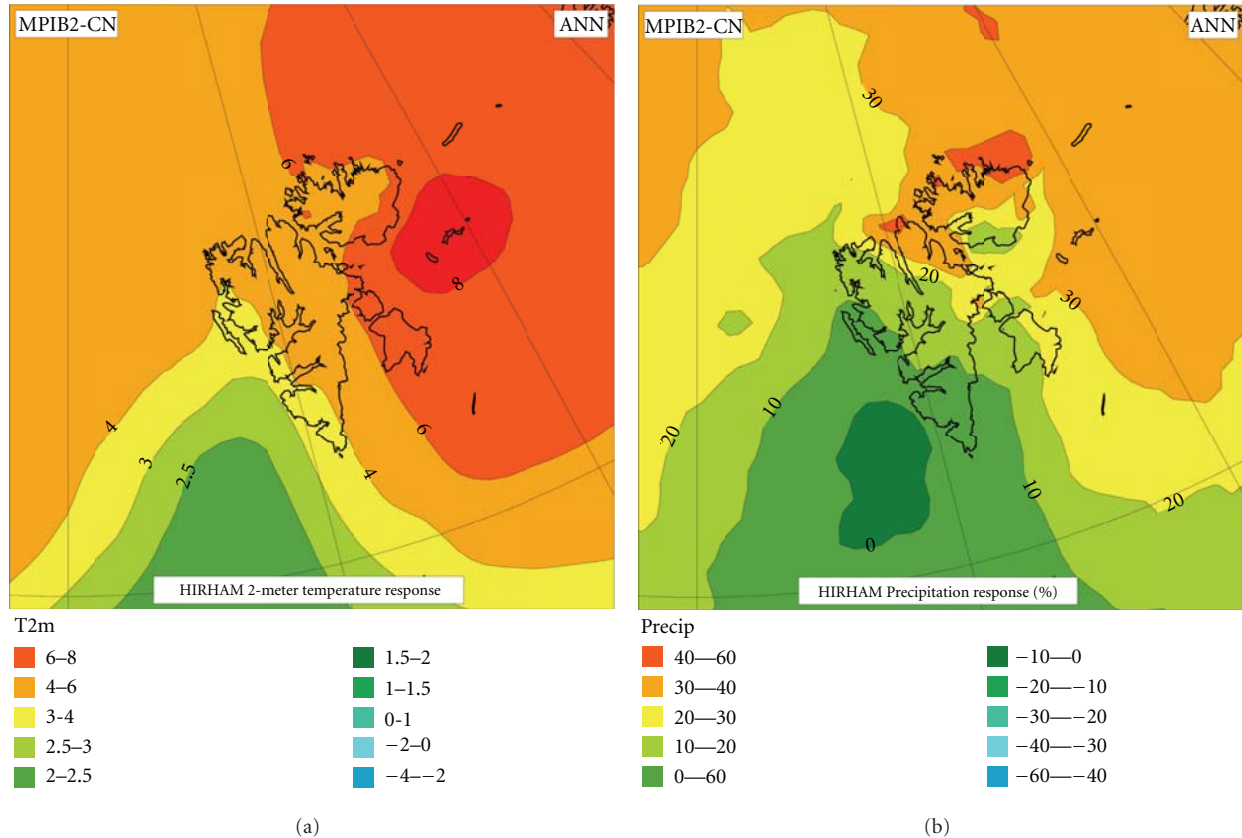


FIGURE 4: Projected changes from 1961–90 to 2071–2100 in (a) mean annual temperature ($^{\circ}\text{C}$), (b) mean annual precipitation (%). The RCM projections are based on MPIB2 (cf. Table 5).

TABLE 5: RCM simulations for the Svalbard region. The simulations were performed by the regional climate model HIRHAM2/NorACIA [28].

Global model	Emission scenario [35]	Control		Scenario	
		Period	Acronym	Period	Acronym
Max-Planck Inst.	IS92a	1981–2010	MPI92a	2021–2050	MPI92b
ECHAM4	SRES B2	1961–1990	MPICN	2071–2100	MPIB2
Hadley Centre	SRES A2	1961–1990	HADCN	2071–2100	HADA2
HadAM3H	SRES B2	1961–1990	HADCN	2071–2100	HADB2
Hadley Centre	SRES A1 B	1961–1990	HADA1	2021–2050	HADA1b
HadCM3	SRES A1B	1961–1990	HADA1	2071–2099	HADA1c

panel indicate which quantile in the downscaled results that matches the observed trend. For all seasons, the observed trend falls within the 10–90 confidence interval, suggesting that the downscaled results do span the observations. This comparison constitutes an evaluation of the downscaled warming trends for the past from the CMIP3 runs, but it does not validate the realism in trends for the future. The large spread in modelled historical trends indicates that the CMIP3 ensemble contains some models with unrealistic results for the Svalbard region and implies that large uncertainties are linked to projected trends for future climate.

Projected changes in percentiles of annual and seasonal temperatures for the ensembles of ESD (48 members) and RCM (4 members valid for 2071–2100) simulations are summarised in Table 6. The RCM data was calibrated before computation of percentiles; for each pair of control/scenario, the data were adjusted from the difference between the control and the mean of all control simulations 1961–1990. For Svalbard Airport/Longyearbyen, the 50-percentiles for annual mean temperatures indicate an increase of almost 7°C from 1961–1990 to 2071–2100. For winter temperatures, the 50-percentile is around 10°C higher in the 2071–2100 period. The increases in the annual 50-percentile at Bjørnøya in the

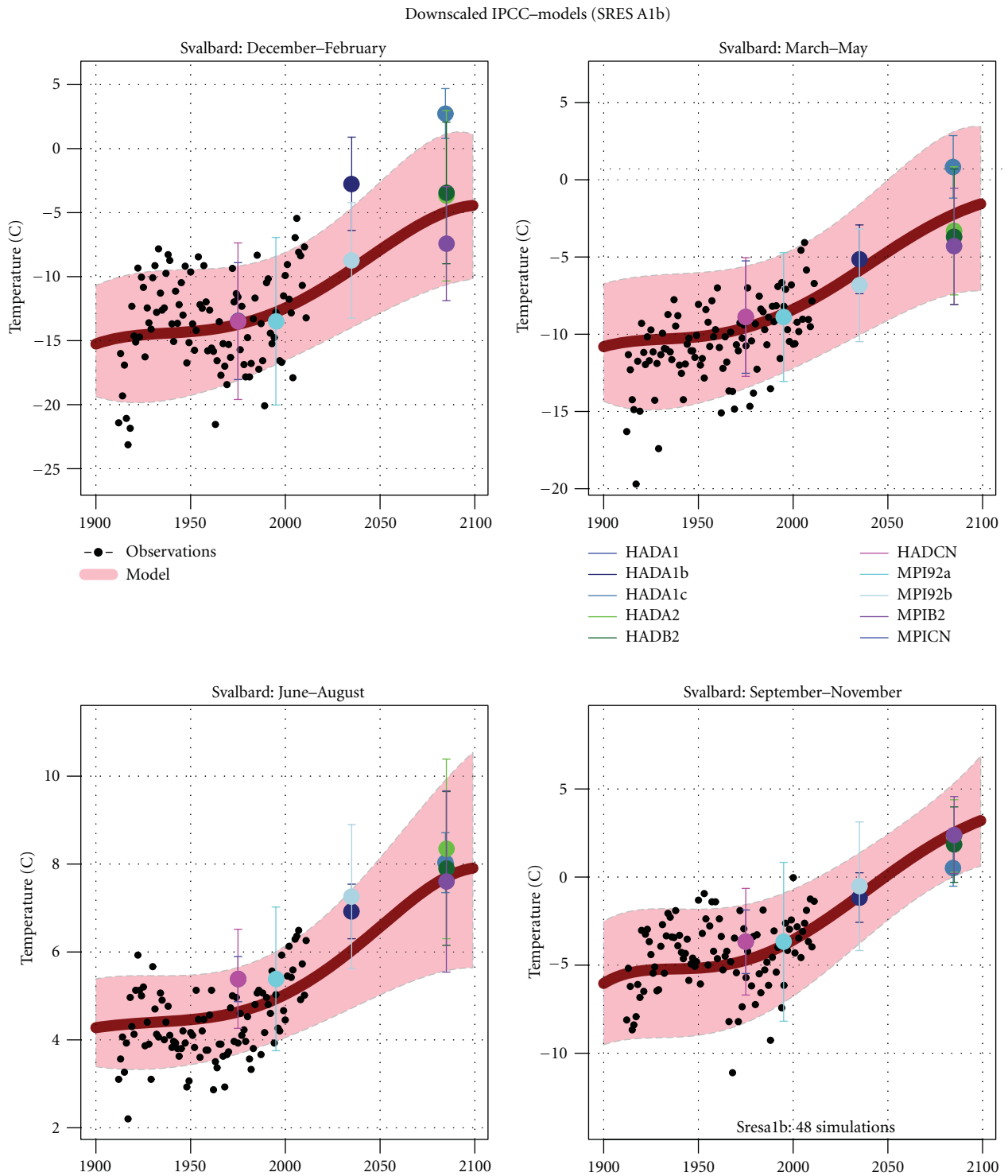


FIGURE 5: Temperature projections for Svalbard Airport/Longyearbyen: results from ESD and RCM downscalings for winter, spring, summer, and autumn. The hatched area (pink) shows 5% and 95% interval from ESD estimates, the black dots show observed values, and the thick line (red) show median (50%) value for the ESD ensemble. The coloured symbols indicate the median value for the different runs with NorACIA-RCM, and the vertical lines show the 5- and 95-percentiles for the RCM runs. The RCM values are plotted on the central year in the respective time slices. For acronyms, see Table 5.

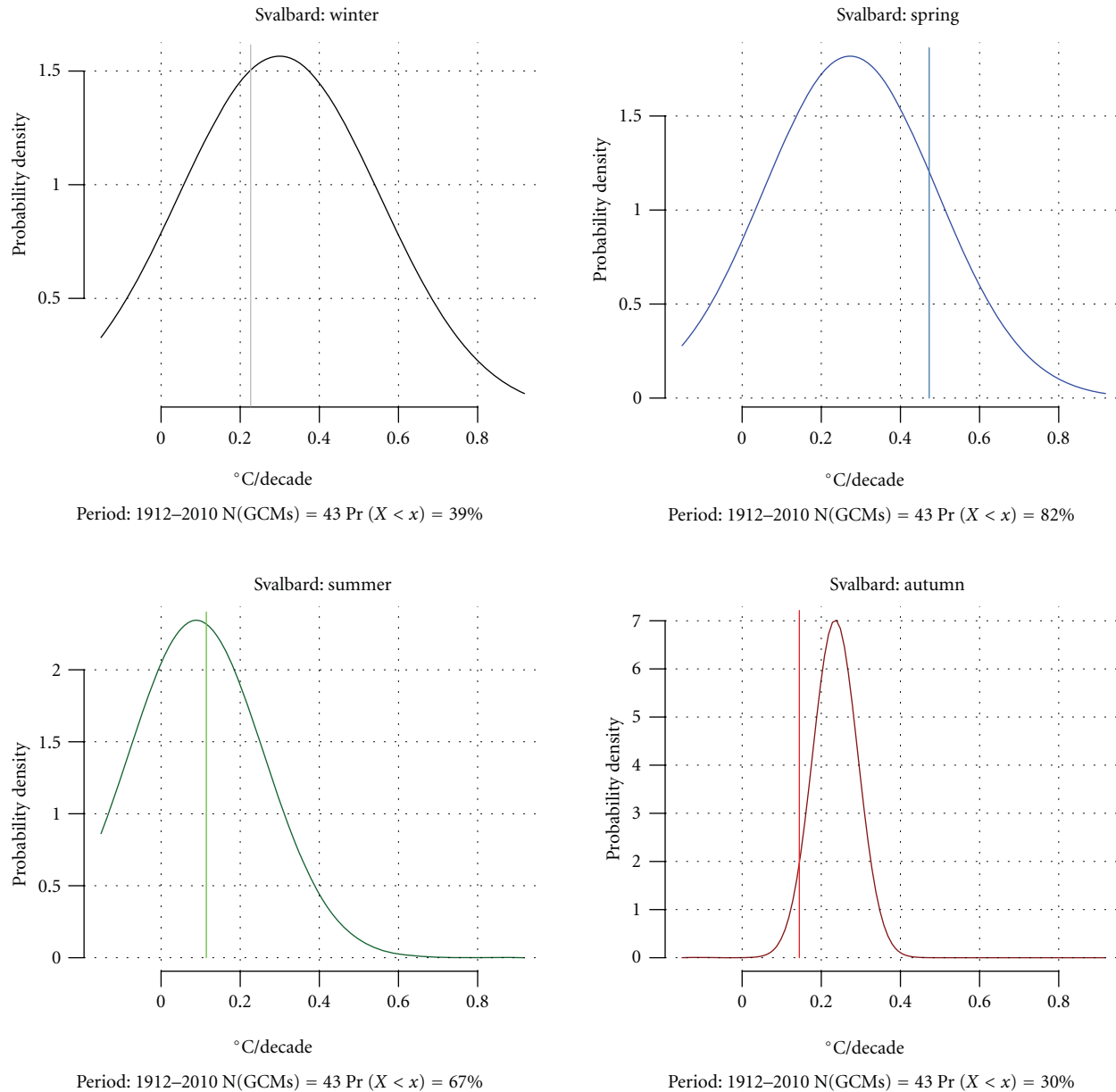


FIGURE 6: Comparison of downscaled and observed trends for the 1912–2010 period. The curve shows the probability density function of the downscaled results from 43 ESD simulations and the vertical line the observed trend. The probability (Pr) signifies the quantile in the PDF matching the observed trend.

ESD and RCM-ensembles are 6.2 and 4.1°C , respectively. While the large ESD ensemble indicates the highest increase for the 95-percentile temperatures, the picture is more mixed in the smaller RCM ensemble. But both ensembles indicate a substantial increase ($\sim 12^{\circ}\text{C}$) in the upper 5% of the winter season temperatures in the Longyearbyen area.

4.2. Precipitation. The ACIA [1] climate projections for the Arctic (60 – 90°N) indicate an annual total precipitation increase by roughly 12% from 1981–2000 to 2071–2090. IPCC [2] states that increase in the amount of precipitation is very likely at high latitudes. The spatial pattern of the projected precipitation change [2] shows the greatest percentage

increase over the Arctic Ocean (30 to 40%) and the smallest (and even a slight decrease) over the northern North Atlantic ($<5\%$). By the end of the 21st century, the projected change in the annual mean Arctic precipitation for the A1B emission scenario varies from 10 to 28%, with an ensemble median of 18%. The percentage precipitation increase is largest in winter and smallest in summer, consistent with the projected warming.

The projected increase in annual precipitation based on the RCM simulation MPIB2 (Figure 4(b)) shows an increase from a few percent southwest of Spitsbergen to more than 40% in the north-eastern parts of the archipelago. The spatial pattern of changes in precipitation is quite

TABLE 6: Projected changes in 5-, 50-, and 95-percentile annual and seasonal temperatures ($^{\circ}\text{C}$) from 1961–90 to 2071–2100 for Svalbard Airport and Bjørnøya.

(a) Empirical-statistical downscaling.

Percentile	Svalbard Airport/Longyearbyen					Bjørnøya				
	Annual	Winter	Spring	Summer	Autumn	Annual	Winter	Spring	Summer	Autumn
5%	4.7	6.9	6.0	1.5	5.9	5.2	8.0	6.7	2.4	4.7
50%	6.8	9.4	7.6	2.5	7.3	6.2	7.8	7.6	3.9	5.2
95%	8.5	11.4	9.5	3.9	9.5	9.0	12.7	9.9	6.4	7.1

(b) Regional climate models.

Percentile	Svalbard Airport/Longyearbyen					Bjørnøya				
	Annual	Winter	Spring	Summer	Autumn	Annual	Winter	Spring	Summer	Autumn
5%	4.8	8.1	5.3	2.0	6.4	4.8	8.9	5.2	2.6	3.1
50%	6.6	10.4	6.4	2.8	5.6	4.1	5.5	4.0	2.2	3.1
95%	6.6	11.9	7.3	3.3	5.1	4.4	4.8	7.8	2.9	3.4

similar to the temperature pattern (Figure 4(a)), reflecting that precipitable water increases by increasing temperature. Projected changes in precipitation from the six simulations with the NorACIA-RCM are summarized in Table 7. The projected increase in mean annual precipitation up to year 2100 in the Longyearbyen area is 12% and for Bjørnøya 8%. The precipitation is projected to increase during all seasons with the largest increase during spring. It should be noted that precipitation is quite scarce in the Longyearbyen area, implying that despite large relative increase, the absolute increase in seasonal precipitation may just be a few millimetres.

Benestad [34] carried out ESD for monthly precipitation totals for a selection of Norwegian Arctic sites, based on the most recent global climate model simulations. The results indicated that the secular variations in the actual observations were stronger than seen in the ESD results for the past. Also, the statistical links between the local (observed) and the large-scale (ERA40) precipitation was weak in general and of a very local nature [39]. In addition, some of the global models may not reproduce the regional precipitation characteristics in this region very well, thus introducing further errors and uncertainties in trying to identify the important spatial rainfall patterns in the AOGCMs. Consequently, the ESD-based projections for precipitation in the Spitsbergen area were considered to be rather uncertain, and the results are not included in this paper.

As an indicator for changes in extreme daily precipitation, Førland et al. [28] used the 5-percent exceedance value “95-percentile”. For the MPIB2 simulation, they found that for 1-day rainfall, this 95% value at the end of this century over most of the Spitsbergen region may be exceeded 1–1.5 times more frequently than in present day climate. Also, changes in number of days with “heavy rainfall” (i.e., daily precipitation larger than 20 mm) were studied [28]. In present climate, there may pass many years in the Svalbard region between each event which fulfils this definition of “heavy rainfall.” Thus, even though the projected change in

relative frequency is considerable, events with daily rainfall above 20 mm will be quite unusual (~ 1 day per year) also in the end of this century.

5. Changes in Daily Temperatures in Longyearbyen up to Year 2050

For impact and adaptation studies, climate development during the next 30–50 years is more appropriate for planning purposes than changes up to the end of this century. As seen from Figure 5, the temperature increase up to year 2100 is close to linear. Estimated large-scale temperature changes for the next 40 years will thus be approximately 1/3 of the values for the 110 year period in Table 6. The vulnerable fauna and flora in the Svalbard region is exposed to extreme temperatures, and thus knowledge on daily temperatures above or below certain threshold values are important. To study changes in daily temperatures in the Svalbard Airport/Longyearbyen area up to year 2050, the daily values from the RCM simulation MPI92a (Table 5) was adjusted as outlined in Section 3.1.

It is important to keep in mind that projections based on a single AOGCM and a single RCM only provide a rough idea of which direction the local climate may change [40, 41]. However, Figure 5 shows that, except for the summer season, the warming up to 2021–2050 in the RCM simulations based on MPI92b is close to the median of the ESD ensemble. For the summer season, the MPI92b warming is in the upper part of the ensemble. Table 8 shows that the adjusted daily temperatures for the control period are in good accordance with the observed values during 1981–2010.

The annual 1% values (Table 8) illustrate that on average there are 3–4 days per year when the daily mean temperature drops below -28°C or exceeds 9.5°C in present climate. During the 2021–2050 period, the 1% value is -23°C while the 99% value is 11°C . For the summer season, the projected 1% value will be well above zero, and the temperature threshold exceeded on average just once a year will be around

TABLE 7: Changes in 5-, 50-, and 95-percentile precipitation totals (%) from 1961–90 to 2071–2100 for Svalbard Airport and Bjørnøya. The projections are based on RCM simulations.

Percentile	Svalbard Airport/Longyearbyen					Bjørnøya				
	Annual	Winter	Spring	Summer	Autumn	Annual	Winter	Spring	Summer	Autumn
5%	17	−4	35	−12	10	9	1	40	0	12
50%	12	4	28	11	21	8	4	17	8	5
95%	15	6	21	9	4	7	−2	20	3	1

+12°C. While in the present climate there is on average one winter day every year with daily mean temperature lower than −31°C, the projected value for 2021–2050 is −25°C.

In present climate, the Svalbard Airport/Longyearbyen area experiences around 240 days per year with daily mean temperature below zero (Table 9). During 2021–2050, the number of days per year with mean temperature below zero will be reduced to around 200 according the projection based on MPI92b. Days with very low mean temperature (< −20°C) is projected by MPI92b to decrease from around 30 in present climate to around 10 during 2021–2050. For the Nordic region, the thermal growing season is often defined as the time of the year when the daily mean temperature exceeds +5°C [42]. Table 9 indicates that number of thermal growing days will increase from around 50 in present climate to around 75 in the 2021–2050 period.

6. Conclusions

- (i) The large-scale warming in the Arctic during the latest decades is recognized also at the measuring sites in the Svalbard region. During the latest two decades, the annual temperature at the different stations in the region has increased by 1.0–1.2°C per decade. The winter warming has been quite dramatic, with an increase of 2–3°C per decade at all stations. During the 1966–1988 and 1989–2011 periods, there is a positive linear trend for all seasons at all stations. However, during 1943–1965, there was a rather strong winter cooling (0.9–1.8°C per decade) at all stations, leading also to a negative trend in the annual temperatures.
- (ii) Results from several downscalings by both dynamical (regional climate models) and empirical-statistical techniques project a substantial future warming in the Svalbard region. In general, there is good accordance between the results from the two different downscaling techniques. For the Svalbard Airport/Longyearbyen area, the projected warming from 1961–90 to 2071–2100 equals 0.6°C per decade for annual temperatures and 0.9°C per decade for the winter season. This is very close to the values reported by Hanssen-Bauer [13], and a much higher warming rate than observed during the latest 100 years, where the linear temperature increase was ca. 0.25°C per decade both annually and for the winter season. Thus, the projections indicate a future rate in temperature increase three times stronger than in the

observational series during 1912–2011. The strongest temperature increase is projected for areas where the sea-ice extent will be reduced.

- (iii) Linear temperature trends from the empirical-statistically downscaled CMIP3 runs forced with observed greenhouse gas emissions were compared with observed trends at Svalbard Airport 1912–2010. For all seasons, the observed trend falls within the 10–90% confidence interval, suggesting that the downscaled results do span the observations. It is however, evident that there is a large spread in modelled trends indicating that the downscaled CMIP3-ensemble contains some models with unrealistic results. It should, therefore, be stressed that large uncertainties are linked to projections of future climate development in the Svalbard region.
- (iv) For daily temperatures, the adjusted values from one simulation with a regional climate model indicate that the lower threshold for daily temperatures experienced in average just 3–4 times per year (1% value) will increase from −28°C in present climate to around −23°C for the period 2021–2050. For the summer season, the projections indicate that days with mean temperature below zero will not occur anymore towards the mid of this century. Number of days per year with thermal conditions for growing (mean temperature above +5°C) will increase from 50 days in present climate to around 75 during 2021–2050.
- (v) There are substantial measuring errors for precipitation in the harsh Arctic climate at Svalbard, and several relocations of rain gauges have further complicated the analyses of long-term precipitation trends. However, all the long series from the Svalbard region indicate an increase in annual precipitation. At Svalbard Airport, the annual measured precipitation has in average increased by 2% per decade, while the increase at Bjørnøya and Ny-Ålesund are 3–4% per decade.
- (vi) RCM simulations project an increase in annual precipitation up to year 2100 of a few percent southwest of Spitsbergen and more than 40% in north-eastern parts of the archipelago. The empirical-statistical projections for the region were hampered by weak correlations between local and large-scale precipitation, and because several of the global models did not reproduce the regional precipitation characteristics.

TABLE 8: Percentiles (1 and 99) of daily temperatures ($^{\circ}\text{C}$) at Svalbard Airport in present and future climate. Control and scenario values are based on postprocessed temperatures from MPI92a.

	1%			99%		
	Obs 1981–2010	Control 1981–2010	Scenario 2021–2050	Obs 1981–2010	Control 1981–2010	Scenario 2021–2050
Spring	−27.2	−27.8	−24.2	2.9	2.7	5.7
Summer	−1.7	−0.8	0.9	11.3	10.8	12.2
Autumn	−19.8	−21.2	−16.5	7.0	6.5	7.5
Winter	−31.2	−30.5	−24.6	2.4	1.3	2.8
Year	−27.9	−27.8	−23.0	9.7	9.5	10.9

TABLE 9: Number of days per year with daily mean temperature (T $^{\circ}\text{C}$) below or above threshold values at Svalbard Airport. Control and scenario values are based on postprocessed temperatures from MPI92a.

	Winter			Summer			Year		
	Obs 1981–2010	Control 1981–2010	Scenario 2021–2050	Obs 1981–2010	Control 1981–2010	Scenario 2021–2050	Obs 1981–2010	Control 1981–2010	Scenario 2021–2050
$T < -20$	17.3	19.9	5.7	0	0	0	27.1	31.0	9.9
$T < -10$	54.6	55.1	36.1	0	0	0	109.1	107.5	70.3
$T < 0$	86.1	86.2	80.1	3.6	5.0	0	234.9	239.4	202.5
$T > 5$	0.1	0	0.0	46.2	44.7	66.7	50.0	48.4	75.2
$T > 10$	0	0	0	2.8	2.8	7.9	2.9	2.8	8.0

Consequently, the ESD-based projections for precipitation in the Spitsbergen area were considered to be rather uncertain, and the results are not included in this paper.

- (vii) It should be noted that the downscaled scenarios presented here all depend on results from AOGCMs where sea ice representation is rather crude, even though it has improved somewhat lately [2]. The recent loss of sea ice may enhance the regional and local Arctic warming, not only by altering the energy budget, but also by leading to a modification of large-scale atmospheric circulation. The further climate development in the Arctic will thus probably be closely linked to the development of the sea ice conditions.

Acknowledgments

This study is part of a Norwegian (<http://www.noracia.npolar.no/>) followup of the Arctic Climate Impact Assessment (<http://www.amap.no/acia/>). Thanks to our colleagues Ketil Isaksen, Øyvind Nordli, and Hanna Szewczyk-Bartnicka for assistance with Figures 1, 2, and 3. The authors also thank the two anonymous reviewers for valuable comments and suggestions.

References

- [1] ACIA, *Arctic Climate Impact Assessment*, Cambridge University Press, 2005, <http://www.amap.no/acia/>.
- [2] IPCC, *Climate Change 2007: The Physical Science Basis. Contribution of Working Group I to the Fourth Assessment Report of the Intergovernmental Panel on Climate Change*, Cambridge University Press, 2007, Edited by S. Solomon, D. Qin et al.
- [3] G. H. Miller, R. B. Alley, J. Brigham-Grette et al., “Arctic amplification: can the past constrain the future?” *Quaternary Science Reviews*, vol. 29, no. 15–16, pp. 1779–1790, 2010.
- [4] P. L. Langen and V. A. Alexeev, “Polar amplification as a preferred response in an idealized aquaplanet GCM,” *Climate Dynamics*, vol. 29, no. 2–3, pp. 305–317, 2007.
- [5] M. C. Serreze, A. P. Barrett, and J. J. Cassano, “Circulation and surface controls on the lower tropospheric air temperature field of the Arctic,” *Journal of Geophysical Research*, vol. 116, Article ID D07104, 2011.
- [6] SWIPA, “Snow, Water, Ice and Permafrost in the Arctic,” 2011, <http://www.amap.no/swipa/>.
- [7] G. A. Meehl, C. Covey, T. Delworth et al., “The WCRP CMIP3 multimodel dataset: a new era in climatic change research,” *Bulletin of the American Meteorological Society*, vol. 88, no. 9, pp. 1383–1394, 2007.
- [8] J. Räisänen, “CO₂-induced changes in interannual temperature and precipitation variability in 19 CMIP2 experiments,” *Journal of Climate*, vol. 15, no. 17, pp. 2395–2411, 2002.
- [9] Ø. Nordli, “The Svalbard airport temperature series,” *Bulletin of Geography-physical geography series*, no.3/2010:5–26, 2010.
- [10] E. J. Førland, I. Hanssen-Bauer, and Ø. Nordli, “Climate statistics and long-term series of temperature and precipitation at Svalbard and Jan Mayen,” DNMI-Report 21/97, Norwegian Meteorological Institute, Oslo, Norway, 1997.
- [11] Ø. Nordli, I. Hanssen-Bauer, and E. J. Førland, “Homogeneity analyses of temperature and precipitation series from Svalbard and Jan Mayen,” DNMI-Report 16/96, Norwegian Meteorological Institute, Oslo, Norway, 1996.
- [12] WMO, “Calculation of monthly 30-year standard normals,” WMO-TD 341, World Meteorological Organisation, Geneva, Switzerland, 1989.

- [13] I. Hanssen-Bauer, "Temperature and precipitation in Svalbard 1912–2050: measurements and scenarios," *Polar Record*, vol. 38, no. 206, pp. 225–232, 2002.
- [14] I. V. Polyakov, R. V. Bekryaev, G. V. Alekseev et al., "Variability and trends of air temperature and pressure in the maritime Arctic, 1875–2000," *Journal of Climate*, vol. 16, no. 12, pp. 2067–2077, 2003.
- [15] I. Hanssen-Bauer and E. J. Førland, "Long-term trends in precipitation and temperature in the Norwegian Arctic: can they be explained by changes in atmospheric circulation patterns?" *Climate Research*, vol. 10, no. 2, pp. 143–153, 1998.
- [16] I. G. Rigor, R. L. Colony, and S. Martin, "Variations in surface air temperature observations in the Arctic, 1979–97," *Journal of Climate*, vol. 13, no. 5, pp. 896–914, 2000.
- [17] J. E. Overland and M. Wang, "Large-scale atmospheric circulation changes are associated with the recent loss of Arctic sea ice," *Tellus A*, vol. 62, no. 1, pp. 1–9, 2010.
- [18] J., Overland, M. Wang, and J. Walsh, "Atmosphere," 2011, <http://www.arctic.noaa.gov/reportcard/atmosphere.html>.
- [19] R. E. Benestad, "What can present climate models tell us about climate change?" *Climatic Change*, vol. 59, no. 3, pp. 311–331, 2003.
- [20] L. Bengtsson, V. A. Semenov, and O. M. Johannessen, "The early twentieth-century warming in the arctic—a possible mechanism," *Journal of Climate*, vol. 17, no. 20, pp. 4045–4057, 2004.
- [21] R. Sneyers, "On statistical analysis of series of observations," WMO Technical Note 143, Geneva, Switzerland, 1990.
- [22] E. J. Førland and I. Hanssen-Bauer, "Increased precipitation in the Norwegian Arctic: true or false?" *Climatic Change*, vol. 46, no. 4, pp. 485–509, 2000.
- [23] A. Sorteberg, T. Furevik, H. Drange, and N. G. Kvamstø, "Effects of simulated natural variability on Arctic temperature projections," *Geophysical Research Letters*, vol. 32, no. 18, Article ID L18708, 4 pages, 2005.
- [24] R. E. Benestad, "On latitudinal profiles of zonal means," *Geophysical Research Letters*, vol. 32, no. 19, Article ID L19713, 4 pages, 2005.
- [25] J. E. Walsh, W. L. Chapman, V. Romanovsky, J. H. Christensen, and M. Stendel, "Global climate model performance over Alaska and Greenland," *Journal of Climate*, vol. 21, no. 23, pp. 6156–6174, 2008.
- [26] J. E. Haugen and T. Iversen, "Response in extremes of daily precipitation and wind from a downscaled multi-model ensemble of anthropogenic global climate change scenarios," *Tellus A*, vol. 60, no. 3, pp. 411–426, 2008.
- [27] M. Stendel, J. H. Christensen, and D. Petersen, "Arctic climate and climate change with a focus on greenland," *Advances in Ecological Research*, vol. 40, pp. 13–43, 2008.
- [28] E. J. Førland, R. E. Benestad, F. Flatøy et al., "Climate development in North Norway and the Svalbard region during 1900–2100," Norwegian Polar Institute Report 128, 2009.
- [29] S. Uppala, P. W. Kållberg, A. J. Simmons et al., "The ERA-40 re-analysis," *Quarterly Journal of the Royal Meteorological Society*, vol. 131, no. 612, pp. 2961–3012, 2005.
- [30] T. Engen-Skaugen, "Refinement of dynamically downscaled precipitation and temperature scenarios," *Climatic Change*, vol. 84, no. 3–4, pp. 365–382, 2007.
- [31] F. Giorgi and B. Hewitson, "Regional climate information—evaluation and projections," in *Climate Change 2001: the Scientific Basis. Contribution of Working Group I to the Third Assessment Report of the Intergovernmental Panel on Climate Change*, J. T. Houghton, Y. Ding, D. J. Griggs et al., Eds., pp. 583–638, Cambridge University Press, Cambridge, UK, 2001.
- [32] I. Hanssen-Bauer, C. Achberger, R. E. Benestad, D. Chen, and E. J. Førland, "Statistical downscaling of climate scenarios over Scandinavia," *Climate Research*, vol. 29, no. 3, pp. 255–268, 2005.
- [33] R. E. Benestad, "A new global set of downscaled temperature scenarios," *Journal of Climate*, vol. 24, no. 8, pp. 2080–2098, 2011.
- [34] R. E. Benestad, "Empirical-Statistical downscaled Arctic temperature and precipitation series," Met.no Report 10/2008 Climate, 2008.
- [35] R. E. Benestad, "Extension of the NorACIA and EALAT downscaling," Met.no Note 21, 2010.
- [36] E. J. Førland, R. E. Benestad, I. Hanssen-Bauer, and J. E. Haugen, *Future Climate Development in the NorACIA-Region. Combined Results from Simulations with Different Climate Models*, Brief Report Series, no. 023, Norwegian Polar Institute, 2011, (In Norwegian).
- [37] SRES, *IPCC Special Report on Emissions Scenarios*, Cambridge University Press, Cambridge, UK, 2000.
- [38] P. D. Jones, "The early twentieth century Arctic high—fact or fiction?" *Climate Dynamics*, vol. 1, no. 2, pp. 63–75, 1987.
- [39] R. E. Benestad, I. Hanssen-Bauer, and E. J. Førland, "An evaluation of statistical models for downscaling precipitation and their ability to capture long-term trends," *International Journal of Climatology*, vol. 27, no. 5, pp. 649–665, 2007.
- [40] N. Oreskes, D. A. Stainforth, and L. A. Smith, "Adaptation to global warming: do climate models tell us what we need to know?" *Philosophy of Science*, vol. 77, no. 5, pp. 1012–1028, 2010.
- [41] T. Palmer, "A CERN for climate change," *Physics World*, vol. 24, no. 14–15, 2011.
- [42] E. J. Førland, T. E. Skaugen, R. E. Benestad, I. Hanssen-Bauer, and O. E. Tveito, "Variations in thermal growing, heating, and freezing indices in the Nordic Arctic, 1900–2050," *Arctic, Antarctic, and Alpine Research*, vol. 36, no. 3, pp. 347–356, 2004.

Research Article

Short-Period Internal Waves under an Ice Cover in Van Mijen Fjord, Svalbard

E. G. Morozov,¹ S. V. Muzylev,¹ A. S. Shestov,^{2,3} and A. V. Marchenko^{2,3,4,5}

¹*P.P. Shirshov Institute of Oceanology, Russian Academy of Sciences, Moscow 117997, Russia*

²*Department of Aerophysics and Space Research, Moscow Institute of Physics and Technology, 141700 Dolgoprudny, Russia*

³*Department of Arctic Technology, The University Centre in Svalbard, 9171 Longyearbyen, Norway*

⁴*N.N. Zubov State Oceanographic Institute, Moscow 119034, Russia*

⁵*Sustainable Arctic Marine and Coastal Technology (SAMCoT), Centre 7491 for Research-Based Innovation (CRI), Trondheim, Norway*

Correspondence should be addressed to E. G. Morozov, egmorozov@mail.ru

Received 15 September 2011; Accepted 17 December 2011

Academic Editor: Irina Repina

Copyright © 2011 E. G. Morozov et al. This is an open access article distributed under the Creative Commons Attribution License, which permits unrestricted use, distribution, and reproduction in any medium, provided the original work is properly cited.

Temperature and velocity fluctuations measured in Van Mijen Fjord in Svalbard and interpreted as the fluctuations induced by internal waves revealed the existence of short-period internal waves with an amplitude of approximately 1 m and a period of approximately 5–10 min that correlate with the ice cover fluctuations of the same period with an amplitude of a few millimeters.

1. Introduction

We analyze the measurements of temperature, velocity, and pressure at the bottom to study the influence of internal waves on the ice cover. The “rigid lid” approximation is almost always used in the theoretical study of internal waves under the ice cover or even without it. This approximation filters off the surface mode and adequately describes the properties of both the internal waves in ice-free conditions and long internal waves under the ice cover [1, 2]. In the “rigid lid” approximation, the vertical velocity at the surface is assumed to be equal to zero; therefore, due to the kinematic condition, the internal waves cannot cause any vertical displacements of the ice cover. Such conclusion is, however, inconsistent with the experimental data obtained for relatively deep parts of the Arctic Ocean [3–6] and also contradicts the theoretical results [7, 8], according to which internal waves may be reflected in the fluctuations of the ice cover at frequencies comparable with the Brunt-Väisälä frequency. Scientists from the Shirshov Institute of Oceanology (Russian Academy of Sciences) and The University Centre in Svalbard (UNIS) carried out marine studies in the shallow Van Mijen Fjord in Svalbard to perform experimental tests of the theoretical conclusion

concerning the possible influence of short internal waves on the fluctuations of the compact ice cover.

2. Brief Theory of Internal Waves under an Ice Cover

In the theoretical approach, the ice cover of the ocean surface can be considered as a thin elastic plate floating on the sea surface. The theoretical description of the ice cover fluctuations should take into account the elastic properties of the ice plate, the compression forces, and the ice inertia. If the processes inside the ice cover are ignored the main equations and boundary conditions of the ice cover should be similar to the equations and conditions in the situation when the sea surface is free of ice.

The only exception is the dynamic condition that may be expressed under the constant ice thickness h in the following form [7–11]:

$$P|_{z=0} = \rho_0 g \eta + [\rho_0 (B \Delta^2 + Q \Delta) \eta] + \rho_0 M \frac{\partial^2 \eta}{\partial t^2}. \quad (1)$$

Here, P is the pressure, η the ice surface deflection, g the acceleration due to gravity, ρ_0 the seawater density at the

boundary with the ice, t the time, Δ the horizontal Laplace operator, and

$$B = \frac{Eh^3}{12(1-s^2)\rho_0}, \quad Q = \frac{Kh}{\rho_0}, \quad M = \frac{\rho_I h}{\rho_0}. \quad (2)$$

Here, B is the cylindrical rigidity of the ice, the E Young's modulus, s the Poisson's ratio, K the ice compression coefficient, $\rho_I = \text{const}$ the ice density, and $h = \text{const}$ the ice thickness.

In (1), the summands proportional to B , M , and Q result from the respective elastic ice properties, the inertial forces, and the compression forces, which influence the ice cover. The characteristic values (2) for the ice are as follows [12, 13]: $E = 3 \cdot 10^9 \text{ N/m}^2$, $s = 0.3$, $K = 2 \cdot 10^5 \text{ N/m}^2$, $\rho_0 = 1025 \text{ kg/m}^3$, and $\rho_I = 0.9 \rho_0$. With the ice thickness $h = 0.5 \text{ m}$ observed during the experiment, we obtain the following estimates for the coefficients: $B \approx 3.35 \cdot 10^4 \text{ m}^5/\text{s}^2$, $Q \approx 97.6 \text{ m}^3/\text{s}^2$, and $M = 0.45 \text{ m}$. In the case of the ice-free surface, when $h = 0$ and, consequently, $B = Q = M = 0$, dynamic condition (1) acquires the standard form $P|_{z=0} = \rho_0 g \eta$.

We designate the characteristic horizontal scale of the wave motions as L . Comparing the summand in (1), which describes the contribution of the pressure determined by the elastic properties of the ice cover (summand proportional to the cylindrical ice rigidity B) into $P|_{z=0}$, with the value of the gravity potential at the surface of the liquid $U_s = \rho_0 g \eta$, we find that these summands are of the same order if $L \sim L_{\text{eg}}$, where

$$L_{\text{eg}} = \left(\frac{B}{g}\right)^{1/4} = \left[\frac{Eh^3}{12(1-s^2)\rho_0 g}\right]^{1/4}. \quad (3)$$

We assume that the properties of the waves under the elastic plate characterized by the lengths $L \gg L_{\text{eg}}$, are close to these parameters of the waves in the liquid with a free surface, and the ice cover insignificantly influences the wave motions in the sea. At the same time, for short waves with lengths $L \ll L_{\text{eg}}$ the elasticity forces of the plate prevail over the gravity forces.

Let us compare the gravity potential U_s with the pressure determined by the compression forces in the ice cover (with the summands proportional to Q). We obtain that they are of the same order if $L \sim L_{\text{cg}}$, where

$$L_{\text{cg}} = \left(\frac{Q}{g}\right)^{1/2} = \left(\frac{Kh}{\rho_0 g}\right)^{1/2}. \quad (4)$$

If the ice thickness is $h_* = 12(1-s^2)K^2/\rho_0 g E$, we get that $L_{\text{cg}} \approx L_{\text{eg}}$; therefore, for the ice cover with a thickness exceeding h_* , the inequality $L_{\text{cg}} > L_{\text{eg}}$ is valid. The contribution of the elastic forces to $P|_{z=0}$ is comparable with that of the compression forces if characteristic motion scale is $L \sim L_{\text{ec}}$, where

$$L_{\text{ec}} = \frac{L_{\text{eg}}^2}{L_{\text{cg}}} = \sqrt{\frac{B}{Q}} = h \sqrt{\frac{E}{12(1-s^2)K}}. \quad (5)$$

Since inequality $L_{\text{cg}} > L_{\text{eg}}$ is valid for the ice thickness greater than h_* , then $L_{\text{ec}} > L_{\text{eg}} > L_{\text{cg}}$. Although, at $L > L_{\text{ec}}$,

the ice compression forces exceed the elasticity forces, the gravity force appears to be decisive for the wave motion. At $L < L_{\text{ec}}$, the determining role belongs either to the gravity force when $L \in (L_{\text{ec}}, L_{\text{cg}})$ or to the elasticity if $L < L_{\text{eg}}$.

Usually we can neglect the role of the inertia forces in the case of compact ice cover. However, we note that due to (1) an increase in the wavelength is accompanied by an unlimited growth of the pressure at the lower ice boundary. In order to exclude its unlimited growth, the ice deflection should tend to zero with the simultaneous wavelength reduction. We also note that all the estimates were obtained under the assumption that the motions in the horizontal plane are uniform. Near the lateral boundaries and in the case of sharp bottom topography gradients, these estimates should be revised.

The previous qualitative results are valid for the waves of any type under compact ice cover, while the quantitative data are now obtained for the flexure-gravity waves [7], edge waves near the straight coast above the sloping bottom [11], waves spreading along the ice field edge [14, 15], and internal waves [7, 8]. We emphasize three issues, which are important for the description of internal waves when the water stratification in the basin allows the Brunt-Väisälä frequency N to be considered constant.

- (1) The dispersion equation for such waves takes the following form:

$$\lambda_n \tan \lambda_n H = \frac{N^2 - \omega_n^2}{g + Bk^4 - Qk^2 - M\omega_n^2}, \quad (6)$$

where $\lambda_n = k\sqrt{(N^2 - \omega_n^2)}/\omega_n$, ω_n is the frequency of internal waves, k the magnitude of the wave number, $H = \text{const}$ the basin depth, and n the mode number.

- (2) The ice thickness h provides an insignificant impact on the dispersion equation (6) [7, 8]; therefore, it can be presented with high accuracy in its classical form:

$$\omega_n(k) \approx \frac{kH}{\sqrt{n^2\pi^2 + k^2H^2}}N. \quad (7)$$

- (3) One can show for internal waves propagating in the lateral direction that the amplitude of the ice deflection η_n for the mode with the n number and the pressure amplitude $p_n(z)$ at depth z are connected by the following relation [7, 8]:

$$\eta_n = \frac{p_n(z)}{\rho_0[g + Bk_n^4(\omega) - Qk_n^2(\omega) - M\omega^2]} \times \frac{\cos \lambda H}{\cos \lambda(H+z)}. \quad (8)$$

If $z = -H$, the following relationship exists between the ice deflection and the pressure at the bottom: $p_{b,n} = p_n(-H)$:

$$\eta_n = \left(\frac{p_{b,n}}{g\rho_0}\right) \frac{g \cos \lambda H}{g + Bk_n^4(\omega) - Qk_n^2(\omega) - M\omega^2}. \quad (9)$$

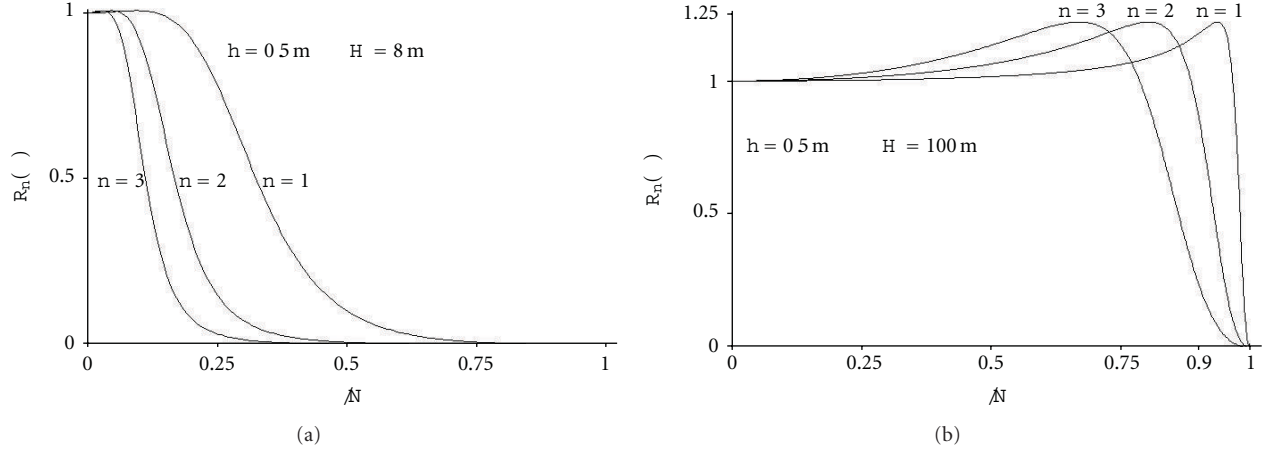


FIGURE 1: Transfer function determining the correction factor for the hydrostatic relation between the amplitudes of the near-bottom pressure and the ice deflection with the thickness of the ice cover $h = 0.5$ m and the sea depth (a) $H = 8$ m ($K = 2 \times 10^5$ N/m²) and (b) $H = 100$ m ($K = 10^6$ N/m²).

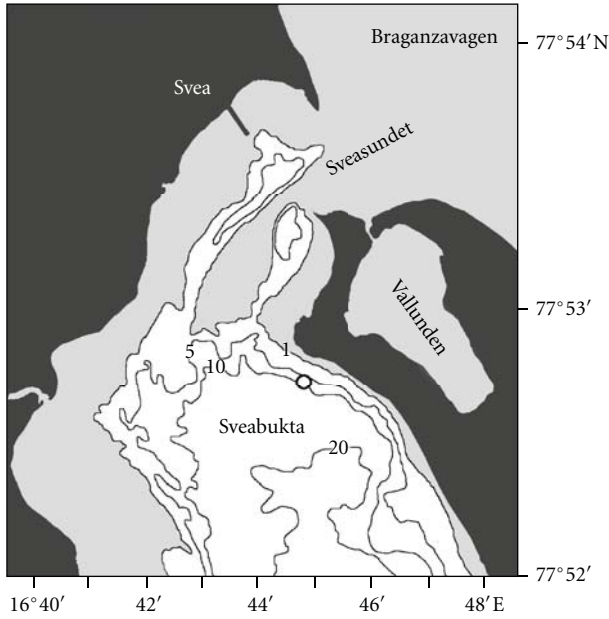


FIGURE 2: Schematic map of the measurement site. Gray color shows shallow (<1 m) regions. Black color denotes land. The circle indicates the site of measurements.

Relation

$$R_n(\omega) = \left| \frac{g \cos \lambda H}{g + Bk_n^4(\omega) - Qk_n^2(\omega) - M\omega^2} \right| \quad (10)$$

can be interpreted as a transfer function that determines the correction factor for the hydrostatic relationship between the pressure at the bottom and ice deflection.

The dependences of the transfer function $R_n(\omega)$ for both the conditions of the performed natural experiment and the above-mentioned values obtained for the coefficients B , Q , and M (Figure 1(a)) and the conditions described in [10]

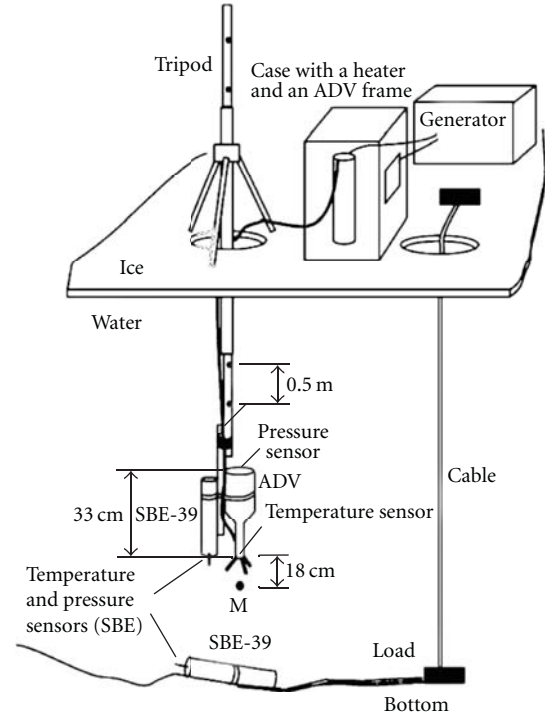


FIGURE 3: Schematic location of the measuring devices (M corresponds to the current measurement point).

(Figure 1(b)) are shown in Figure 1. The form of the transfer function $R_n(\omega)$ significantly depends on the depth of the basin (the deeper the basin, the closer the maximum of the transfer function to the Brunt-Väisälä frequency) and the compression coefficient Q (the greater the latter, the larger the maximum of the transfer function). We note that, immediately near the Brunt-Väisälä frequency, when the internal waves are very short, the transfer function tends to zero due to (10); that is, in this frequency range, the ice cover should flatten.

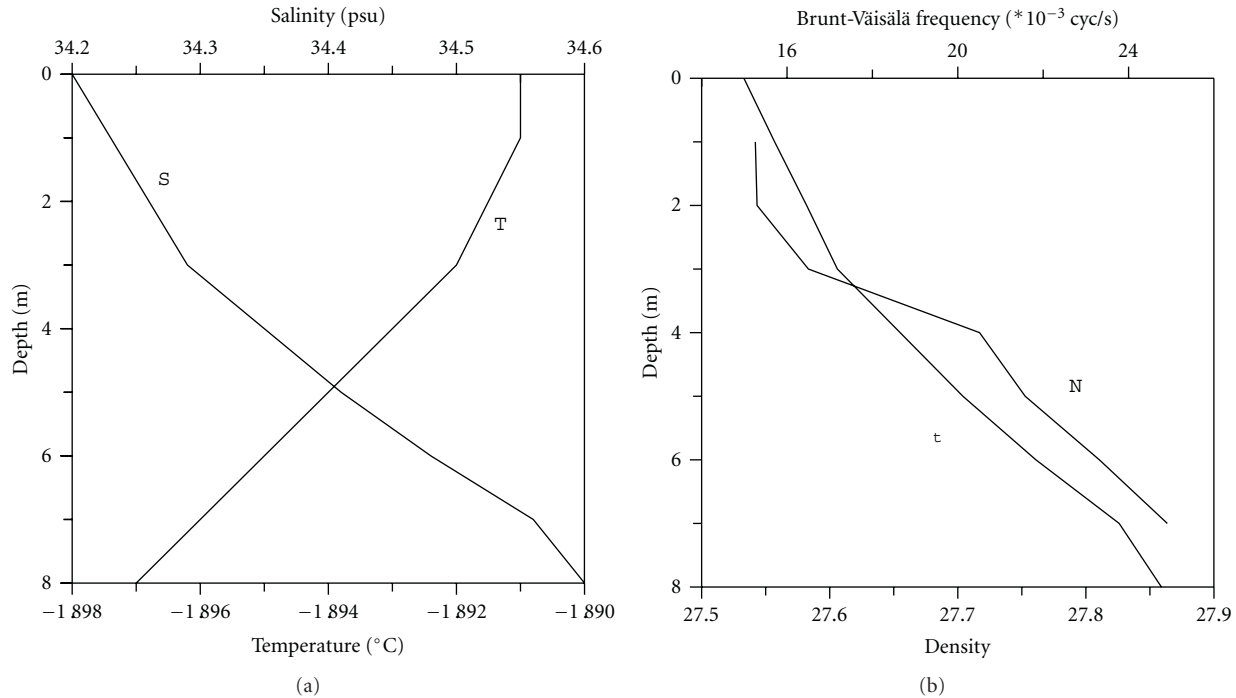


FIGURE 4: Vertical distribution of temperature (T), salinity (S), density (σ_t), and Brunt-Väisälä frequency (N) in the study region.

3. Measurements of Internal Waves in the Van Mijen Fjord under the Ice Cover

In 2008, simultaneous measurements of internal waves and pressure at the sea bottom that reflect the fluctuations of the ice cover were carried out in the Van Mijen Fjord. Figure 2 demonstrates the location of the study region.

Temperature profiler SBE 39 with a high-accuracy pressure sensor and a current meter (SonTek ADV Ocean Probe) were used during the field works. The SBE 39 profiler measures the temperature with a resolution of 0.0001°C and the pressure with a resolution of 0.002% of the pressure scale of 20 dbar, which corresponds to a pressure resolution of 0.004 dbar (or, approximately, to 0.4 mm of depth). The ADV measuring instrument provides data of three velocity components with a resolution of 0.01 cm/s. Measurements were conducted under the ice using the instruments mounted on a vertical support rod with a tripod standing on the ice (Figure 3).

The pressure meter SBE 39 was located at the bottom to measure the fluctuations of the ice cover. The measurements were conducted under the ice 50–60 cm thick in the region with strong tidal currents: the heights of the spring tide reached 2 m, and the maximal tide velocity was as high as 10 cm/s. During the observation period, the water temperature was close to the freezing point (approximately -1.9°C). Insignificant vertical temperature gradient ($1 \times 10^{-3}^\circ\text{C/m}$) and high salinity (0.05 psu/m) gradients were characteristic of the measurement period. Figure 4 illustrates the vertical distribution of the temperature, salinity, density, and Brunt-Väisälä frequency. The profile of the density practically repeats that of the salinity, which indicates that the

downward density changes are determined by the variations in the salinity. The Brunt-Väisälä frequency in the study region was approximately $15\text{--}25 \times 10^{-3} \text{ cyc/s}$ with twofold downward variations.

The most representative results of the measurements of short-period internal waves were obtained at the site with coordinates $77^\circ 52.79' \text{ N}$ and $16^\circ 43.73' \text{ E}$ and a depth of approximately 10 m on the underwater slope of the sill between the deep and shallow parts of the bay. The calculations of the spectrum of temperature fluctuations show that, at frequencies exceeding the Brunt-Väisälä frequency, the spectrum sharply decreases with the increasing frequency, while, at the frequencies slightly lower than the buoyancy frequency, several peaks are observed. Let us analyze fluctuations with such periods.

The spectrum of the temperature fluctuations in the range of the short-period oscillations (Figure 5(a)) is characterized by two peaks with frequencies of 0.0015 and 0.003 cyc/s, which correspond to the periods of approximately 10 and 5.5 min; the spectrum of the velocity fluctuations is characterized by similar patterns, although a significant peak is observed only at a frequency of 0.003 cyc/s or 5.5 min (Figure 5(b)).

The spectra of pressure fluctuations were also calculated from the data of bottom-located meter SBE 39. As it follows from (9), these pressure variations are responsible for fluctuations of the ice cover. Figure 5(c) demonstrates the spectrum of the pressure fluctuations, which is characterized by a peak at the period of approximately 5.5 min (frequency 0.003 cyc/s). Such fluctuations were also reported in [16]. The amplitude of the pressure fluctuations at the bottom with such a period is 0.005–0.006 dbar, which corresponds,

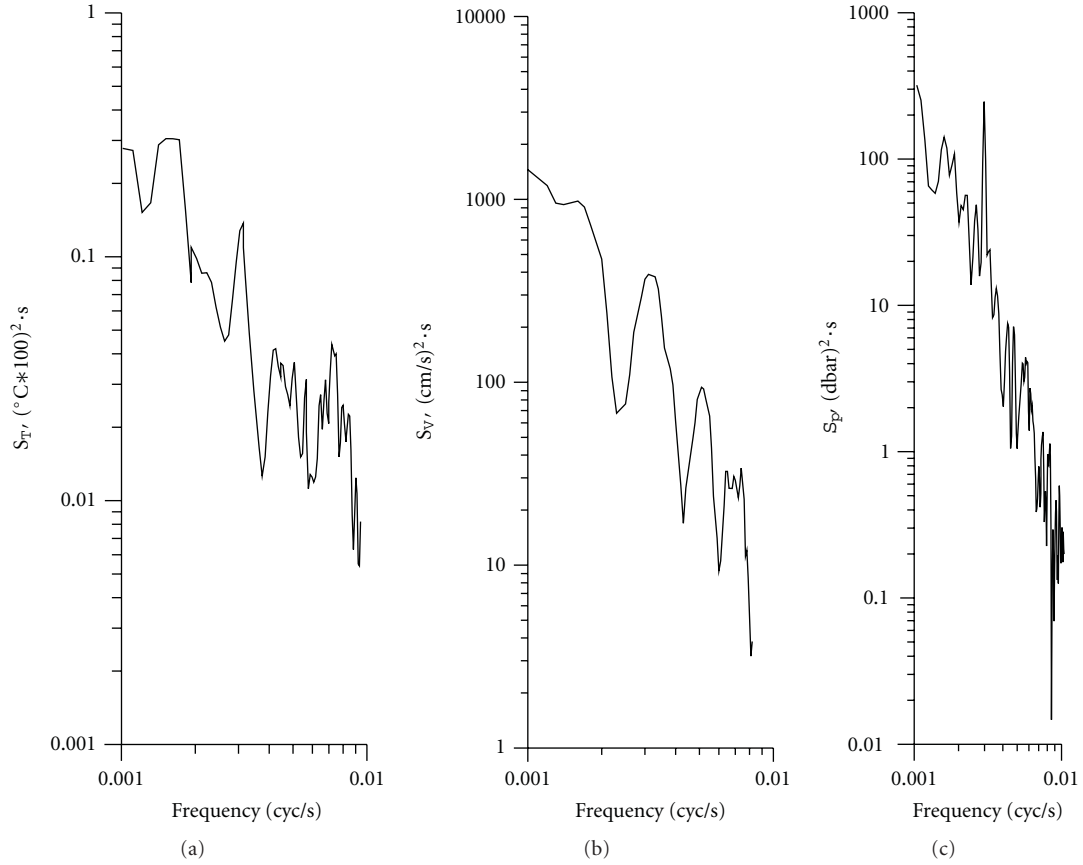


FIGURE 5: (a) spectrum of the temperature fluctuations in the high-frequency range; (b) spectrum of the current velocity fluctuations in the high-frequency range; (c) spectrum of the pressure fluctuations at the bottom in the high-frequency range.

according to (10), approximately to the amplitude of 5-6 mm of the fluctuations of the ice cover.

4. Discussion and Conclusions

Short intense internal waves can probably break the ice cover. Indeed, according to relation (1) for the pressure at the lower surface of the ice if $L \ll L_{eg}$, or $L \ll L_{ec}$ the value of relation $\rho_0(B\Delta^2 + Q\Delta)\eta$ increases as the internal wavelength decreases. In other words, the contribution to pressure of the elastic and compression-tension forces applied to the ice cover increases. The following formula for maximal stress σ_{max} at the surface of bended elastic plate can be used to estimate ice break up by internal waves: $\sigma_{max} \approx aEhk^2/2$ [13 Landau Lifshits]. In our case, $a = 5$ mm, $E = 3$ GPa, $h = 0.5$ m and $k = 0.32$ cyc/m (wave length is about 20 m) according to the dispersion equation (7), where $H = 10$ m and $N = 0.028$ cyc/s. The ice stress σ_{max} is estimated as 0.38 MPa. This value is close to the flexural strength of sea ice [17]. Thus, short internal waves can break up the ice cover.

It is possible that such phenomenon was observed during the expedition of R/V "Polarstern" in 1986 in the Weddell Sea [18, page 75] when the solid ice cover with a thickness of 0.8 m was suddenly broken [10]. A similar event occurred in the spring of 1988 near Sakhalin Island [19]. According to the

data of observations, internal waves were evidently generated by an intense cyclone.

Thus, the study of short internal waves is important since they can influence the ice surface. The influence of atmospheric and oceanic processes and especially internal waves on the stability of the ice cover and ice cover depletion currently observed in the Arctic region in the summer season is the hot issue of polar meteorology and oceanography [2, 20]. The winter measurements of temperature, velocity, and pressure fluctuations under ice in the frequency range of internal waves in the shallow Arctic Fjord in Spitsbergen demonstrate that the temperature and velocity fluctuations with periods of 5–10 min and the amplitude of the internal waves slightly less than 1 m correlate with the fluctuations of the ice cover of the same period and an amplitude of a few millimeters. These results are consistent with the theory.

Acknowledgments

The authors thank Professor F. Nilsen (UNIS) and K. Johansen for their help in conducting the field studies. This work was supported by the Russian Foundation for Basic Research (project nos. 08-05-00120, 08-05-00124, 09-05-00599, 10-08-01010, 11-05-00448, 11-08-00076, and 12-05-00889). The authors also thank anonymous reviewers for their valuable remarks.

References

- [1] E. G. Morozov, V. G. Neiman, S. V. Pisarev, and S. Yu. Erofeeva, "Internal tidal waves in the Barents Sea," *Doklady Earth Sciences*, vol. 393, no. 8, pp. 1124–1127, 2003.
- [2] E. G. Morozov and S. V. Pisarev, "Internal waves and polynya formation in the Laptev sea," *Doklady Earth Sciences*, vol. 398, no. 7, pp. 983–986, 2004.
- [3] P. V. Czipott, M. D. Levine, C. A. Paulson, D. Menemenlis, D. M. Farmer, and R. G. Williams, "Ice flexure forced by internal wave packets in the Arctic ocean," *Science*, vol. 254, no. 5033, pp. 832–835, 1991.
- [4] V. N. Smirnov, "Oscillations of the ice cover induced by internal waves in an icy ocean," *Doklady Akademii Nauk SSSR*, vol. 206, no. 5, pp. 1106–1108, 1972.
- [5] V. N. Smirnov, *Dynamic Processes in Sea Ice*, Gidrometeoizdat, St. Petersburg, Russia, 1996.
- [6] V. N. Smirnov, A. N. Shushlebin, and V. G. Korostelev, "Results of experimental measurements of the parameters of surface and internal waves in the Arctic ocean and the sea of Okhotsk," in *Surface and Internal Waves in the Arctic Seas*, I. V. Lavrenov and E. G. Morozov, Eds., Gidrometeoizdat, St. Petersburg, Russia, 2002.
- [7] S. V. Muzylev, "Internal waves under an ice cover," *Doklady Earth Sciences*, vol. 418, no. 1, pp. 145–148, 2008.
- [8] S. V. Muzylev and L. N. Oleinikova, "On the theory of internal waves under ice cover," *Oceanology*, vol. 47, no. 2, pp. 172–177, 2007.
- [9] L. D. Landau and E. M. Lifshitz, *Theory of Elasticity*, Pergamon, Oxford, UK, 1967.
- [10] A. K. Liu and E. Mollo-Christensen, "Wave propagation in a solid ice pack," *Journal of Physical Oceanography*, vol. 18, no. 11, pp. 1702–1712, 1988.
- [11] S. V. Muzylev, "Edge waves under ice cover at a straight coast with a sloping beach," *Oceanology*, vol. 46, no. 4, pp. 465–471, 2006.
- [12] V. V. Bogorodsky and V. P. Gavrilov, *Ice: Physical Properties, Modern Methods in Glaciology*, Gidrometeoizdat, Leningrad, Russia, 1983.
- [13] M. Coon, D. C. Echert, and G. S. Knoke, "Ice in surface waters," in *Proceedings of the 14th International Symposium on Ice*, H. T. Shen, Ed., pp. 1049–1055, Balkema, 1999.
- [14] A. Marchenko, "Parametric excitation of flexural-gravity edge waves in the fluid beneath an elastic ice sheet with a crack," *European Journal of Mechanics B*, vol. 18, no. 3, pp. 511–525, 1999.
- [15] A. V. Marchenko, "Flexural gravity waves," *Trudy Instituta Obshchei Fiziki*, vol. 56, pp. 65–111, 1999.
- [16] A. Marchenko, I. Langen, and A. Shestov, "Hydrological characteristics of the strait separating Braganzavagen from Sveabukta in Van Mijen Fjord," in *Coastal Technology—Coast 2008*, NTNU, Trondheim, Norway, 2008.
- [17] A. Marchenko, A. Shestov, A. Karulin et al., "Field studies of sea water and ice properties in Svalbard fjords," in *Proceedings of the International Conference on Port and Ocean Engineering under Arctic Conditions (POAC '11)*, pp. 148–160, 2011.
- [18] "The Winter-Expedition of RV "Polarstern" to the Antarctic (ANT V/1–3)," *Berichte zur Polarforschung*, Nr. 39, Alfred-Wegener-Institut für Polar- und Meeresforschung, Bremerhaven, Germany, 1987.
- [19] J. R. Marko, "Observations and analyses of an intense waves-in-ice event in the Sea of Okhotsk," *Journal of Geophysical Research*, vol. 108, no. 9, pp. 3296–3309, 2003.
- [20] I. V. Polyakov, L. A. Timokhov, V. A. Alexeev et al., "Arctic ocean warming contributes to reduced polar ice cap," *Journal of Physical Oceanography*, vol. 40, no. 12, pp. 2743–2756, 2010.

Research Article

Characteristics of Temperature and Humidity Inversions and Low-Level Jets over Svalbard Fjords in Spring

Timo Vihma,¹ Tiina Kilpeläinen,^{2,3} Miina Manninen,^{2,4} Anna Sjöblom,^{2,3} Erko Jakobson,^{5,6} Timo Palo,⁷ Jaak Jaagus,⁷ and Marion Maturilli⁸

¹Meteorological Research, Finnish Meteorological Institute, 00101 Helsinki, Finland

²Department of Arctic Geophysics, The University Centre in Svalbard, 9171 Longyearbyen, Norway

³Geophysical Institute, University of Bergen, 5020 Bergen, Norway

⁴Department of Physics, University of Helsinki, 00014 Helsinki, Finland

⁵Department of Physics, University of Tartu, 50090 Tartu, Estonia

⁶Tartu Observatory, 61602 Tõravere, Estonia

⁷Department of Geography, University of Tartu, 50090 Tartu, Estonia

⁸Research Unit Potsdam, Alfred Wegener Institute for Polar and Marine Research, D-14473 Potsdam, Germany

Correspondence should be addressed to Timo Vihma, timo.vihma@fmi.fi

Received 9 June 2011; Revised 7 December 2011; Accepted 13 December 2011

Academic Editor: Igor N. Esau

Copyright © 2011 Timo Vihma et al. This is an open access article distributed under the Creative Commons Attribution License, which permits unrestricted use, distribution, and reproduction in any medium, provided the original work is properly cited.

Air temperature and specific humidity inversions and low-level jets were studied over two Svalbard fjords, Isfjorden and Kongsfjorden, applying three tethered systems. Tethered systems operation practices notably affected observations on inversion and jet properties. The inversion strength and depth were strongly affected by weather conditions at the 850 hPa level. Strong inversions were deep with a highly elevated base, and the strongest ones occurred in warm air mass. Unexpectedly, downward longwave radiation measured at the sounding site did not correlate with the inversion properties. Temperature inversions had lower base and top heights than humidity inversions, the former due to surface cooling and the latter due to adiabatic cooling with height. Most low-level jets were related to katabatic winds. Over the ice-covered Kongsfjorden, jets were lifted above a cold-air pool on the fjord; the jet core was located highest when the snow surface was coldest. At the ice-free Isfjorden, jets were located lower.

1. Introduction

Temperature inversions are common in the Arctic, especially in winter [1–3]. They can be generated by various mechanisms, including (a) surface cooling due to a negative radiation budget, the effects of which are transmitted to near-surface air via a downward sensible heat flux [4], (b) direct radiative cooling of the air [5, 6], (c) warm-air advection over a cold surface [7, 8], and (d) subsidence [1, 9]. Also specific humidity inversions (hereafter *humidity inversions*) are common in the Arctic [10] and they often coincide with temperature inversions [11]. Despite the importance of humidity inversions for the Arctic stratus [12], the mechanisms generating humidity inversions have received much less attention than those generating temperature inversions. Condensation, gravitational fallout of the condensate, deposition of

hoar frost at the surface, turbulent transport of moisture, and subsidence are processes in vertical dimension that contribute to the generation of humidity inversions [13]. In addition, horizontal advection of moist air masses from lower latitudes is an essential large-scale process; the advection peaks above the atmospheric boundary layer (ABL) but there is still significant uncertainty on its vertical distribution [14].

A low-level wind maximum called a low-level jet (LLJ) is a typical feature in the wind profile in the Arctic, in particular in the presence of temperature inversions, when the LLJ is often located at the top of the temperature inversion [15]. LLJs can be generated by a variety of mechanisms, including (a) inertial oscillations due to temporal [16, 17] and spatial [18] variations in the surface friction, (b) baroclinicity [19], (c) directional shear of other origin [20], (d) ice breeze

(a sea-breeze-type mesoscale circulation; [21]), (e) katabatic winds [22], and (f) barrier winds [23].

Major challenges still remain in understanding temperature and humidity inversions, LLJs, and other features in the stable boundary layer (SBL). The Arctic SBL is long-living with a strong but quantitatively poorly known interaction of gravity waves and turbulence [24]. Under very stable stratification, the shear related to a low-level jet often provides a source of turbulence more important than the surface friction, resulting in an upside-down structure of the SBL [25]. Further, shallow convection over leads and polynyas complicates ABL processes in the sea ice zone [26, 27]. Hence, numerical weather prediction (NWP) and climate models usually have their largest errors in the SBL [28–31], which calls for more analyses on the temperature and humidity profiles and low-level jets in the Arctic atmosphere.

Arctic fjords are usually surrounded by a complex orography of mountains, valleys, and glaciers, which complicates the dynamics of the air flow [32]. In Svalbard, some fjords are completely covered by sea ice in winter and spring whereas others are partly ice-free; in the latter the surface temperature varies largely in space. The low-level wind field is strongly influenced by the local orography [33]. Due to the combined effects of the complex orography and thermal heterogeneity of the fjord surface, the dynamic and thermodynamic processes affecting the state of the ABL are complex. Several studies have addressed boundary-layer and mesoscale processes in the Svalbard region, including observations on surface-layer turbulence [34, 35] and ABL structure [36, 37] and modelling studies with validation against observations from satellite [38], research aircraft [8, 39], unmanned aircraft [40], automatic weather stations [41], and rawinsonde soundings [42]. What has been lacking so far is a thorough observational analysis on temperature and humidity inversions and low-level jets, based on a data set more extensive than those in previous case studies [8, 39].

Our study is motivated by two aspects. First, better understanding on the ABL structure over fjords is needed to improve NWP and climate models and to improve the skill of duty forecasters to predict near-surface weather in conditions of complex orography, where present-day operational models are not particularly reliable [42]. Considering climate modelling, the vertical profiles of wind, temperature, and humidity closely interact with the turbulent surface fluxes, which further control the deep water formation in fjords with potentially far-reaching effects on the climate system [43]. Second, several studies on the structure of the ABL in polar regions have been based on tethersonde soundings (e.g., [17, 36, 37]), but a detailed investigation on the effects of the sounding strategy (above all, vertical resolution and maximum height) on the observations of inversions and LLJs is still lacking. To respond to these needs, we analyse (1) the effects of synoptic-scale flow and surface conditions on the temperature and humidity inversions, (2) the effects of synoptic-scale flow, near-surface temperatures, and orography on LLJs, and (3) the sensitivity of the results to the method of taking tethersonde soundings. We study the ABL over Isfjorden and Kongsfjorden on the basis of data from three different tethersonde systems operated in spring 2009. We have

TABLE 1: Vaisala DigiCORA TT12 tethersonde sensors with accuracies and resolutions.

Variable	Sensor	Absolute accuracy*	Resolution
Air temperature	Capacitive wire F-Thermocap	0.5°C	0.1°C
Relative humidity	Thin-film capacitor	5%	0.1%
Wind speed	Three-cup anemometer	0.2 m s ⁻¹	0.1 m s ⁻¹
Wind direction	Digital compass	See the text	1°
Atmospheric pressure	BAROCAP silicon sensor	1.5 hPa	0.1 hPa

* The accuracy of vertical differences is better than the absolute accuracy, because in the UNIS and UT soundings the same sensors were used for the whole profile and in the AWI tethersonde the sensors were intercalibrated. We assume that the accuracy of vertical differences in air temperature and relative humidity is close to the sensor resolution.

already applied these data to verify high-resolution numerical model simulations [44], but without addressing the above-mentioned aspects 1–3.

2. Observations

2.1. Tethersonde System. Three basically similar tethersonde systems (DigiCORA TT12, Vaisala) were operated at coastal areas of Svalbard in March–April 2009. The measurements near Longyearbyen on the southern coast of Isfjorden were made by the University Centre in Svalbard (UNIS) and the measurements at Ny Ålesund on the southern coast of Kongsfjorden by the University of Tartu (UT) and the Alfred Wegener Institute for Polar and Marine Research (AWI) (Figure 1). The UNIS tethersonde system consisted of one tethersonde and the UT system of three tethersondes at approximately 15 m intervals in the vertical, attached to a tethered balloon (Figure 2). The UNIS and UT balloons were ascended and descended with a constant speed of approximately 1 m s⁻¹ to gain vertical profiles of temperature, humidity, pressure, wind speed, and wind direction. The AWI system (Figure 2) consisted of six tethersondes, which were kept at constant altitudes, from 100 m to 600 m at 100 m intervals in the vertical, to record time series. The sampling interval of the tethersondes altered from 1 to 5 seconds. The tethersonde systems were only operated in nonprecipitating conditions (except of very light snow fall) with wind speeds less than 10 m s⁻¹. The tethered balloons were neither ascended into thick clouds nor operated in temperatures lower than approximately –25°C. Technical information on the tethersonde sensors is given in Table 1.

2.2. Measurements at Isfjorden. Isfjorden, which covers an area of 3084 km², is situated on the west coast of Spitsbergen, the largest island of the archipelago of Svalbard. The fjord is orientated in a southwest to northeast direction and has a 10 km wide mouth to the open ocean. The measurement site (78° 15'N, 15° 24'E) was located on the southern coast of

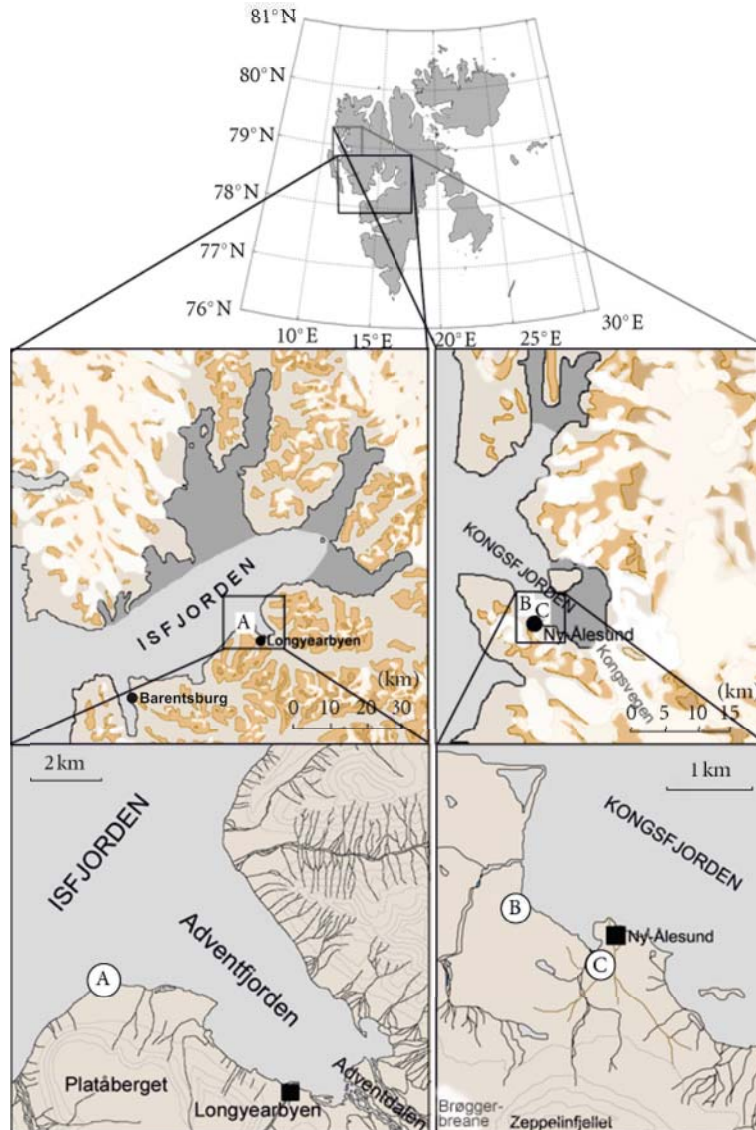


FIGURE 1: The locations of measurement site of UNIS (A) in Isfjorden, and UT (B) and AWI (C) in Kongsfjorden. In the middle panel, the dark gray shows the areas fully covered with land-fast sea ice and the light gray shows the areas with sea ice concentration varying between 0.2 and 0.9. In the lowest panel, the terrain height is shown with 100 m isolines.

Isfjorden, approximately 30 m from the shoreline, and had an undisturbed over-fjord fetch of approximately 25–40 km in a 175° wide sector from southwest clockwise to northeast (Figure 1). The local orography around the site is very complex, consisting of mountains rising to heights of 400–1100 m, valleys, and glaciers.

At Isfjorden, the tethered sonde campaign started on 29 March 2009 (day length 14 h 51 min), and ended on 5 April 2009 (day length 16 h 51 min). Altogether 27 soundings were made. Because the measurement site was in the vicinity of the Svalbard Airport, the balloon could only be operated when the airport was closed. The operating hours were often restricted to early mornings and afternoons (Figure 3). The balloon was always lifted as high as the cloud conditions, wind speed, and the buoyancy of the small (2.5 m³) balloon

allowed. The maximum heights of the soundings varied from 230 to 890 m.

Tower measurements were made next to the UNIS tethered sonde sounding site (some 20 m apart). In 2008, a 30 m tower was equipped with meteorological sensors at several levels [34]; here we applied the measurements of air temperature and relative humidity (HMP45C, Vaisala) at the height of 10 m, wind speed, and wind direction (A100LK and W200P, Vector instruments) at the heights of 10, 15, and 25 m, as well as the surface pressure (CS100, Campbell Scientific). In addition, a net radiometer (CNR1, Kipp & Zonen) was deployed to measure the downward and upward shortwave and longwave radiative fluxes, and a sonic anemometer (CSAT3, Campbell Scientific) at the height of 2.7 m was applied to measure turbulent fluxes of sensible heat and momentum.

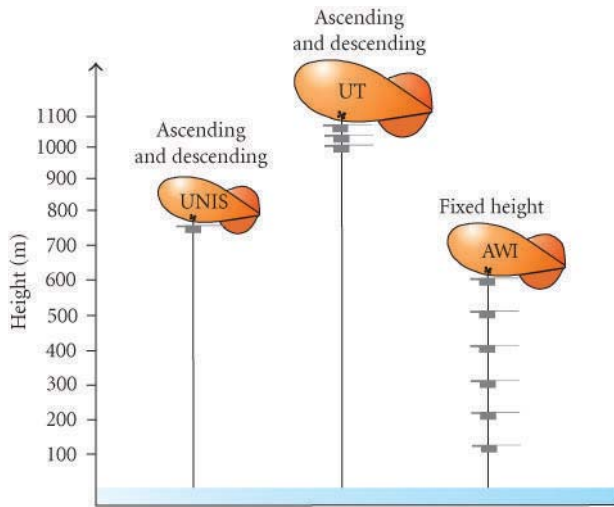


FIGURE 2: Schematic figure on the tethered sounding systems of the University Centre in Svalbard (UNIS), University of Tartu (UT), and Alfred Wegener Institute (AWI). The size of balloons is not in the scale of the vertical axis.

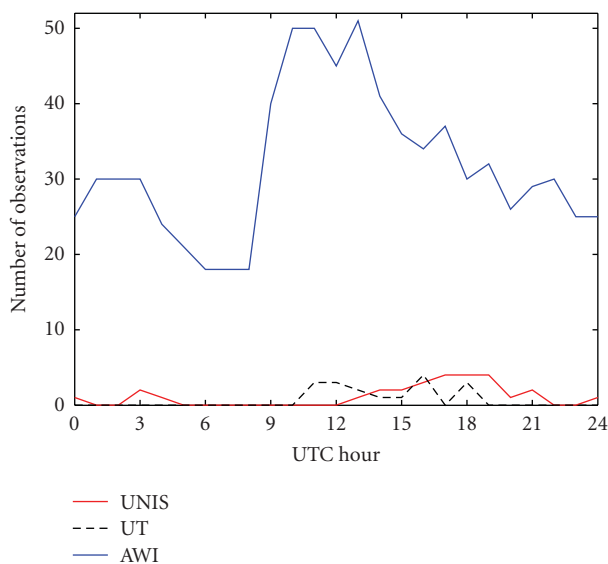


FIGURE 3: Diurnal distribution of tethered sounding observations.

In addition, the prevailing cloud and sea ice conditions were observed visually. The sea ice conditions were also analysed based on the sea ice charts produced by the Norwegian Meteorological Institute. In front of the measuring site, Isfjorden remained mostly free of ice, although there was occasionally pancake ice forming over night. The inner parts of the fjord branches were covered with land-fast ice (Figure 1).

2.3. Measurements at Kongsfjorden. Kongsfjorden is situated on the west coast of Spitsbergen and covers an area of approximately 220 km². The fjord is orientated from northwest to southeast and has a 10 km wide mouth to the open ocean. The measurement sites of UT (78°56'N, 11°51'E) and AWI (78°55'N, 11°55'E) were located on the southern coast of

Kongsfjorden, 1.4 km apart from each other (Figure 1). At the measurement sites, the fjord is approximately 4–9 km wide in a 140–160° wide sector. The local orography around the sites is very complex.

The tethered sounding measurements of UT were made between 21 March (day length 12 h 51 min) and 2 April 2009 (day length 16 h 16 min); altogether 17 soundings were made. Depending on the cloud conditions, wind speed, and the buoyancy of the 7 m³ balloon, the maximum height of the soundings varied from 600 to 1500 m with an average of 1200 m. The measurements of AWI were made between 12 March (day length 10 h 24 min) and 5 April 2009 (day length 17 h 13 min). The tethered balloon was launched whenever the weather conditions were appropriate, and kept at a constant altitude as long as the weather conditions and battery capacity allowed. During the campaign, 13 individual time series, 5 to 16 h each, were collected. The AWI tethered sounding data covered all hours of the day whereas the UT soundings were only made between 10 and 19 UTC (Figure 3). Moreover, AWI carries out regular rawinsonde soundings at Ny Ålesund daily at 11 UTC, with the launching site next to the AWI tethered sounding site. We also applied these data from the period of our campaign (14 rawinsonde soundings).

The near-surface temperature, relative humidity, and wind were measured at a 10 m weather mast of AWI, located approximately 300 m from the AWI sounding site. A 10 m weather mast of UT, equipped with wind, temperature, and humidity sensors (Aanderaa Co.) was situated at the coast, approximately 500 m from the AWI sounding site and 1 km from the UT sounding site. At this location, the downward and upward longwave radiation were measured by a pair of Eppley PIR pyrgeometers, and the downward and upward shortwave radiation by a pair of Eppley PSP pyranometers, and a sonic anemometer (Metek USA-1) was applied to measure the sensible heat flux. The cloud conditions were observed visually. The sea ice cover was estimated based on the sea ice charts produced by the Norwegian Meteorological Institute. The inner part of the fjord was covered with land-fast ice and the area towards the fjord mouth partly with drifting ice (Figure 1). Next to the measurement sites, a compact field of drifting ice prevailed.

3. Data and Analysis Methods

Only the ascent profiles of temperature, humidity, and wind direction were used in the analyses of the tethered sounding data. However, to smoothen out the overestimation of wind speed during the descent and underestimation during the ascent, the values from both wind profiles were averaged. The profile data of UNIS were averaged over every 5 m to keep as good a resolution as possible. The data of UT was averaged over the three tethered soundings. Due to the limited accuracy of the height measurements of each individual tethered sounding, a 10 m averaging interval was used for the UT profiles. The near-surface air temperature and humidity were taken from the lowest measurement altitude of 5 m, and the wind speed and wind direction from the height of 10 m. The tethered sounding time series of AWI were averaged over 10 min at each level, which

gave 770 vertical profiles based on the six tethersondes. The weather mast measurements and near-surface measurements of radiative and turbulent fluxes were averaged over 30 min.

Wind direction measurements made with the tether-sonde systems suffered from a systematic compass malfunction due to extreme sensitivity to sensor tilt in the vicinity of the magnetic pole. The differences between the tether-sonde ascent profile and weather mast wind direction sensor readings were mostly within 30°. We concluded that the tether-sonde wind directions were not accurate enough to study the turning of the wind in the ABL, but the data still made it possible to detect from which of the nearby glaciers, mountains, or fjord branches the air mass was advected.

The operational analyses of the European Centre for Medium-Range Weather Forecasts (ECMWF), with 25 km horizontal resolution, were applied to get information on the geopotential height, wind speed, wind direction, temperature, temperature advection, relative humidity, and specific humidity at the 850 hPa pressure level, above the local mountains. The air masses were classified as marine or Arctic according to the wind direction at the 850 hPa level. Due to the tongue of the open ocean west of Svalbard and sea ice east and even southeast of Svalbard, the marine sector was defined as 200–290°, while the other wind directions represented the Arctic sector.

The terminology used to define a temperature inversion follows Andreas et al. [17]. The height of the inversion base z_{Tb} and the temperature of the inversion base T_b were taken from the level immediately below the temperature inversion (Figure 4). The top of the temperature inversion is the subsequent level where the temperature starts to decrease. The height and temperature of this level were taken as the height of the inversion top z_{Tt} and the temperature of the inversion top T_t . Hence, temperature inversion strength $TIS = T_t - T_b$, and temperature inversion depth $TID = z_{Tt} - z_{Tb}$. To ensure that no artificial inversions are generated due to measurement inaccuracy, cases where the temperature change through the inversion was 0.3°C or less were ignored. Thin negative lapse layers that occasionally occurred within the inversion layers were also ignored and considered to be within the inversion layer when they were less than 10 m thick and the temperature change within them was less than 0.3°C. A specific humidity inversion terminology, such as the specific humidity at the inversion base (q_b at z_{qb}) and at the inversion top (q_t at z_{qt}) was determined analogously to temperature inversion (Figure 4). Accordingly, humidity inversion strength $QIS = q_t - q_b$, and humidity inversion depth $QID = z_{qt} - z_{qb}$. Layers with a humidity increase larger than 0.02 g kg⁻¹ were considered as humidity inversion layers. Thin (less than 10 m) layers of humidity decrease within the inversion layer were ignored.

A low-level jet was defined following Stull [15] as the level where there is a local wind speed maximum with wind speeds at least 2 m s⁻¹ higher than wind speeds above it. As LLJs related to katabatic winds in Isfjorden often occur very close to the surface, the wind maxima often occurred at the lowest observation level of 10 m. The level of maximum wind speed was defined as the jet core height z_j , with the jet core wind speed U_j ; z_a is the height of the subsequent wind minimum,

TABLE 2: Comparison of simultaneous soundings by AWI and UT. UT₆₀₀ refers to the inversion statistics based solely on the lowermost 600 m of the UT data. N denotes the number of simultaneous observations for each variable. See Section 3 for definition of variables.

Variable/ N	AWI	UT	UT ₆₀₀
TID/5	193 m	106 m	109 m
TIS/5	3.9°C	4.5°C	4.1°C
T_b /5	-20.0°C	-19.5°C	19.5°C
T_t /5	-16.1°C	-14.9°C	-15.4°C
QID/8	203 m	124 m	59 m
QIS/8	0.07 g kg ⁻¹	0.18 g kg ⁻¹	0.11 g kg ⁻¹
Q_b /8	0.61 g kg ⁻¹	0.52 g kg ⁻¹	0.52 g kg ⁻¹
Q_t /8	0.68 g kg ⁻¹	0.70 g kg ⁻¹	0.62 g kg ⁻¹
z_j /3	208 m	213 m	213 m
$U_j - U_a$ /3	2.9 m s ⁻¹	3.9 m s ⁻¹	3.7 m s ⁻¹
U_j /3	5.2 m s ⁻¹	6.2 m s ⁻¹	6.2 m s ⁻¹

and U_a the corresponding wind speed (Figure 4). The LLJ depth was defined as $z_a - z_j$.

4. Temperature and Humidity Inversions

Inversions were observed during variable synoptic situations. Over Kongsfjorden, the 850 hPa level wind speed ranged from 0 to 20 m s⁻¹, the air temperature from -28 to -12°C, and the temperature advection from -2.9 to 2.6°C h⁻¹. Most common were moderate northerly winds (mean speed 7.3 m s⁻¹) with a weak cold-air advection (mean -0.3°C h⁻¹). Over Isfjorden, the 850 hPa level wind speed varied from 3 to 10 m s⁻¹, the air temperature from -20 to -11°C, and the temperature advection from -1.2 to 0.8°C h⁻¹.

4.1. Effects of the Sounding Practice. To quantify the methodological effects on observed temperature and humidity inversions, we compared the simultaneous soundings of AWI and UT. To distinguish between the effects of vertical resolution (10 m for UT (see Section 3), 100 m for AWI) and maximum sounding altitude (600–1500 m for UT, 600 m for AWI) in generating differences in the observed inversion properties, we also calculated the inversion statistics separately for a subset of the UT data only including the lowermost 600 m of the profiles (data from upper levels were ignored). The differences between this data subset (hereafter UT₆₀₀ data) and simultaneous AWI soundings are solely due to vertical resolution.

The largest relative differences between the AWI and the original UT data sets, of the order of 100%, were found in TID, QIS, and QID, with thicker inversions in the AWI data but stronger inversions in the UT data (Table 2). The differences in TID were almost entirely due to the coarse vertical resolution of the AWI data set, where many elevated inversions were sampled as surface based (UT and UT₆₀₀ data gave practically same mean values, demonstrating an insignificant effect of maximum altitude). On the contrary, both

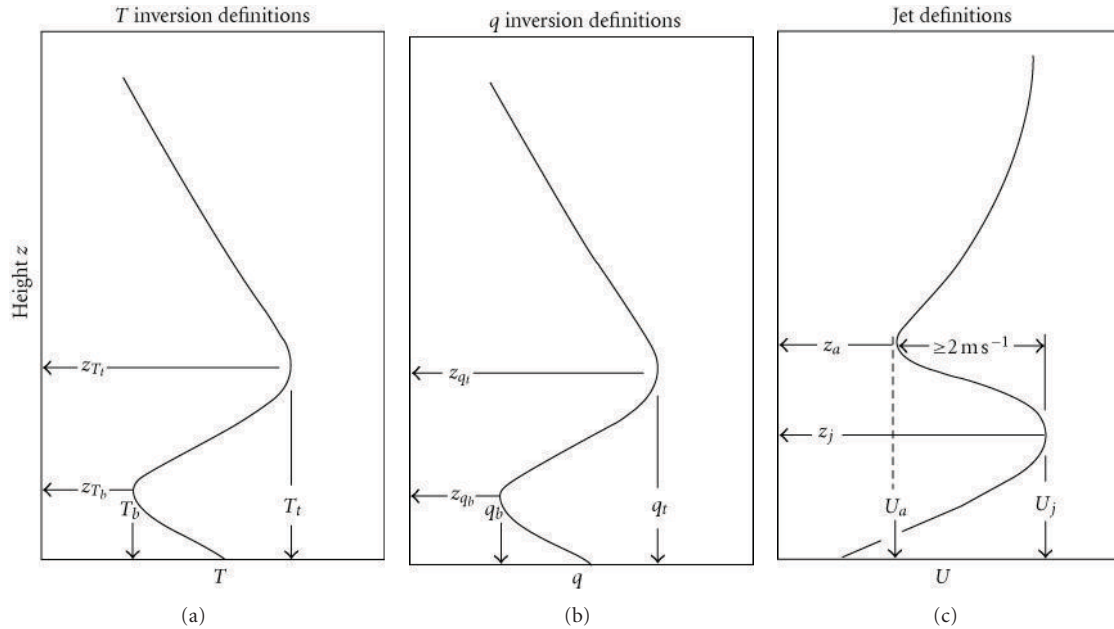


FIGURE 4: (a) Parameters of a temperature T inversion: z_{Tb} is the height of the temperature inversion base, z_{Tt} the temperature inversion top height, T_b the temperature at the inversion base, and T_t the temperature at the inversion top; (b) Parameters of a humidity inversion: z_{qb} is the height of the humidity inversion base, z_{qt} the humidity inversion top height, q_b the specific humidity at the inversion base, and q_t the specific humidity at the inversion top. (c) Parameters of a low-level jet. z_j is the height of the jet core and U_j the wind speed of the jet core. z_a is the height of the wind minimum above the jet core and U_a the wind speed there. Modified from Andreas et al. [17].

the vertical resolution and maximum altitude were essential in generating differences in QID and QIS: the three data sets yielded dramatically different mean values (Table 2). For QID the AWI data yielded the largest values, as many elevated inversions were sampled as surface based and separate inversion layers were often counted as one. For QIS, however, the largest values were found in the UT data; the AWI data missed both the maximum humidities that occurred above 600 m and the minimum humidities that were not detected due to the coarse vertical resolution. TIS was less affected by the sounding practice, because temperature inversions on average reached lower heights than humidity inversions. UT data also allowed better detection of the fine structure of the wind profiles, resulting in stronger LLJs and core wind speeds (Table 2). As the LLJs occurred in the lowermost 600 m, the differences in core winds were solely due to vertical resolution, but the jet strength was also affected by the wind minimum, which was sometimes located above 600 m.

The data sets included four cases with simultaneous soundings by both tether sondes and the AWI rawinsonde system. In two of these cases the rawinsonde data missed the strong temperature inversions that occurred in the lowermost 100 m layer. Using UT tether sonde data as reference, the warm bias in the rawinsonde data was up to 4.5°C .

4.2. Basic Inversion Properties. Statistics of temperature and humidity inversions are summarized in Table 3. Looking at the mean values of all three data sets (UNIS, UT, and AWI), the temperature inversions had a lower base height than the humidity inversions, but the humidity inversions were thicker and had a higher top. The reason for the tem-

perature inversions not reaching as high altitudes as humidity inversions is the adiabatic cooling; no comparable mechanism affects the specific humidity in unsaturated air (the tether sondes did not enter into clouds). The reason for the lower base height for temperature inversions is that the snow surface acted as a heat sink: the observed sensible heat flux was from air to snow for 90% of the time in Isfjorden and 93% of the time in Kongsfjorden. Surface-based temperature inversions were therefore common and, in the case of an elevated inversion, forced convection was seldom strong enough to generate a thick mixed layer below the elevated inversion. On the contrary, the snow surface was seldom a sink for air humidity. The observations indicated that the surface-specific humidity (calculated from the surface temperature based on the longwave radiation data) exceeded the air-specific humidity (weather mast data from 2–10 m height) for 79% and 63% of the time in Isfjorden and Kongsfjorden, respectively. Such conditions did not favour surface-based humidity inversions.

The mean profiles for air masses of marine and Arctic origin are shown in Figure 5. Considering the temperature profiles, UNIS soundings showed that the marine air masses were much warmer than the Arctic ones, but the temperature inversions were stronger in the marine than Arctic air mass (mean TIS 2.3 and 1.6°C , resp.). This was partly due to the warmer air at higher altitudes and partly due to the surface cooling (down to -9°C on average) during the flow of marine air masses over western parts of Svalbard archipelago before reaching the sounding site. At Kongsfjorden, the marine air masses were typically $2\text{--}3^\circ\text{C}$ warmer than the Arctic ones. Contrary to Isfjorden, the both Kongsfjorden data

TABLE 3: Statistics of temperature and humidity inversions. See the text for definition of the symbols.

Data set*	Temperature inversions			Humidity inversions		
	Variable	Mean	Std	Variable	Mean	Std
UNIS	z_{Tb} (m)	107	192	z_{qb} (m)	210	222
UNIS	$z_{Tt} - z_{Tb}$ (m)	54	39	$z_{qt} - z_{qb}$ (m)	62	57
UNIS	T_b ($^{\circ}\text{C}$)	-15.9	5.0	q_b (g kg^{-1})	0.77	0.35
UNIS	$T_t - T_b$ ($^{\circ}\text{C}$)	1.4	1.0	$q_t - q_b$ (g kg^{-1})	0.77	0.07
UT	z_{Tb} (m)	423	374	z_{qb} (m)	472	334
UT	$z_{Tt} - z_{Tb}$ (m)	92	59	$z_{qt} - z_{qb}$ (m)	103	106
UT	T_b ($^{\circ}\text{C}$)	-18.2	4.5	q_b (g kg^{-1})	0.72	0.50
UT	$T_t - T_b$ ($^{\circ}\text{C}$)	1.7	1.8	$q_t - q_b$ (g kg^{-1})	0.11	0.14
AWI	z_{Tb} (m)	85	146	z_{qb} (m)	201	156
AWI	$z_{Tt} - z_{Tb}$ (m)	184	120	$z_{qt} - z_{qb}$ (m)	270	152
AWI	T_b ($^{\circ}\text{C}$)	-18.0	3.5	q_b (g kg^{-1})	0.47	0.28
AWI	$T_t - T_b$ ($^{\circ}\text{C}$)	3.4	2.6	$q_t - q_b$ (g kg^{-1})	0.43	0.40

* Number of cases in the data sets: UNIS 39, UT 42, AWI 851.

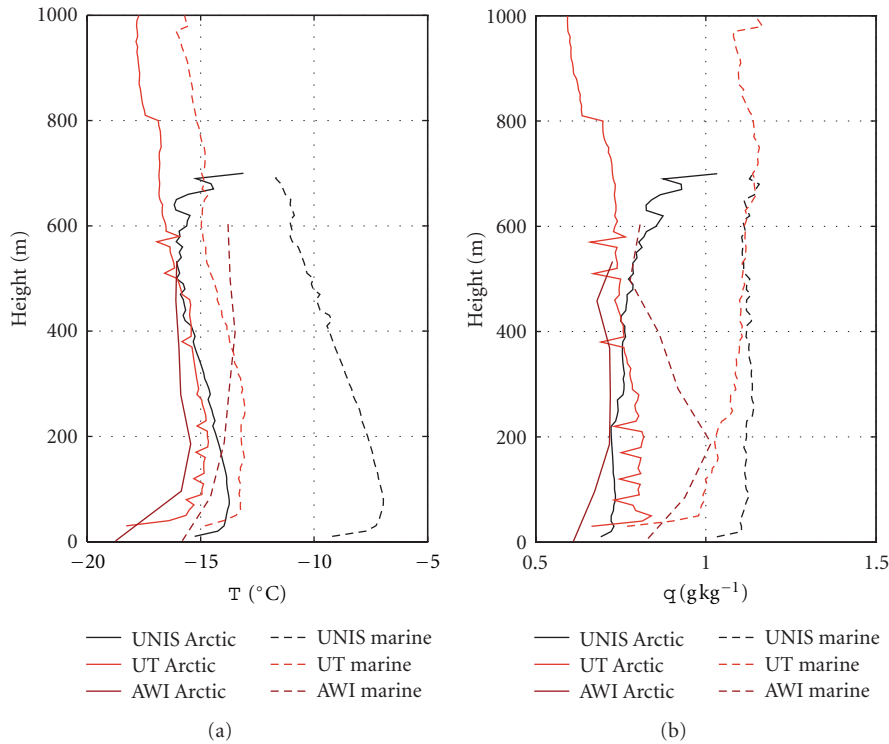


FIGURE 5: Mean profiles of the air temperature and specific humidity according to the UNIS, UT, and AWI soundings in cases of air masses of marine and Arctic origin.

sets (UT and AWI) indicated stronger temperature inversions in the Arctic than marine air masses. This is because the marine air masses entering in Kongsfjorden were colder than in Isfjorden; they either arrived from more northern areas or travelled a longer distance over Svalbard.

Considering the humidity profiles, UT, AWI, and UNIS data sets all indicated that the marine air masses were moister than the Arctic ones throughout the layer covered by the soundings (Figure 5(b)). The individual profiles often included elevated inversions, but their heights varied a lot,

and therefore they do not clearly appear in the mean profiles. The mean profiles show humidity inversions right upwards from the lowest atmospheric observation height (2 or 9 m) but, as mentioned above, the surface-specific humidity usually exceeded the near-surface value in the air.

4.3. Relationships between Variables. In this subsection, we only consider the properties of the strongest inversion of each vertical profile. First we report the strongest statistical relationships between the inversion properties, which do

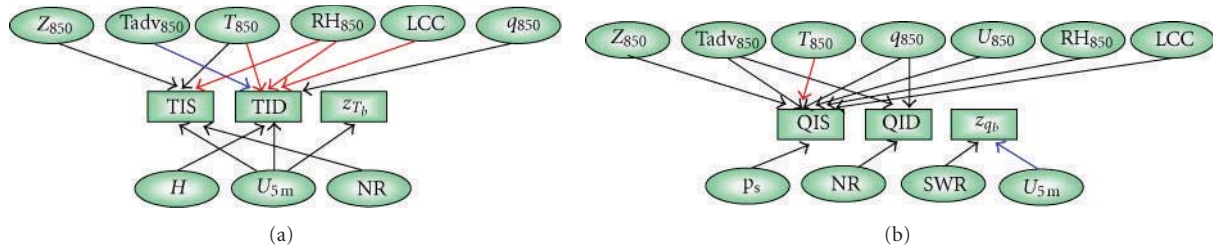


FIGURE 6: A schematic presentation of the observed relationships between inversion properties and other meteorological variables for (a) temperature and (b) humidity inversions. The thick red arrows denote statistically significant relationships detected from at least two tethersonde data sets, and the thick blue arrows mark the relationships with the highest correlation coefficients found in a single tethersonde data set (UT).

not necessarily have any causal links. In all three data sets, TIS increased with increasing TID (correlation coefficient r ranged from 0.48 to 0.70), but QIS and QID had a significant positive correlation only in the AWI data set ($r = 0.40$). In the UT data, z_{qb} was related to z_{Tb} ($r = 0.76$), TIS ($r = -0.62$), and QID ($r = 0.52$). The last finding is interesting: the higher the inversion base was, the thicker was the inversion, which demonstrates the dominating role of variations in the moisture content far above the surface, typically controlled by synoptic-scale processes.

Next we focus on potentially causal relationships, studying how the strength, depth, and base height of temperature and humidity inversions are affected by the large-scale flow variables at 850 hPa level, above the mountain tops (wind speed U_{850} , air temperature T_{850} , specific humidity q_{850} , relative humidity RH_{850} , temperature advection T_{adv850} , and the height of the pressure level Z_{850}), as well as total cloud cover (TCC), low cloud cover (LCC), 5 m wind speed (U_{5m}), and the surface fluxes of sensible heat (H), net radiation (NR), downward solar radiation (SWR), and downward longwave radiation (LWR). The fluxes are defined positive towards the surface. The statistically significant correlations are presented in Table 4, and a schematic summary of the relationships between variables in Figure 6.

4.3.1. Isfjorden. On average, TIS increased with increasing Z_{850} and decreasing NR, q_{850} , and RH_{850} (Table 4). Temperature inversions were accordingly strong in high-pressure conditions with dry air. TID increased with increasing (downward) surface sensible heat flux and decreasing q_{850} . QIS was affected by the 850 hPa variables and the surface pressure. A large QID was surprisingly related to a low q_{850} . This was because in cases with a large q_{850} there was either no humidity inversion (marine air mass occupied the whole atmospheric column up to the 850 hPa level) or only a very shallow internal boundary layer with a thin humidity inversion was generated at the sounding site. This was qualitatively in agreement with the UT results from Kongsfjorden, where warm-air advection decreased QID.

We observed a positive correlation between the near-surface wind speed and TIS ($r = 0.51$) and TID ($r = 0.44$). An explanation for this uncommon result is that the strongest and deepest inversions were associated with strong katabatic winds at the measurement site. Although the direct effect

TABLE 4: Potentially causal variables that have highest correlation coefficient (r) with the properties of inversions and low-level jets. Only $|r| \geq 0.4$ with significance level exceeding 95% are marked. See the text for definition of the symbols.

Variable	Statistical relationships		
	AWI	UT	UNIS
TIS	$U_{5m}: -0.40$	No significant correlations	NR: -0.46
	$T_{850}: 0.55$		$Z_{850}: 0.40$
	$RH_{850}: -0.56$		$q_{850}: -0.50$
TID	$T_{850}: 0.43$	$T_{adv850}: 0.76$	$H: 0.49$
	$RH_{850}: -0.45$	$RH_{850}: -0.56$	$q_{850}: -0.43$
		$T_{850}: 0.54$	
z_{Tb}	Not analysed	$U_{5m}: 0.58$	No significant correlations
QIS	$T_{850}: 0.64$	$Z_{850}: 0.52$	$P: -0.46$
	$q_{850}: 0.48$	$U_{850}: -0.53$	$T_{850}: 0.53$
		LCC: 0.50	$T_{adv850}: 0.43$
QID	No significant correlations	NR: -0.50	$q_{850}: -0.40$
		$T_{adv850}: -0.52$	
z_{qb}	SWR: $r = 0.53$	$U_{5m}: r = 0.65$	No significant correlations

of a strong near-surface wind is to erode the inversions, the katabatic wind strengthened the inversions by advecting cold near-surface air to the measurement site.

4.3.2. Kongsfjorden. In the AWI data set, TIS and TID correlated with T_{850} and RH_{850} (Table 4): strong and thick temperature inversions were favoured by warm, dry air at 850 hPa level. A low RH_{850} kept LWR low, which strengthened inversions. A high T_{850} had, however, two competing effects: to directly strengthen inversions and to increase LWR, which tends to weaken inversions. The former effect dominated. In the UT data, TID was strongly affected by T_{adv850} ($r = 0.76$) and significantly also with RH_{850} and T_{850} . A multiple linear regression analysis [45] using T_{adv850} and RH_{850}

as variables explaining TID yielded a high r of 0.88 with a root-mean-square error of only 30 m. It is noteworthy that inclusion of surface variables did not improve the regression. See Section 6 for further discussion.

In the AWI results, QIS was largest when the air at 850 hPa level was warm and moist (Table 4). In the UT data, a large QIS was favoured by a high Z_{850} and LCC, as well as a low U_{850} . A large NR and warm-air advection decreased QID. The stronger the wind speed, the higher were z_{Tb} and z_{qb} .

4.4. Differences between Day and Night. We analysed the differences between day and night on the basis of the AWI data (Figure 2). Despite the high latitude (small diurnal amplitude in the solar zenith angle), the data showed clear diurnal cycles in downward and upward components of solar radiation, upward longwave radiation, surface temperature (T_s), T_{2m} , q_{2m} , and RH_{2m} as well as in the strength and depth of temperature and humidity inversions (Figure 7; the quantitative numbers were naturally affected by the coarse vertical resolution). The diurnal cycles of TID and QID originated solely from the diurnal cycles in the inversion base heights. Our observations on daytime maximum of z_{qb} are qualitatively in agreement with the daytime maximum of the base height of low clouds observed over the Antarctic sea ice [45].

The causal factors correlating (negatively) with the daytime TIS were RH_{850} and U_{5m} . The daytime TID increased with increasing TIS. At night, warm air at the 850 hPa level tended to generate strong and deep temperature inversions. These warm air masses were often close to saturation at the 850 hPa level, suggesting that very small increase in the air humidity could have resulted in large changes in the inversion properties. Both during day and night, warm and moist air at the 850 hPa level favoured strong humidity inversions. The 850 hPa variables did not have any significant effect on daytime QID, but at night moist air at the 850 hPa level with a large LWR and a warm and moist surface favoured thick inversions.

4.5. Strongest Inversions. The strongest humidity inversion over Kongsfjorden (0.76 g/kg) was observed on 20 March at 12 UTC with warm air (-15°C) advected from west at 850 hPa level. During the preceding 24 h, the cloud cover had been 6–8 octas, but at noon it reduced to 3 octas, the snow surface cooled by 2.7°C , and evaporation stopped.

The strongest temperature inversion over Kongsfjorden (10.9°C) was observed on a clear night (22–23 UTC) on 30 March when T_s had decreased from -13 to -26°C in 8 h but T_{850} was still high (-15°C), just starting to decrease. Over Isfjorden, the by far strongest temperature and humidity inversions (6.5°C and 0.28 g kg^{-1} , resp.) were observed on 30 March 03–04 UTC, that is, during the same synoptic situation but 19 h earlier than in Kongsfjorden. The air was warm with the near-surface and 850 hPa air temperatures 2.3 and 6.0°C higher, respectively, than the mean values during the campaign. Some 30–36 h earlier strong southerly winds had advected warm, moist, and cloudy air over Svalbard. The wind calmed down the day before, and in the night of 30

March wind turned to northwest, remaining weak (4 m s^{-1} both at the surface and 850 hPa level), and the cloud fraction decreased from seven to three octas. The ECMWF analyses indicated subsidence of 0.03 m s^{-1} at the 850 hPa level, which may have contributed to the breaking of the cloud cover. Accordingly, the warm, moist air at higher altitudes, the weak winds, and the break of the cloud cover generated optimal conditions for strong inversions.

The model experiments of Kilpeläinen et al. [44] showed that such inversions in a warm air mass were particularly challenging for the Weather Research and Forecast (WRF) model. During the warm period from 27 to 31 March, the simulated temperature profiles were basically slightly stable with a lapse rate of -5 to -8°C km^{-1} from the surface to the 850 hPa level, only occasionally interrupted by weak, thin inversions. When the maximum temperature and humidity inversions were observed over Isfjorden, the modeled inversion strengths were only 0.3°C and 0.04 g kg^{-1} . Altogether 163 temperature inversions were observed during the campaign, but only 80 were simulated, with TIS, TID, and QIS generally underestimated [44].

5. Low-Level Jets

5.1. Overview on the Wind Conditions. Due to the limitations of the tethersonde system described in Section 2.1, the observed wind speeds at both fjords were mostly weak or moderate. At Isfjorden, the main wind direction was southeasterly both near the surface and above the temperature inversion. The LLJs over Isfjorden were divided into two groups. Group 1 consists of 15 cases with the jet core wind direction between 130 and 240° and the jet core below 100 m. These jets were caused by a katabatic flow from Platåberget (Figure 1). Group 2 consists of three cases with the jet core wind directions between 280 and 340° . The origin of these LLJs is not clear. Hereafter we only analyse the Group 1 LLJs.

At Kongsfjorden, the surface wind directions were variable but wind above the near-surface temperature inversion was usually easterly or southeasterly. In all LLJs of the AWI data and in 13 of the 15 LLJs of the UT data, the core wind directions were southeasterly; we interpret the jets to be generated by katabatic flow from Kongsvegen Glacier (Figure 1, [41]). The LLJ statistics are summarized in Table 5. No diurnal cycle was detected from the LLJ properties (z_j , $U_j - U_a$ and U_j).

5.2. Variables Related to Low-Level Jet Properties. At Isfjorden, z_j was large when the air was warm (Figure 8) from the surface to the inversion top, the atmospheric pressure was low, and the 850 hPa flow was weak. At Kongsfjorden, the results were very different from Isfjorden (Figure 8): z_j was larger and correlated negatively with the near-surface air temperature ($r = -0.65$ in UT data). High LLJs over Kongsfjorden were also associated with warm-air advection; the larger the advection, the higher the jet core ($r = 0.51$ in UT data).

We interpret the different results as follows. At Isfjorden, LLJs had their cores below 120 m altitude, and were related

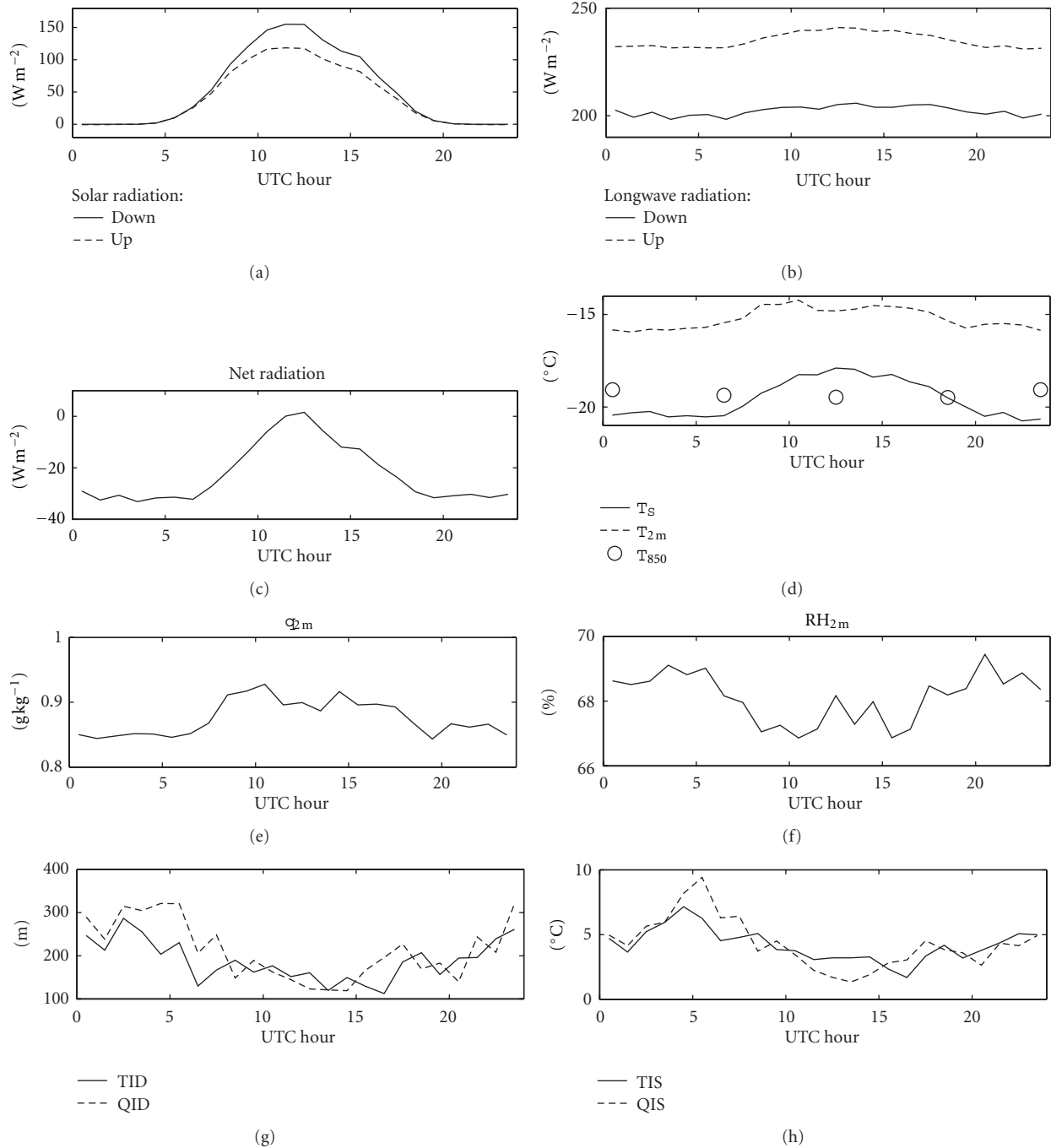


FIGURE 7: Average diurnal cycles of surface-layer observations and inversion properties, based on AWI soundings at Kongsfjorden.

to a katabatic flow from Platåberget. The near-surface air temperatures observed at the sounding site characterized the temperature of the katabatic flow at the coast. The fjord was ice-free with a constant surface temperature of about -1.8°C , and the air over the fjord was therefore heated via the turbulent fluxes from the sea. Hence, the colder the air flowing downslope, the closer to the surface it remained (Figure 8). At Kongsfjorden, however, the fjord in front of the observation site was frozen. Because of (a) adiabatic warming of the katabatic flow and (b) stronger stratification over the flat sea

ice than on the slope (where the katabatic flow mixed the near-surface air), the katabatic flow was elevated above the cold-air pool on the sea ice and the flat sounding site. This interpretation is supported by observations and model results from Wahlenbergfjorden, Svalbard [35], Antarctic [46, 47], and midlatitude mountain valleys [48]. The above is also supported by the fact that in the Kongsfjorden UT data set the LLJ core was always above the temperature inversion top but at Isfjorden the LLJ core was more often located below the inversion top than above it. The role of warm-air

TABLE 5: Statistics of low-level jet parameters.

Isfjorden (UNIS)		
Variable (20 cases)	Mean	std
z_j (m)	65	65
$z_a - z_j$ (m)	230	115
U_j (m s^{-1})	5.7	1.3
$U_j - U_a$ (m s^{-1})	3.0	0.7
Kongsfjorden (UT)		
Variable (15 cases)	Mean	std
z_j (m)	514	361
$z_a - z_j$ (m)	224	102
U_j (m s^{-1})	6.5	1.1
$U_j - U_a$ (m s^{-1})	3.6	1.0
Kongsfjorden (AWI)		
Variable (355 cases)	Mean	std
z_j (m)	206	103
$z_a - z_j$ (m)	268	106
U_j (m s^{-1})	5.6	1.8
$U_j - U_a$ (m s^{-1})	3.6	1.2

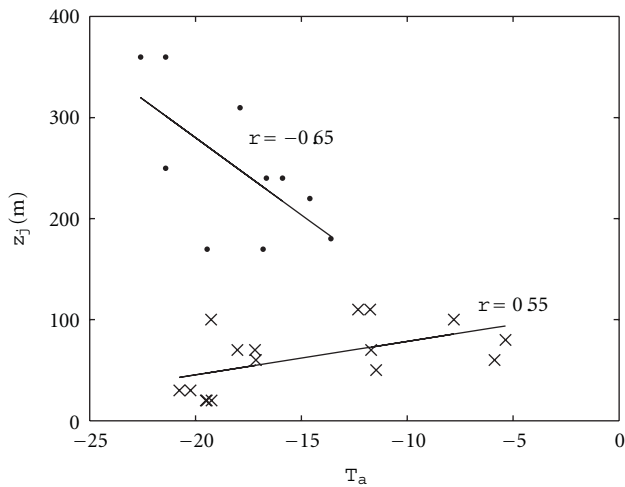


FIGURE 8: Dependence of the height of the LLJ core (z_j) on near-surface air temperature (T_a) in Isfjorden (crosses) and Kongsfjorden (dots).

advection in lifting the LLJ core is in accordance with the above; when the warm air masses of the free atmosphere meet the mountain or glacier slopes, they mix with the katabatic flow, increasing its temperature, which favours the lift of the flow above the cold-air pool on the valley bottom (the advection at 850 hPa level approximately represents the advection at the altitude of the upper parts of the Kongsvegen glacier (800 m) and the surrounding mountains (up to 1260 m)). Figure 9 schematically illustrates the mechanisms.

At Isfjorden, the LLJ core wind speed U_j was stronger when temperature inversions were deep, surface net radiation was negative, and clouds were few. In the AWI Kong-

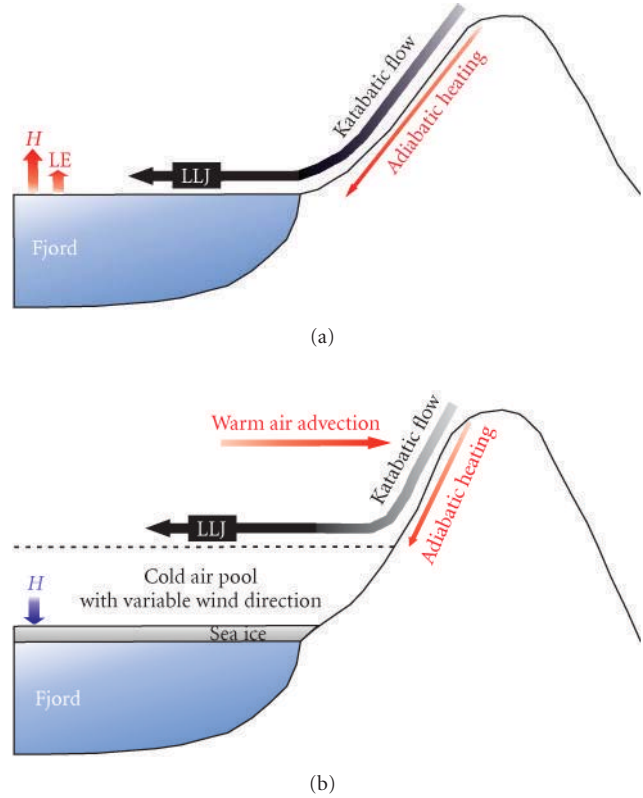


FIGURE 9: A schematic presentation of katabatic flows over (a) ice-free Isfjorden and (b) ice-covered Kongsfjorden. H and LE denote the turbulent fluxes of sensible and latent heat, respectively.

sfjorden data set, U_j increased with increasing T_{850} and decreasing LCC. Accordingly, factors related to stable stratification favoured a strong U_j in both fjords. The core wind speed did not, however, correlate with the local stratification at the measurement sites (expressed in terms of the near-surface Richardson number or stability parameter z/L , where L is the Obukhov length). This was because katabatic winds are generated due to stable stratification on sloping surfaces, but as the wind speed increases the local stratification is reduced due to wind-induced mixing [47], and the Obukhov length is not a relevant stability parameter over the slope, where turbulence is mostly governed by the LLJ [49, 50].

Due to the problems in wind direction measurements, the tethersonde data did not allow studies on the role of directional shear in the generation of LLJs, but the AWI rawinsonde sounding data demonstrated the importance of this effect. In 5 of the 14 rawinsonde soundings made during the campaign, the jet occurred at the same height with a remarkable ($>90^\circ$) change in the wind direction. In four of these five cases, the strongest winds were southeasterly ($90\text{--}130^\circ$), indicating an air mass origin in the Kongsvegen glacier (Figure 1). Accordingly, the directional shear was related to the katabatic winds lifted above the cold-air pool. Synoptic-scale baroclinicity, calculated on the basis of the thermal wind in the ECMWF analyses, did not contribute to the generation of the observed LLJs.

6. Discussion

The simultaneous soundings with different practices yielded different results for temperature and specific humidity inversions as well as LLJs. Such a sensitivity analysis seems not to have been published previously, although captive balloons have been applied in meteorological research since the 1800s [51] with systems comparable to ours since the 1970s [52]. The simultaneous AWI and UT soundings in Kongsfjorden revealed differences of the order of 100% in TID, QID, and QIS, with thicker inversions in the AWI data but stronger ones in the UT data, demonstrating the importance of a high vertical resolution. The rawinsonde sounding data, in turn, included large errors close to the surface. In addition to the measurement methodology, the actual values of the inversion parameters depend on the definitions, which vary in the literature. The results of Serreze et al. [1] for the Svalbard region, mostly based on radiosonde soundings in Barentsburg on the southern coast of Isfjorden (Figure 1), are comparable to our observations on TIS. Serreze et al. [1] showed, however, a mean TID of approximately 450 m for our study region in April–June, which is much higher than our data indicated. A potential explanation is that radiosonde soundings detect weak inversions at altitudes higher than those reached by a tethered sonde, and these are identified as a part of the near-surface inversion (if two inversion layers were separated by a layer less than 100 m thick, Serreze et al. [1] embedded this intermediate layer within the overall inversion layer).

The strength, depth, and base height of temperature and humidity inversions were related to each other. In general, strong inversions were deep and had their base at a high altitude. In both fjords, TIS, TID, QIS, and QID were affected by conditions both at the local surface and at the 850 hPa pressure level, the latter being more important characterizing the effects of the large-scale flow over the Svalbard mountains. In general, dry air at 850 hPa level favoured strong but thin temperature inversions, and warm air at 850 hPa level favoured strong humidity inversions. Considering individual cases, the largest TIS and QIS both over Isfjorden and Kongsfjorden were observed in conditions of warmer-than-average air at the 850 hPa level during the campaign. Kilpeläinen et al. [44] demonstrated that such inversions represent a challenge for numerical models, and our analyses suggested reasons for this: when the air mass is warm and the cloud cover breaks up, strong inversions are rapidly generated via surface cooling. Such changes in the cloud cover are very difficult to be reproduced by models [53].

Local radiative fluxes at the snow surface did not dominate the inversion properties (Table 4). In particular, the downward longwave radiation did not have a statistically significant role in any of the data sets. This is understandable because (a) the inversion strength and depth respond to the cumulative effect of surface forcing over the air mass trajectory, and the radiative fluxes measured at the fjord shore seldom represented the large-scale surface conditions under the trajectory well, and (b) via the effects of clouds, anomalies in the downward solar and longwave radiation compensated for each other. Hence, net radiation had more effect on the inversion properties (Table 4). Among the near-surface

variables, wind speed was the most important in affecting inversion properties: TIS, z_{Tb} , and z_{qb} over Kongsfjorden. Mixing due to a strong near-surface wind effectively erodes the inversion layer, resulting in weaker and more elevated inversions. Note, however, that at the coast of Isfjorden, the strongest and deepest inversions were associated with strong near-surface katabatic flows, which strengthened the inversions by advecting cold air.

We found strong correlations between inversion properties and 850 hPa variables. The strongest one resulted from a multiple regression with $T_{adv_{850}}$ and RH_{850} as explaining variables for TID, yielding $r = 0.88$. Besides basic understanding of the factors affecting inversions, such relationships may have some applicability. For example, many measurements on air chemistry and aerosols are regularly carried out in Svalbard, and information on the ABL structure is important for interpretation of the data [54]. Considering short-term forecasting, TID can be diagnosed from the output of operational numerical models, but the highest resolutions presently applied in operational NWP models for Svalbard are 4 and 8 km, which make them very liable to errors in a fjord with a complex orography [42]. The model products for 850 hPa variables are, however, more reliable [55]; via established empirical relationships with inversion properties they may provide a useful tool to forecast the inversion properties. However, this requires further studies.

7. Conclusions

We presented a unique set of tethered sonde sounding data from two Svalbard fjords. We note, however, that due to restrictions to sounding activity caused by weather conditions and aviation safety rules, the results obtained do not well represent the full statistics of weather conditions during the campaign, just a selected subset. The most important findings of the study were as follows.

- (i) A tethered sonde sounding practice with a high vertical resolution was essential as it allowed detection of strong near-surface inversions and low-level jets, which were not well detected by rawinsonde soundings.
- (ii) The properties of temperature and humidity inversions over Svalbard fjords in early spring were strongly affected by the synoptic-scale weather conditions above the mountains.
- (iii) The strongest individual temperature and humidity inversions were observed in warm and moist (in the sense of specific humidity) air masses. In general, however, the strength and depth of the temperature inversions increased with decreasing relative humidity at the 850 hPa level.
- (iv) Although temperature inversions are often generated by radiative cooling of the surface, in our data the downward longwave radiation measured at the sounding site did not correlate with the inversion strength, depth, and base height.

- (v) Humidity inversions occurred as frequently as temperature inversions, but humidity inversions on average (a) had a larger base height and (b) were thicker than the temperature inversions. This was due to (a) the role of the snow surface as a sink for heat but usually not for moisture, and (b) the effect adiabatic cooling in reducing the temperature inversion depth.
- (vi) Over the ice-covered Kongsfjorden, the jet core was located highest when the near-surface air was coldest: jets were lifted above the cold-air pool and associated inversion layer over the fjord. At the coast of the ice-free Isfjorden, jet cores were located lower, often below the inversion top, and the core height was highest in cases of warmest air.

Acknowledgments

The fieldwork in Ny-Ålesund, Kongsfjorden, was supported by the European Centre for Arctic Environmental Research (ARCFAC) and the target financed project SF0180049s09 of the Ministry of Education and Research of the Republic of Estonia, and the data analyses by the 6th EU Framework Programme project DAMOCLES (Grant 18509). In particular, the authors thank Jürgen Graeser and Marcus Schumacher for their contribution in the field work, and Christof Lüpkes, Anne Sandvik, and three anonymous reviewers for their constructive comments on the paper.

References

- [1] M. C. Serreze, J. D. Kahl, and R. C. Schnell, "Low-level temperature inversions of the Eurasian Arctic and comparisons with Soviet drifting station data," *Journal of Climate*, vol. 5, no. 6, pp. 615–629, 1992.
- [2] J. D. Kahl, M. C. Serreze, and R. C. Schnell, "Tropospheric low-level temperature inversions in the Canadian Arctic," *Atmosphere-Ocean*, vol. 30, no. 4, pp. 511–529, 1992.
- [3] M. Tjernström and R. G. Graverson, "The vertical structure of the lower Arctic troposphere analysed from observations and the ERA-40 reanalysis," *Quarterly Journal of the Royal Meteorological Society*, vol. 135, no. 639, pp. 431–443, 2009.
- [4] R. A. Brost and J. C. Wyngaard, "A model study of the stably stratified planetary boundary layer," *Journal of the Atmospheric Sciences*, vol. 35, no. 8, pp. 1427–1440, 1978.
- [5] J. C. Andre and L. Mahrt, "The nocturnal surface inversion and influence of clear-air radiative cooling," *Journal of the Atmospheric Sciences*, vol. 39, no. 4, pp. 864–878, 1982.
- [6] S. W. Hoch, P. Calanca, R. Philipona, and A. Ohmura, "Year-round observation of longwave radiative flux divergence in Greenland," *Journal of Applied Meteorology and Climatology*, vol. 46, no. 9, pp. 1469–1479, 2007.
- [7] J. E. Overland and P. S. Guest, "The Arctic snow and air temperature budget over sea ice during winter," *Journal of Geophysical Research*, vol. 96, no. 3, pp. 4651–4662, 1991.
- [8] T. Vihma, J. Hartmann, and C. Lüpkes, "A case study of an on-ice air flow over the Arctic marginal sea-ice zone," *Boundary-Layer Meteorology*, vol. 107, no. 1, pp. 189–217, 2003.
- [9] N. Busch, U. Ebel, H. Kraus, and E. Schaller, "The structure of the subpolar inversion-capped ABL," *Meteorology and Atmospheric Physics*, vol. 31, no. 1-2, pp. 1–18, 1982.
- [10] J. A. Curry, W. B. Rossow, D. Randall, and J. L. Schramm, "Overview of Arctic cloud and radiation characteristics," *Journal of Climate*, vol. 9, no. 8, pp. 1731–1746, 1996.
- [11] M. C. Serreze, R. G. Barry, and J. E. Walsh, "Atmospheric water vapor characteristics at 70°N," *Journal of Climate*, vol. 8, no. 4, pp. 719–731, 1995.
- [12] J. Sedlar and M. Tjernström, "Stratiform cloud—inversion characterization during the Arctic melt season," *Boundary-Layer Meteorology*, vol. 132, no. 3, pp. 455–474, 2009.
- [13] J. Curry, "On the formation of continental polar air," *Journal of the Atmospheric Sciences*, vol. 40, no. 9, pp. 2278–2292, 1983.
- [14] E. Jakobson and T. Vihma, "Atmospheric moisture budget over the Arctic on the basis of the ERA-40 reanalysis," *International Journal of Climatology*, vol. 30, no. 14, pp. 2175–2194, 2010.
- [15] R. B. Stull, *An Introduction to Boundary Layer Meteorology*, Kluwer Academic Publishers, Dordrecht, The Netherlands, 1988.
- [16] A. J. Thorpe and T. H. Guymer, "The nocturnal jet," *Quarterly Journal of the Royal Meteorological Society*, vol. 103, no. 438, pp. 633–653, 1977.
- [17] E. L. Andreas, K. J. Claffey, and A. P. Makshtas, "Low-level atmospheric jets and inversions over the Western Weddell Sea," *Boundary-Layer Meteorology*, vol. 97, no. 3, pp. 459–486, 2000.
- [18] A. S. Smedman, M. Tjernström, and U. Högström, "Analysis of the turbulence structure of a marine low-level jet," *Boundary-Layer Meteorology*, vol. 66, no. 1-2, pp. 105–126, 1993.
- [19] T. Vihma, J. Uotila, and J. Launiainen, "Air-sea interaction over a thermal marine front in the Denmark Strait," *Journal of Geophysical Research*, vol. 103, no. C12, pp. 27665–27678, 1998.
- [20] R. M. Banta, "Stable-boundary-layer regimes from the perspective of the low-level jet," *Acta Geophysica*, vol. 56, no. 1, pp. 58–87, 2008.
- [21] R. H. Langland, P. M. Tag, and R. W. Fett, "An ice breeze mechanism for boundary-layer jets," *Boundary-Layer Meteorology*, vol. 48, no. 1-2, pp. 177–195, 1989.
- [22] I. A. Renfrew and P. S. Anderson, "Profiles of katabatic flow in summer and winter over Coats Land, Antarctica," *Quarterly Journal of the Royal Meteorological Society*, vol. 132, no. 616, pp. 779–802, 2006.
- [23] J. C. King and J. Turner, *Antarctic Meteorology and Climatology*, Cambridge University Press, Cambridge, UK, 1997.
- [24] S. S. Zilitinkevich and I. N. Esau, "Resistance and heat/mass transfer laws for neutral and stable planetary boundary layers: old theory advanced and re-evaluated," *Quarterly Journal of the Royal Meteorological Society*, vol. 131, pp. 1863–1892, 2005.
- [25] L. Mahrt, "Stratified atmospheric boundary layers," *Boundary-Layer Meteorology*, vol. 90, no. 3, pp. 375–396, 1999.
- [26] C. Lüpkes, T. Vihma, G. Birnbaum, and U. Wacker, "Influence of leads in sea ice on the temperature of the atmospheric boundary layer during polar night," *Geophysical Research Letters*, vol. 35, no. L03805, 5 pages, 2008.
- [27] C. Lüpkes, V. M. Gryanik, B. Witha, M. Gryschka, S. Raasch, and T. Gollnik, "Modeling convection over Arctic leads with LES and a non-eddy-resolving microscale model," *Journal of Geophysical Research*, vol. 113, Article ID C09028, 17 pages, 2008.
- [28] G. S. Poulos and S. P. Burns, "An evaluation of bulk Ri-based surface layer flux formulas for stable and very stable conditions with intermittent turbulence," *Journal of the Atmospheric Sciences*, vol. 60, no. 20, pp. 2523–2537, 2003.

- [29] M. Tjernström, M. Zagar, G. Svensson et al., “Modelling the Arctic boundary layer: an evaluation of six ARCMIP regional-scale models using data from the SHEBA project,” *Boundary-Layer Meteorology*, vol. 117, no. 2, pp. 337–381, 2005.
- [30] E. M. Tastula and T. Vihma, “WRF model experiments on the Antarctic atmosphere in winter,” *Monthly Weather Review*, vol. 139, no. 4, pp. 1279–1291, 2011.
- [31] E. Atlaskin and T. Vihma, “Validation of numerical weather prediction results for wintertime nocturnal boundary-layer temperatures,” submitted to *Quarterly Journal of the Royal Meteorological Society*.
- [32] R. G. Barry, *Mountain Weather and Climate*, Cambridge University Press, Cambridge, UK, 2008.
- [33] E. J. Førland, I. Hanssen-Bauer, and P. O. Nordli, “Climate statistics and longterm series of temperature and precipitation at Svalbard and Jan Mayen,” DNMI Report, Klima 21/97, p. 72, 1997.
- [34] T. Kilpeläinen and A. Sjöblom, “Momentum and sensible heat exchange in an ice-free Arctic fjord,” *Boundary-Layer Meteorology*, vol. 134, pp. 109–130, 2010.
- [35] E. Mäkiranta, T. Vihma, A. Sjöblom, and E. M. Tastula, “Observations and modelling of the atmospheric boundary layer over sea ice in a Svalbard fjord,” *Boundary-Layer Meteorology*, vol. 140, no. 1, pp. 105–123, 2011.
- [36] H. J. Beine, S. Argentini, A. Maurizi, G. Mastrantonio, and A. Viola, “The local wind field at Ny-Ålesund and the Zeppelin mountain at Svalbard,” *Meteorology and Atmospheric Physics*, vol. 78, pp. 107–113, 2001.
- [37] S. Argentini, A. P. Viola, G. Mastrantonio, A. Maurizi, T. Georgiadis, and M. Nardino, “Characteristics of the boundary layer at Ny-Ålesund in the Arctic during the ARTIST field experiment,” *Annals of Geophysics*, vol. 46, no. 2, pp. 185–196, 2003.
- [38] A. D. Sandvik and B. R. Furevik, “Case study of a coastal jet at Spitsbergen—Comparison of SAR- and model-estimated wind,” *Monthly Weather Review*, vol. 130, no. 4, pp. 1040–1051, 2002.
- [39] T. Vihma, C. Lüpkes, J. Hartmann, and H. Savijärvi, “Observations and modelling of cold-air advection over Arctic sea ice,” *Boundary-Layer Meteorology*, vol. 117, no. 2, pp. 275–399, 2005.
- [40] J. Reuder, P. Brisset, M. Jonassen, M. Müller, and S. Mayer, “The small unmanned meteorological observer SUMO: a new tool for atmospheric boundary layer research,” *Meteorologische Zeitschrift*, vol. 18, no. 2, pp. 141–147, 2009.
- [41] J. Livik, *An Observational and Numerical Study of Local Winds in Kongsfjorden, Spitsbergen*, M.S. thesis, Geophysical Institute, University of Bergen, Bergen, Norway, 2011.
- [42] T. Kilpeläinen, T. Vihma, and H. Ólafsson, “Modelling of spatial variability and topographic effects over Arctic fjords in Svalbard,” *Tellus A*, vol. 63, no. 2, pp. 223–237, 2011.
- [43] U. Schauer, “The release of brine-enriched shelf water from Storfjord into the Norwegian Sea,” *Journal of Geophysical Research*, vol. 100, no. C8, pp. 16015–16028, 1995.
- [44] T. Kilpeläinen, T. Vihma, M. Manninen et al., “Modelling the vertical structure of the atmospheric boundary layer over Arctic fjords in Svalbard,” submitted to *Quarterly Journal of the Royal Meteorological Society*.
- [45] T. Vihma, M. M. Johansson, and J. Launiainen, “Radiative and turbulent surface heat fluxes over sea ice in the western Weddell Sea in early summer,” *Journal of Geophysical Research*, vol. 114, no. C04019, 18 pages, 2009.
- [46] I. A. Renfrew, “The dynamics of idealized katabatic flow over a moderate slope and ice shelf,” *Quarterly Journal of the Royal Meteorological Society*, vol. 130, no. 598, pp. 1023–1045, 2004.
- [47] T. Vihma, E. Tuovinen, and H. Savijärvi, “Interaction katabatic winds and near-surface temperatures in the Antarctic,” *Journal of Geophysical Research*, vol. 116, no. D21119, 14 pages, 2011.
- [48] C. B. Clements, C. D. Whiteman, and J. D. Horel, “Cold-air-pool structure and evolution in a mountain basin: Peter Sinks, Utah,” *Journal of Applied Meteorology*, vol. 42, no. 6, pp. 752–768, 2003.
- [49] B. Grisogono, L. Kraljevic, and A. Jericevic, “The low-level katabatic jet height versus Monin-Obukhov height,” *Quarterly Journal of the Royal Meteorological Society*, vol. 133, no. 629, pp. 2133–2136, 2007.
- [50] R. M. Banta, Y. L. Pichugina, and W. A. Brewer, “Turbulent velocity-variance profiles in the stable boundary layer generated by a nocturnal low-level jet,” *Journal of the Atmospheric Sciences*, vol. 63, no. 11, pp. 2700–2719, 2006.
- [51] J. L. DuBois, R. P. Multhauf, and C. A. Ziegler, *The Invention and Development of the Radiosonde, with a Catalog of Upper-Atmospheric Telemetering Probes in the National Museum of American History*, Smithsonian Studies in History and Technology, no. 53, Smithsonian Institution Press, Washington, DC, USA, 2002.
- [52] A. L. Morris, D. B. Call, and R. B. McBeth, “A small tethered balloon sounding system,” *Bulletin of the American Meteorological Society*, vol. 56, no. 9, pp. 964–969, 1975.
- [53] M. Tjernström, J. Sedlar, and M. D. Shupe, “How well do regional climate models reproduce radiation and clouds in the Arctic? An evaluation of ARCMIP simulations,” *Journal of Applied Meteorology and Climatology*, vol. 47, no. 9, pp. 2405–2422, 2008.
- [54] M. Tuckermann, R. Ackermann, C. Gözl et al., “DOAS-observation of halogen radical-catalysed arctic boundary layer ozone destruction during the ARCTOC-campaigns 1995 and 1996 in Ny-Ålesund, Spitsbergen,” *Tellus B*, vol. 49, no. 5, pp. 533–555, 1997.
- [55] C. Lüpkes, T. Vihma, E. Jakobson, G. K. Langlo, and A. Tetzlaff, “Meteorological observations from ship cruises during summer to the central Arctic: a comparison with reanalysis data,” *Geophysical Research Letters*, vol. 37, no. L09810, 4 pages, 2010.

Research Article

Spectral Analysis of the Svalbard Temperature Record 1912–2010

Ole Humlum,^{1,2} Jan-Erik Solheim,³ and Kjell Stordahl⁴

¹ Department of Geosciences, University of Oslo, P.O. Box 1047 Blindern, N-0316 Oslo, Norway

² Department of Geology, University Centre in Svalbard (UNIS), P.O. Box 156, N-9171 Longyearbyen, Svalbard, Norway

³ Department of Physics and Technology, University of Tromsø, N-9037 Tromsø, Norway

⁴ Telenor Norway, Finance, N-1331 Fornebu, Norway

Correspondence should be addressed to Ole Humlum, ole.humlum@geo.uio.no

Received 14 September 2011; Revised 14 December 2011; Accepted 20 December 2011

Academic Editor: Igor N. Esau

Copyright © 2011 Ole Humlum et al. This is an open access article distributed under the Creative Commons Attribution License, which permits unrestricted use, distribution, and reproduction in any medium, provided the original work is properly cited.

Climate development with possible anthropogenic effects occurs on a background of natural climatic variations, which may be considerable, and especially in the Arctic. Natural climate variations however remain poorly understood, although they remain important for discriminating between natural and anthropogenic influences on current climate change. Using the Svalbard (78°N) surface air temperature record 1912–2010 as an example, we here suggest a road ahead to identify and describe such natural climate variations. By means of Fourier and wavelet analysis the record is decomposed into time-frequency space, to extract information on periodic signals and their amplitude and variation over time. By this we identify several cyclic variations on the time scale investigated. These oscillations are present in the annual record, as well as in seasonal subsets of the record. Using only three oscillations it is possible to hindcast the Svalbard temperature record well. We suggest that such persistent oscillations may be used for forecasting the overall features of future temperature changes for a limited period, about 10–25% of the record length. Our main focus is on identifying the character of recurrent natural temperature variations, but we also comment briefly on possible physical explanations for some of the identified cyclic variations.

1. Introduction

Climate science is a composite science that draws on theory and method from an astonishingly wide range of related disciplines. It, however, shares with other sciences a clearly definable general objective, succinctly defined by Braithwaite [1] as “*To establish general laws covering the behaviour of empirical events or objects ... and thereby to enable us to connect together our knowledge of separately known events, to make reliable predictions of events as yet unknown.*”

In accordance with Faegri’s [2] empirical law—the longer the period of climatic change, the wider the area similarly affected—we can expect that for a long period, say an Ice Age, the temperature change would encompass the entire globe, while for shorter periods of change, the change would only include correspondingly smaller areas. Over short periods of time, of the order of decades only, the climatic change over one region could differ even more from that of another nearby. The climatic record must consequently be studied region by region to establish the different characteristics of change in each individual region, both for ensuring correct

input in climate models and for establishing an orderly sequence of past climatic changes as a basis for their possible prediction [3].

Here, we will concern ourselves with the climatic changes during the last 98 years in the Svalbard region of the Arctic, by attempting to identify recurrent, natural temperature variations documented by the Svalbard 1912–2010 meteorological record. Our main focus is the mean annual surface air temperature (MAAT), although we will also consider the two seasonal subsets (DJF; winter) and (JJA; summer) of this record.

Most meteorological series display significant decadal or multiyear periodic behaviour, which so far have not been fully included in analytic climate models (see, e.g., Solomon et al. [5]), mainly because of still incomplete knowledge on the detailed character of such variations. For example, the Pacific Oscillation that gives rise to El Niño and La Niña has been known for over a century, and in the North Atlantic a similar oscillation, the North Atlantic Oscillation (NAO), is known to influence weather in this region. In addition, from several different environmental records an

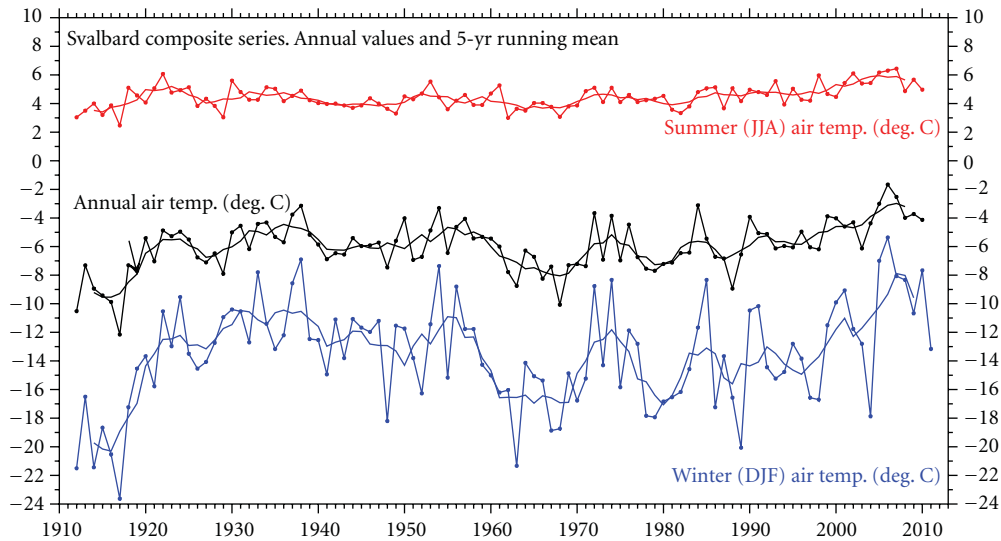


FIGURE 1: The Svalbard temperature record 1912–2010 [4], showing the mean annual air temperature (MAAT), the average summer temperature (JJA), and the average winter temperature (DJF). Thin lines show annual values, and thick lines show the simple 5 yr average. The linear MAAT increase 1912–2010 is 0.23°C per decade.

about 60 yr climate cycle is known (see, e.g., Klyashtorin and Lyubushin [6]). Thus, during the last few years there has been an increasing realisation of important oscillatory phenomena in the earth's global weather system, not the least as knowledge on such cyclic variations is important to discriminate between natural and anthropogenic influences on current climate change. This suggests that an attempt of identifying cyclic variations is timely for improving understanding of past, present, and future climate variations.

To exemplify how natural, cyclic temperature variations might be identified and analysed, we here first present the Svalbard meteorological record 1912–2010, followed by a brief introduction to the wavelet and Fourier analysis techniques, before proceeding to a spectral analysis of the Svalbard record. We chose to focus on one temperature series instead of using averaged series covering larger regions, such as, for example, global or hemispheric series. We do this because the common procedure of averaging individual data series with different levels of autocorrelation may change the statistical structure of the resulting averaged time series notably, compared to the original series, an issue previously pointed out by Polyak [7]. The present analysis is building on an initial and broader analysis [4], but here we take a more detailed view on the Svalbard record, including issues relating to statistical significance and seasonal subsets of the record.

2. The Svalbard Temperature Record

Special climatic interest has often been attached to the Svalbard region because of the high latitude and the fact that this part of the Arctic apparently displays an extraordinary high climatic variability, partly reflecting global temperature trends. This was recognized early by both Ahlmann [8] and Lamb [9], and later by Rogers et al. [10], but also in the

third IPCC report [11] attention was again drawn to the high climatic sensitivity of the Svalbard region.

Climatic variations in Svalbard during the 20th century are documented by monthly meteorological data since November 1911 by Førland et al. [12], and the Svalbard record (Figure 1) is the longest meteorological record from the High Arctic. The modern official Svalbard meteorological station is located near the main settlement in Svalbard, Longyearbyen ($78^{\circ}13'N$, $15^{\circ}33'E$, about 2000 inhabitants), in central Spitsbergen. The station is located at the Svalbard Airport (24 m asl.), about 3 km NW of Longyearbyen, near the shore of the large fjord Isfjorden. Monthly temperature data were obtained from the eKlima portal run by the Norwegian Meteorological Institute, and MAAT, DJF, and JJA values of 1912–2010 calculated from this.

The Svalbard record is a homogenized composite record, established from observations made at different stations in central Spitsbergen, mainly around the large fjord Isfjorden, extending from the west coast to interior Spitsbergen. The individual meteorological stations have been described by Hanssen-Bauer et al. [13], and a survey of meteorological statistics for the Norwegian Arctic presented by Førland et al. [12]. It is generally difficult to establish reliable long-term meteorological series from Arctic areas, as weather observations here primarily are aimed for forecasting purposes, and usually little care is taken to prevent inhomogeneities caused by relocations, change in local environment (buildings), and instrumental changes (Nordli et al. [14]). In addition, the station network in the Arctic is sparse, so it is often difficult to find good reference series for use in homogeneity studies.

To overcome these difficulties and to homogenise meteorological time series from Svalbard, Nordli et al. [14] used data from several North Atlantic regions in the homogeneity testing of the Svalbard series. The following stations were used as reference: Tromsø (Norway), Vardø (Norway), Makkaur Lighthouse (Norway), Ekkerøy (Norway),

Longyearbyen (Svalbard), Stykkisholmur (Iceland), Teigarhorn (Iceland), Scoresbysund (Greenland), and Ammassalik (Greenland). In addition, data from parallel Svalbard measurements and metadata archives was used as supplementary information. The Standard Normal Homogeneity Test (Alexandersson [15], Hanssen-Bauer and Førland [16]) was applied on the series, and the results were validated by a study of the individual stations history. By this homogeneity monthly series for air temperature and precipitation were established for Svalbard Airport back to late 1911 [14]. The absence of visible irregularities in the Svalbard temperature record itself (Figure 1) as well as in the wavelet diagrams (Figures 3 and 5), corresponding to the timing of known station changes, testifies to the quality of the homogenisation carried out.

A prominent feature of the homogenised Svalbard temperature record is a marked warming 1917–1922, which changed MAAT at sea level from about -12.2°C to -4.9°C . However, it is not known if the low starting temperature in the record (Figure 1) is typical for Little Ice Age conditions in Svalbard, or if it only represents the culmination of a decadal-scale cold period in the transition to warmer conditions following the Little Ice Age. Comparisons with early records from northern Norway (e.g., Alta Airport, 70.0°N 23.4°E , 1880–1939; Vardø, 70.37°N 31.10°E , 1840–2010; Mehavensletnes, 71.9°N 27.8°E , 1899–1940) suggest that this might well be the case. Judging from these stations, Svalbard MAAT in the decade leading up to 1912 presumably was 1 to 3°C above what was recorded between 1912 and 1917. If so, the linear trend of 0.23°C per decade calculated for the 1912–2010 Svalbard MAAT record indicates an unrealistic high overall temperature increase rate for the past century. If one instead calculates the trend between the two temperature peaks in 1938 and 2006, the linear decadal trend is 0.14°C only. Clearly it is precarious to calculate an overall trend from a low to a peak value. We will briefly return to this issue later.

Following the 1917–1922 temperature rise, the Svalbard record is characterised by a warm period lasting until around 1955, a relatively cold period lasting to about 1990, and a renewed warming lasting until at least 2006. A number of decadal-scale variations are apparently superimposed on this overall pattern of change. From Figure 1, it is seen that MAAT variations mainly are derived from variations in winter temperature, and that the summer temperature shows small variations only. Since about 1990 the Svalbard MAAT has increased about $3\text{--}4^{\circ}\text{C}$, but it is not possible to determine if this temperature increase is the leading edge of a more permanent increase as suggested by climate models, or merely represents a typical decadal-scale oscillation. Indeed, decreasing MAAT since 2006 suggests an oscillation.

3. Fourier and Wavelet Analyses

Visual inspection of climate data series often suggests the existence of recurrent variations, and Fourier analysis represents a valuable tool for the identification of such natural variations. However, describing the character (persistence, period and amplitude) of cyclic patterns might be difficult as they often come and go, lasting only for a limited period

at each appearance. Especially the dynamics over time of the individual cycles can be complicated to analyse. For this reason, oscillations may prove difficult to characterise fully from a normal Fourier power spectrum. To overcome the problem encountered when cyclic variations change their period and amplitude, we therefore employed wavelet analysis [17] to identify and describe oscillating variations in the Svalbard temperature record as a supplement to the Fourier analysis. A more thorough description of the wavelet analysis is given by Torrence and Compo [18] and by Humlum et al. [4]. Wavelet analysis has previously been brought into use in climate studies (e.g., Lau and Weng [19], Torrence and Compo [18], Baliunas et al. [20], Isaksson et al. [21], Butler et al. [22], Chylek et al. [23], and Humlum et al. [4]), but until now the technique only has received modest interest from the climate community in general.

In general, according to the Nyquist-Shannon sampling theorem [24], only frequencies lower than $fs/2$ should be considered in the analysis, where fs is representing the sampling frequency. As an example, for a data series representing annual values only frequencies lower than 0.5 yr^{-1} should be considered, corresponding to periods longer than 2 yr.

4. Fourier Analysis of the Svalbard MAAT Record

Before carrying out a Fourier analysis on the Svalbard MAAT series, the data series was taken at face value and the 1912–2010 linear trend of 0.23°C was removed. The result of the Fourier analysis is shown in Figure 2. The Svalbard MAAT record is seen to be dominated by three periods of about 68.4, 25.7, and 16.8 yr length, all with amplitude greater than 0.8°C . In addition to these three dominant periods, five periods with amplitude about 0.5°C are also present in the spectra. These periods have lengths of about 36.7, 12.3, 8.7, 5.1, and 2.5 yr, respectively.

The significance levels shown in Figure 2 are peak-based critical limit significance levels, which are of particular merit in ascertaining the significance of the largest spectral component [25]. In this type of test, one seeks to disprove the null hypothesis postulating either a white noise signal with no autocorrelation ($\text{AR}(1) = 0.0$), or a red noise signal with autocorrelation ($\text{AR}(1) > 0.0$). Red noise is present when the background power decreases with increasing frequency, and the autoregressive value is a measure of the similarity between observations in a time series as a function of the time separation between them. For the Svalbard 1912–2010 MAAT series the AR coefficient was determined to 0.48.

With the background set, the peak spectral power was then compared against the various critical limits (Figure 2). A 90% critical limit is that level where in only 1 of 10 separate random noise signals the highest peak would achieve this height strictly due to random chance. Likewise, for a peak reaching the 50% critical limit there is a 50-50 probability that this could have arisen strictly from chance. The critical limit test used here is different from traditional confidence or significance levels that apply to a single data set only. For example, a standard 90% confidence limit would specify a level where 10% of the points in a single spectrum would

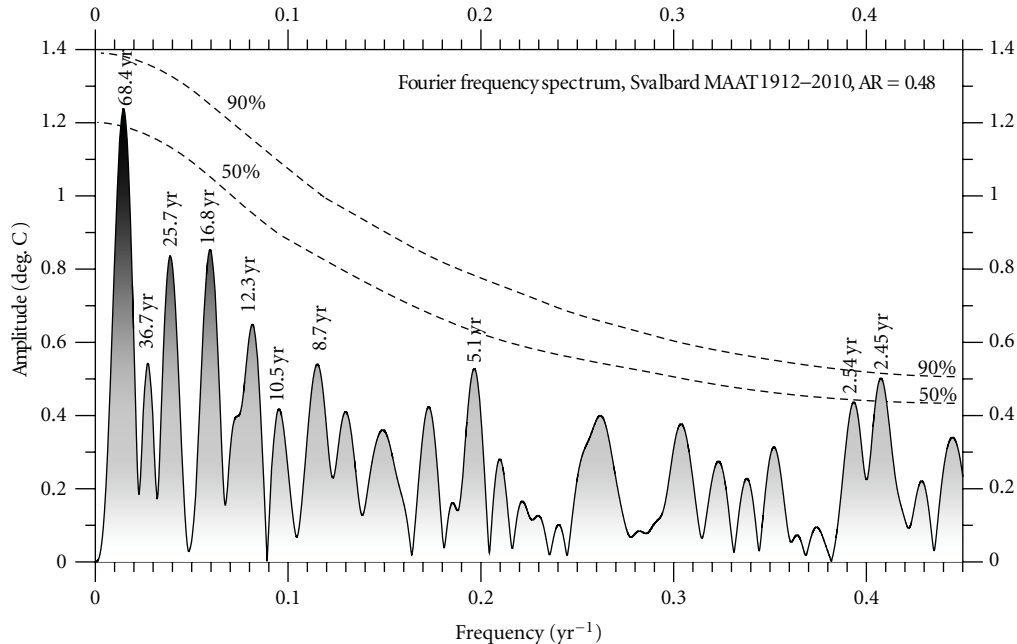


FIGURE 2: Fourier analysis (using Best Exact N composite algorithm) of the detrended Svalbard 1912–2010 MAAT series. The record is dominated by three periods of about 68.4, 25.7, and 16.8 yr length, all with amplitude greater than 0.8°C . In a statistical sense; however, the 2.45 yr peak is most important. The stippled lines indicate peak-based critical limit significance levels, while the grey tone indicates increasing amplitude. Only frequencies lower than 0.45 yr^{-1} are shown.

be expected to lie above this height strictly due to random chance.

Exposed to the critical limit test none of the frequency peaks shown in Figure 2 are statistically very strong. Only the 2.45 yr peak approaches the 90% critical limit, and for that reason the alternative null hypothesis, that the observed oscillations represent noise, cannot be rejected using the peak-based critical limit test. However, this does not imply that the oscillations observed are red noise, but merely that the evidence is too weak to demonstrate their statistical significance. Further, as we later will demonstrate by wavelet analysis, the reason for the weak Fourier peak strength is partly that few of the oscillations are entirely stable over time, but instead vary somewhat in strength and frequency. By this their Fourier peak strength is reduced. A similar observation lead Polyak [7] to suggest that such periods might represent random phenomena only. However, as several of the strongest oscillations seen in Figure 2 recur in data from other stations within the North Atlantic region (Humlum et al. [26]), we imply that the Svalbard temperature signal is not entirely random. In addition, the effect (the amplitude) of at least three of the identified oscillations is large ($>0.8^{\circ}\text{C}$), and these oscillations are therefore not unimportant. Even though their significance only is close to the 50% critical limit, they remain important to understand the Svalbard MAAT series. Likewise, it is possible for a statistical significant factor to be of little practical importance if the effect of the factor is small.

Strong periods like the 68.4, 25.7, and 16.8 yr periods may have weaker harmonics if they are not perfect sine variations, which might explain some of the shorter periods found by the Fourier analysis, for example, 36.7, 12.3, and

8.7 yr, respectively. Such shorter periods may therefore not be providing new information as to their origin, except that the fundamental variation deviates from being a perfect sine variation. On the other hand, an observed potential harmonic variation needs not to be derived from a longer oscillation, but may represent an independent oscillation. Great care should therefore be exercised when interpreting spectral information like shown in Figure 2.

As to the possible origin of some of these periods, the 10.5 yr period with about 0.4°C amplitude may possibly represent a solar signal in the record, while the stronger 8.7 yr period is nearly identical to a well-known lunar orbital period (8.85 yr) and may therefore not be a harmonic of the longer 16.8 yr period, but a real oscillation in its own rights. The possible origin of some of the other identified periods will be discussed further below. The 2.45 yr oscillation is strong both in a statistical sense and with regard to amplitude. This explains why seldom more than two very cold or warm years in a row are recorded in Svalbard.

5. Wavelet Analysis of the Svalbard MAAT Record

Before analysing the Svalbard temperature record it was detrended by fitting a linear trend 1912–2010 to the data and then subtracting this from the data. The detrended data set was then decomposed by a continuous wavelet transform, whereby a time-frequency representation of the embedded signals was constructed with good time and frequency resolution. As the Fourier analysis (Figure 2) suggested the existence of more than 10 oscillations with amplitude of at least 0.4°C in the data set, we specified a wave number of 10.

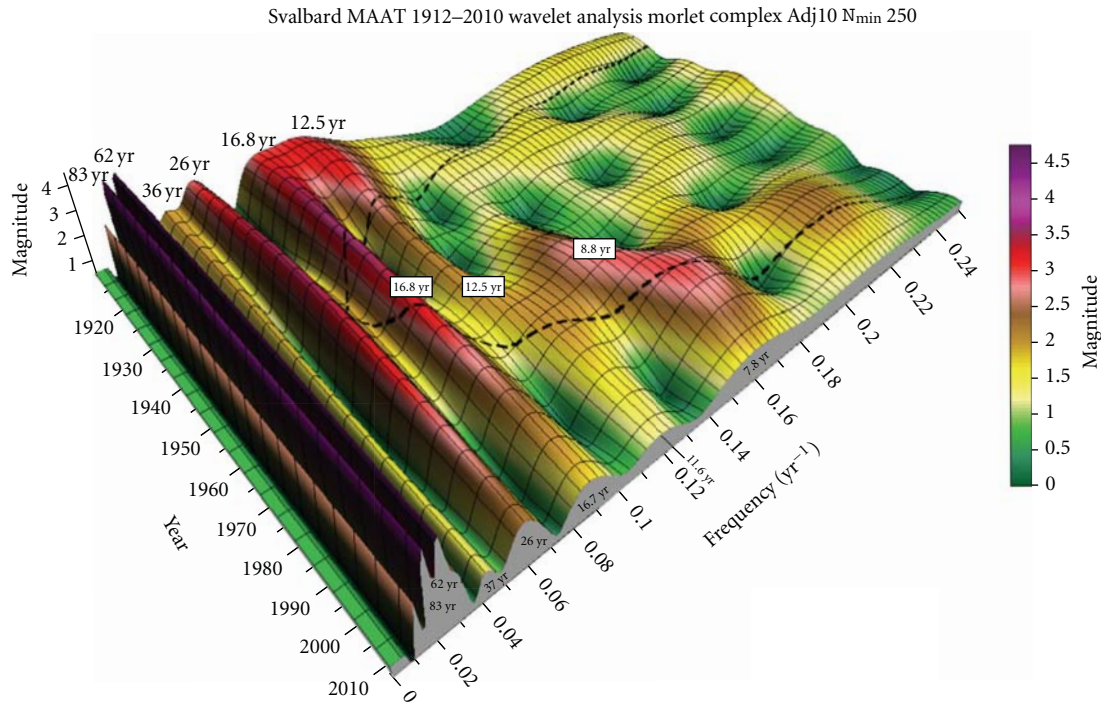


FIGURE 3: Diagram showing the continuous wavelet time-frequency spectrum for the Svalbard MAAT series 1912–2010 [4]. Time (AD) and frequency (yr^{-1}) of cyclic variations embedded in the temperature data are shown along the horizontal axes. Frequencies higher than 0.25 yr^{-1} are not shown, corresponding to showing only periods longer than 4 yr. The vertical axis (and colour scale) shows the magnitude of the Continuous Wavelet Spectrum at a given time and frequency. The magnitude is calculated as $\sqrt{\text{Re}^* \text{Re} + \text{Im}^* \text{Im}}$, where Re is the real component of a given segment's FFT at a given frequency and Im is the imaginary component. Usually the magnitude is 3–4 times the corresponding amplitude. The dotted line indicates the extent of the cone of influence, where the magnitude of oscillations may be diminished artificially due to zero padding, especially towards the ends of the time scale, see, for example, the 26 and 7.8 yr period.

Figure 3 shows the complex component of the wavelet in the time and frequency domain for the Svalbard MAAT record. This type of wavelet diagram has constant power across the time duration of the individual oscillations, achieved by combining both positive and negative peaks (the real component) into a single peak, and thereby more clearly than the real component showing the extent of the identified oscillations in both the time and frequency domain. As we used zero padding (extending the data series with zeros at the end) to eliminate wraparound artefacts for especially low frequencies, spectral powers may be diminished somewhat within the cone of influence compared to their real values.

The wavelet analysis revealed several cyclic variations in the Svalbard MAAT record. Since 1912 four dominant periods of about 83, 62, 26, and 16.8–16.7 yr characterise the entire record. Both the about 83 and 62 yr oscillations are strong and persistent, but they are entirely located within the cone of influence. The about 26 and 16.8–16.7 yr oscillations are strong, but are moving towards somewhat less influence in recent years. A weaker oscillation of about 36–37 yr is also visible in the record, but with decreasing influence in recent years. However, the recent apparent decrease in spectral powers for these periods may be an artefact derived from zero padding.

A couple of shorter oscillations were also identified in the Svalbard MAAT record: about 12.5–11.6 and 8.8–7.8 yr. However, in contrast to the above oscillations periods, these

shorter oscillations do not represent stable phenomena, which is why they do not show up with similar strength in the Fourier analysis (Figure 2). The 12.5 yr period was initially strong, but the signal declined somewhat in magnitude and period (now 11.6 yr) over the observational period. However, the decline of magnitude may partly be an artefact of zero padding, but not the gradual change of frequency. Concurrent with this development, the about 8.8 yr period increased in importance until around 1985, after which a weakening apparently has begun, although perhaps also a zero padding effect. At the same time a slight frequency increase has taken place, so the modern period length is somewhat shorter, about 7.8 yr. Analyses of the real component (not shown here) demonstrate that both oscillations presently are near their minimum power, and they are presumably going to gain importance in the coming years. The shorter periods all are relatively weak, and the main control on the Svalbard MAAT record has always been the longer periodic variations; especially the 83, 62, 26, and 16.8–16.7 yr cycles (Figure 3). In addition to the periods shown in Figure 3 (truncated at 4 yr), the about 2.5 yr period found by the Fourier analysis (Figure 2) was also identified by the wavelet analysis. This period was strong mainly between 1965 and 1980, and less so since then.

Most of the periods identified by the wavelet analysis are also recognised by the Fourier analysis (Figure 2). However, some of the periods may be interrelated: the 62, 37–36, 26,

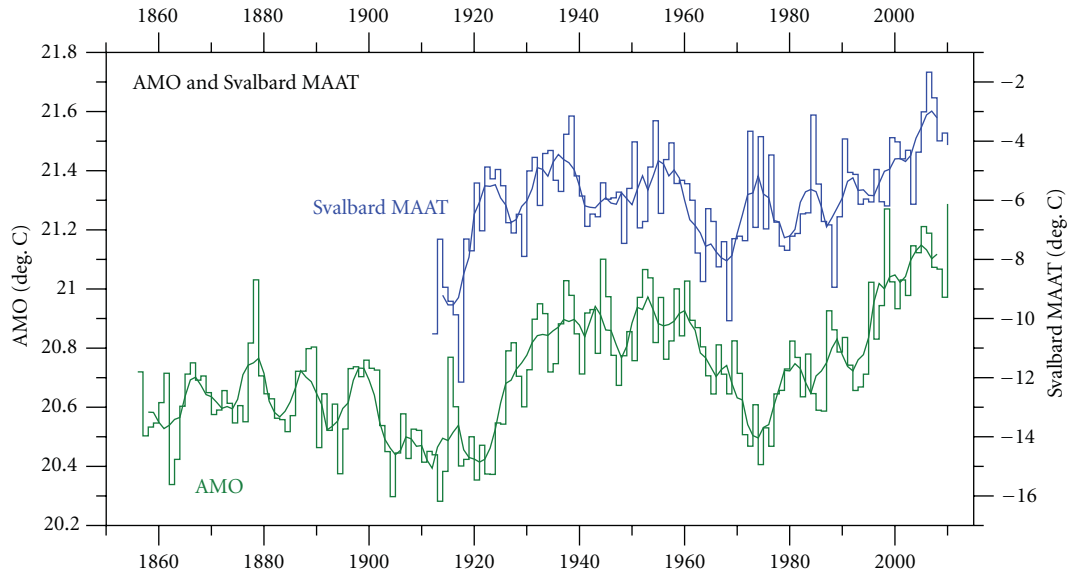


FIGURE 4: Svalbard MAAT 1912–2010 (blue) and Atlantic Multidecadal Oscillation (AMO, green) annual index values 1856–2010. The thick lines are the simple running 5 year average. Note that the temperature scales are different.

and 16.8-16.7 yr periods may possibly represent sub-harmonics of the about 8.8 yr period.

5.1. Potential Physical Controls on the Observed Cycles. A physical explanation may be suggested for some of the cycles identified, as discussed in some detail by Humlum et al. [4]. The precession of both the Moon's orbital nodes and the Earth's *nutation* has an approximate period of 18.6 yr. By causing small accelerations and decelerations of the tidal bulges moving around Earth, this may cause small changes in ocean currents transporting heat towards high latitudes, for example, in the North Atlantic. The resulting variations in sea surface temperature might then influence the temperature of the atmosphere above the oceans (Keeling and Whorf [27]), whereby there may be a potential link between orbital variations of the Moon and the MAAT recorded at meteorological stations located near a major ocean, such as the meteorological station at Svalbard Airport.

Orbital variations of the Moon and the Earth have since long been suggested to influence upon long-period ocean tides, climate cycles, and variations of marine biomasses (Pettersson [28–31]). Later Maksimov and Smirnov [32] and Currie [33–35] analysed surface temperatures in the North Atlantic and found temperature cycles close to the 18.6 yr lunar nodal cycle. In addition, the 18.6 yr nodal tide has a poleward velocity component [36] and amplitude of approximately 7% of the lunar diurnal component [37], which may influence the ocean surface layer and air temperatures at high latitudes (Royer [38]; Keeling and Whorf [27]). Yndestad [39–41] actually was able to identify harmonic and sub-harmonic lunar nodal cycles of $18.6/3 = 6.2$ yr, 18.6, $3 \times 18.6 = 55.8$ yr, and $4 \times 18.6 = 74.4$ yr in temperature series from the Barents Sea between mainland Norway and Svalbard.

The 62, 37-36, 26, 16.8, and 8.8 yr periods identified by the wavelet analysis (Figure 3) may potentially all be

interpreted as lunar signals. The 8.8 yr period is very close to the fundamental 8.8504 yr lunar period, also known as the period of recession of line of apsides, and the longer periods may represent subharmonics of this fundamental period. On the other hand, this does not have to be so, and some of these periods may represent oscillations in their own rights. As one example, the 62 yr period is known from other records (e.g., [6]), and an about 60 yr long period has also been found in the movement of the barycentre of the solar system [42].

The similarity between the identified Svalbard 62 yr MAAT period and the variation of the Atlantic Multidecadal Oscillation (AMO, [43]) should also be noted (Figure 4). AMO is a mode of variability occurring in the North Atlantic Ocean sea surface temperature field and basically represents an index of North Atlantic sea surface temperatures (SST). This similarity also applies to the overall changes of MAAT during the observational period, emphasising the influence of Atlantic sea surface temperatures on air temperature recorded in Svalbard.

The longer 83 yr period may correspond to the solar Gleissberg cycle (named after Wolfgang Gleißberg), ranging from 50 to 140 yr, with a maximum around 88 yr [44], corresponding to four times the Hale cycle of 22 yr. However, given the limited length (98 yr) of the Svalbard MAAT data series, this long oscillation is located entirely in the cone of influence and its apparent presence should therefore not be interpreted in too much detail.

Thus, both lunar and solar signals may be present in the Svalbard record. Most of the cycles identified longer than 15 yr appear to have an almost stationary cycle length and stationary signal magnitude, while the shorter cycles are less stable and tend to come and go with time (Figure 3). More work on this is needed, but it remains a possibility that these short and not very strong oscillations should be considered as noise only. Indeed, the Fourier analysis (Figure 2) suggests that this might be the case. However, several of

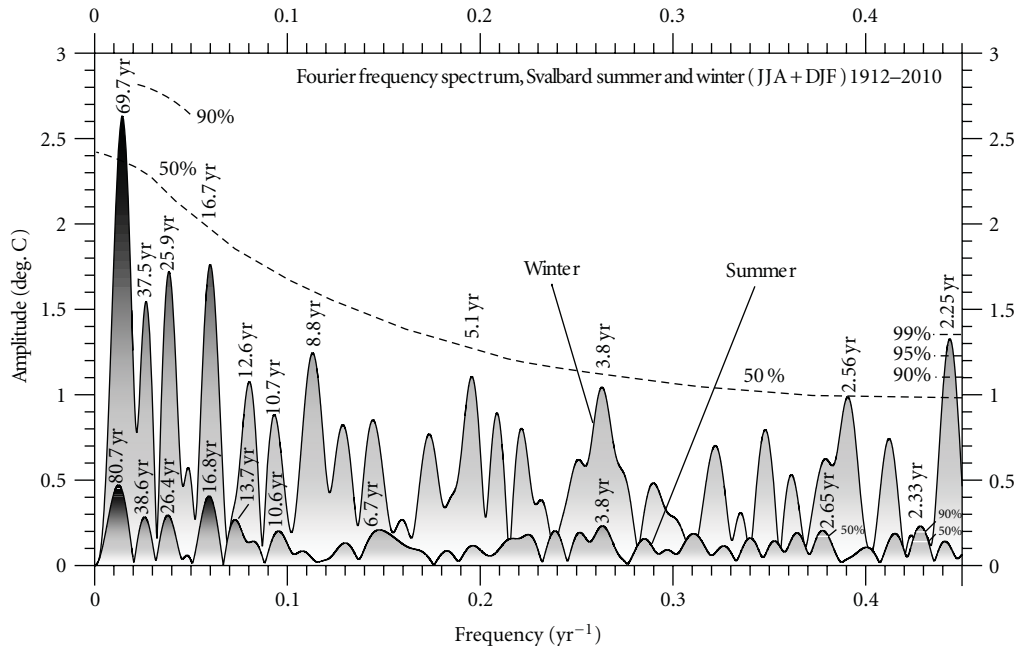


FIGURE 5: Fourier analysis (using Best Exact N composite algorithm) of the detrended Svalbard 1912–2010 winter (DJF) and summer (JJA) series. The amplitude of the winter signal is larger than the summer signal. The winter record is dominated by three periods of about 69.7, 25.9 and 16.7 yr length, all with amplitude greater than 1.7°C. The summer record is dominated by three periods of about 80.7, 26.4, 16.8, and 13.7 yr length, all with amplitude about 0.3°C or higher. The grey tone indicates increasing amplitude within each record. The stippled lines (white solid line for summer data) indicate peak-based critical limit significance levels. Only frequencies lower than 0.45 yr⁻¹ are shown.

the stronger periods identified in the Svalbard MAAT record resemble similar periods observed in Barents Sea surface temperatures (Yndestad [39–41]), again emphasising that air temperatures in Svalbard probably are strongly influenced by oceanographic and sea ice conditions (see, e.g., Benestad et al. [45]), and that these periods are real phenomenon, worthy of analysis.

6. The Svalbard Winter and Summer Temperature Record Compared

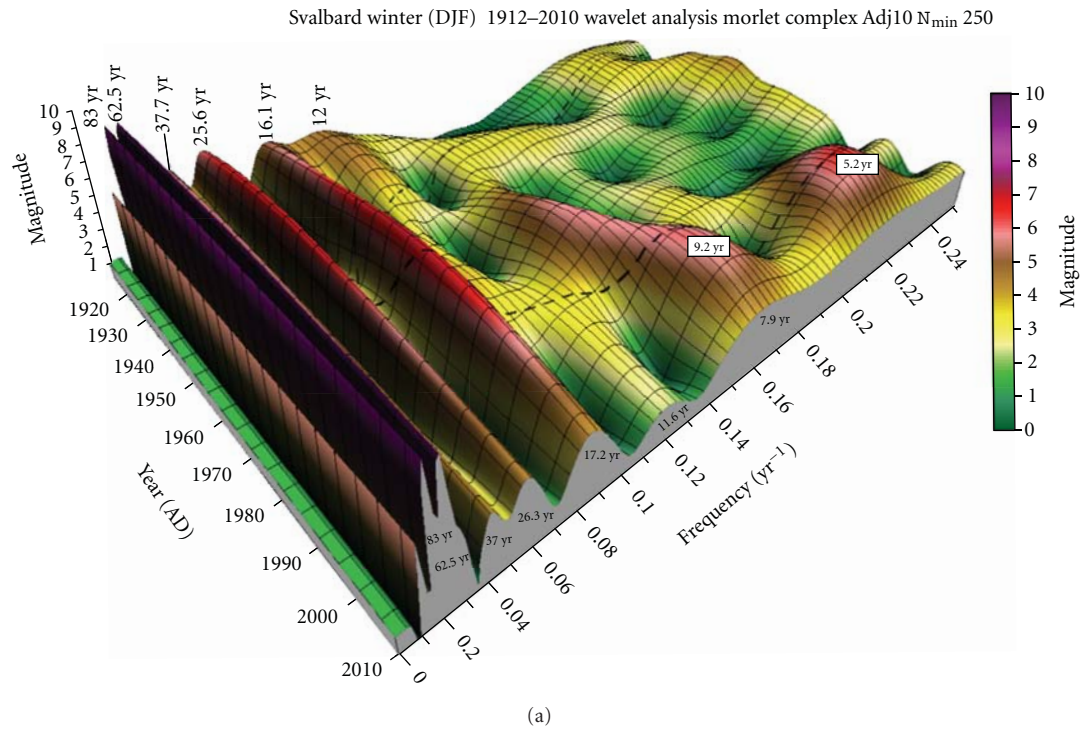
Figure 1 show clear differences between the Svalbard summer (JJA) and winter (DJF) air temperature, especially as to their variability. Figure 5 shows the result of Fourier analyses of these two data series, after removing 1912–2010 linear decadal trends of 0.25°C (DJF) and 0.10°C (JJA), respectively.

The Svalbard winter record is seen to be dominated by three periods of about 69.7, 25.9, and 16.7 yr length, all with amplitude greater than 1.7°C, much like what was the case for the MAAT record, reflecting the importance of winter temperatures for the MAAT. The 69.7 yr peak is close to the 75% critical limit, indicating that in only 1 of 4 separate random noise signals the highest peak would achieve this height strictly due to random chance. However, in a statistical sense the about 2.25 yr oscillation (amplitude about 1.3°C) is by far the most significant, almost reaching the 99% critical limit. This explains why seldom more than two very cold or warm winters in a row occur in Svalbard.

The summer record (lower graph in Figure 5) is dominated by two periods of 80.7 and 16.8 yr, both with amplitude exceeding 0.4°C. Two additional periods, 26.4 and 13.7 yr, reach peak amplitude values about 0.3°C. The most statistical significant period is the 2.33 yr oscillation, which however has small amplitude only, about 0.2°C. This demonstrates that it is possible for a statistically significant factor to be of little practical importance, and vice versa.

Thus, according to the Fourier spectral analysis, there are both similarities and differences between Svalbard winter and summer temperatures 1912–2010. However, we feel encouraged by the overall degree of similarity in the spectra of the winter and summer series. The autoregressive value was found to be somewhat higher for the summer data ($AR(1)_{\text{summer}} = 0.47$) than for the winter data ($AR(1)_{\text{winter}} = 0.43$). In general the winter temperature amplitudes are much larger than the summer amplitudes, and the discrepancy as to frequency of winter and summer oscillations are seen to increase with increasing frequency, presumably again reflecting that periodic oscillations shorter than 15 yr come and go, while longer oscillations tend to be more persistent. However, at the same time it should be borne in mind that the ability of determining oscillations decreases with increasing period length.

Figure 6 shows the result of wavelet analyses of the Svalbard winter and summer temperature record. The strong signal magnitude of the winter record (upper diagram) is apparent when compared to the summer record (lower diagram). Since 1912 four dominant periods of about 83,



Svalbard summer (JJA) 1912–2010 wavelet analysis morlet complex Adj10 N_{\min} 250

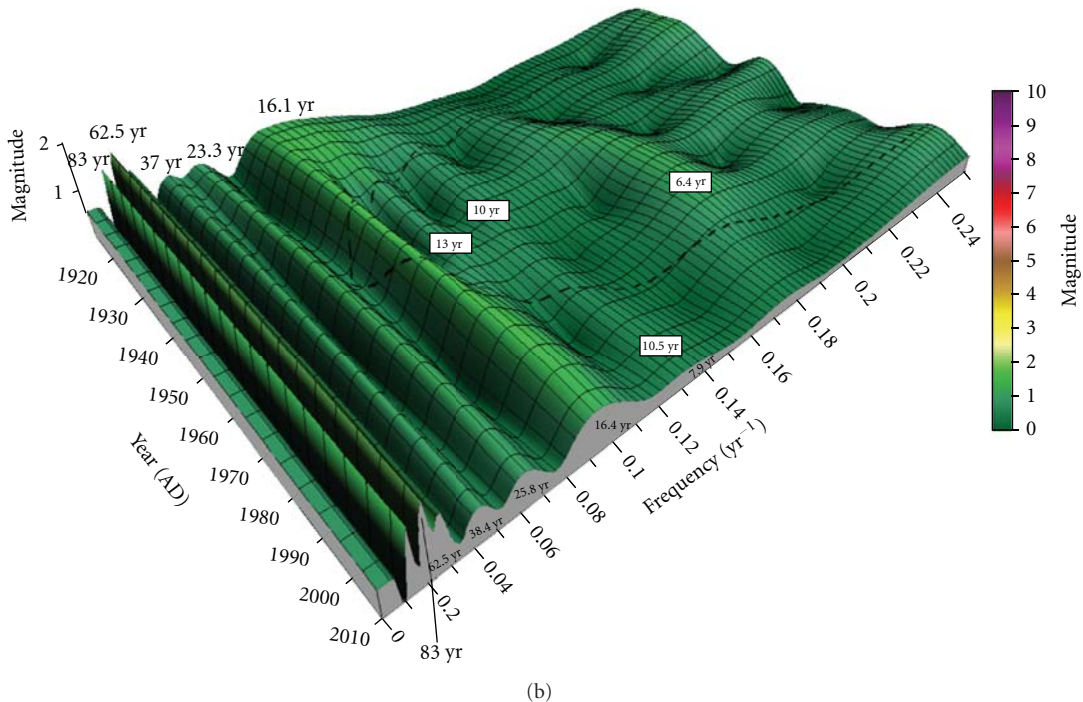


FIGURE 6: Diagrams showing the continuous wavelet time-frequency spectrum for the Svalbard winter (DJF) and summer (JJA) temperature series 1912–2010. The time (AD) and frequency (yr^{-1}) of cyclic variations embedded in the temperature data shown along the horizontal axes. Frequencies higher than 0.25 yr^{-1} are not shown, corresponding to showing only periods longer than 4 yr. The vertical axis (and colour scale) shows the magnitude of the Continuous Wavelet Spectrum at a given time and frequency. The magnitude is calculated as $\sqrt{\text{Re} \cdot \text{Re} + \text{Im} \cdot \text{Im}}$, where Re is the real component of a given segment's FFT at a given frequency and Im is the imaginary component. Usually the magnitude is 3–4 times the corresponding amplitude. The dotted line indicates the extent of the cone of influence. Identical colour scales have been used for both diagrams to emphasise the winter–summer difference as to signal magnitude. The winter data shows the edge effect of zero padding, see, for example, the 5.2 and 9.2 yr oscillations.

62.5, 25.6–26.3, and 16.1–17.2 yr characterise the winter record. Weaker 11.9–12 and 7.9–9.2 yr periods are also present. The summer record is dominated by 83, 62.5, 25.3–25.8, and 16.1–16.4 yr periods. From a spectral point of view, the similarity between the two seasonal records is striking, especially for oscillations longer than about 10 yr, although the magnitude of the seasonal signals is very different. The colour scale is identical for the two diagrams, emphasising the difference as to signal magnitude. It is also seen that while all four main periods are strong, the about 26 and 16–17 yr oscillations are changing towards somewhat smaller influence in recent years. A weaker oscillation of about 37–38 yr is visible in both seasonal records, but with reduced influence in recent years. All these relatively long periods have been relatively stable over the entire 1912–2010 time range with regard to both magnitude and frequency, even within the cone of influence, where spectral powers may be artificially diminished because of zero padding.

The fact that the result of the seasonal analyses resembles the result of the MAAT record suggests the oscillations identified to be real features and not just noise or artefacts derived from the averaging procedure used to produce the annual record. The fact that other North Atlantic temperature records display similar oscillations (Humlum et al. [26]) lends support to this notion. We therefore feel confident that these oscillations most likely represent phenomena worthy of analysis.

During summer the daily meteorological conditions are highly influenced by the incoming solar radiation, which at 78° 13' N are continuously above the horizon from 19 April to 23 August. Nevertheless, because of the nearby ocean, the air temperature usually stays relatively low, with July having an average temperature of 6.5°C (1981–2010). Summer air temperatures are also influenced by local wind conditions, partly reflecting land-sea breeze effects because of relatively small regional air pressure differences during the summer. All these factors are relatively stable from summer to summer.

During winter the meteorological conditions are very different from the summer. The sun stays below the horizon from 28 October to 14 February, and there is very little incoming solar radiation from December to February. The ground is snow covered, and much of the surrounding ocean and fjords are covered by sea ice. So whenever calm conditions prevail, inversions tend to develop and temperatures will be low at Svalbard Airport. However, conditions are frequently windy during the winter, destroying inversions, and from time to time warm air masses are advected towards Svalbard from the North Atlantic. Whenever this happens, the air temperature will rise significantly, as much as 10–15°C within few hours. In winters with high frequency of such events, the average temperature will be high and vice versa in winters where advection of warm air masses occurs less often. Also local foehn effects may be important during the winter. Together, this explains the high degree of winter temperature variability compared to the summer variability.

Advection of warm air masses from lower latitudes towards Svalbard occurs at all seasons, but is most frequent during the winter. This explains why the Svalbard air temperature is well coupled to North Atlantic temperature

conditions both in summer and winter, and why several oscillations can be recognised in the spectra of both summer and winter temperature records (Figure 5). Had this not been so, one would expect at least potential solar signals to be absent from the winter data.

The 62, 37–36, 26, and 16–17 yr periods identified by the wavelet analysis in the winter and summer record (Figure 6) may potentially be interpreted as lunar signals. In addition, the 62 yr period may be directly linked to the AMO [43], an index for Atlantic surface temperatures. The shorter 7.9–9.2 yr period visible in the winter record is close to the fundamental 8.8504 yr lunar period, and the above-mentioned longer periods may possibly represent sub-harmonics of this. However, as discussed above, some of these longer periods may represent oscillations in their own rights, as they also appear in other types of environmental records. As one example, the long 83 yr period visible in both Svalbard seasonal records may possibly correspond to the solar Gleissberg cycle [44].

Thus, when considering summer and winter periodic variations identified in the entire 98 yr Svalbard temperature record, oceanographic, lunar, and solar signals all appear potentially to be present. Most of the cycles identified longer than 15 yr appear to have almost stationary cycle length and magnitude, while the shorter cycles tend to come and go with time. However, our main purpose here is not the physical interpretation of the various oscillations, and a more thorough analysis would probably require an analysis of simultaneous wind strength and direction data.

7. Modelling the Svalbard MAAT Record 1912–1990

As the above wavelet analyses show most of the dominant oscillations to be stationary or quasistationary phenomena, it is feasible to construct a harmonic or sinusoidal model approximating the original data. Here we choose to focus on the Svalbard MAAT record only, investigating both hind-casting and forecasting ability of such a modelling approach, again building on a previous analysis [4].

The algorithm used for our modelling attempt was obtained by a nonlinear optimization procedure, described in [4]. As some of the individual periods are slowly changing with time (Figure 3), the chosen sinusoids had to be optimized for frequencies, amplitudes, and phases for the entire period investigated, and they may therefore differ somewhat from both the modern situation and the result of the Fourier analysis (Figure 2). However, when the strongest cyclic variations are relatively stable, as demonstrated by the wavelet analysis to be the case for the Svalbard MAAT record, this does not represent a major problem for the construction of a harmonic model. The coefficient of determination (r^2) along with the sample size (N) represents a guide for the degree of success of the model optimization.

When carrying out the nonlinear optimization to construct a harmonic or sinusoidal model approximating the original data, it is in principle possible to incorporate any number of periodic variations identified by the wavelet

analysis (Figure 3). However, to keep the analysis simple and by this demonstrate the value of our approach, we decided to take into account only three important periodic variations, as the wavelet analysis suggested a relatively low number of dominant periodic variations to describe the overall features of the record. Had we instead chosen to incorporate a higher number of periodic variations, the hindcasting ability of our model would improve, but using a sufficient high number of variations anything may be modelled. However, here our main purpose is to demonstrate that a low number (three) of periodic variations apparently explain all main features of the Svalbard temperature record. The resulting modelled data series was finally retrended to produce a hindcast comparable to the real Svalbard MAAT 1912–1990 (Figure 7).

To investigate the length of the realistic forecasting time range, if any, we next conducted a series of out-of sample tests where the Svalbard MAAT series was truncated stepwise back in time from the last year in the record (2010). From the truncated series we generated forecasts for the period between the year of truncation and 2010, to compare with known data for this period. By this it turned out that we could still produce useful forecast until 2010 when truncating as early as 1990. The nonlinear optimization for the truncated 1912–1990 data series resulted in a optimized model combining three periods of 71.7, 24.9, and 15.3 yrs. By this the original data were hindcasted with a coefficient of determination $r^2 = 0.36$ ($N = 78$). For comparison, a linear regression of the same data yielded a coefficient of determination (r^2) of only 0.02.

Our three-period-only model reproduces all main features displayed by the Svalbard 1912–1990 record (Figure 7), including the rapid early 20th century warming 1917–1922, the warm peak 1930–1940, and another warm period centred on 1955–1957, the subsequent cold period culminating 1967–1968, and increasing temperatures from then until around 2006. In other words, had we made this forecast back in 1991, the now observed temperature peak 2005–2007 could have been forecasted, even though in 1991 there were no indications for such a future development.

The forecasted 1991–2010 period represents about 26% of the length of the truncated 1912–1990 Svalbard series. We investigated the distribution of annual model errors (model minus measured MAAT) and found no change in the error distribution and its magnitude at the truncation year 1990. Errors 1991–2010 remain essentially identically to those characterising the previous period 1912–1990, with random distribution between positive and negative values. This demonstrates that our simple three-period-only model manages to stay on track in relation to the observed data for the whole period, both before and after 1990. The typical annual model error is 1–4°C, which for the individual year is a considerable error. Obviously our model should not be tested (falsified) within such a short-time period, but over several years. The fit between modelled values and the simple moving 9 yr average suggests a forecasting falsification time range of about 9 years for our simple 1912–1990 three-period-only model.

More work on the useful forecasting time range for this approach is clearly needed. However, our preliminary

experience from undertaking out-of-sample tests like the above on several other meteorological series suggests the useful forecasting time range to be 10–25% of the length of the background data series. Time series where the dominant periods vary with regard to length and strength obviously have a relatively short forecasting time range, while series characterised by more stable dominant periods (like the Svalbard series) have longer forecasting time ranges.

8. Modelling and Forecasting Using the Svalbard MAAT Record 1912–2010

We next developed an optimized model for the entire 1912–2010 observational period, still using only three input periods. This resulted in a model combining periods of 74.3, 24.5, and 17.1 yr (see Table 1 for listing of periods), by which the original data were hindcasted with a coefficient of determination $r^2 = 0.47$ ($N = 98$). For comparison, a linear regression of the same data yielded a coefficient of determination (r^2) of 0.14. It may be noted that the 74.3 yr period found and used by the optimized model might be seen as related to the fundamental 18.6 yr lunar period ($4 \times 18.6 = 74.4$ yr), and that the 24.5 yr period is identical to a third harmonic cycle of the 74.4 yr cycle ($74.4/3 = 24.5$ yr). The 17.1 yr model period is close to the 16.9–16.7 yr period found by the wavelet analysis (Figure 3). In principle, even the best optimized model may yield results without real physical meaning, but, in our opinion, when it is possible to relate known physical phenomena to the results this lends support to the value of the model.

From Figure 8 it is seen that our three-period-only optimized model reproduces all main features displayed by the Svalbard MAAT record, including the rapid early 20th century warming 1917–1922, the warm peak 1930–1940, another warm period centred on 1955–1957, the subsequent cold period peaking 1967–1968, a warm period 1970–1975, a cold period around 1980, and finally the subsequent warming until 2006/2007.

Annual model errors are typically 1–3°C. The somewhat smaller error margin compared to the 1912–1990 analysis is due to the longer data set and improved determination of dominant oscillations. The spread of annual errors is seen to be random and does not show a trend towards dominance of either positive or negative values, demonstrating that our simple three-period model stays on track for the entire record. The wavelet analyses (Figures 3 and 6) suggests the dominant variations in the record to be stable with respect to both strength and magnitude. This suggests that variations which are strong now are likely to continue without major changes at least some time into the future, and therefore likely to influence the future Svalbard MAAT. Based on the optimized 1912–2010 model we therefore generated a forecast of Svalbard MAAT until 2035, as shown in the right-hand part of Figure 8. This represents about 25% of the original data series length.

Our forecast suggests future MAAT in Svalbard to decline until around 2015–2017, to be followed by a new warming period, peaking around 2026. Following this future

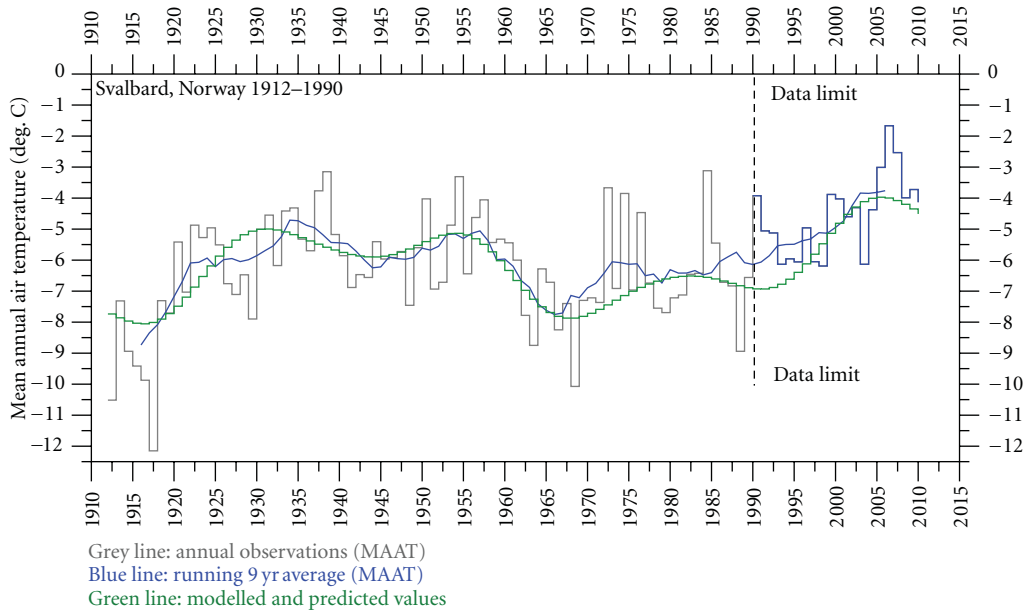


FIGURE 7: The truncated Svalbard MAAT series 1912–1990, redrawn from [4]. The grey line shows annual observed values. The thin blue line shows the measured values 1991–2010, which were excluded from analysis. The thick blue line shows the simple running 9 yr average of the original data. MAAT values modelled using three cycles only are shown by the green line. The 1991–2010 part of this represents the out-of-sample forecast. The coefficient of determination (r^2) for the hindcasting period is 0.36 ($N = 78$). The overall linear temperature trend 1912–1990 is 0.099°C per decade, and this overall trend is assumed to continue beyond 1990 when plotting the forecasted data.

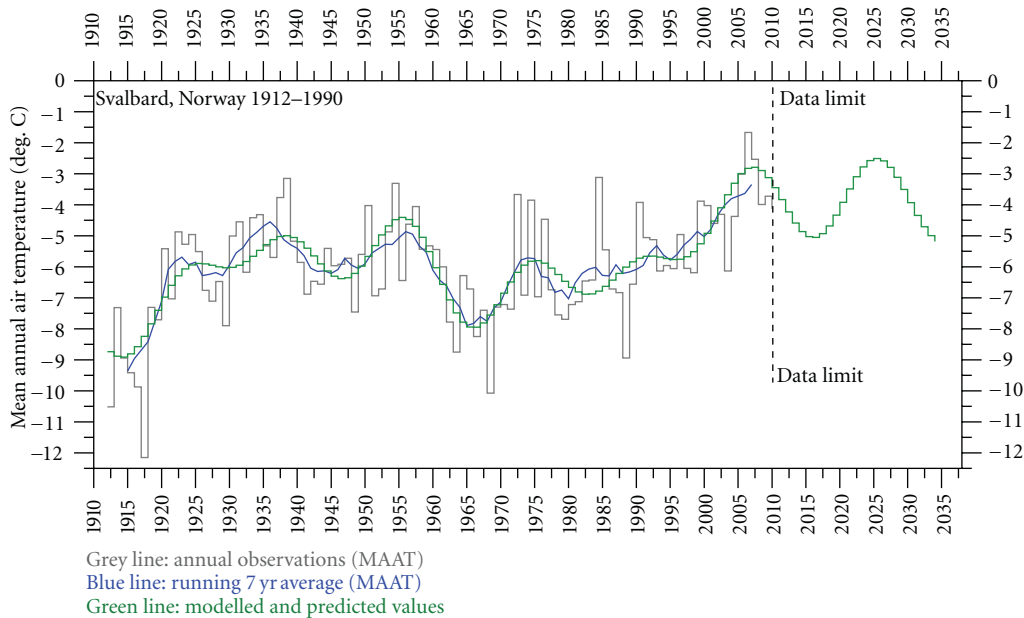


FIGURE 8: The Svalbard MAAT series 1912–2010, redrawn from [4]. The grey line shows annual values, and the blue line shows the simple running 7 yr average of these original data. MAAT values modelled from three cycles only are shown by the green line. The coefficient of determination (r^2) for the hindcasting period is 0.47 ($N = 98$). The linear temperature trend 1912–2010 is 0.23°C per decade. This overall trend is assumed to continue beyond 2010 when plotting the forecasted data. As mentioned above, this trend may be unrealistically high, being influenced by the data series starting at a low and ending at a high value.

temperature peak MAAT again is forecasted to decline. As mentioned previously, our forecast may be influenced by an unrealistic high linear trend 1912–2010. Should the real overall trend be lower, which we consider likely, this would change our forecast towards correspondingly lower

temperatures than shown in Figure 7. As our model hindcast 1912–2010 (Figure 8) is close to the moving simple 7 yr average, we suggest a falsification time scale of about 7 years. Incorporating additional periods in the model would produce a more detailed forecast and a somewhat shorter

TABLE 1: Length of cyclic variations found in the Svalbard 1912–2010 MAAT record by Fourier and wavelet analysis, and period length used for reproducing the MAAT 1912–1990 and 1912–2010 MAAT record with only three input periods, respectively. Parentheses around Fourier values indicate that these variations may possibly represent harmonics of the longer 68.4 yr variation. Italic columns indicate periods used in the models (Figures 7 and 8).

Cycle length	80–100	50–79	30–49	20–29	15–19	11–14	9–11	8–9
Fourier analysis		68.4	(36.7)	25.7	16.8	(12.3)	10.5	8.7
Wavelet	83	62	36	26	16.8-16.7	12.5–11.6		8.8
Model 1912–1990		71.7		24.9	15.3			
Model 1912–2010		74.3		24.5	17.1			

falsification time range, but here our aim is to demonstrate that all main features of the Svalbard temperature record may be reproduced by combining a low number of periodic variations only. Table 1 shows all the main periods found or used in the above analysis of the Svalbard MAAT record.

Solheim et al. [46] uses a model based on the empirical relation between solar cycle length and Svalbard MAAT to forecast temperatures in the Svalbard region the coming decade. This analysis is entirely different from the approach used in the present paper, but also results in a forecast of overall decreasing temperatures during the next decade, in concert with the forecast presented here. This agreement lends support to our interpretation that some of the oscillations identified in the Svalbard temperature record may be derived from solar variations, and that the oscillations identified in the present paper are real phenomena worthy of analysis, even though their statistical level of significance may appear relatively low when seen in isolation from other records.

9. Conclusions

- (1) This study has identified persistent cyclic variations in the Svalbard temperature record. These oscillations are also found when considering seasonal data (summer and winter), supporting the notion that the oscillations are real features, even though their statistical significance is relatively low.
- (2) Some of the identified cycles appear to correspond to known cyclic variations in the Moons' orbit around Earth, while others may reflect solar variations.
- (3) Natural cycles that have remained strong over long time are likely to continue without major changes into at the near future. Knowledge on such natural oscillations is therefore essential for forecasting future climate. Forecasts based on Fourier and wavelet analysis should therefore not be considered purely statistical, as they are based on observed dynamics characterising past climate change.
- (4) Strength and persistence of several cyclic variations identified in the Svalbard temperature record suggests that a natural cycle-based forecasting of future climate may be feasible for the Svalbard record, at least for a limited time ranges. Our empirical exper-

ience suggests a forecasting time range of 10–25% of the total record length.

- (5) For Svalbard our experimental forecast suggests that the observed late 20th century warming is not going to continue, but are likely to be followed by variable, but generally not higher temperatures for at least the coming 20–25 years. The falsification time scale for this forecast is about 7 years.
- (6) The natural cycle climate model forecast described in the present paper is seen as supplementary to projections derived from analytic climate models, and thereby represents a complimentary approach to climate forecasting based on such analytic models.

Acknowledgments

The present study was carried out partly at the University of Oslo, and partly at the University Centre in Svalbard (UNIS). The Wavelets package AutoSignal v.1.7 by SeaSolve Software Inc, was used for data analysis. The Svalbard temperature data series used was obtained from the eKlima Internet data portal run by the Norwegian Meteorological Institute. The paper benefited considerably from the comments of an anonymous referee.

References

- [1] R. B. Braithwaite, *Scientific Explanation*, Harper Torch, New York, NY, USA, 2nd edition, 1960.
- [2] K. Faegri, "On the value of palaeoclimatological evidence," in *Proceedings of the Royal Meteorological Society, Centenary Proceedings*, pp. 87–95, 1950.
- [3] I. I. Schell, D. A. Corkum, and E. N. Sabbagh, "Recent climatic changes in the Eastern North American sub-arctic," in *Proceedings of the 24th Alaska Science Conference, Climate of the Arctic*, G. Weller and S. A. Bowling, Eds., pp. 76–81, Fairbanks, Alaska, USA, August 1973.
- [4] O. Humlum, J.-E. Solheim, and K. Stordahl, "Identifying natural contributions to late Holocene climate change," *Global and Planetary Change*, vol. 79, no. 1-2, pp. 145–156, 2011.
- [5] S. Solomon, K. H. Rosenlof, R. W. Portmann et al., "Contributions of stratospheric water vapor to decadal changes in the rate of global warming," *Science*, vol. 327, no. 5970, pp. 1219–1223, 2010.
- [6] L. B. Klyashtorin and A. A. Lyubushin, *Cyclic Climate Changes and Fish Productivity*, Vniro Publishing, Moscow, Russia, 2007.

- [7] I. Polyak, *Computational Statistics in Climatology*, Oxford University Press, Oxford, UK, 1996.
- [8] H. W. Ahlmann, *Glacier Variations and Climatic Fluctuations*, Bowman Memorial Lectures, American Geographical Society, New York, NY, USA, 1953.
- [9] H. H. Lamb, *Climate, Present, Past and Future, Climatic History and the Future*, vol. 2, Methuen and Co, London, UK, 1977.
- [10] J. C. Rogers, L. Yang, and L. Li, "The role of Fram Strait winter cyclones on sea ice flux and on Spitsbergen air temperatures," *Geophysical Research Letters*, vol. 32, no. 6, Article ID L06709, 4 pages, 2005.
- [11] J. T. Houghton, Y. Ding, D. J. Griggs et al., "Climate change 2001: the scientific basis," in *Proceedings of the Contribution of Working Group I to the 3rd Assessment Report of the Intergovernmental Panel on Climate Change*, Cambridge University Press, 2001.
- [12] E. J. Førland, I. Hanssen-Bauer, and P. Ø. Nordli, "Climate statistics & longterm series of temperature and precipitation at Svalbard and Jan Mayen," Tech. Rep. 21/97 klima, Det Norske Meteorologiske Institutt, 1997.
- [13] I. Hanssen-Bauer, M. Kristensen Solås, and E. L. Steffensen, "The climate of Spitsbergen," Tech. Rep. 39/90, The Norwegian Meteorological Institute, 1990.
- [14] P. Ø. Nordli, I. Hanssen-Bauer, and E. Førland, "Homogeneity analyses of temperature and precipitation series from Svalbard and Jan Mayen," Tech. Rep. 16/96, The Norwegian Meteorological Institute, 1996.
- [15] H. Alexandersson, "A homogeneity test applied to precipitation data," *Journal of Climatology*, vol. 6, no. 6, pp. 661–675, 1986.
- [16] I. Hanssen-Bauer and E. J. Forland, "Homogenizing long Norwegian precipitation series," *Journal of Climate*, vol. 7, no. 6, pp. 1001–1013, 1994.
- [17] J. Morlet, *Sampling Theory and Wave Propagation*, NATO ASI Series, Vol Fl, Springer, 1983.
- [18] C. Torrence and G. P. Compo, "A practical guide to wavelet analysis," *Bulletin of the American Meteorological Society*, vol. 79, no. 1, pp. 61–78, 1998.
- [19] K.-M. Lau and H. Weng, "Climate signal detection using wavelet transform: how to make a time series sing," *Bulletin of the American Meteorological Society*, vol. 76, no. 12, pp. 2391–2402, 1995.
- [20] S. Baliunas, P. Frick, D. Sokoloff, and W. Soon, "Time scales and trends in the Central England temperature data (1659–1990): a wavelet analysis," *Geophysical Research Letters*, vol. 24, no. 11, pp. 1351–1354, 1997.
- [21] E. Isaksson, D. Divine, J. Kohler et al., "Climate oscillations as recorded in Svalbard ice core d18O records between AD 1200 and 1997," *Geografiska Annaler, Series A*, vol. 87, no. 1, pp. 203–214, 2005.
- [22] C. J. Butler, A. García-Suárez, and E. Pallé, "Trends and cycles in long Irish meteorological series," *Proceedings of the Royal Irish Academy Biology and Environment*, vol. 107, no. 3, pp. 157–165, 2007.
- [23] P. Chylek, C. K. Folland, H. A. Dijkstra, G. Lesins, and M. K. Dubey, "Ice-core data evidence for a prominent near 20 year time-scale of the Atlantic Multidecadal Oscillation," *Geophysical Research Letters*, vol. 38, no. 13, Article ID L13704, 2011.
- [24] C. E. Shannon, "Communication in the presence of noise," *Proceedings of the Institute of Radio Engineers*, vol. 37, no. 1, pp. 10–21, 1949.
- [25] SeaSolve, *AutoSignal. Pioneering Automated Signal Analysis and Advanced Filtering. User's Manual*, SeaSolve Software, Framingham, Mass, USA, 2003.
- [26] O. Humlum, J.-E. Solheim, and K. Stordahl, "Identifying natural oscillations in North Atlantic temperature records," In press.
- [27] C. D. Keeling and T. P. Whorf, "Possible forcing of global temperature by the oceanic tides," *Proceedings of the National Academy of Sciences of the United States of America*, vol. 94, no. 16, pp. 8321–8328, 1997.
- [28] O. Pettersson, "On the probable occurrence in the Atlantic current of variations periodical, and otherwise, and their bearing on metrological and biological phenomena," *Rapports et Procès-Verbaux des Réunions de Conseil Permanent International pour l'Exploration de la Mer*, vol. 42, pp. 221–240, 1905.
- [29] O. Pettersson, "Climatic variations in historic (sic) and prehistoric time," in *Svenska Hydrografisk Biologiska Kommissionens Skrifter*, vol. 5, p. 26, 1914.
- [30] O. Pettersson, "Long periodical (sic) variations of the tidegenerating force," *Publication Circular Conseil Permanent International pour l'Exploration de la Mer*, vol. 65, pp. 2–23, 1915.
- [31] O. Pettersson, "The tidal force. A study in geophysics," *Geografiska Annaler*, vol. 18, pp. 261–322, 1930.
- [32] I. V. Maksimov and N. P. Smirnov, "A contribution to the study of causes of long-period variations in the activity of the Gulf Stream," *Oceanology*, vol. 5, pp. 15–24, 1965.
- [33] R. G. Currie, "Evidence for 18.6 year MN signal in temperature and drought conditions in North America since AD 1800," *Journal of Geophysical Research*, vol. 86, no. 11, pp. 11055–11064, 1981.
- [34] R. G. Currie, "Evidence for 18.6-year lunar nodal drought in western North America during the past millenium," *Journal of Geophysical Research*, vol. 89, no. 1, pp. 1295–1308, 1984.
- [35] R.G. Currie, "Examples and implications of 18.6- and 11-year terms in world weather records," in *Proceedings of the International Symposium of Climate History, Periodicity, and Predictability*, pp. 378–403, Barnard College, Columbia University, 1987, Edited by M. R. Rampino, J. E. Sanders, W. S. Newman and L. K. Konigsson, Van Nostrand Reinhold Publishing, New York, NY, USA, pp. 588.
- [36] I. V. Maksimov and N. P. Smirnov, "A long-term circumpolar tide and its significance for the circulation of ocean and atmosphere," *Oceanology*, vol. 7, pp. 173–178, 1967.
- [37] G. Neuman and W. J. Pierson, *Principles of Physical Oceanography*, Prentice-Hall, Englewood Cliffs, NJ, USA, 1966.
- [38] T. C. Royer, "High-latitude oceanic variability associated with the 18.6-year nodal tide," *Journal of Geophysical Research*, vol. 98, no. 3, pp. 4639–4644, 1993.
- [39] H. Yndestad, "Earth nutation influence on the temperature regime of the Barents Sea," *ICES Journal of Marine Science*, vol. 56, no. 3, pp. 381–387, 1999.
- [40] H. Yndestad, *A Lunar-Nodal Spectrum in Arctic Time Series*, ICES CM, 2003.
- [41] H. Yndestad, "The influence of the lunar nodal cycle on Arctic climate," *ICES Journal of Marine Science*, vol. 63, no. 3, pp. 401–420, 2006.
- [42] N. Scafetta, "Empirical evidence for a celestial origin of the climate oscillations and its implications," *Journal of Atmospheric and Solar-Terrestrial Physics*, vol. 72, no. 13, pp. 951–970, 2010.
- [43] M. E. Schlesinger and N. Ramankutty, "An oscillation in the global climate system of period 65–70 years," *Nature*, vol. 367, no. 6465, pp. 723–726, 1994.
- [44] C. de Jager, S. Duhau, and B. van Geel, "Quantifying and specifying the solar influence on terrestrial surface temperature," *Journal of Atmospheric and Solar-Terrestrial Physics*, vol. 72, no. 13, pp. 926–937, 2010.

- [45] R. E. Benestad, I. Hanssen-Bauer, T. E. Skaugen, and E. J. Førland, "Associations between sea-ice and the local climate on Svalbard," Tech. Rep. 07/02, Norwegian Meteorological Institute, 2002.
- [46] J.-E. Solheim, H. Humlum, and K. Stordahl, "A relation between the sunspot cycle length and Svalbard temperatures," *Advances in Meteorology*, vol. 2012, Article ID 543146, 8 pages, 2012.

Research Article

20-Year Climatology of NO_3^- and NH_4^+ Wet Deposition at Ny-Ålesund, Svalbard

Rafael Kühnel,^{1,2} Tjarda J. Roberts,¹ Mats P. Björkman,^{1,2} Elisabeth Isaksson,¹ Wenche Aas,³ Kim Holmén,¹ and Johan Ström⁴

¹Norwegian Polar Institute, Fram Centre, 9296 Tromsø, Norway

²Faculty of Mathematics and Natural Sciences, Oslo University, Postbox 1032, Blindern, 0315 Oslo, Norway

³Norwegian Institute for Air Research, P.O. Box 100, N-2027 Kjeller, Norway

⁴Department of Applied Environmental Science, Stockholm University, Svante Arrhenius väg 8, 11418 Stockholm, Sweden

Correspondence should be addressed to Rafael Kühnel, rafael.kuhnel@npolar.no

Received 14 September 2011; Accepted 9 December 2011

Academic Editor: Anna Sjöblom

Copyright © 2011 Rafael Kühnel et al. This is an open access article distributed under the Creative Commons Attribution License, which permits unrestricted use, distribution, and reproduction in any medium, provided the original work is properly cited.

A 20-year dataset of weekly precipitation observations in Ny-Ålesund, Svalbard, was analysed to assess atmospheric wet deposition of nitrogen. Mean annual total nitrogen deposition was $74 \text{ mg N}/(\text{m}^2 \text{ yr})$ but exhibited large interannual variability and was dominated by highly episodic “strong” events, probably caused by rapid transport from European sources. The majority (90%) of precipitation samples were defined as “weak” ($<2 \text{ mg N}/\text{m}^2$) and contributed an annual baseline of $\sim 17 \text{ mg N}/(\text{m}^2 \text{ yr})$, whereas 10% of precipitation samples were defined as “strong” ($>2 \text{ mg N}/\text{m}^2$) and additionally contributed up to $225 \text{ mg N}/(\text{m}^2 \text{ yr})$. Nitrate deposition largely occurred in samples within the solid-precipitation season (16 September–2 June), and ammonium deposition occurred equally in both solid and liquid seasons. Trends of reactive nitrogen emissions from Europe are uncertain, and increasing cyclonic activity over the North Atlantic caused by a changing climate might lead to more strong deposition events in Svalbard.

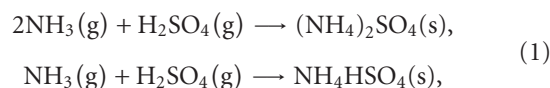
1. Introduction

Human activities release reactive nitrogen such as NH_3 and NO_x ($\text{NO} + \text{NO}_2$) to the atmosphere through energy production, fertilizer production, and cultivation of crops [1–4]. The resulting nitrogen-enriched air masses can be transported into remote, nutrient-limited regions such as the Arctic [5], primarily in the form of PAN (peroxyacetyl nitrate), but also as nitrate and ammonium aerosol. Furthermore, deposition of reactive nitrogen through precipitation is considered to be the main pathway for transfer of atmospheric nitrogen to the high Arctic surface [6]. The deposition of reactive nitrogen in the Arctic therefore results from the complex interplay of emissions, atmospheric transport, chemistry, precipitation, and snowpack processes as described below.

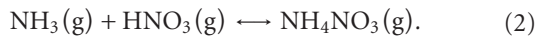
Ice core analyses from Svalbard [7] and Greenland [8] showed an increase in nitrate concentrations in the 1950's, followed by a drop in the 1980's in the Svalbard ice cores. A trend analysis of recent precipitation observations in Europe could not find any significant trends for nitrate in

Ny-Ålesund [9, 10]. In Europe and North America, the nitrogen emissions are expected to further decrease due to current and future legislations though there are regional differences which may affect the Arctic in particular. The expected intensification of shipping activity might lead to an increase of nitrogen emissions in the Arctic [4]. Reduction protocols and improvements in technology counteract the increase of nitrogen emissions, and some progress has been made in reducing emissions in the last decade [11, 12]. For general background information on the role of nitrogen in the environment, the reader is referred to the recently published “European Nitrogen Assessment” [13] as well as Monks et al. [14].

The atmospheric fate of nitrate and ammonia is linked to sulphur through atmospheric chemistry. Ammonia will neutralize sulphuric acid to ammonium sulphate particles by the reactions



where *g* and *s* indicate the gaseous and particulate phase. Remaining ammonia might neutralize nitric acid to form ammonium nitrate particles



The concentrations of sulphuric acid will thereby determine to a certain extent how much ammonia is left for the neutralization of nitric acid. Details on those processes can be found in Seinfeld and Pandis [15]. Sulphur emissions have been largely reduced over the past 20 years caused by actions undertaken in western and northern European countries to reduce air pollution through sulphate and changes in the economical situation in eastern European countries [16]. The reduction might have led to a shift towards the formation of more ammonium nitrate particles. Nitric acid is a volatile gas that undergoes dry deposition readily while ammonium nitrate particles dry deposit only slowly. The shift towards more ammonium nitrate has therefore an effect on the lifetime of $x\text{NO}_3$ in the air [17]. It has been estimated that the reduction in Sulphur emissions has led to an increase of $x\text{NO}_3$ in air of 15–30% [17]. These changes in the atmospheric chemistry may cause nonlinearity in trends, compared to the emission trends, due to shift in equilibrium and changes in oxidation capacity of the atmosphere [14, 17, 18]. How this influences the deposition of nitrate in the Arctic is, however, unclear.

The planetary layer of the Arctic troposphere is characterized by subzero temperatures throughout most of the year. During winter, the lack of solar radiation leads to stable stratified surface layer. Therefore, turbulent exchanges between atmospheric layers are reduced, and chemical reactions, especially photochemical processes, between different species (e.g., SO_2 to sulphate, NO_x to nitrate) are slowed down. This leads to longer species lifetimes in the Arctic troposphere [19, 20] during winter. Nitrogen-enriched air masses from middle latitudes can be transported over longer distances due to inhibited dilution and scavenging once they reached the Arctic.

The transport of air parcels is assumed to follow surfaces of constant potential temperature in the absence of diabatic heating. Above the Arctic, surfaces of constant potential temperature form a dome with minimum temperatures in the Arctic boundary layer. Regions with strong horizontal gradients of potential temperature near the surface are referred to as the polar front that builds a transport barrier [21]. Direct transport is less restricted by the polar dome in the cold months, when the polar front is situated south of important source regions, and cyclonic activity in the middle latitudes is enhanced [19, 22]. In addition, air masses are able to penetrate the polar front after diabatic cooling through the snow-covered surface in the northern parts of Eurasia. In the summer months, the polar front is situated further north and builds a more effective barrier in the lower atmosphere, isolating the Arctic from the midlatitudes [23]. Diabatic heating over midlatitude landmasses mixes air vertically. Air that is transported towards the Arctic without diabatic heating is forced to ascent along the isentropic surfaces. Such air masses might enter the Arctic Dome at higher

altitudes by subsidence. It is, however, assumed that these air masses would be scavenged during ascent and are thereby cleaned from nitrogen constituents before entering the Arctic dome [23]. The differences in the transport patterns between summer and winter can be seen in how long time that air has spent in the Arctic. The mean time that air has spent north of 70°N is about 6 days in January and about 10 days in July in the Svalbard region [23].

Model studies predict that the occurrence of synoptic patterns dominated by strong Icelandic low-pressure systems will increase while the frequency of strong Arctic high-pressure patterns decreases during the winter months (December–February) [24]. The same study predicts an increase in the frequency of synoptic patterns with low pressure over the Arctic Ocean and around Greenland during the summer months (June–August). This results in a prediction for increased frequency of intense cyclones in the Atlantic storm tracks, hence increased probability of strong air-mass transport into the Arctic from midlatitudes. In addition, increase of net precipitation over the Arctic cap of 20% during the next century is predicted [25].

Precipitation is in general low in the Arctic due to the stable stratification of air masses, low temperatures, and hence low water vapour content [19, 20]. Annual precipitation in the period from 1960 to 1990 in the Svalbard region ranged between 190 and 525 mm [26]. Precipitation on Svalbard can occur as snow and rain throughout the year due to large temperature variations. However, accurate precipitation observations are difficult [27] in the Arctic due to high wind speeds and drift snow that can lead to biases. Thus, true precipitation has been estimated to be approximately 50% higher than the uncorrected observations for Ny-Ålesund, Svalbard [28]. Monthly precipitation in Svalbard shows the highest precipitation in March and during August to October, whereas the months with the lowest precipitation are April to June [26]. This seasonality corresponds to the fact that most of the precipitation in Svalbard is connected to cyclonic activity, which is low in spring and high in autumn and winter [22]. Førland et al. [26] did find that annual precipitation has increased by 25% to 30% during the past 85 years, mostly due to increased spring and summer precipitation. It is possible that the observed trend in precipitation amount is a result of an ongoing shift in cyclonic activity.

During winter, precipitation occurs largely as snow and accumulates in the snowpack. Pollution scavenged by snow, such as NO_3^- (an oxidation product of NO_x), and ammonium (NH_4^+) is also accumulated within the snowpack. Photolytic reactions in the surface snow may alter the snowpack composition, releasing NO_x back to the atmosphere [29] although observations to date have found such NO_x reemission to be limited in the Ny-Ålesund area [30]. The remaining accumulated nitrogen is released in spring during snowmelt, providing a periodic input of reactive nitrogen in the melt water, which can act as a fertilizer to local ecosystems. The winter snowpack, thereby, acts as a temporal buffer to this process. However, nitrogen that is scavenged by rain during summer will be available to those ecosystems instantaneously. The Arctic is a nutrient

limited region, especially for nitrogen and phosphorus [31] and therefore susceptible to changes in nitrogen deposition [32, 33]. The amount and timing of deposition events play a key role. Strong nitrogen deposition events in spring or early summer could alter the growth season substantially, while the impact of strong nitrogen deposition in autumn might be negligible. Detailed studies on a strong episodic nitrogen deposition event in summer 1999 showed the importance of such events on glacial ecosystems during the melt-season [34, 35].

In order to assess the present and future importance of deposited nitrogen as a nutrient to Arctic ecosystems, or as a potential source of NO_x to the atmosphere, it is necessary to quantify the deposition of reactive nitrogen through precipitation and the driving mechanisms behind it. This is particularly important given the ongoing anthropogenic emissions of reactive nitrogen to the atmosphere that can be transported and deposited in the nutrient-limited Arctic, as revealed by Svalbard ice-core records over the 20th century. Here, we present a detailed analysis of weekly precipitation samples over more than two decades (1982–2007), a climatology of nitrate (NO_3^-) and ammonium (NH_4^+) wet deposition in Ny-Ålesund, Svalbard.

2. Methods

2.1. Data Origin and Quality. Sampling of the chemical composition of precipitation has been performed by the Norwegian Institute for Air Research (NILU), facilitated logistically by the Norwegian Polar Institute (NPI), since 1980 in Ny-Ålesund on behalf of the Norwegian Climate and Pollution Agency [10, 17], and is publicly available [36]. Precipitation was collected on a weekly basis using a bulk collector from NILU products, a bucket funnel system in summer and a snow sampler, so called particulate fallout collector, in winter. The collectors are made of high density polyethylene with a opening diameter of 200 mm and a height of 400 mm [37]. The collector has a bird ring to prevent bird droppings; however, the birds are sometimes able to contaminate the sample. These samples are deleted from the official dataset. Furthermore, the precipitation is frequently influenced by substantial sea salt episodes due to the proximity to open ocean. This is especially a problem for the sulphate measurements which need to be corrected for sea salt in order to quantify the contribution of anthropogenic sulphur. This leads to some uncertainty in the non-sea-salt sulphate estimates, since the sea-salt correction ratios are not always ideal. A bulk collector will to some extent also collect dry deposition as deposition of gaseous and particulate may occur. The magnitude of this is difficult to quantify, and it may vary by season. It is worth noticing that the collector, and funnel is washed every week, also between periods with no rain, preventing to a large extent collection of dry deposition in dry periods. The precipitation amount is measured by measuring the volume of liquid water precipitate or its equivalent of melted snow. An aliquot of the sample is sent to the laboratory at NILU for analysis using ion chromatograph.

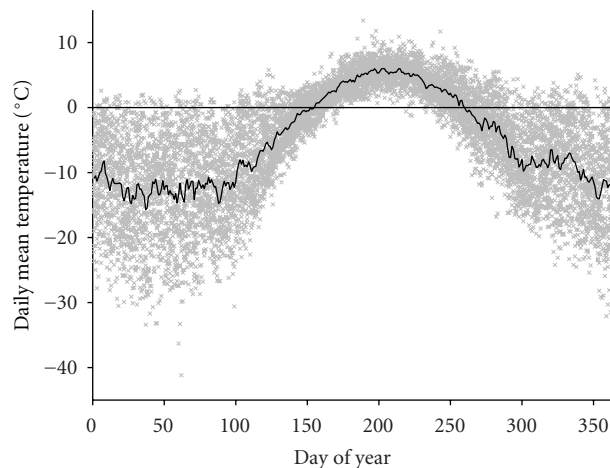


FIGURE 1: Daily mean temperature at Ny-Ålesund. Solid line indicates the average for each day over the period 13.9.1982 till 17.9.2007.

The data used in this study covers the time from 13 September 1982 for nitrate (NO_3^-) and non-sea-salt sulphate (nss-SO_4^{2-}) and from 12 September 1987 for ammonium (NH_4^+) to 17 September 2007. About 15% of the samples, both for nitrate and ammonium, are missing or considered invalid due to suspected contamination or because there was too little sample to be analysed.

The precipitation amount from the bulk collector has been used to calculate the deposition in this work. However, there are sometimes relatively large differences between the precipitation amount measured by the bulk collector and the official amount measured by a rain gauge. The precipitation amount of the official rain gauge has been used in these cases. Though it implies that on occasion, there is relatively large uncertainty in the deposition measurements. This is due to the measuring conditions at Ny-Ålesund that are sometimes very challenging.

The weekly deposited mass of nitrogen (mg N/m^2) and non-sea-salt sulphur (mg S/m^2) was calculated as the product of nitrogen respectively sulphur concentration (mg N/L , mg S/L) and precipitation amount (mm).

2.2. Definition of Solid and Liquid Precipitation Season. Figure 1 shows the daily mean temperatures at Ny-Ålesund for the period of interest, observed by the Norwegian Meteorological Office, and freely available [38]. The relative number of the different precipitation types: “Snow,” “Mixed,” and “Rain” for the same period of time can be seen in Figure 2. As expected, there is a close relationship between temperature and precipitation type. From DOY 150 on, a rapid shift in temperature and precipitation type from subzero to plus degrees, respectively, snow to rain can be observed. From about DOY 250, temperatures are predominately subzero. This is accompanied by an increase in the relative occurrence of snow precipitation in favour of liquid precipitation.

Since the type of precipitation is important for the efficiency by which nitrogen is deposited, deposition was divided into solid and liquid precipitation seasons. The solid

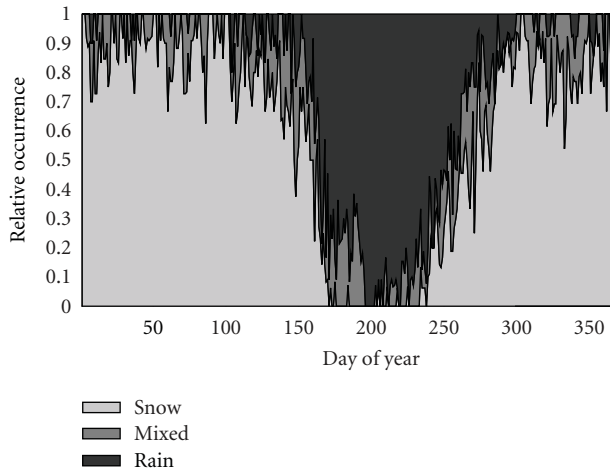


FIGURE 2: Relative occurrence of precipitation types in the period 13.9.1982 till 17.9.2007 at Ny-Ålesund.

season (16 September–2 June) was defined as the period of the year, in which the daily mean 2 m-temperature was on average below 0°C . The liquid season (3 June–15 September) was defined accordingly as the period with averaged daily mean temperatures above 0°C . For annual budgets, the precipitation year was defined to be the time covered by a solid season and the following liquid season (16 September–15 September).

2.3. Data Classification. The precipitation samples were divided into two categories: “weak deposition” and “strong deposition.” The following method was used to define these categories.

The accumulated mass of deposited nitrogen was calculated for each precipitation year. Hereby, only samples below a given magnitude were included in the calculation. The relative standard deviation (RSD: standard deviation of the sample divided by the sample mean) in these annual budgets was then calculated. The procedure was repeated, whereby the limiting magnitude was varied to cover the whole spectrum of observed nitrogen deposition magnitudes. So each limiting magnitude can be attributed to a specific value of relative interannual variation. The limiting magnitude of the minimum RSD was used to divide all samples into the categories “weak” and “strong.” Budgets consisting only of “weak” samples can be interpreted as a relative constant baseline deposition that can be augmented by “strong” samples. The relative standard deviation was used since variations of different magnitudes were compared.

The relative interannual variation was found to be the smallest for a limiting magnitude of $1\text{--}3\text{ mg N/m}^2$, both for ammonium and nitrate. The absolute minimum was at a size limit of 2.3 mg N/m^2 for nitrate and 2.7 mg N/m^2 for ammonium. Varying the threshold showed that the actual position of the threshold in the range between 1 and 3 mg N/m^2 had little effect on the results presented. Thus, 2 mg N/m^2 was chosen as the threshold between “weak-” and “strong” deposition.

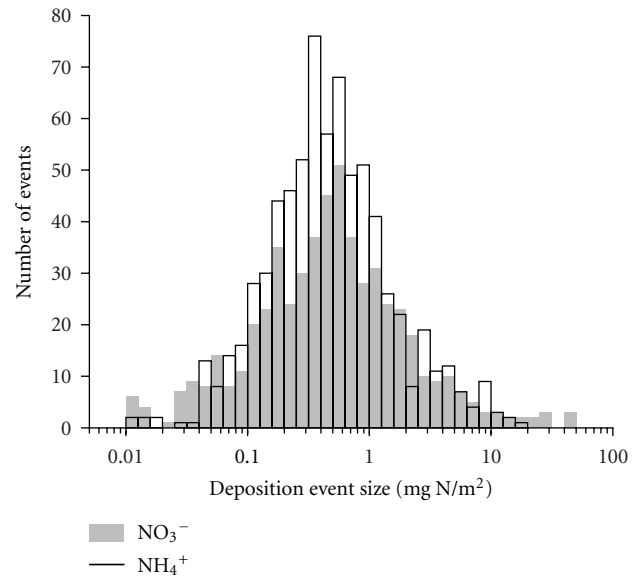


FIGURE 3: Histogram of nitrogen deposition samples. Grey bars show nitrate histogram; black lines show ammonium histogram.

The nitrogen deposition samples have been split into four categories to study if concentration or precipitation amount is the important factor leading to high nitrogen deposition. Those categories were “high concentration-high precipitation amount” (CP), “high concentration-low precipitation amount” (Cp), “low concentration-high precipitation amount” (cP) and “low concentration-low precipitation amount” (cp). Samples with concentrations above the 75th-percentile of all concentrations were categorized as high concentration samples, and the ones below this threshold were denoted as low. The same was true for the precipitation amounts. The categorisation has been done separately for a dataset consisting of only strong, respectively weak deposition samples. Ratios of the number of samples in each category to all samples have been calculated.

2.4. Correlations of Nitrate, Ammonium, and Non-Sea-Salt Sulphate. Pearson correlation coefficients were calculated between nitrate, ammonium, and non-sea-salt sulphate, where nss-sulphate was determined by correcting the measured total sulphate concentration with the concentrations of sea-salt constituents (Na, Cl, Mg) using the reference method defined by EMEP and WMO/GAW [39, 40]. Correlations were determined for both ion concentrations and deposited mass. Only samples where all three components were available have been used for the calculations. Correlations were calculated for three different compositions of data, the complete set of samples, a set that consisted of samples only within the solid-season and a set that consisted of samples only within the liquid season.

3. Results

3.1. Event Distribution and Annual Budgets. The number of nitrogen deposition samples shows a log-normal distribution (Figure 3) with a median distribution at approximately

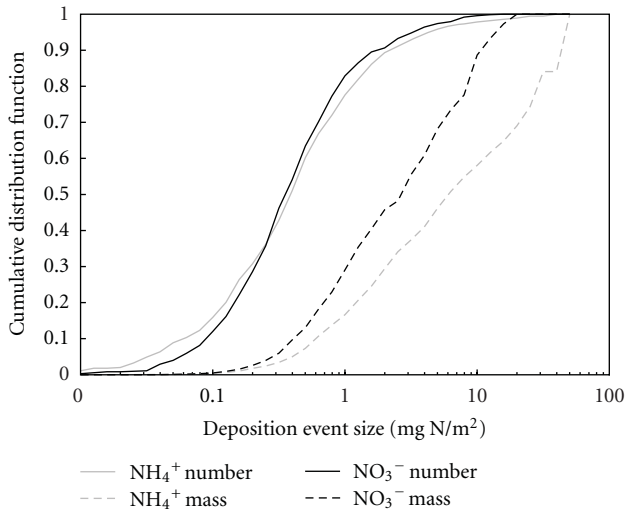


FIGURE 4: Cumulative distribution function of number and mass distributions for nitrate and ammonium.

TABLE 1: Mean annual number fraction of samples that deliver less or equal mass to the threshold level, and mass fraction of deposited nitrogen through these samples. The precipitation year as defined in the Section 2 was used for the calculations of the annual mean.

Sample threshold	Number fraction		Mass fraction	
	Nitrate	Ammonium	Nitrate	Ammonium
0.5 mg N/m ²	0.54	0.50	0.17	0.11
1 mg N/m ²	0.78	0.72	0.39	0.26
2 mg N/m ²	0.90	0.86	0.58	0.45
3 mg N/m ²	0.93	0.90	0.61	0.53

0.5 mg N/m² both for nitrate and ammonium. Cumulative distribution functions of the number and mass distributions for nitrate and ammonium are shown in Figure 4. The higher fraction of mass is deposited by “strong” samples (>2 mg N/m²), which are few, approximately 10%, while approximately 90% of all samples are “weak” (<2 mg N/m²). “Weak” samples contribute on average only to 50% of the annual nitrogen mass (Table 1).

The budgets for the solid- and liquid precipitation seasons show that most of the nitrate is deposited in the solid precipitation season (Figure 5), where also a large interannual variability can be found caused by strong deposition samples. The deposited mass of nitrogen through nitrate ranges from 6 to 60 mg N/m² in the solid precipitation season with an average of 22 mg N/(m² yr). In the liquid precipitation season, the mass of nitrogen deposited through nitrate shows values between 1 and 28 mg N/m² and an average of 7 mg N/(m² yr). The relative standard deviation gives an indication for the difference of variances between weak and strong samples. Nitrate shows a RSD of 0.23 for weak samples and 0.93 for strong samples.

The picture is somewhat different for ammonium (Figure 6). There is still a large interannual variability caused by strong-deposition samples. However, this is caused by both samples in the solid- and liquid precipitation season.

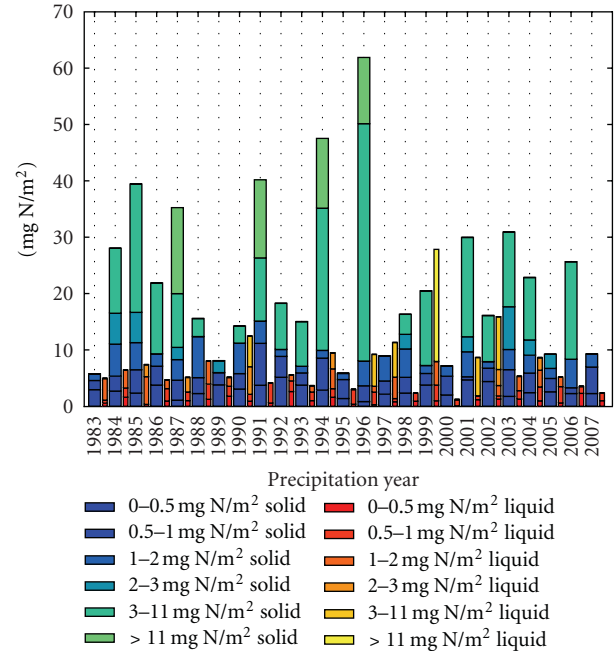


FIGURE 5: Annual budgets for nitrogen wet deposition through nitrate. Wide bars: solid precipitation season; narrow bars: liquid precipitation season.

The deposited mass of nitrogen through ammonium ranges from 5 to 66 mg N/m² in the solid precipitation season with an average of 22 mg N/(m² yr). The mass of nitrogen deposited through ammonium shows values between 4 and 98 mg N/m² with an average of 24 mg N/(m² yr) in the liquid precipitation season. The RSD is 0.28 for weak samples and 1.22 for strong samples.

The budgets for nss-sulphate (Figure 7) show similar behaviour as that of nitrate. The interannual variability is strong, and most of the deposition takes place in the solid season. Between 12 to 212 mg S/m² are deposited in each solid season with an average of 77 mg S/(m² yr). Deposition ranges from 5 to 58 mg S/m² in the liquid season with an average of 26 mg S/(m² yr). Less nss-sulphate is deposited in the solid seasons after 1996. The RSD for the weak and strong samples is 0.34 and 0.64, respectively.

The mass of total nitrogen contributed through nitrate plus ammonium varies between 24 and 236 mg N/m². The annual average is 74 mg N/(m² yr). Between 11 and 128 mg N/m² are deposited in the solid season with an average of 44 mg N/(m² yr). In the liquid season, total nitrogen deposition varies between 7 and 108 mg N/m² and shows an average of 31 mg N/(m² yr). On average 17 mg N/(m² yr) of total nitrogen are delivered by small samples. The RSD is 0.33 for weak samples and 0.93 for strong samples.

The monthly distributions for the deposited mass of nitrogen through nitrate and ammonium (Figure 8) show a distinct seasonal cycle. The median varies around 0.5 mg N/m² both for nitrate and ammonium. The bulk of nitrate deposition is highest during spring (Apr–July) while there is a minimum in autumn (September–November). The same minimum can be seen in the case of ammonium. In

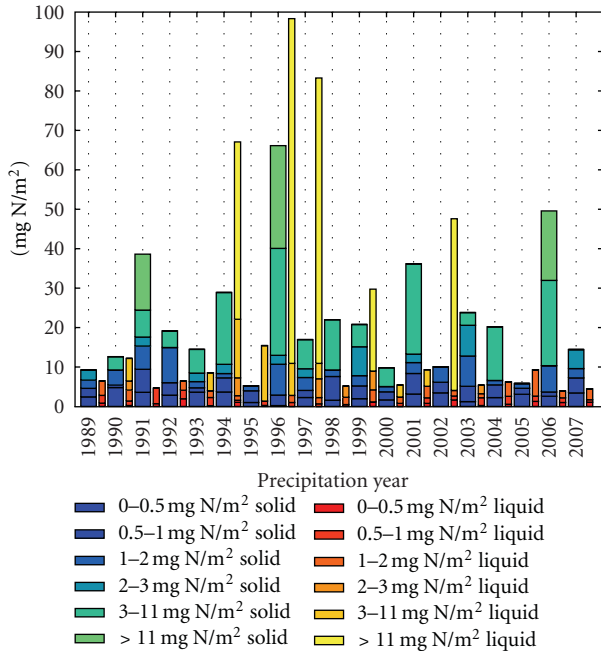


FIGURE 6: Annual budgets for nitrogen wet deposition through ammonium. Wide bars: solid precipitation season; narrow bars: liquid precipitation season.

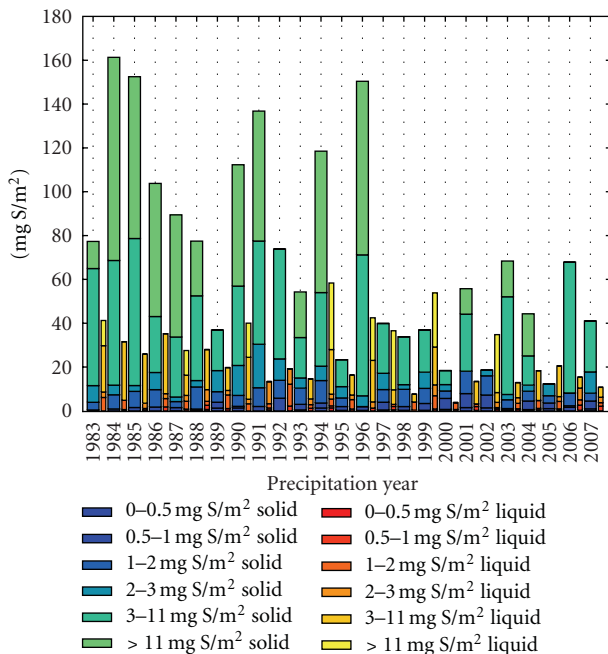


FIGURE 7: Annual budgets for wet deposition of sulphur through non-sea-salt sulphate. Wide bars: solid precipitation season; narrow bars: liquid precipitation season.

addition to the spring maximum in April to May, ammonium shows a second maximum during summer (July–September) with the highest values for the bulk of deposition samples (2nd–3rd Quartile) and increased variability. The highest number of strong samples of nitrate deposition occurs during the winter months November till March while

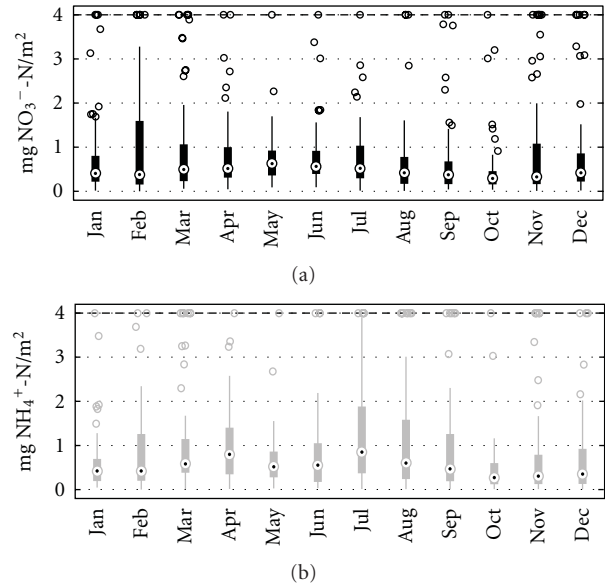


FIGURE 8: Monthly distribution of nitrogen wet deposition through nitrate (a) and ammonium (b). Black dots show the median; boxes show 25th–75th percentile; lines extend to most extreme data points that are not outliers; empty circles show outliers; outliers are defined as data points, that are $1.5 \times (P_{75} - P_{25})$ above P_{75} or below P_{25} , where P_{25} and P_{75} are the 25th and 75th percentile. Outliers $> 4 \text{ mg N/m}^2$ were set to 4 mg N/m^2 .

there is a minimum from May till August. For ammonium, there is a second maximum in the strong samples number from July to September.

3.2. Nitrate-Ammonium-nss-Sulphate Correlations. For all three sets of correlations (Table 2): nitrate-ammonium, nitrate-nss-sulphate, and ammonium-nss-sulphate, the deposition load correlations show higher values than those for the precipitation concentrations.

The nitrate-ammonium deposited mass- and concentration correlation coefficients show an increase from the total precipitation year to the solid season. The deposited mass correlation coefficient increased from 0.46 to 0.69, and the concentration correlation coefficient increased from 0.30 to 0.66. The comparison of the total precipitation year to the liquid season shows almost equal correlation coefficients for the deposited mass but a drop for the concentration correlation coefficients from 0.30 to 0.12.

The deposited mass correlation coefficient of nitrate-nss-sulphate shows a small increase from the total precipitation year to the solid season, from 0.79 to 0.82, and a small drop from the total precipitation year to the liquid season, from 0.79 to 0.71. The opposite trend can be observed for the concentration correlation coefficients. It drops from 0.63 for the total precipitation year to 0.57 for the solid season and rises to 0.69 for the liquid season.

The deposited mass correlation coefficients of ammonium-nss-sulphate are 0.62 for the total precipitation year, but distinct higher for the solid season with 0.70 and the liquid season with 0.80. The correlations for the concentrations

TABLE 2: Pearson correlation coefficients of nitrate, ammonium, and nss-sulphate for the complete precipitation year, solid- and liquid season. The values in brackets show the 0.95 confidence interval.

		Total	Solid season	Liquid season
$\text{NO}_3^- - \text{NH}_4^+$	Mass	0.46 (0.39–0.52)	0.69 (0.63–0.74)	0.45 (0.31–0.57)
	Concentration	0.30 (0.22–0.38)	0.66 (0.60–0.72)	0.12 (–0.04–0.28)
$\text{NO}_3^- - \text{SO}_4^{2-}$	Mass	0.79 (0.72–0.82)	0.82 (0.78–0.85)	0.71 (0.63–0.79)
	Concentration	0.63 (0.58–0.68)	0.57 (0.50–0.64)	0.69 (0.60–0.78)
$\text{NH}_4^+ - \text{SO}_4^{2-}$	Mass	0.62 (0.56–0.67)	0.70 (0.65–0.75)	0.80 (0.73–0.85)
	Concentration	0.43 (0.35–0.49)	0.60 (0.53–0.67)	0.37 (0.22–0.51)

TABLE 3: Ratio of the number of samples in the categories low/high concentration (c/C) and low/high precipitation amount (p/P) to the number of all samples, calculated for both nitrate and ammonium. Values for weak and strong samples are shown separately. Values in brackets show the number of samples in each category.

Category	Nitrate		Ammonium	
	Weak samples	Strong samples	Weak samples	Strong samples
cp	0.56 (407)	0.00 (0)	0.56 (310)	0.01 (3)
Cp	0.17 (124)	0.02 (14)	0.15 (83)	0.04 (23)
cP	0.17 (124)	0.05 (35)	0.15 (86)	0.05 (28)
CP	0.00 (0)	0.04 (27)	0.00 (0)	0.04 (22)

show an increase in the solid season and a slight decrease in the liquid season. The correlation for the total season is 0.43, the one of the solid season 0.60 and the one of the liquid season 0.37.

3.3. What Causes High Nitrogen Deposition, Precipitation Amount, or Concentration of Nitrate and Ammonium? The ratios of the number of samples in the different categories to all samples described above are similar for nitrate and ammonium (Table 3). The majority of weak samples are associated with low concentrations and low precipitation amount (cp), which is about half the samples. The remaining weak samples are evenly distributed to the categories cP and Cp with a ratio of 0.17 for nitrate and 0.15 for ammonium. Approximately 10 percent of all samples are strong, that is, $>2 \text{ mg N/m}^2$ (Figure 4). In the case of ammonium, those are almost evenly distributed between the categories Cp, cP, and CP with 0.04 to 0.05. Nitrate, however, shows a smaller ratio for category Cp with 0.02, while the ratios in the categories cP and CP are almost identical with 0.04 to 0.05.

The annual seasonality of the samples in the single categories shows distinctly different characteristics. For category cp, the samples are uniformly distributed throughout the year with values $<1.5 \text{ mg N/m}^2$. The events of category Cp in contrast show an increased number in the summer months, with most of the samples delivering less than 2 mg N/m^2 and some in the range up till 10 mg N/m^2 . The categories involving high precipitation, cP and CP, follow the precipitation seasonality closely in the case of nitrate with strong-deposition samples from September to April. Category cP seems to lack this characteristic for ammonium. The samples with the strongest ammonium deposition are to

be found in category CP in the months January to March and June to September.

4. Discussion

4.1. Budget and Seasonality Difference in Mechanisms. Weak samples are frequent but contribute on average only about half of the mass of the annual nitrogen loading, even though these events account for about 90% of the number of the samples. With small differences between years, on average about 17 mg N/m^2 is delivered each year by weak samples. The remaining mass of deposited nitrogen is a result of a small number of strong samples that may contribute up to $225 \text{ mg N/(m}^2 \text{ yr)}$. Those samples are sporadic and lead to a strong interannual variability. There are years with no strong samples as well as years with several ones. This results in a total deposition that is highly dependent on if and how many strong samples occur. For comparison, the average nitrogen deposition for 95 sites on the European mainland was 550 mg N/m^2 in the year 2009 with a standard deviation of 370 mg N/m^2 . The large standard deviation shows that deposition is highly dependent on location [41].

Precipitation sampling, particularly snow sampling, is difficult in the Arctic due to high wind speeds. Therefore, the result might be biased to some extent. It was estimated that true precipitation is in general higher than measured observations and that the error is highest in the winter months. Estimated ratios between observed and true precipitation amounts are 0.59 for solid and 0.93 for liquid precipitation [28]. Snow occurs during winter, when wind speeds are typically higher than in the summer months when it rains, and catch efficiencies are therefore lower for snow. However, strong winds may blow surface snow into the sampler and falsely raise the measured precipitation amount or alter the chemical concentrations of the sampled snow. While the first effect would lead to an underestimation of precipitation in the solid season, the second one would overestimate precipitation amount and make further chemical analysis difficult. Another factor that influences the data quality is dry deposition. Since the sampler is an open bucket system, it will to some extent also sample dry deposition. This would lead to observations that are positively biased. The sampler is rinsed between each sampling period to keep this effect at a minimum. It is assumed that the impact on the collected data is small; however, a faster sampling rate or a wet only sampler would be needed to better avoid dry deposition. It is important to keep these factors in mind when interpreting the results.

Dispersion of air masses will tend to lower the concentrations of air pollutants. Soluble species, like nitrogen and sulphate compounds, are affected by scavenging processes that will remove all or a fraction of the chemical constituents. The probability of scavenging and the degree of dilution via dispersion increase with increasing transport time. The intensity and sporadic nature of strong samples suggest that those might be caused by fast and direct transport while weak samples are related to nitrogen-enriched air masses with longer travel times. A cluster study of Eneroth et al. [22] identified transport from the Eurasian continent and the North Atlantic as the main patterns for transport of mid-latitude air to Svalbard. The same study found that large positive anomalies of CO₂ during winter are associated with transport from Eurasian anthropogenic sources [22]. It is, therefore, likely that strong samples are caused by rapid transport from European sources.

For nitrate, the strong events occur mainly during the solid precipitation season (Figure 5), hence during the winter months. Ammonium deposition seems to be dominating in the liquid precipitation season including several years with strong samples which are not present for nitrate (Figure 6). The solid precipitation season is similar to that of nitrate, a fact which is also evident by the raised correlation coefficients of nitrate and ammonium both for the deposited mass and the concentration (Table 2). This codeposition of ammonium and nitrate might be expected if both species are cotransported following their industrial/agricultural emissions from similar source regions. However, no significant correlation can be found between ammonium and nitrate in the liquid precipitation season.

The correlation coefficients between nitrate, ammonium, and nss-sulphate of the deposited mass of nitrogen are in general higher than those for the concentrations. This is probably caused by the precipitation component in the calculation of the deposited mass. Since it is the same for all three chemical components, it has an equalizing effect on the correlations and in addition applies a weighting so that low precipitation values are less important.

Nitrate and nss-sulphate are well correlated both in the solid and liquid season and both for the deposited mass and the concentration without any significant change in the correlation coefficients. This suggests that it is the same mechanisms that drive the transport and deposition. Nitrate and ammonium show significant higher correlation coefficients for the solid season both for the deposited mass and concentration, and a distinctively lower correlation for the concentration in the liquid season. This pattern is also evident in the correlations of ammonium with nss-sulphate.

Transport and source regions might, therefore, be the same for nitrate, sulphate, and ammonium in the solid season. Low temperatures and the lack of sunlight as well as a stable stratification reduce interactions between chemical components during winter and thereby leave them as largely passive tracers. However, in the liquid season, the deposition of ammonium may have a different cause. This might suggest an additional summer source for ammonia, either local (e.g., ammonia gas emissions from bird guano with subsequent

ammonium deposition to the sampler) or long range (e.g., biomass burning or forest fires).

Concentrations of nitrogen and sulphate components in air are higher in winter than in summer [10, 42], which corresponds to the stronger deposition of nitrate and sulphate in the solid season compared to the liquid season. A direct comparison of air concentrations and wet deposition is difficult, as can be seen for example in Hodson et al. [35], since both are connected by complex scavenging and wash-out processes. However there are similarities in the long-term trends of nitrogen and sulphur compounds in air concentrations and deposition. A decreasing trend of sulphate deposition and air concentrations of sulphur compounds can be observed, whereas both deposition and air concentrations of nitrogen compounds did not show significant trends [9].

Dividing the samples in categories of high and low concentration/precipitation (cp, Cp, cP, and CP) gave no clear indication on whether precipitation amount, concentration, or both are the driving factor for nitrogen deposition. The samples are distributed rather evenly into the categories. The seasonality of the categories gave an indication that categories of low precipitation amount (cp and Cp) contribute a distinct smaller part to the nitrogen budget compared to the events including high precipitation.

It should be mentioned that this classification is highly dependent on the threshold criteria of dividing samples into high or low concentration/precipitation. The 75th percentile was used in this study. Variations of this threshold for nitrate are found to have significant effects on the results. As the threshold was moved from the 50th to the 100th percentile, the categories Cp and cP gradually lost all their samples to category cp. Their ratios showed, therefore, a linear decrease, while the ratio in cp exhibited a linearly increase. Samples from CP were either lost to Cp, cP, or cp by raising the threshold.

5. Conclusions

A dataset of weekly precipitation observations over the past 20 years in Ny-Ålesund, Svalbard, was analysed to assess atmospheric nitrogen wet deposition through ammonium and nitrate. The analysed data included precipitation observations from 1982 till 2007. A solid (16 September–2 June) and liquid (3 June–15 September) precipitation season was defined in accordance with the average form in which precipitation occurred during those periods. The deposition samples were divided into the categories “weak” (<2 mg N/m²) and “strong” (>2 mg N/m²).

Nitrate deposition occurred mainly during the solid season, whereas ammonium deposition occurred equally in both the solid and liquid season. Weak and strong samples showed a ratio of occurrence of 9/1. However, the contribution to the deposited mass of nitrogen through weak and strong samples had a ratio of 1/1. A strong interannual variability was observed due to the episodicity of the strong samples.

The mean annual sum of total nitrogen deposition (nitrate + ammonium) was 74 mg N/(m² yr). Weak samples contribute an annual baseline of nitrogen deposition of

approximately 17 mg N/(m² yr) that can be augmented by strong samples. Rapid and direct transport is likely the key factor for strong samples.

No significant trend has been observed for nitrate concentrations in precipitation in Ny-Ålesund over the last two decades [9]. However, future trends of nitrogen emissions are unclear, and cyclonic activity in the North Atlantic is predicted to increase [24]. With these predictions, an increase in strong deposition events in Svalbard can be expected. Even without increased emissions of nitrogen in Europe, an increased frequency of intense cyclones in the North Atlantic would increase the probability for more strong deposition events in Svalbard. As terrestrial and glacial ecosystems in the high Arctic are nitrogen and phosphorus limited, we highlight the importance of episodic nitrogen precipitation events to remote areas.

Event-based sampling campaigns are necessary to further assess the structure of nitrogen deposition in remote areas. Sampling rates of approximately one week are longer than the timescales of typical precipitation events. Precipitation events with different chemical signature might, therefore, occur during a single sampling period and in addition synoptic weather patterns hence air-mass transport might change substantially over one week. Event-based sampling would, therefore, provide the possibility to study the transport and sources of nitrogen deposition in much greater detail.

Acknowledgments

The authors would like to thank the Norwegian Institute for Air Research (NILU) and the Norwegian Meteorological Office (Met.no) for providing precipitation data. The measurements in Ny Ålesund are part of the Norwegian national monitoring program of atmospheric deposition, financed by The Climate and Pollution Agency (Klif). This study was a part of the collaborative, interdisciplinary project “Sources, sinks and impacts of atmospheric nitrogen deposition in the Arctic” (NSINK). They would like to thank the Marie Curie Fellowship for funding the NSINK project. Tjarda J. Roberts, Johan Ström, and Elisabeth Isaksson additionally acknowledge financial support from CRAICC.

References

- [1] J. N. Galloway, W. H. Schlesinger, H. Levy, A. Michaels, and J. L. Schnoor, “Nitrogen fixation: anthropogenic enhancement-environmental response,” *Global Biogeochemical Cycles*, vol. 9, no. 2, pp. 235–252, 1995.
- [2] J. N. Galloway, F. J. Dentener, D. G. Capone et al., “Nitrogen cycles: past, present, and future,” *Biogeochemistry*, vol. 70, no. 2, pp. 153–226, 2004.
- [3] S. Grice, J. Stedman, A. Kent et al., “Recent trends and projections of primary NO₂ emissions in Europe,” *Atmospheric Environment*, vol. 43, no. 13, pp. 2154–2167, 2009.
- [4] G. P. Peters, T. B. Nilssen, L. Lindholt et al., “Future emissions from shipping and petroleum activities in the Arctic,” *Atmospheric Chemistry and Physics*, vol. 11, no. 11, pp. 5305–5320, 2011.
- [5] R. R. Dickerson, “Reactive nitrogen compounds in the Arctic,” *Journal of Geophysical Research*, vol. 90, no. 6, pp. 10739–10743, 1985.
- [6] M. H. Bergin, “The contributions of snow, fog, and dry deposition to the summer flux of anions and cations at Summit, Greenland,” *Journal of Geophysical Research*, vol. 100, no. 8, pp. 16275–16288, 1995.
- [7] E. Isaksson, M. Hermanson, S. Hicks et al., “Ice cores from Svalbard—useful archives of past climate and pollution history,” *Physics and Chemistry of the Earth*, vol. 28, no. 28–32, pp. 1217–1228, 2003.
- [8] M. G. Hastings, J. C. Jarvis, and E. J. Steig, “Anthropogenic impacts on nitrogen isotopes of ice-core nitrate,” *Science*, vol. 324, no. 5932, p. 1288, 2009.
- [9] L. R. Hole, J. H. Christensen, T. Ruoho-Airola, K. Tørseth, V. Ginzburg, and P. Glowacki, “Past and future trends in concentrations of sulphur and nitrogen compounds in the Arctic,” *Atmospheric Environment*, vol. 43, no. 4, pp. 928–939, 2009.
- [10] W. Aas et al., “Monitoring of long-range transported air pollutants,” Annual Report OR 29/2011, Norwegian Institute for Air Research, 2011.
- [11] J. W. Erisman, P. Grennfelt, and M. Sutton, “The European perspective on nitrogen emission and deposition,” *Environment International*, vol. 29, no. 2–3, pp. 311–325, 2003.
- [12] V. Vestreng, L. Ntziachristos, A. Semb, S. Reis, I. S. A. Isaksen, and L. Tarrasón, “Evolution of NO_x emissions in Europe with focus on road transport control measures,” *Atmospheric Chemistry and Physics*, vol. 9, no. 4, pp. 1503–1520, 2009.
- [13] M. A. Sutton et al., Ed., *The European Nitrogen Assessment*, Cambridge University Press, 2011.
- [14] P. S. Monks, C. Granier, S. Fuzzi et al., “Atmospheric composition change—global and regional air quality,” *Atmospheric Environment*, vol. 43, no. 33, pp. 5268–5350, 2009.
- [15] J. H. Seinfeld and S. N. Pandis, *Atmospheric Chemistry and Physics: From Air Pollution to Climate Change*, John Wiley & Sons, 2nd edition, 2006.
- [16] EMEP, Eme Assessment Part 1, European Perspective, Norwegian Meteorological Institute, EMEP Assessment Report, 2004.
- [17] H. Fagerli and W. Aas, “Trends of nitrogen in air and precipitation: model results and observations at EMEP sites in Europe, 1980–2003,” *Environmental Pollution*, vol. 154, no. 3, pp. 448–461, 2008.
- [18] D. Fowler, J. Muller, R. I. Smith, J. N. Cape, and J. W. Erisman, “Nonlinearities in source receptor relationships for sulfur and nitrogen compounds,” *Ambio*, vol. 34, no. 1, pp. 41–46, 2005.
- [19] L. A. Barrie, “Arctic air pollution: an overview of current knowledge,” *Atmospheric Environment*, vol. 20, no. 4, pp. 643–663, 1986.
- [20] G. E. Shaw, “The Arctic haze phenomenon,” *Bulletin of the American Meteorological Society*, vol. 76, no. 12, pp. 2403–2413, 1995.
- [21] A. Klonecki, P. Hess, L. Emmons, L. Smith, J. Orlando, and D. Blake, “Seasonal changes in the transport of pollutants into the Arctic troposphere—model study,” *Journal of Geophysical Research D*, vol. 108, no. 4, p. 21, 2003.
- [22] K. Eneoth, E. Kjellstrom, and K. Holmen, *A Trajectory Climatology for Svalbard; Investigating How Atmospheric Flow Patterns Influence Observed Tracer Concentrations*, Pergamon-Elsevier Science, 2003.
- [23] A. Stohl, “Characteristics of atmospheric transport into the Arctic troposphere,” *Journal of Geophysical Research D*, vol. 111, no. 11, Article ID D11306, p. 17, 2006.
- [24] J. J. Cassano, P. Uotila, and A. Lynch, “Changes in synoptic weather patterns in the polar regions in the twentieth and

- twenty-first centuries, part 1: Arctic,” *International Journal of Climatology*, vol. 26, no. 8, pp. 1027–1049, 2006.
- [25] J. J. Cassano, P. Uotila, A. H. Lynch, and E. N. Cassano, “Predicted changes in synoptic forcing of net precipitation in large Arctic river basins during the 21st century,” *Journal of Geophysical Research G*, vol. 112, no. 4, Article ID G04S49, p. 20, 2007.
- [26] E. J. Førland, I. Hanssen-Bauer, and P. Ø. Nordli, “Climate statistics & longterm series of temperature and precipitation at Svalbard and Jan Mayen,” Tech. Rep., The Norwegian Meteorological Institute, 1997.
- [27] S. V. Krupa, “Sampling and physico-chemical analysis of precipitation: a review,” *Environmental Pollution*, vol. 120, no. 3, pp. 565–594, 2002.
- [28] I. Hansen-Bauer, E. J. Førland, and P. Ø. Nordli, “Measured and true precipitation at Svalbard,” Tech. Rep., The Norwegian Meteorological Institute, 1996.
- [29] A. M. Grannas, A. E. Jones, J. Dibb et al., “An overview of snow photochemistry: evidence, mechanisms and impacts,” *Atmospheric Chemistry and Physics*, vol. 7, no. 16, pp. 4329–4373, 2007.
- [30] H. J. Beine, F. Domine, A. Ianniello et al., “Fluxes of nitrates between snow surfaces and the atmosphere in the European high Arctic,” *Atmospheric Chemistry and Physics*, vol. 3, no. 2, pp. 335–346, 2003.
- [31] G. R. Shaver and F. S. Chapin, “Response to fertilization by various plant-growth forms in an alaskan tundra—nutrient accumulation and growth,” *Ecology*, vol. 61, no. 3, pp. 662–675, 1980.
- [32] C. Gordon, J. M. Wynn, and S. J. Woodin, “Impacts of increased nitrogen supply on high Arctic heath: the importance of bryophytes and phosphorus availability,” *New Phytologist*, vol. 149, no. 3, pp. 461–471, 2001.
- [33] S. J. T. Arens, P. F. Sullivan, and J. M. Welker, “Nonlinear responses to nitrogen and strong interactions with nitrogen and phosphorus additions drastically alter the structure and function of a high arctic ecosystem,” *Journal of Geophysical Research G*, vol. 113, no. 3, Article ID G03S09, 2008.
- [34] T. J. Roberts, A. Hodson, C. D. Evans, and K. Holmen, “Modelling the impacts of a nitrogen pollution event on the biogeochemistry of an Arctic glacier,” *Annals of Glaciology*, vol. 51, no. 56, pp. 163–170, 2010.
- [35] A. Hodson, T. J. Roberts, A. C. Engvall, K. Holmén, and P. Mumford, “Glacier ecosystem response to episodic nitrogen enrichment in Svalbard, European High Arctic,” *Biogeochemistry*, vol. 98, no. 1–3, pp. 171–184, 2010.
- [36] Eklima, <http://ebas.nilu.no>.
- [37] Nilu Particulate Fallout and Precipitation Collectors, <http://www.niluinnovation.com/ProductsDivision/ParticulateFalloutandPrecipitationCollectors/tabid/1937/Default.aspx>.
- [38] Ebas, <http://www.eklima.no>.
- [39] EMEP, “Manual for sampling and chemical analysis,” EMEP/CCC Report 1/95, Norwegian Institute for Air Research, 1996.
- [40] WMO, “Manual for the gaw precipitation chemistry programme—guidelines, data quality objectives and standard operating procedures (Wmo Td No. 1251),” WMO Report 160, 2004.
- [41] A. G. Hjellbrekke and A. M. Fjæraa, “Data report 2009 acidifying and eutrophying compounds and particulate matter,” EMEP/CCC Report 1/2011, Norwegian Institute for Air Research, 2011.
- [42] D. Hirdman, H. Sodemann, S. Eckhardt et al., “Source identification of short-lived air pollutants in the Arctic using statistical analysis of measurement data and particle dispersion model output,” *Atmospheric Chemistry and Physics*, vol. 10, no. 2, pp. 669–693, 2010.